Demographics of supermassive black holes

Andreas Schulze

Leibniz-Institut für Astrophysik Potsdam (AIP)

Dissertation zur Erlangung des akademischen Grades
doctor rerum naturalium (Dr. rer. nat.)
in der Wissenschaftsdisziplin Astrophysik
Eingereicht an der Mathematisch-Naturwissenschaftlichen Fakultät
der Universität Potsdam

Mai 2011

Published online at the
Institutional Repository of the University of Potsdam:
URL http://opus.kobv.de/ubp/volltexte/2011/5446/
URN urn:nbn:de:kobv:517-opus-54464
http://nbn-resolving.de/urn:nbn:de:kobv:517-opus-54464

Contents

Abstract

Supermassive black holes are a fundamental component of the universe in general and of galaxies in particular. Almost every massive galaxy harbours a supermassive black hole (SMBH) in its center. Furthermore, there is a close connection between the growth of the SMBH and the evolution of its host galaxy, manifested in the relationship between the mass of the black hole and various properties of the galaxy's spheroid component, like its stellar velocity dispersion, luminosity or mass. Understanding this relationship and the growth of SMBHs is essential for our picture of galaxy formation and evolution. In this thesis, I make several contributions to improve our knowledge on the census of SMBHs and on the coevolution of black holes and galaxies.

The first route I follow on this road is to obtain a complete census of the black hole population and its properties. Here, I focus particularly on active black holes, observable as Active Galactic Nuclei (AGN) or quasars. These are found in large surveys of the sky. In this thesis, I use one of these surveys, the Hamburg/ESO survey (HES), to study the AGN population in the local volume ($z \approx 0$). The demographics of AGN are traditionally represented by the AGN luminosity function, the distribution function of AGN at a given luminosity. I determined the local ($z < 0.3$) optical luminosity function of so-called type 1 AGN, based on the broad band B_J magnitudes and AGN broad Hα emission line luminosities, free of contamination from the host galaxy. I combined this result with fainter data from the Sloan Digital Sky Survey (SDSS) and constructed the best current optical AGN luminosity function at $z \approx 0$. The comparison of the luminosity function with higher redshifts supports the current notion of "AGN downsizing", i.e. the space density of the most luminous AGN peaks at higher redshifts and the space density of less luminous AGN peaks at lower redshifts.

However, the AGN luminosity function does not reveal the full picture of active black hole demographics. This requires knowledge of the physical quantities, foremost the black hole mass and the accretion rate of the black hole, and the respective distribution functions, the active black hole mass function and the Eddington ratio distribution function. I developed a method for an unbiased estimate of these two distribution functions, employing a maximum likelihood technique and fully account for the selection function. I used this method to determine the active black hole mass function and the Eddington ratio distribution function for the local universe from the HES. I found a wide intrinsic distribution of black hole accretion rates and black hole masses. The comparison of the local active black hole mass function with the local total black hole mass function reveals evidence for "AGN downsizing", in the sense that in the local universe the most massive black holes are in a less active stage then lower mass black holes.

The second route I follow is a study of redshift evolution in the black hole-galaxy relations. While theoretical models can in general explain the existence of these relations, their redshift evolution puts strong constraints on these models. Observational studies on the black hole-galaxy relations naturally suffer from selection effects. These can potentially bias the conclusions inferred from the observations, if they are not taken into account. I investigated the issue of selection effects on type 1 AGN samples in detail and discuss various sources of bias, e.g. an AGN luminosity bias, an active fraction bias and an AGN evolution bias. If the selection function of the observational sample and the underlying distribution functions are known, it is possible to correct for this bias. I presented a fitting method to obtain an unbiased estimate of the intrinsic black hole-galaxy relations from samples that are affected by selection effects.

Third, I try to improve our census of dormant black holes and the determination of their masses. One of the most important techniques to determine the black hole mass in quiescent galaxies is via stellar dynamical modeling. This method employs photometric and kinematic observations of the galaxy and infers the gravitational potential from the stellar orbits. This method can reveal the presence of the black hole and give its mass, if the sphere of the black hole's gravitational influence is spatially resolved. However, usually the presence of a dark matter halo is ignored in the dynamical modeling, potentially causing a bias on the determined black hole mass. I ran dynamical models for a sample of 12 galaxies, including a dark matter halo. For galaxies for which the black hole's sphere of influence is not well resolved, I found that the black hole mass is systematically underestimated when the dark matter halo is ignored, while there is almost no effect for galaxies with well resolved sphere of influence.

Zusammenfassung

Supermassereiche Schwarze Löcher sind ein fundamentaler Bestandteil unseres Universims im Allgemeinen, und von Galaxien im Besonderen. Fast jede massereiche Galaxie beherbergt ein supermassereiches Schwarzes Loch in seinem Zentrum. Außerdem existiert eine enge Beziehung zwischen dem Wachstum des Schwarzen Loches und der Entwicklung seiner umgebenden Galaxie. Diese zeigt sich besonders in der engen Beziehung zwischen der Masse eines Schwarzen Loches und den Eigenschaften der sphäroidalen Komponente der Galaxie, beispielsweise seiner stellaren Geschwindigkeitsdispersion, seiner Leuchtkraft und seiner Masse. Diese Beziehung erklären zu können, sowie das Wachstum von Schwarzen Löchern zu verstehen, liefert einen wichtigen Beitrag zu unserem Bild der Entstehung und Entwicklung von Galaxien. In dieser Arbeit steuere ich verschiedene Beiträge dazu bei unser Verständnis des Vorkommens Schwarzer Löcher und der Beziehung zu ihren Galaxien zu verbessern.

Zunächst versuche ich ein vollständiges Bild der Anzahl und Eigenschaften Schwarzer Löcher zu erhalten. Dazu beschränke ich mich auf aktive Schwarze Löcher, wie man sie im Universum als Aktive Galaxienkerne (AGN) in großen Himmelsdurchmusterungen finden kann. Ich benutze eine solche Durchmusterung, das Hamburg/ESO Survey (HES), um die AGN Population im lokalen Universum zu studieren. Dazu habe ich die optische Leuchtkraftfunktion von AGN des Typs 1 bestimmt. Diese habe ich mit anderen Ergebnissen leuchtschwächerer AGN kombiniert um die bisher beste AGN Leuchtkraftfunktion bei $z \approx 0$ zu erhalten. Der Vergleich mit Ergebnissen bei höherer kosmischer Rotverschiebung bestätigt unser Bild des sogenannten "AGN downsizing". Dies sagt aus, dass leuchtkräftige AGN bei hoher Rotverschiebung am häufigsten vorkommen, während leuchtschwache AGN bei niedriger Rotverschiebung am häufigsten sind.

Allerdings verrät uns die AGN Leuchtkraftfunktion allein noch nicht das ganze Bild der Demographie Schwarzer Löcher. Vielmehr sind wir an den zugrunde liegenden Eigenschaften, vor allem der Masse und der Akkretionsrate der Schwarzen Löcher, sowie deren statistischen Verteilungsfunktionen, interessiert. Ich habe eine Methode entwickelt um diese beiden Verteilungsfunktionen zu bestimmen, basierend auf der Maximum-Likelihood-Methode. Dabei berücksichtige ich vor allem vollständig die Auswahleffekte der Stichprobe. Ich habe diese Methode benutzt um die aktive Massenfunktion Schwarzer Löcher, sowie die Verteilungsfunktion ihrer Akkretionsraten für das lokale Universum aus dem HES zu bestimmen. Sowohl die Akkretionsraten, als auch die Massen der Schwarzen Löcher zeigen intrinsisch eine breite Verteilung, im Gegensatz zur schmaleren beobachtbaren Verteilung. Der Vergleich der aktiven Massenfunktion mit der gesamten Massenfunktion Schwarzer Löcher zeigt ebenfalls Hinweise auf "AGN downsizing", in dem Sinne, dass im lokalen Universum die schwersten Schwarzen Löcher weniger aktiv sind als ihre leichteren Verwandten.

Als nächstes habe ich mich mit Untersuchungen zur zeitlichen Entwicklung in den Beziehungen zwischen Schwarzem Loch und Galaxie beschäftigt. Diese kann helfen unser theoretisches Veständnis der physikalischen Vorgänge zu verbessern. Beobachtungen sind immer auch Auswahleffekten unterworfen. Diese können die Schlussfolgerungen aus den Beobachtungen zur Entwicklung in den Beziehungen beeinflussen, wenn sie nicht entsprechend berücksichtigt werden. Ich habe den Einfluss von Auswahleffekten auf Typ 1 AGN Stichproben im Detail untersucht, und verschiedende möchgliche Einflussquellen identifiziert, die die Beziehung verfälschen können. Wenn die Auswahlkriterien der Stichprobe, sowie die zugrunde liegenden Verteilungen bekannt sind, so ist es möglich für die Auswahleffekte zu korrigieren. Ich habe eine Methode entwickelt, mit der man die intrinsische Beziehung zwischem Schwarzem Loch und Galaxie aus den Beobachtungen rekonstruieren kann.

Schließlich habe ich mich auch inaktiven Schwarzen Löchern und der Bestimmung ihrer Massen gewidmet. Eine der wichtigsten Methoden die Masse Schwarzer Löcher in normalen Galaxien zu bestimmen ist stellardynamische Modellierung. Diese Methode benutzt photometrische und kinematische Beobachtungen, und rekonstruiert daraus das Gravitationspotenzial aus der Analyse stellarer Orbits. Diese Methode kann ein supermassereiches Schwarzes Loch im Zentrum der Galaxie entdecken und seine Masse bestimmen, sofern das gravitative Einflussgebiet des Schwarzen Loches räumlich aufgelöst wird. Bisher wurde in diesen Modellen allerdings der Einfluss des Halos aus Dunkler Materie vernachlässigt. Dieser kann aber die Bestimmung der Masse des Schwarzen Loches beeinflussen. Ich habe 12 Galaxien mit Hilfe stellardynamischer Modellierung untersucht und dabei auch den Einfluss des Halos aus Dunkler Materie berücksichtigt. Für Galaxien bei denen der Einflussbereich des Schwarzen Loches nicht sehr gut aufgelöst war, wird die Masse des Schwarzen Loches systematisch unterschätzt, wenn der Dunkle Materie Halo nicht berücksichtigt wird. Auf der anderen Seite ist der Einfluss gering, wenn die Beobachtungen diesen Einflussbereich gut auflösen können.

Chapter 1

Introduction

1.1. Active Galactic Nuclei

1.1.1. AGN phenomenology

Active Galactic Nuclei (AGN) are essential ingredients of our universe. AGN activity constitutes an important phase in the life and evolution of galaxies. Thus, we need to understand these objects and their connection to their host galaxies for a comprehensive picture of galaxy formation and evolution. Furthermore, AGNs are excellent laboratories to study high energy and strong gravity processes.

AGN are sub-divided into several sub-classes, like Seyfert galaxies, QSOs or quasars, Blazars, LINERs and Radio galaxies. While they all differ in appearance, they share some common properties. Characteristic are prominent high-ionization emission lines, especially in Seyfert galaxies and QSOs. The additional sub-classes of Seyfert 1 galaxies and type 1 QSOs show narrow forbidden lines, like [O III] or [N II], and broad permitted lines ($FWHM > 1000$ km s^{-1}), like the Balmer lines or Mg II in their spectra. On top of the broad lines, often also a narrow component is present. On the other hand, Seyfert 2 galaxies and type 2 QSOs also show narrow forbidden lines, but lack broad lines. Their permitted lines are also narrow.

Seyfert galaxies and QSOs form a continuous population, with their main difference being the luminosity of the nuclear point source. Seyfert galaxies harbour lower luminosity AGN, whereas QSOs are high luminosity AGN. Indeed, QSOs belong to the most luminous objects in the universe. While in Seyfert galaxies the AGN host galaxy is conspicuous, in QSOs it is outshined by the luminous AGN. A careful subtraction of the point source in QSOs is required to reveal the underlying host galaxy (e.g. McLeod & Rieke 1994a,b; Bahcall et al. 1997; McLure et al. 1999), utilizing high resolution ground based or *Hubble Space Telescope* (*HST*) observations. These studies showed that QSOs preferentially (although not exclusively) reside in massive elliptical galaxies, whereas Seyfert host galaxies are mainly spiral galaxies. This morphological difference is understood by the fact that more luminous AGN on average harbour more massive black holes, and the presence of a tight correlation between the mass of the black hole and the mass of the galaxies bulge component (see Section 1.3.1).

A fraction of the AGN population is radio-loud, including radio-loud quasars ($\sim$ 10%), radio galaxies and blazars. Furthermore, AGN show a broad spectral energy distribution (SED), ranging from X-rays or even γ-rays, over the UV and optical to infrared (IR), up to the radio regime (at least for radio-loud AGN). On narrow frequency ranges, the SED can be approximated well by a power law of the form $f_\nu \sim \nu^{-\alpha}$, with typical values in the optical regime of $0 \lesssim \alpha \lesssim 1$ (e.g. Vanden Berk et al. 2001).

Almost all AGN show rapid optical variability, on nearly all time scales, from years up to a few days. This variability is not only observed in the continuum but also in the broad emission lines. Light travel arguments imply that emission with variability of a few days has to originate in a region of the size of a few light-days. Thus, AGN variability provides evidence for small spatial scales related to the AGN phenomenon.

1.1.2. AGN structure

Our standard model of the AGN structure is already able to explain a large fraction of the AGN phenomenology. The different AGN classes are unified by means of intrinsic luminosity and orientation. Nevertheless, many open questions on the structure and properties of AGN remain.

It is now well established that the energy source of AGN is accretion of gas and dust onto supermassive black holes (Salpeter 1964; Lynden-Bell 1969). This is based on theoretical grounds, as it is the only possible explanation for the observed AGN phenomena (e.g. Rees 1984). Furthermore, there is strong evidence for the presence of a compact, massive object, most probably a supermassive black hole in the center of quiescent galaxies (see section 1.2).

The gravitational potential energy of the infalling material is converted into kinetic energy and through dissipation into heat and radiation. The emitted luminosity is

$$L = \eta \dot{M} c^2 \,, \tag{1.1}$$

were $\dot{M} = dM/dt$ is the mass accretion rate onto the black hole, and η is the radiative efficiency of the energy production in terms of the rest mass energy. This efficiency depends on the radius at which the emission process occurs. For non-rotating Schwarzschild black holes the innermost stable orbit is at $r = 6GM_\bullet/c^2$, corresponding to a maximum efficiency of $\eta = 0.057$. For maximally rotating Kerr black holes the efficiency increases up to $\eta = 0.42$ (Novikov & Thorne 1973). The commonly adopted value is $\eta \approx 0.1$. Thus, to power a luminous QSO with $L_{\rm Bol} \approx 10^{46}$ erg s^{-1} an accretion rate of $\dot{M} \approx 2 M_\odot$ yr^{-1} is required. This means that during QSO phases the black hole is growing with time through mass accretion.

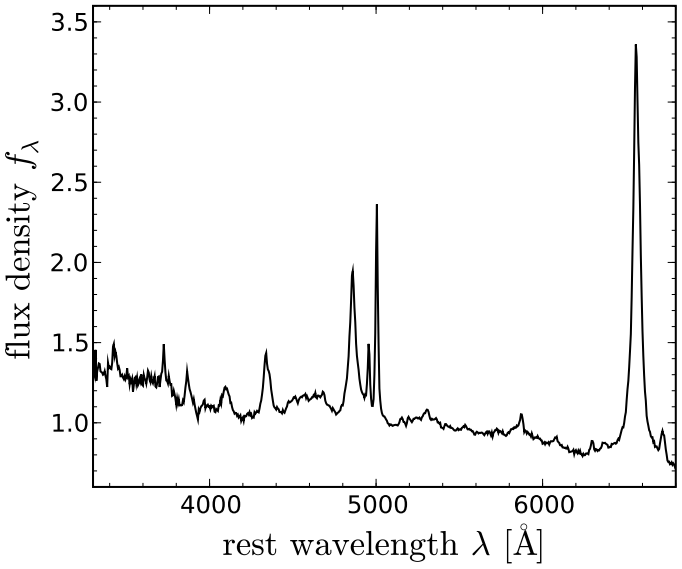

Fig. 1.1. Composite quasar spectrum from the Hamburg/ESO Survey QSO sample in the rest-frame wavelength optical range. All spectra with $z < 0.3$ have been used to construct the composite. The most prominent emmission lines are the broad Balmer lines and the narrow [O III] doublet.

An indication for the maximum luminosity of an accreting black hole is given by the Eddington luminosity

$$L_{\rm Edd} = \frac{4\pi\, G\, c\, m_p}{\sigma_T} M_\bullet \cong 1.3 \times 10^{38} \left(\frac{M_\bullet}{M_\odot}\right) {\rm erg\,s^{-1}}\,, \qquad (1.2)$$

with G the Gravitational constant, c the speed of light, m_p the proton mass and σ_T the Thomson cross section. Its the luminosity in the equilibrium state between the gravitational force and the force from radiation pressure. The Eddington limit is the luminosity limit in the case of spherical accretion. However, super-Eddington accretion is possible for non-spherical accretion, e.g. within a disk, while the radiation is primarily emitted along the disk axis.

Indeed, in AGN the accretion onto the black hole is funneled through a disk. Within the disk, angular momentum has to be transported outwards, while the gas is carried inwards, allowing accretion onto the black hole. This is achieved by viscosity in the disk, probably due to turbulent motion (Shakura & Sunyaev 1973). A possible source for this turbulence are magnetorotational instabilities (Balbus & Hawley 1991), however the details are currently poorly known. The emitted spectrum from an AGN accretion disk is the composite of thermal spectra with individual temperatures throughout the disk, peaking around $\sim$ 100 Å. The disk emission mainly contributes to the UV and soft X-rays, giving rise to the "big blue bump" observed in the UV in the AGN SED (Shields 1978). The additional soft X-ray to hard X-ray emission is believed to originate in a hot corona of ionized plasma, surrounding the accretion disk, radiating via bremsstrahlung and/or inverse Compton scattering of disk photons.

Usually, the disk is assumed to be optically thick and geometrically thin, corresponding to an radiatively efficient accretion flow. An alternative accretion mode is an optically thin, geometrically thick disk, corresponding to an radiatively inefficient accretion flow (RIAF). This can be for example via an advection dominated accretion flow (ADAF; Narayan & Yi 1994; Yuan 2007). The kinetic energy is not radiated, but either advected with the matter into the black hole, or redirected into an outflow. Such a mode is expected for low luminosity AGNs, like Low Ionization Nuclear Emission Region galaxies (LINERs). This picture has been challenged recently by the observation of SEDs in low luminosity AGN showing a big blue bump (Maoz 2007), but they are also consistent with ADAF model spectra (Yu et al. 2011).

The optical emission lines in AGN spectra are thought to originate in two separate regions, at different distances from the central black hole. The broad emission lines are emitted in a relatively dense ($n_e \sim 10^{10}$ cm^{-3}), unresolved area, the so-called broad line region (BLR), close to the accretion disk. The BLR is photonionized by the UV radiation from the disk, producing the observed broad recombination lines. The line widths of 500 km/s up to 10000 km/s full width at half maximum (FWHM) are interpreted as Doppler shifts from bulk gravitational motion of optically thick gas clouds in the vicinity of the black hole (of the order of several light-days). The geometry and kinematics of the BLR are poorly known. A common, simple assumption is a spherical BLR. However, there is also evidence for a disk-like structure, at least for radio-loud AGN (Wills & Browne 1986; Brotherton 1996; Vestergaard et al. 2000). Also for radio-quiet AGN a non-spherical BLR is implied (McLure & Dunlop 2002; Smith et al. 2005; Labita et al. 2006). The question if the BLR also exhibits inflows and/or outflows is still unresolved. An observational tool to study the BLR, and potentially also probe their structure, is reverberation mapping (see 1.2.2).

The narrow emission lines originate in optically thin gas, spatially extended on scales up to several kpc, the narrow line region (NLR). The NLR can be spatially resolved. The electron density in the NLR is in the range $n_e \sim 10^4 - 10^6$ cm^{-3}, sufficiently low for forbidden lines to arise, which would be collisionally suppressed otherwise. The line widths range from 200 km/s to 900 km/s FWHM.

The main difference between Seyfert 1 and Seyfert 2 galaxies is the presence or absence of broad emission lines. Both classes are successfully joined in the standard unified paradigm, based on an orientation effect (Antonucci 1993). This postulates the presence of a dusty torus, or some sort of toroidal obscuring region, outside of the BLR but inside of the NLR. If the viewing angle is nearly edge-on, the BLR is shielded from our view by the torus - the AGN appears as a Seyfert 2, with a much weaker AGN continuum radiation and without an observed BLR. If the viewing angle is face-on, the BLR is seen and the AGN is classified as a Seyfert 1. The narrow lines are emitted on a larger scale in the NLR and are thus always seen.

This unification is also valid for the higher luminosity quasars, with type-1 QSOs corresponding to Seyfert 1s and type-2 QSOs corresponding to Seyfert 2s, although most QSOs detected in optical/UV AGN surveys are type-1 and only a few type-2 QSOs are known (Zakamska et al. 2003). Indeed, it is known that the type 2 fraction depends on AGN luminosity, with a decrease of the type 2 fraction for increasing luminosity. This trend is seen at all wavelengths, in the optical (Hao

et al. 2005; Simpson 2005), in the mid-IR (Maiolino et al. 2007; Treister et al. 2008) and in X-rays (Ueda et al. 2003; Hasinger 2008). In the unified scheme, this corresponds to a decrease of the opening angle of the torus, with increasing luminosity.

Strong support for the unified picture comes from spectropolarimetric observations of Seyfert 2 galaxies (Antonucci & Miller 1985; Tran 1995a,b) and type 2 QSOs (Zakamska et al. 2005). The first discussed case was the prototypical Seyfert 2 galaxy NGC 1068, which revealed weak broad lines in the polarised light. This is due to light from the BLR reflected into our line of sight by dust and electrons in the NLR. Thus, NGC 1068 contains a BLR, hidden to our view by an obscuring torus.

The continuum radiation from the accretion disk is absorbed by the dusty torus, and re-emitted in the mid-infrared. Interferometric observations of nearby Seyfert 2s in the mid-infrared could even spatially resolve the torus, as a geometrically thick, dust distribution of clumpy material (Jaffe et al. 2004; Tristram et al. 2007; Raban et al. 2009). They support ideas of a clumpy torus, as a continuation of the BLR beyond the dust sublimation radius (e.g. Elitzur & Shlosman 2006; Elitzur 2008; Nenkova et al. 2008).

Radio-loud AGN additionally posses a relativistic outflowing jet, mainly observed in the radio. It originates in the vicinity of the black hole, perpendicular to the accretion disk, and can extend to large scales, up to megaparsecs, where it runs into a lobe. Radio-loud AGN can also be largely unified by orientation (Antonucci 1993; Urry & Padovani 1995). In powerful radio galaxies (of so-called FR II type), the AGN is viewed, analog to Seyfert 2s, more edge-on, while in radio-loud quasars we see the AGN under a smaller viewing angle. In Blazars (BL Lac objects and Optically Violent Variable quasars), we view the AGN almost face-on, thus with a small angle to the relativistic jet. This scheme can adequately explain the observed diversity in radio-loud AGN. The SED in radio-loud AGN, and in particular in blazars, is dominated by non-thermal emission from the jet. This is mainly synchrotron radiation in the radio to the UV/X-ray regime, and inverse Compton scattering from X-rays up to the γ-ray regime.

Further information on the history of AGN, their phenomenology, properties and structure can be found for example in Shields (1999), Peterson (1997), Krolik (1999), Osterbrock & Ferland (2006) and Mo et al. (2010).

1.1.3. AGN Surveys

To study the AGN population as a whole, first of all well-defined AGN samples have to be constructed. These are derived from AGN surveys. These surveys provide a list of AGN candidates, which have to be confirmed by follow-up spectroscopy. There are different selection techniques, each with their own advantages and drawbacks, finding often different kinds of objects.

Radio surveys were historically the first survey method. They can find AGN that do not show prominent emission lines and would otherwise not be selected as AGN. However, only $\sim$ 10% of all AGN are radio-loud, thus the results are not representative for the whole population. Recent large radio surveys include the NRAO VLA Sky Survey (Condon et al. 1998) and FIRST (Faint Images of the Radio Sky at Twenty-cm; Becker et al. 1995).

The most common search technique in the optical is colour selection, to distinguish QSOs from stars. The classical method is via UV excess (e.g. Schmidt & Green 1983; Marshall et al. 1983). QSOs have a high UV flux and thus a blue $U-B$ colour, compared to stars. A cut in $U-B$ plus optionally an additional morphological restriction to point sources turned out to be effective in selecting QSOs for $z \lesssim 2.3$. At larger z Lyα is redshifted into the B band and the $U-B$ colours become comparable to stars. A selection in multi-colour space is able to extend this range significantly (Warren et al. 1991; Fan et al. 1999; Richards et al. 2002a). An extension of this colour space into the near-IR is able to find QSOs at $z \gtrsim 4$ (e.g. Fan et al. 2001a; Willott et al. 2007; Richards et al. 2009; Glikman et al. 2010), as well as QSOs missed by optical colour selection (Maddox et al. 2008).

Another optical selection technique is slittless spectroscopy (Hewett et al. 1985, 1995; Wisotzki et al. 1996). An objective prism or grism is placed in front of a wide field telescope and so low resolution spectra of all objects within the field of view are obtained. With this technique a large number of spectra are obtained within a single exposure, however at the risk of spectral overlaps, in particular in crowded fields. The selection can be based on emission lines or quasar like SEDs.

Additionally, AGN samples free of any preselection can be obtained as a by-product of large spectroscopic surveys (Gavignaud et al. 2006; Merloni et al. 2010), based on the prominent emission lines in their spectra.

Quasars belong to the most luminous objects in most wavelengths regions, including X-rays. Indeed, luminous X-ray emission of a point source is an efficient tracer of AGN activity, also picking up optically obscured AGN. Large X-ray surveys by satellite missions like ROSAT, Chandra and XMM-Newton collected large samples of AGN (e.g. Miyaji et al. 2000; Hasinger et al. 2005). Nevertheless, follow up spectroscopy of these AGN candidates is sometimes hampered by their faint optical appearance.

Having selected a well defined sample in such a survey, one is able to study the statistical properties of the population as a whole, i.e. derive AGN demographics.

1.1.4. AGN evolution

It is known for a long time that the quasar space density is not constant with redshift, but there is an increase in the space density towards higher z. This has been indicated by simple tests on quasar surveys, like the $\log N - \log S$ test or the $V/V_{\rm max}$ test (e.g. Schmidt 1968; Wills & Lynds 1978).

More detailed information on the AGN population and its evolution can be obtained from the AGN luminosity function (LF), giving the number density of AGN per luminosity interval:

$$\phi(L,z) = \frac{{\rm d}^2 N}{{\rm d}V{\rm d}L}(L,z)\,. \tag{1.3}$$

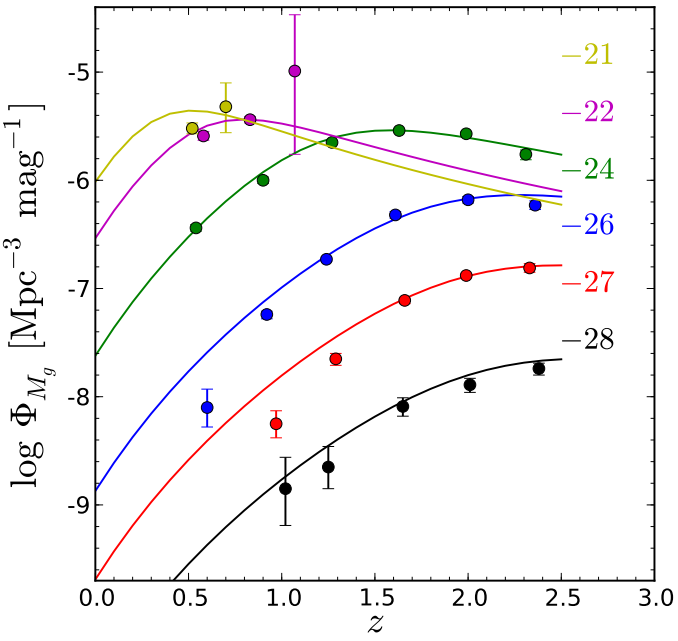

Fig. 1.2. Space density of optically selected type 1 QSOs in different luminosity bins. The peak in the space density is shifted towards lower z for fainter sources. The circles show the binned data from Croom et al. (2009), determined from SDSS and 2SLAQ, the solid lines give their best fit LDDE model.

The most common parameterisation for the AGN LF is a double power law (Marshall 1987; Boyle et al. 2000)

$$\phi(L) = \frac{\phi^*/L_*}{(L/L_*)^\alpha + (L/L_*)^\beta} \tag{1.4}$$

where L_* is a characteristic break luminosity and α and β are the bright-end slope and faint-end slope.

Studies of the QSO luminosity function found a strong increase of their space density toward higher z, with a maximum at $z \approx 2$ and a decrease of the space density thereafter (Warren et al. 1994; Schmidt et al. 1995; Fan et al. 2001b; Wolf et al. 2003). Several simple evolutionary models have been suggested to parameterise AGN evolution, like pure density evolution (PDE) or pure luminosity evolution (PLE). While they provide an adequate fit to specific surveys (e.g. Boyle et al. 2000; Croom et al. 2004), especially covering the bright end of the LF, they fail as a proper model for the full AGN LF evolution. The simple PLE model breaks down at low redshift (Koehler et al. 1997), at high redshift (e.g. Richards et al. 2006) and at fainter luminosities (Bongiorno et al. 2007, e.g.).

X-rays surveys required a luminosity dependent density evolution model (LDDE; Ueda et al. 2003; Hasinger et al. 2005; Silverman et al. 2008), due to their coverage of the faint end of the AGN LF. They found a flattening of the faint-end slope with redshift. This means that the space density for less luminous AGN peaks at lower z, as shown in Fig. 1.2. This behaviour is known as "AGN cosmic downsizing", in analogy to the downsizing behaviour found for galaxies (Cowie et al. 1996). The AGN downsizing behaviour has also been observed in the optical AGN LF (Bongiorno et al. 2007; Croom et al. 2009) and is consistent with a compilation of the bolometric luminosity function (Hopkins et al. 2007).

The inferences drawn from the AGN LF evolution on the growth of black holes are discussed in section 1.4.

1.2. Supermassive black holes

1.2.1. Direct dynamical BH measurements

It is well established that almost every massive galaxy contains a supermassive black hole (SMBH) with $10^6 - 10^{10}\,M_\odot$ in its center (Kormendy & Richstone 1995). These SMBHs in normal, quiescent galaxies are the silent witnesses of past AGN activity and black hole growth. The first step to study these SMBHs is to verify their existence and determine their masses. In this section, we present various direct methods to measure the mass of central black holes. Reviews on this subject can be found in Kormendy & Richstone (1995) and Ferrarese & Ford (2005).

A critical condition for the detection of a central SMBH is that the black hole's sphere of influence is at least approximately resolved. The sphere of influence is defined by the radius at which the gravitational influence of the central black hole still significantly influences the stellar dynamics, given by

$$R_{\rm inf} = \frac{GM_\bullet}{\sigma_*} = 10.8\,{\rm pc}\left(\frac{M_\bullet}{10^8\,M_\odot}\right)\left(\frac{\sigma_*}{200\,{\rm km\,s^{-1}}}\right)^{-2}. \tag{1.5}$$

While the radius of the sphere of influence is no strict limit, it is clear that for a spatial resolution much smaller than this, the gravitational influence of the SMBH is not resolvable. Thus this criterion restricts our ability to detect a black hole of arbitrary mass in a given galaxy. High spatial resolution is required, for most galaxies only achievable by HST or ground-based adaptive optics (AO) observations.

The black hole in the Galactic Center

The closest SMBH is located in the center of our own Milky Way, ~ 8 kpc away. While in the optical our view is blocked by dust, in the radio a bright source has been found, known as Sgr A*. This objects has to be very compact, smaller than 1 AU, based on Very Long Baseline Interferometry (VLBI) measurements (Doeleman et al. 2001), and also massive, based on a lack of proper motions (Reid et al. 2003).

In the near-IR, high resolution astrometric observations have been carried out to measure proper motions and radial velocities of individual stars in the vicinity of Sgr A* (e.g. Ghez et al. 2003; Schödel et al. 2003). These confirm the presence of a massive object at the position of Sgr A*, with a mass of $4.3 \times 10^6\,M_\odot$ (Gillessen et al. 2009), constraining the central mass density to $\rho > 3 \times 10^{19}\,M_\odot\,{\rm pc}^{-3}$. This high density leaves the presence of a SMBH as the only realistic possibility. The sphere of influence is clearly resolved to several orders of magnitude. Thus the center of the Milky Way provides the best evidence for a black hole in the center of a galaxy.

H_2O Megamaser gas dynamics

The detection of a Keplerian H_2O Megamaser disk in a few active galaxies allows the verification and mass determination of

SMBHs in other galaxies with unprecedented accuracy. Such luminous water masers can form in the torus of an AGN (Neufeld et al. 1994). When illuminated and heated by X-ray emission from the innermost accretion disk, a warped, circumnuclear molecular disk, with high water abundance, may form in the midplane direction. This molecular disk gives rise to collisionally pumped H_2O emission at 22 GHz. Additionally, a large path-length through the disk is required for a sufficiently strong signal, so the disk should be seen almost edge-on. This restricts water maser candidates to Seyfert 2 galaxies and LINERS. Unfortunately, Megamasers are not common, and the detection of a rotating disk in the maser emission is even more rare.

The best example is in the Seyfert 2 galaxy NGC 4258. VLBI observations revealed water maser emission in a thin, warped, nearly edge-on molecular disk, extending from 0.17 – 0.28 pc from the central massive object (e.g. Miyoshi et al. 1995; Herrnstein et al. 1999). The spatially resolved disk emission displays Keplerian motion around a SMBH with $3.8 \times 10^7\,M_\odot$ (Herrnstein et al. 2005). The use of VLBI allows a spatial resolution two orders of magnitude higher than with optical telescopes (like HST), which is crucial for the resolution of the black hole's sphere of influence and the detection of lower mass SMBHs.

Until recently, only a hand full of other H_2O Megamaser disks were known, with less reliable black hole mass estimates, either because the disk could not be spatially resolved (e.g. Henkel et al. 2002), the rotation turned out to be not Keplerian (Greenhill & Gwinn 1997) or the disk inclination is not known (Greenhill et al. 2003). Recently, Kuo et al. (2011) reported the detection of spatially resolved maser disks in seven additional galaxies. Most of them show clear Keplerian rotation in thin, almost edge-on disks, allowing a secure black hole mass measurement. These observations significantly boosted the sample of H_2O Megamaser black hole masses.

Gas kinematics

A fraction of all galaxies posses disks of ionized gas in their nuclear regions (e.g. Tran et al. 2001). The dynamics of these gas disks can be used to infer the presence of SMBHs in the center of these galaxies. Gas dynamical methods have been applied successfully to several elliptical (Ferrarese et al. 1996; Macchetto et al. 1997; Dalla Bontà et al. 2009) and spiral galaxies (Sarzi et al. 2001; Devereux et al. 2003). HST resolution turned out to be essential for gas dynamical studies, to resolve the black hole's sphere of influence, beyond very nearby galaxies, like Centaurus A (Marconi et al. 2001; Neumayer et al. 2007).

The central region of the galaxy is mapped spectroscopically, using either long slit spectra along different positions or Integral Field Unit (IFU) spectroscopy. A two-dimensional velocity field is reconstructed from the measured emission lines. A model velocity field is then fitted to the data. The modeled rotational velocity is based on the gravitational potential of the central massive object, the stellar density and the contribution of the gas disk itself, usually assuming a thin rotating disk, and is projected along the line-of-sight. This projection requires knowledge of the inclination angle of the disc. The SMBH mass is then derived as one of the free parameters in the fit. If the inclination angle is not well constrained, the uncertainty of the mass measurement can increase significantly.

Another potential drawback of gas dynamics measurements are non-gravitational motions that may affect the gas disk. However, their presence can be deduced from the observed velocity field and the respective galaxy can be dismissed for a gas dynamical mass determination.

Stellar kinematics

While gas disk are only present in a fraction of galaxies and can be affected by non-gravitational motions, stars can always be observed in galaxies and their motion is purely gravitational. Most galaxies can be treated as collisionless stellar systems. Thus the stellar motion is determined by a gravitational potential, given by all stars in the galaxy and the central SMBH (plus the contribution from dark matter). Studying the motion of stars within the range of gravitational influence of the black hole, can reveal its presence and mass. Generally, stellar dynamical modeling is not only able to determine the black hole mass, but also the galaxy's mass-to-light ratio, the orbital structure (e.g. Cappellari et al. 2007) and the dark matter halo (e.g. Thomas et al. 2007).

The first such study was performed on M 87 by Sargent et al. (1978), assuming a spherically symmetric and isotropic galaxy configuration. However, these simplifying assumptions are in general not justified and more sophisticated dynamical models are required. A spherical, isotropic stellar system conserves only one integral of motion, namely the energy.

In current stellar dynamical models usually axisymmetry is assumed. A still relative simple approach is based on anisotropic spherical Jeans models (Binney et al. 1990; van der Marel et al. 1998; Cappellari 2008), using two integrals-of-motion. Compared to more elaborate models, this approach is computationally less expensive, and the results can be assessed and inspected more directly. However, further assumptions are required that do not have to be fulfilled and the solutions are rarely unique. It is commonly used to independently verify the results from more general modeling (e.g. Cretton & van den Bosch 1999; Cappellari et al. 2009).

A more general approach is the Schwarzschild (1979) orbit-superposition method. This numerical method computes an orbit library in a given gravitational potential and fits these orbits to the data. Usually three integrals of motion are used. The input data are the stellar surface brightness profile and spectral measurements along several position angles. From the latter, the line-of-sight velocity distributions (LOSVDs) at different positions in the galaxy are deduced. The surface brightness profile is deprojected to a three-dimensional luminosity distribution, and converted to a mass distribution, assuming a fixed mass-to-light ratio for the whole galaxy. Together with the central SMBH this defines the gravitational potential. In this potential a large and representative number of stellar orbits are computed by numerical integration of the equations of motion. Each orbit contributes to the LOSVD at a given position. These predicted LOSVDs are fitted to the observed LOSVDs at the observed positions in the galaxy. The best fit solution provides the orbital

structure and goodness of fit for the input mass-to-light ratio and $M_\bullet$. The overall best fit is found by repeating this procedure for a grid of the free parameters. Therefore, the method is computationally expensive. The observed LOSVDs are given either as moments of a Gauss-Hermite fit to the data, or in nonparametric binned form. Further details can be found in Chapter 7, or e.g. in Cretton & van den Bosch (1999), Thomas et al. (2004) and Siopis et al. (2009).

The Schwarzschild technique has been applied very successfully in the last years, and led to the detection of a large number of SMBHs in quiescent galaxies (van der Marel et al. 1998; Gebhardt et al. 2003; Shapiro et al. 2006; Gültekin et al. 2009a). Nevertheless, this method also suffers from uncertainties and potential systematics. First, the deprojection requires the knowledge of the inclination of the galaxy, which often is only poorly known. Dust or a weak AGN in the center can affect the LOSVD measurements. The assumption of axisymmetry does not hold for all galaxies, and triaxial Schwarzschild modeling indicated that this can affect the measured black hole mass (van den Bosch & de Zeeuw 2010). Finally, also the presence of the dark matter halo, not accounted for in most cases, can bias the mass determination (Gebhardt & Thomas 2009). This thesis made a contribution to a better understanding of this last point. The performed work and the results are presented in Chapter 7.

Direct comparisons of black hole mass determinations from different methods for the same galaxy are sparse. There are a few cases with both, gas dynamical and stellar dynamical mass measurements. For IC 1459 both seem to disagree (Cappellari et al. 2002). However, both measurements are highly uncertain, preventing to draw firm conclusions. For NGC 3379 (Shapiro et al. 2006) and Centaurus A (Cappellari et al. 2009), good agreement has been found between both methods. Siopis et al. (2009) presented a stellar dynamical mass measurement of the Maser galaxy NGC 4258, finding broad agreement between the two, while their results suffer from uncertainties due to the presence of the AGN and dust. Finally, Onken et al. (2007) presented a tentative stellar dynamical mass measurement for the Seyfert 1 galaxy NGC 4151 that is in broad agreement with the value from reverberation mapping (see next section).

1.2.2. Reverberation mapping

Dynamical methods require the resolution of the black hole's sphere of influence and are therefore limited to relatively nearby systems. For broad line (type 1) AGN an alternative method exists, studying the dynamics of the BLR via reverberation mapping (Blandford & McKee 1982; Peterson 1993). This technique uses the variability of quasars in the continuum and the emission lines. A luminosity change in the ionizing UV continuum will lead to a response of the broad emission lines with a time delay, due to the light travel time. An average time delay τ for the BLR clouds can be obtained from the cross-correlation of the continuum light curve with the emission line light curve. This time delay yields the size of the line-emitting region for the particular emission line, thus an estimate of the size of the BLR, via $R_{\rm BLR} = c\tau$.

The great advantage of this method is that it does not depend on high spatial resolution to measure the size of the BLR. Spatial resolution is effectively traded for time resolution. Therefore, the continuum and emission line light curve have to be measured reliably, demanding extensive observational monitoring campaigns. In general, this technique is not limited by distance. However, in practice luminous high-z AGN have large time delays, exaggerated by cosmological time dilation, and low variability amplitudes. Only few objects have been measured yet above $z \sim 0.3$ (Kaspi et al. 2007).

The dynamics of the broad line region can reveal the presence of the central SMBH, if the motion of the BLR clouds is dominated by gravity and not by outflows or radiation pressure. In this case, virial equilibrium is present, and $M_\bullet$ is given by:

$$M_\bullet = \frac{f R_{\rm BLR} \Delta V^2}{G} \,, \tag{1.6}$$

where $R_{\rm BLR}$ is the size of the BLR, ΔV is the broad line width in km/s and f is a scaling factor of order unity, which depends on the structure, kinematics and orientation of the BLR. The scale factor f effectively converts the measured broad line width into the velocity of the BLR clouds. The validity of the virial assumption has been verified by the measurement of time lags and line widths for different broad lines in the same spectrum. Different lines show different time delays and have different line widths, but they follow the expected virial correlation $\tau \propto \Delta V^{-2}$ (Wandel et al. 1999; Peterson & Wandel 2000; Onken & Peterson 2002).

A significant uncertainty is the value of f, as the BLR structure is poorly known. For the simple assumption of a spherical BLR, $f = 0.75$ with no dispersion (e.g. Krolik 2001). However, the BLR is probably not spherical. For a disk-like BLR, f depends on the viewing angle and the disk structure. The common approach to determine f is using the $M_\bullet - \sigma_*$ relation for quiescent galaxies. As discussed in section 1.3.1, there is a close correlation between black hole mass and stellar velocity dispersion in the galaxy's bulge component, both for quiescent galaxies and active galaxies (e.g. Gebhardt et al. 2000b; McLure & Dunlop 2001). Onken et al. (2004) used this relation to determine an average scale factor $\langle f \rangle 05.5$, by normalizing the reverberation mapping masses to the $M_\bullet - \sigma_*$ relation (see also Collin et al. 2006; Woo et al. 2010).

A direct determination of f and thus $M_\bullet$ from reverberation mapping could potentially be obtained by velocity resolved reverberation mapping (Welsh & Horne 1991; Horne et al. 2004). Using not only the line flux, but the full line profile, the BLR velocity field, and therefore the BLR structure, can be recovered. While this approach was hampered by poor spectroscopic data in the past, recently first promising results on velocity resolved reverberation mapping have been published (e.g. Bentz et al. 2009b, 2010).

Another open question is what line width estimate to use. While often the FWHM is used, there is evidence that the line dispersion $\sigma_{\rm line}$, i.e. the second central moment of the line profile, is the preferable width measurement for reverberation mapping data. Peterson et al. (2004) found that, using $\sigma_{\rm line}$ from

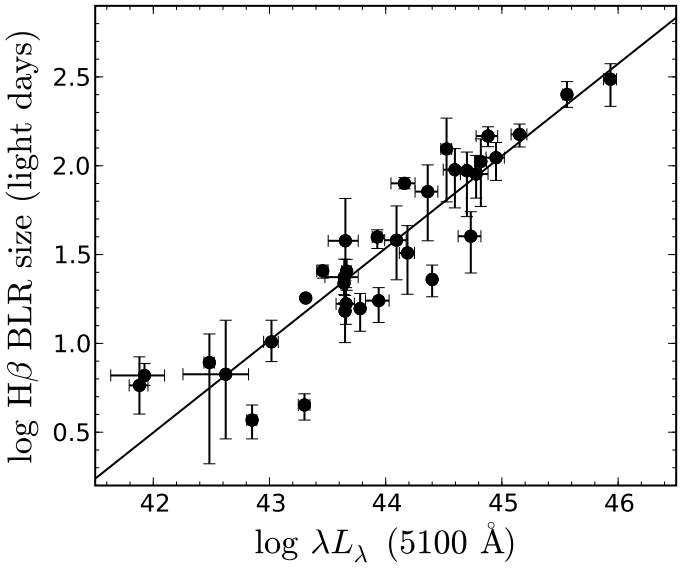

Fig. 1.3. Broad line region size - AGN continuum luminosity scaling relationship. The symbols show the average Hβ time lags for the reverberation mapping sample, the solid line is the best fit scaling relation (data from Bentz et al. 2009a).

the root-mean-squared (rms) spectrum, the virial relationship $\tau \propto \Delta V^{-2}$ is better reproduced. Furthermore, Collin et al. (2006) determined average f factors for both line widths. While for $\sigma_{\rm line}$ they found the value of f to be independent of line shape, this was not the case using the FWHM. Thus, they argue for $\sigma_{\rm line}$ as the less biased width estimate.

1.2.3. The 'virial method'

While reverberation mapping is able to directly determine $M_\bullet$ in broad line AGN, this comes at the cost of extensive observing campaigns. Therefore, this method is not suited to study large AGN samples, in particular at high redshift. Fortunately, reverberation mapping established an observational scaling relation between the BLR size and the AGN continuum luminosity, usually measured at 5100 Å, of the form $R_{\rm BLR} \propto L^\gamma$ (Kaspi et al. 2000, 2005). In the earlier studies $\gamma \approx 0.7$ was found. However, these results are biased due to the host galaxy contribution to the continuum luminosity, mainly for faint AGN. Bentz et al. (2006) corrected for this host contribution using HST imaging and found $\gamma \approx 0.5$ for the slope of the scaling relation (see also Bentz et al. 2009a). This value is in good agreement with the theoretical expectation taken from a simple BLR photoionisation model. If the shape of the ionizing continuum is independent of luminosity and all AGN have a similar ionisation parameter and particle density in their BLR then it follows that $R_{\rm BLR} \propto L^{0.5}$. The observations turned out to be consistent with this simple picture. These photoionisation equilibrium considerations have even been used in the past to estimate AGN black hole masses without a calibration to reverberation mapping (e.g. Dibai 1980; Wandel & Yahil 1985).

The scaling relation offers the opportunity to estimate black hole masses of quasars directly from a single-epoch spectrum, using L as a surrogate for the BLR size. Thus, $M_\bullet$ for large statistical samples of broad line AGN can be obtained (e.g. McLure & Dunlop 2004; Vestergaard 2004; Shen et al. 2008b). While the scaling relation so far is only established for Hβ, also other broad lines, like Hα, Mg II and C IV are commonly used, but they rely on an additional cross-calibration (e.g. McLure & Jarvis 2002; Vestergaard 2002; Greene & Ho 2005; Vestergaard & Peterson 2006; McGill et al. 2008). The uncertainty of these 'virial' black hole masses are thought of being of order ~ 0.4 dex (Vestergaard & Peterson 2006), based on the comparison with reverberation mapping masses. Thus, while individual $M_\bullet$ can be off by a factor of 3, they are a powerful tool to study large statistical samples.

Estimating $M_\bullet$ at higher z either requires the observation of Hβ in the near-IR (e.g. Netzer et al. 2007; Greene et al. 2010b) or the use of Mg II or C IV. While Mg II is assumed to be a good tracer of black hole mass, the reliability of C IV has been questioned. It is suspected to be not dominated by virial motions, but have an outflowing wind component (Richards et al. 2002b, 2010; Baskin & Laor 2005; Shen et al. 2008b). On the other hand, black hole masses estimated from the C IV line do not seem to be biased compared to the Balmer line estimates (Greene et al. 2010b; Assef et al. 2010).

Another potential concern for virial black hole masses is the importance of radiation pressure (Marconi et al. 2008). Incorporating radiation pressure force into the virial relation leads to a decrease of the intrinsic scatter from 0.4 dex to 0.2 dex, but also changes the mass distribution and especially the Eddington ratio distribution. However, the validity of this modified virial relation has been questioned, based on the comparison of the Eddington ratio distributions of type 1 and type 2 AGN (Netzer 2009) and on detailed BLR cloud motion calculations (Netzer & Marziani 2010).

1.3. Black hole - galaxy co-evolution

1.3.1. The black hole-bulge relations

With the first significant sample of dynamical black hole mass determinations, a relation appeared between the black hole mass and the blue luminosity of the galaxy's spheroid component (Kormendy & Richstone 1995), i.e. with the whole galaxy for elliptical and with the bulge component for spiral galaxies. Magorrian et al. (1998) reported a correlation between $M_\bullet$ and the bulge mass, based on dynamical modeling. These early results suggested a large scatter of ~ 0.5 dex in the relations, but this was strongly driven by measurement uncertainties. Simultaneously, Gebhardt et al. (2000a) and Ferrarese & Merritt (2000) found a close relationship between $M_\bullet$ and the bulge stellar velocity dispersion σ_*. For this relation a small intrinsic scatter of 0.3 dex was found (Tremaine et al. 2002). A more careful determination of bulge luminosities in the near-IR by Marconi & Hunt (2003) showed that the intrinsic scatter in the $M_\bullet - L_K$ relation is comparable to the $M_\bullet - \sigma_*$ relation. The same is true for the $M_\bullet - M_{\rm Bulge}$ relation (Häring & Rix 2004).

The most recent literature values for these three relations are:

$$\log\left(\frac{M_\bullet}{M_\odot}\right) = 8.12 + 4.24\log\left(\frac{\sigma_*}{200{\rm km\,s^{-1}}}\right), \qquad (1.7)$$

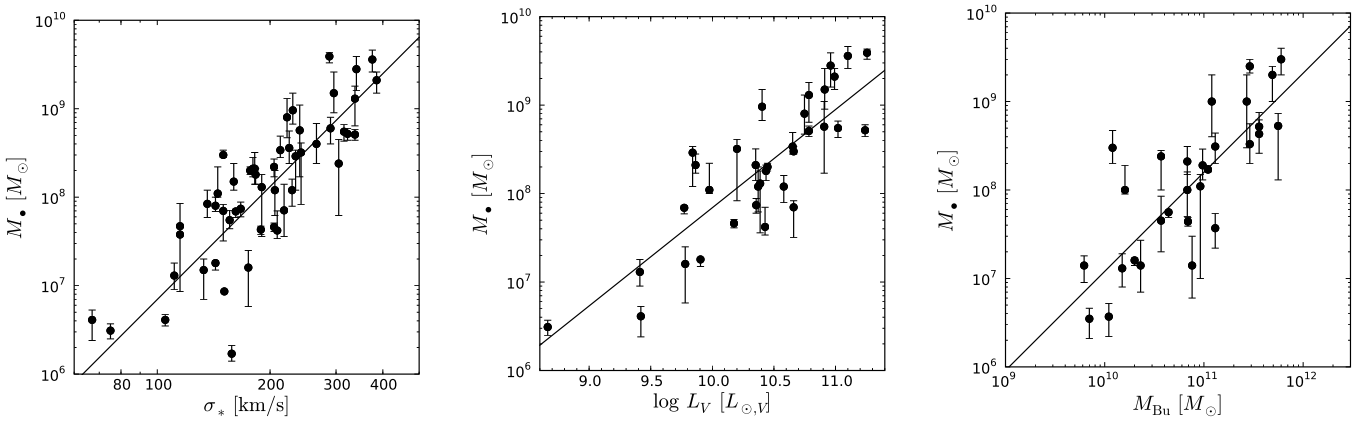

Fig. 1.4. Observed black hole - bulge relations for local quiescent galaxies. The solid line indicated the best fit linear relation. Left panel: $M_\bullet - \sigma_*$ relation from Gültekin et al. (2009b). Middle panel: $M_\bullet - L_V$ relation from Gültekin et al. (2009b). Right panel: $M_\bullet - M_{\rm Bulge}$ relation from (Häring & Rix 2004).

for the $M_\bullet - \sigma_*$ relation, with intrinsic scatter of $\epsilon_0 = 0.44$ (Gültekin et al. 2009b).

$$\log\left(\frac{M_\bullet}{M_\odot}\right) = 8.38 + 0.97\log\left(\frac{L_K}{10^{10.9}\,L_{\odot,K}}\right), \qquad (1.8)$$

for the $M_\bullet - L_K$ relation, with intrinsic scatter of $\epsilon_0 = 0.36$ (Hu 2009).

$$\log\left(\frac{M_\bullet}{M_\odot}\right) = 8.20 + 1.12\log\left(\frac{M_{\rm Bulge}}{10^{11}\,M_\odot}\right), \qquad (1.9)$$

for the $M_\bullet - M_{\rm Bulge}$ relation, with intrinsic scatter of $\epsilon_0 = 0.3$ (Häring & Rix 2004).

As these studies use different samples and slightly different fitting methods, a direct comparison of these relations and their intrinsic scatter have to be taken with care. Especially, the intrinsic scatter is still only poorly known for these relationships. A better understanding of the intrinsic scatter is crucial, as it is an important parameter for studies on black hole growth and black hole-galaxy co-evolution, as shown below. Furthermore, there is evidence that pseudobulges do not follow the black hole-bulge relations of early-type galaxies (e.g. Hu 2008; Graham 2008; Gadotti & Kauffmann 2009; Greene et al. 2010a). They may either follow their own relation with own intrinsic scatter or may show no correlation with black hole mass at all. In both cases, the scatter in the relations is increased when pseudobulges are included in the studied sample.

Presently, it is not clear if one relation is more fundamental than the other. At least, the $M_\bullet - L$ relation is probably just a manifestation of the $M_\bullet - M_{\rm Bulge}$ relation, as bulge luminosity is simply easier to measure than bulge mass. Furthermore, a number of additional relations between $M_\bullet$ and the galaxy properties have been reported. Among them are correlations with the galaxy light concentration (Graham et al. 2001), the galaxy's Sérsic index (Graham & Driver 2007), the gravitational binding energy (Aller & Richstone 2007), the dark matter halo (Ferrarese 2002), and the number of globular clusters (Burkert & Tremaine 2010).

The tight relations between black hole mass and bulge properties indicate the presence of a SMBH in every massive galaxy, containing a significant bulge component. Furthermore, a close relation between the growth of the black hole and the evolution of the galaxy is implied, as will be discussed in the next section.

1.3.2. Black hole - galaxy co-evolution scenarios

The observed tight relations between $M_\bullet$ and the galaxies spheroid component puts strong constraints on theoretical models of galaxy formation and evolution. Their origin needs to be explained theoretically. The presence of the $M_\bullet$–bulge relations can be explained in analytic (Silk & Rees 1998; Fabian 1999; King 2003; Wyithe & Loeb 2003) and semi-analytic models (e.g. Kauffmann & Haehnelt 2000; Cattaneo 2001; Granato et al. 2004; Bower et al. 2006; Croton et al. 2006), as well as in numerical simulations (Di Matteo et al. 2005; Sijacki et al. 2007; Booth & Schaye 2009). However, the details of this connection are not properly understood yet.

An important issue is the growth mechanism of black holes. While usually large amounts of gas and dust are available in the galaxy, these need to be funneled into the central region to be accreted by the black hole. Thus, the gas in the host galaxy must loose its angular momentum efficiently to serve as reservoir for black hole growth. It is commonly assumed that galaxy mergers, in particular major mergers, play a key role in this respect. The strong gravitational interaction disturbs the galaxies and allows large amounts of gas to flow to the center (Hernquist 1989). At a lower level, also minor mergers can induce gas inflows by generating disk instabilities like bars, having the advantage of being more common than major galaxy mergers. Secular evolution processes, like bar instabilities, can also appear in isolated galaxies without the need of a merger and may be able to feed the central SMBH. At the same time, galaxy mergers also trigger star formation, leading to a growth of stellar mass in the galaxies.

The current theoretical picture assumes that AGN feedback is required to establish and maintain the observed $M_\bullet$–bulge relations. During a major merger, star formation is induced and gas is funneled to the center to feed the black hole. This will accrete at a high rate, producing a large amount of energy. A fraction of this energy will heat and unbind the gas in the galaxy. The black hole will now self regulate its growth by quenching

its gas supply through the energy released in the gas. At the same time it will also shut down star formation, preventing further growth of the stellar bulge.

Current theoretical models of AGN feedback distinguish two main modes, the so called QSO mode and the radio mode (Croton et al. 2006). The QSO mode works through radiative feedback, i.e. though the transfer of the QSO radiation to kinetic energy of the host galaxy gas. This leads to a momentum driven wind that stops the gas flow to the central black hole and quenches star formation. The details and the magnitude of this energy transfer are still highly uncertain. In the simulations, usually just a fixed small fraction, ~ 5 %, of the radiated energy is injected to heat the gas. This mode will be effective during radiative efficient, high accretion rate phases, i.e. during the QSO phase. The radio mode works through mechanical feedback via radio jets and lobes, during low accretion, radiatively inefficient AGN phases. These radio jets will transfer a fraction of their mechanical energy into the surrounding gas environment. This generates bubbles in the hot gas, observed as X-ray cavities in galaxy clusters (Fabian et al. 2006; Randall et al. 2011).

As the details of these processes are not settled yet, important constraints can be gained from their predicted redshift evolution. Some numerical simulations (Robertson et al. 2006; Di Matteo et al. 2008; Booth & Schaye 2010), and semi-analytic models (Croton 2006; Hopkins et al. 2009; Lamastra et al. 2010) make predictions for the redshift evolution of the $M_\bullet$−bulge relations. While different in the details, an average trend can be extracted. The $M_\bullet - \sigma_*$ relation is predicted to evolve only weakly, not at all or with a mild negative evolution. On the other hand the $M_\bullet - M_{\rm Bulge}$ relation should evolve stronger with redshift. These predictions need to be confronted with observations, to gain a deeper insight into black hole - galaxy co-evolution, as will be discussed in the next section.

An interesting aspect on the establishment and maintenance of the $M_\bullet$−bulge relations has been raised by Peng (2007). He showed that a linear relation between black hole mass and galaxy mass is a natural consequence within a merger driven galaxy evolution framework. While Peng (2007) and also Hirschmann et al. (2010) argue that this will maintain and tighten the relations with cosmic time, Jahnke & Maccio (2010) even claim that the $M_\bullet$−bulge relations can be fully explained by this effect, superseding the need for AGN feedback.

1.3.3. Observational evidence for evolution in the black hole-bulge relations

While the local $M_\bullet$−bulge relations are relatively well established, at higher redshift they are poorly known. As discussed in the previous section, the redshift evolution of these relations contains important information about its origin and thus about galaxy formation and black hole - galaxy co-evolution. In general, three scenarios are possible: (1) a positive evolution of the $M_\bullet/M_{\rm Bulge}$ ratio, meaning black holes grow before their bulges, (2) a negative evolution, thus galaxy bulges grow ahead of the black holes, (3) no evolution, implying a coeval growth throughout cosmic time. The evolution can be parametrized by an offset

$$\Gamma(z) = \frac{M_\bullet/M_{\rm Bulge}(z)}{M_\bullet/M_{\rm Bulge}(z=0)} \,, \tag{1.10}$$

or $\Delta \log M_\bullet = \log \Gamma$, at the specific redshift studied, or with a slope γ, assuming $\Gamma(z) \propto (1+z)^\gamma$.

In the last years, efforts have been made to determine this evolution, which can broadly be separated into two approaches. The first approach uses integral constraints on the whole galaxy population, employing the black hole mass function (Merloni et al. 2004; Hopkins et al. 2006; Shankar et al. 2009; Somerville 2009). These studies found no or no strong evolution, both in $M_\bullet - M_{\rm Bulge}$ and in $M_\bullet - \sigma_*$.

The second approach is a direct measurement of $M_\bullet$ and the bulge property in individual objects at high z. As already discussed, direct dynamical measurements are not feasible beyond the local volume. Therefore, the best possibility relies on broad line AGN, employing the virial method. In this case, deriving $M_\bullet$ is easy, by just obtaining a spectrum and measuring broad line width and continuum luminosity. However, obtaining the bulge property is difficult, especially hampered by the presence of the bright AGN in the center. Several routes have been followed to achieve this goal, all with their own advantages and drawbacks.

At low to moderate redshift it is still possible to measure stellar velocity dispersions directly. While Shen et al. (2008a) found no significant evolution up to $z < 0.4$, Woo et al. (2006, 2008) claimed an evolution of $\Gamma \approx 3$ at $z \simeq 0.5$. Shields et al. (2003) and Salviander et al. (2007) used the narrow [O III] line as a surrogate of σ_*, applicable to higher z. Shields et al. (2003) found no evidence for evolution for an inhomogeneous sample up to $z \lesssim 3$. On the other hand, Salviander et al. (2007) reported an indication for mild evolution, corresponding to $\gamma \approx 0.7$, up to $z \lesssim 1.2$, with no evolution found for $z < 0.5$. By using the radio CO line width as surrogate of σ_*, Shields et al. (2006) and Ho (2007) see evidence for more massive black holes at given σ_* for $z > 3$.

Alternatively, the $M_\bullet - M_{\rm Bulge}$ relation has been explored. Several authors studied QSO host galaxy luminosities and compared these to the local relation, assuming passive galaxy evolution (Peng et al. 2006a,b; Treu et al. 2007; McLeod & Bechtold 2009; Decarli et al. 2010; Bennert et al. 2010). This requires high spatial resolution (ideally *HST*) observations and a proper QSO-host decomposition. These studies tend to find $\gamma \approx 1.5$. However, the basically unknown mass-to-light ratio introduces significant uncertainties onto these results. The more demanding task is to obtain stellar masses, using multi-colour data. This has been done by Schramm et al. (2008) and Jahnke et al. (2009) via a QSO-host decomposition on imaging data in multiple bands, and by Merloni et al. (2010) via a decomposition from the QSO+host SED. For a small sample of bright QSOs Schramm et al. (2008) found $\Gamma(z \sim 3) \approx 10$. Jahnke et al. (2009) derived *total* stellar masses for 10 AGN, finding no evolution at $z \sim 1.4$, while Merloni et al. (2010) found mild evolution, $\gamma \approx 0.7$ for 89 sources over a similar redshift range. Alternatively, high resolution Integral Field Unit (IFU) observations allow a dynamical mass measurement of QSO host galaxies (Inskip et al. 2011). Also obscured AGN with detectable broad lines were used (Sarria et al. 2010; Nesvadba et al. 2011),

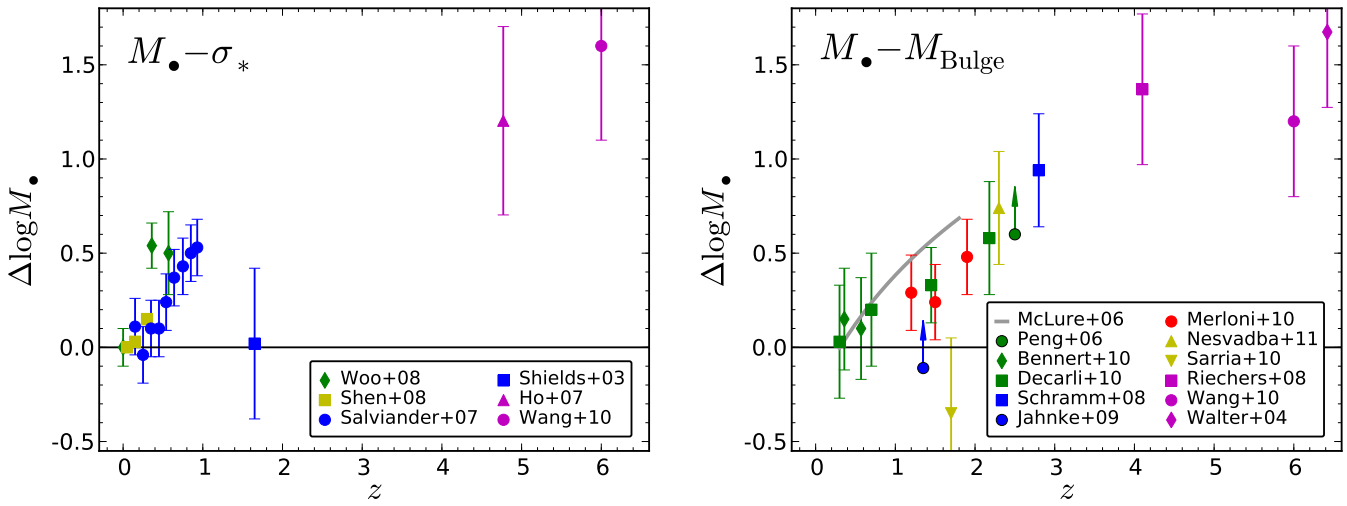

Fig. 1.5. Observed offset from the local $M_\bullet$–bulge relations as a function of redshift, for a compilation of studies on the evolution in the relations. The left panel shows results for the $M_\bullet - \sigma_*$ relation, and the right panel for the $M_\bullet - M_{\rm Bulge}$ relation. Similar observational approaches are indicated by the same colour in the respective panel. Note that these results show the direct measurements, without accounting for selection effects.

for which the determination of the stellar mass is less problematic. McLure et al. (2006) exploited radio-loud unification on a sample of radio selected AGN, composed of radio galaxies and radio-loud quasars. They derived $M_\bullet$ for the quasars and $M_{\rm Bulge}$ for the radio galaxies, finding an evolution of $\gamma \approx 2$, when assuming that both represent the same underlying populations. At the highest redshifts, $z \sim 6$, CO rotation curves were used to determine dynamical masses for a few individual host galaxies of luminous QSOs (Walter et al. 2004; Riechers et al. 2008, 2009; Wang et al. 2010). These are found to be offset from the local relation towards large $M_\bullet$, with $\Gamma \sim 15$.

An important issue for all these studies are selection effects that may bias the sample and can induce an artificial signal of evolution. This has been raised by several authors (Adelberger & Steidel 2005; Fine et al. 2006; Salviander et al. 2007), but the issue received major attention by the work of (Lauer et al. 2007). The main problem is that these objects are selected as AGN, i.e. based on their AGN luminosity, and not based on their galaxy luminosity. Thus, we will preferentially detect more massive black holes, leading to a bias, due to the intrinsic scatter in the $M_\bullet$–bulge relations. Investigating this bias and other potential biases for studies of the evolution in the $M_\bullet$–bulge relations through AGN surveys will be the subject of Chapter 5.

1.4. The growth of supermassive black holes

1.4.1. Constraints from the AGN luminosity function

Black holes mainly grow through mass accretion. During the infall of matter, a fraction η of the rest mass energy is converted into radiation, following Equation (1.1). A characteristic upper limit for the radiated luminosity is the Eddington limit (Equation 1.2), corresponding to an Eddington accretion rate $\dot{M}_{\rm Edd}$,

$$\dot{M}_{\rm Edd} = \frac{L_{\rm Edd}}{\eta\, c^2} = 2.22 \left(\frac{0.1}{\eta}\right)\left(\frac{M_\bullet}{10^8\, M_\odot}\right) M_\odot\, {\rm yr}^{-1} \,. \qquad (1.11)$$

The accretion rate of the black hole is commonly expressed normalised to the Eddington rate. Therefore, the ratio $\lambda = L_{\rm bol}/L_{\rm Edd} = \dot{M}/\dot{M}_{\rm Edd}$, the so-called Eddington ratio, is a representation of the accretion rate of the black hole.

At the same time, the black hole is growing at a rate

$$\dot{M}_\bullet = (1-\eta)\dot{M} = \frac{1-\eta}{\eta\, c^2} L_{\rm bol} \,, \qquad (1.12)$$

as the fraction η is radiated and does not contribute to the growth of the SMBH. With the black hole accreting at a rate λ, $L_{\rm bol} = \lambda L_{\rm Edd}$. The Salpeter timescale then gives the time the black hole needs for accretion at a rate λ to e-fold its mass (Salpeter 1964)

$$t_S = \frac{c\sigma_T}{4\pi G m_p} \frac{\eta}{(1-\eta)\lambda} = 4.5 \times 10^7 {\rm yr}\, \frac{\eta}{0.1(1-\eta)} \lambda^{-1} \,. \qquad (1.13)$$

Furthermore, from Equation (1.12) follows that the QSO luminosity function and its redshift evolution trace the growth history of SMBHs. The comoving black hole mass density accreted during bright QSO phases is given by (e.g. Yu & Tremaine 2002)

$$\rho_\bullet^{\rm QSO}(z') = \int_{z'}^{\infty} \int_0^\infty \frac{1-\eta}{\eta\, c^2} L_{\rm bol}\, \phi(L,z) \frac{dt}{dz}\, dL dz \,, \qquad (1.14)$$

where $\phi(L,z)$ is the redshift dependent QSO luminosity function, as defined by Equation 1.3. Ideally, the bolometric luminosity function (LF) should be used, to account for SMBH growth by the whole AGN population. As this quantity is not a direct observable, the LF in a given band can be used instead. The hard X-ray LF is expected to provide the most complete census of the AGN population, and is therefore especially valuable. A recent estimate, using a determination of the bolometric QSO LF, is $\rho_\bullet^{\rm QSO}(z=0) = 4.8^{+1.2}_{-1.0} \times 10^5\, M_\odot\, {\rm Mpc}^{-3}$, assuming $\eta = 0.1$ and $H_0 = 70\ {\rm km\ s^{-1}}$ (Hopkins et al. 2007).

The derived local black hole mass density through QSO accretion, $\rho_\bullet^{\rm QSO}(z=0)$, can be compared with estimates of the local SMBH mass density in local dormant black holes. This

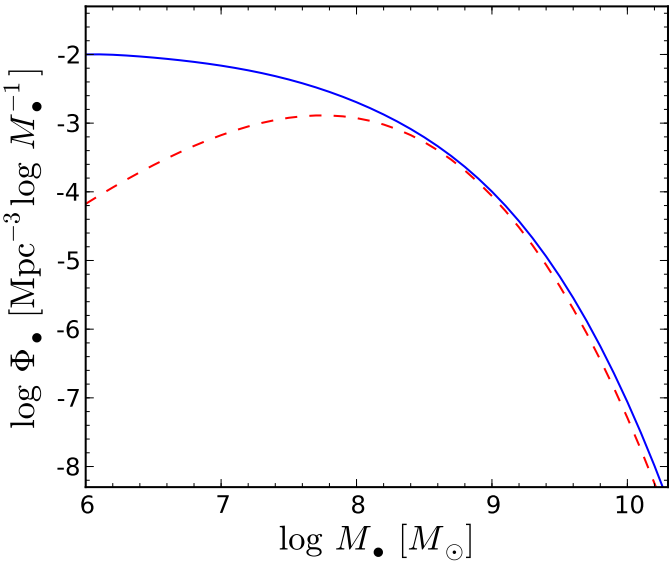

Fig. 1.6. Estimates of the mass function of local dormant black holes. The blue solid line gives the mass function derived from the spheroid luminosity function, estimated from the 2MASS K-band luminosity function from Kochanek et al. (2001), following the approach from Marconi et al. (2004) and employing the $M_\bullet - L_K$ relation from Marconi & Hunt (2003). The red dashed line is the mass function estimated from the stellar velocity dispersion function of early type galaxies from Sheth et al. (2003), using the $M_\bullet - \sigma$ relation from Gültekin et al. (2009b). Note that this estimate is incomplete at the low mass end, as late type galaxies are not included. For both relations an intrinsic scatter of 0.3 dex is assumed.

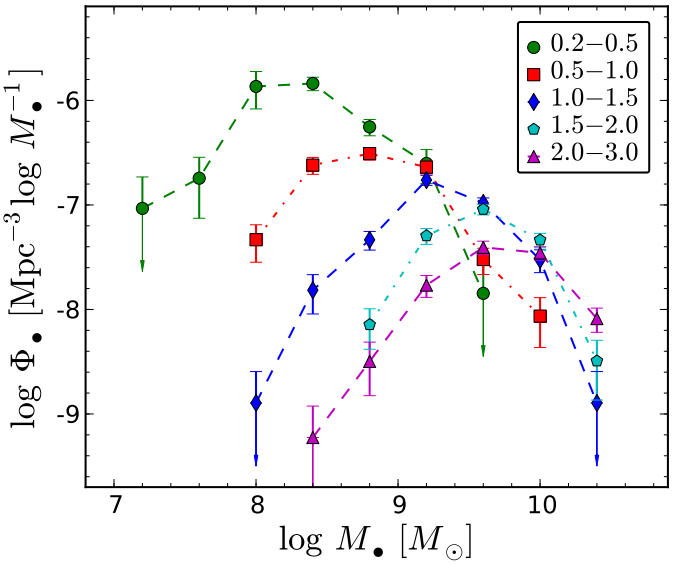

Fig. 1.7. Active black hole mass function from the Large Bright Quasar Survey (LBQS), determined by Vestergaard & Osmer (2009). The mass function is shown in several redshift bins. The turnover at the low mass end is due to incompleteness (also discussed in Chapter 3).

value can be derived from the local spheroid luminosity function or the stellar velocity distribution function, employing the local $M_\bullet - L$ or $M_\bullet - \sigma_*$ relations. The local black hole mass function of quiescent SMBHs is given by (e.g. Yu & Lu 2004; Marconi et al. 2004)

$$\phi_\bullet(M_\bullet) = \int \frac{1}{\sqrt{2\pi}\sigma} \exp\left\{-\frac{(\log M_\bullet - a - b\log x)^2}{2\sigma^2}\right\} \phi_x(x)\, dx\,, \tag{1.15}$$

where x gives the spheroid property, i.e. either $x = \sigma_*$ or $x = L_{\rm sph}$, $\phi_x(x)$ is the respective distribution function of x, and we have assumed a $M_\bullet$–bulge relation of the form $\log M_\bullet = a + b \log x$ with Gaussian intrinsic scatter of dispersion σ. The local mass density locked up locally in SMBHs is then

$$\rho_\bullet(z=0) = \int_{M_{\bullet,\rm min}}^{\infty} M_\bullet \phi_\bullet(M_\bullet)\, dM_\bullet\,. \tag{1.16}$$

The integrated mass density is $\rho_\bullet(z = 0) = (3.2 - 5.4) \times 10^5\, M_\odot\, {\rm Mpc}^{-3}$ (Shankar et al. 2009). This is in broad agreement with the local space density accreted during bright QSO phases, suggesting that the majority of black hole growth occurs in such luminous phases. On the other hand, it implies that all local galaxies with quiescent black holes at least once in cosmic history went through an AGN phase. This argument has been introduced by Soltan (1982) and has been used since then by a number of authors to study black hole growth (e.g. Salucci et al. 1999; Marconi et al. 2004; Shankar et al. 2004).

Further insight into black hole growth can be gained from the black hole mass function itself, by solving a continuity equation

$$\frac{\partial\phi(M_\bullet,t)}{\partial t} + \frac{\partial}{\partial M_\bullet}\left[\phi_\bullet(M_\bullet,t)\langle\dot{M}(M_\bullet,t)\rangle\right] = 0 \tag{1.17}$$

(Small & Blandford 1992; Yu & Tremaine 2002; Yu & Lu 2004; Marconi et al. 2004; Merloni 2004; Merloni & Heinz 2008; Shankar et al. 2009). Here, mergers are neglected, as is commonly done. This continuity equation can be solved given some initial conditions and the QSO LF, plus some additional simplifying assumptions, such as a single, constant Eddington ratio λ. While differing in the details, these studies revealed evidence for anti-hierarchical black hole growth (Merloni 2004; Marconi et al. 2004). The most massive black holes complete most of their growth at early cosmic times, with only minor growth occuring in the local universe. Lower mass black holes have their major growth phases at lower redshift, and may even exhibit significant growth presently. This is a consequence of the AGN downsizing trend found in the AGN LF. These studies also provide estimates of the AGN duty cycle and the mean AGN lifetimes. Furthermore, the cosmic accretion rate history of SMBHs is found to have a similar redshift dependence as the cosmic star formation history, showing that the accretion onto a SMBH and star formation are proportional, at least in a statistical sense. (Marconi et al. 2004).

1.4.2. The active black hole mass function

While already the study of the AGN LF contains a wealth of information on the black hole growth history, they rely on simplifying assumptions. Commonly, a single Eddington ratio is assumed for the whole black hole population, to be able to map the LF to the black hole mass function (BHMF). However, AGNs

are not simply in an on or of state, but accrete at a wide distribution of rates (e.g. Yu et al. 2005; Ho 2009). A remarkable exception in this respect is the work by Merloni (2004) and Merloni & Heinz (2008). They took into account a wide range for the accretion rate distribution. However, to do so they had to incorporate an observed relation between black hole mass, X-ray luminosity and radio luminosity, the AGN radio luminosity function and a prescription of accretion modes. Furthermore, the efficiency η introduces some uncertainty. In general, it can be in the range $\sim 0.04 - 0.31$.

A direct observational determination of the active black hole mass function is able to circumvent most of the current implicit assumptions and uncertainties to directly map the growth of SMBHs. Thus, we can break the degeneracy between black hole mass and accretion rate present in the AGN luminosity function.

However, while the AGN luminosity can be measured relatively easy, the black hole mass is not a direct observable. Therefore, the AGN LF has been studied for a long time, while approaching the determination of the BHMF required the establishment of the virial method within the last years, which made it possible to estimate $M_\bullet$ for large well defined samples. A first attempt on the BHMF has been made by McLure & Dunlop (2004), based on the type 1 QSO sample from the Sloan Digital Sky Survey (SDSS) and by Heckman et al. (2004) for low-z type 2 AGN. Remarkable progress has been reached within the last few years on this field (Greene & Ho 2007; Vestergaard et al. 2008; Vestergaard & Osmer 2009; Kelly et al. 2010; Willott et al. 2010), simultaneous with my work on this topic. Some of these studies revealed direct evidence for cosmic downsizing, as found for the AGN LF. Further evidence for downsizing in the black hole population has also been found by several complimentary studies Heckman et al. (2004); Labita et al. (2009); Gallo et al. (2010).

I present my own results on the determination of the local active BHMF from the Hamburg/ESO Survey (HES) in Chapter 3.

1.4.3. The accretion rate distribution function

The accretion rate or Eddington ratio distribution function has not received much attention yet, despite of its importance for our understanding of black hole growth and the accretion process. The Eddington ratio distribution function (ERDF), together with the BHMF are the physical drivers for the growth of black holes, the observed luminosity functions and the evolution of the AGN population.

Currently, the most detailed observational determination of the ERDF is by Yu et al. (2005), based on a local type 2 AGN sample from the SDSS (see also Heckman et al. 2004; Hopkins & Hernquist 2009). They found the ERDF to cover a wide range and found qualitative agreement with simple theoretical models of the accretion process, namely with a self-similar evolution of the accretion disk. However, this study neglected the contribution from type 1 AGN. In this thesis, I present the first local determination of the ERDF for type 1 AGN, discussed in Chapter 3.

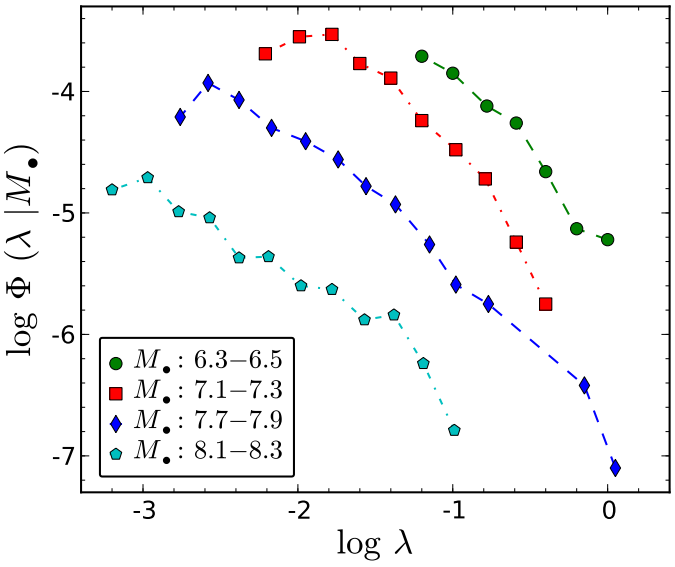

Fig. 1.8. Type 2 AGN Eddington ratio distribution function from Yu et al. (2005) for $z < 0.2$ in a few representative small black hole mass bins. The symbols show the observed distributions in the respective mass bin. The bin size in the legend is given in logarithmic black hole mass (in solar units).

1.5. Outline of this work

As already indicated during this introduction, in this thesis I will cover a wide range of topics within the general framework of supermassive black holes, their properties and their demographics. The thesis is divided into chapters, most of them are meant to be self-contained articles. Two of them are already in press in *Astronomy & Astrophysics*, one is in press in the *Astrophysical Journal* and one is to be submitted to *Astronomy & Astrophysics*. Two chapters present preliminary results, extending work from a previous chapter and are therefore not self-contained. Each chapter contains a separate introduction, focusing on the specific topic to be discussed, and separate conclusions, summing up the results of the individual chapter. The last chapter contains a final summary and discussion of the whole thesis and provides an outlook on future perspectives.

I start in Chapter 2 with the determination of the low-z type 1 AGN LF from the Hamburg/ESO Survey. In Chapter 3, I present a method to determine BHMFs and ERDFs and determine both for the same data set. Chapter 4 extends this work by incorporating uncertainties in the measured properties into the determination of the BHMF and ERDF. Chapter 5 discusses the issue of sample selection effects and their induced biases for observational studies of the evolution in the $M_\bullet$–bulge relationships. Based on this work, in Chapter 6 I present a fitting technique to account for these selection effects and obtain an unbiased estimate of the intrinsic $M_\bullet$–bulge relation. Finally, in Chapter 7 I concentrate on the black hole mass determination for quiescent galaxies, using stellar dynamics. In particular, I investigate the possible effect of including or neglecting the contribution of a dark matter halo in the dynamical modeling on the determined black hole mass.

References

Adelberger, K. L. & Steidel, C. C. 2005, ApJ, 627, L1
Aller, M. C. & Richstone, D. O. 2007, ApJ, 665, 120
Antonucci, R. 1993, ARA&A, 31, 473
Antonucci, R. R. J. & Miller, J. S. 1985, ApJ, 297, 621
Assef, R. J., Denney, K. D., Kochanek, C. S., et al. 2010, arXiv:1009.1145
Bahcall, J. N., Kirhakos, S., Saxe, D. H., & Schneider, D. P. 1997, ApJ, 479, 642
Balbus, S. A. & Hawley, J. F. 1991, ApJ, 376, 214
Baskin, A. & Laor, A. 2005, MNRAS, 356, 1029
Becker, R. H., White, R. L., & Helfand, D. J. 1995, ApJ, 450, 559
Bennert, V. N., Treu, T., Woo, J., et al. 2010, ApJ, 708, 1507
Bentz, M. C., Horne, K., Barth, A. J., et al. 2010, ApJ, 720, L46
Bentz, M. C., Peterson, B. M., Netzer, H., Pogge, R. W., & Vestergaard, M. 2009a, ApJ, 697, 160
Bentz, M. C., Peterson, B. M., Pogge, R. W., Vestergaard, M., & Onken, C. A. 2006, ApJ, 644, 133
Bentz, M. C., Walsh, J. L., Barth, A. J., et al. 2009b, ApJ, 705, 199
Binney, J. J., Davies, R. L., & Illingworth, G. D. 1990, ApJ, 361, 78
Blandford, R. D. & McKee, C. F. 1982, ApJ, 255, 419
Bongiorno, A., Zamorani, G., Gavignaud, I., et al. 2007, A&A, 472, 443
Booth, C. M. & Schaye, J. 2009, MNRAS, 398, 53
Booth, C. M. & Schaye, J. 2010, ArXiv e-prints
Bower, R. G., Benson, A. J., Malbon, R., et al. 2006, MNRAS, 370, 645
Boyle, B. J., Shanks, T., Croom, S. M., et al. 2000, MNRAS, 317, 1014
Brotherton, M. S. 1996, ApJS, 102, 1
Burkert, A. & Tremaine, S. 2010, ApJ, 720, 516
Cappellari, M. 2008, MNRAS, 390, 71
Cappellari, M., Emsellem, E., Bacon, R., et al. 2007, MNRAS, 379, 418
Cappellari, M., Neumayer, N., Reunanen, J., et al. 2009, MNRAS, 394, 660
Cappellari, M., Verolme, E. K., van der Marel, R. P., et al. 2002, ApJ, 578, 787
Cattaneo, A. 2001, MNRAS, 324, 128
Collin, S., Kawaguchi, T., Peterson, B. M., & Vestergaard, M. 2006, A&A, 456, 75
Condon, J. J., Cotton, W. D., Greisen, E. W., et al. 1998, AJ, 115, 1693
Cowie, L. L., Songaila, A., Hu, E. M., & Cohen, J. G. 1996, AJ, 112, 839
Cretton, N. & van den Bosch, F. C. 1999, ApJ, 514, 704
Croom, S. M., Richards, G. T., Shanks, T., et al. 2009, ArXiv:0907.2727
Croom, S. M., Smith, R. J., Boyle, B. J., et al. 2004, MNRAS, 349, 1397
Croton, D. J. 2006, MNRAS, 369, 1808
Croton, D. J., Springel, V., White, S. D. M., et al. 2006, MNRAS, 365, 11
Dalla Bontà, E., Ferrarese, L., Corsini, E. M., et al. 2009, ApJ, 690, 537
Decarli, R., Falomo, R., Treves, A., et al. 2010, MNRAS, 402, 2453
Devereux, N., Ford, H., Tsvetanov, Z., & Jacoby, G. 2003, AJ, 125, 1226
Di Matteo, T., Colberg, J., Springel, V., Hernquist, L., & Sijacki, D. 2008, ApJ, 676, 33
Di Matteo, T., Springel, V., & Hernquist, L. 2005, Nature, 433, 604
Dibai, E. A. 1980, Soviet Ast., 24, 389
Doeleman, S. S., Shen, Z., Rogers, A. E. E., et al. 2001, AJ, 121, 2610
Elitzur, M. 2008, New A Rev., 52, 274
Elitzur, M. & Shlosman, I. 2006, ApJ, 648, L101
Fabian, A. C. 1999, MNRAS, 308, L39
Fabian, A. C., Sanders, J. S., Taylor, G. B., et al. 2006, MNRAS, 366, 417
Fan, X., Narayanan, V. K., Lupton, R. H., et al. 2001a, AJ, 122, 2833
Fan, X., Strauss, M. A., Schneider, D. P., et al. 2001b, AJ, 121, 54
Fan, X., Strauss, M. A., Schneider, D. P., et al. 1999, AJ, 118, 1
Ferrarese, L. 2002, ApJ, 578, 90
Ferrarese, L. & Ford, H. 2005, Space Sci. Rev., 116, 523
Ferrarese, L., Ford, H. C., & Jaffe, W. 1996, ApJ, 470, 444
Ferrarese, L. & Merritt, D. 2000, ApJ, 539, L9
Fine, S., Croom, S. M., Miller, L., et al. 2006, MNRAS, 373, 613
Gadotti, D. A. & Kauffmann, G. 2009, MNRAS, 399, 621
Gallo, E., Treu, T., Marshall, P. J., et al. 2010, ApJ, 714, 25
Gavignaud, I., Bongiorno, A., Paltani, S., et al. 2006, A&A, 457, 79
Gebhardt, K., Bender, R., Bower, G., et al. 2000a, ApJ, 539, L13
Gebhardt, K., Kormendy, J., Ho, L. C., et al. 2000b, ApJ, 543, L5
Gebhardt, K., Richstone, D., Tremaine, S., et al. 2003, ApJ, 583, 92
Gebhardt, K. & Thomas, J. 2009, ApJ, 700, 1690
Ghez, A. M., Duchêne, G., Matthews, K., et al. 2003, ApJ, 586, L127
Gillessen, S., Eisenhauer, F., Trippe, S., et al. 2009, ApJ, 692, 1075
Glikman, E., Bogosavljević, M., Djorgovski, S. G., et al. 2010, ApJ, 710, 1498
Graham, A. W. 2008, ApJ, 680, 143
Graham, A. W. & Driver, S. P. 2007, ApJ, 655, 77
Graham, A. W., Erwin, P., Caon, N., & Trujillo, I. 2001, ApJ, 563, L11
Granato, G. L., De Zotti, G., Silva, L., Bressan, A., & Danese, L. 2004, ApJ, 600, 580
Greene, J. E. & Ho, L. C. 2005, ApJ, 630, 122
Greene, J. E. & Ho, L. C. 2007, ApJ, 667, 131
Greene, J. E., Peng, C. Y., Kim, M., et al. 2010a, ApJ, 721, 26
Greene, J. E., Peng, C. Y., & Ludwig, R. R. 2010b, ApJ, 709, 937
Greenhill, L. J., Booth, R. S., Ellingsen, S. P., et al. 2003, ApJ, 590, 162
Greenhill, L. J. & Gwinn, C. R. 1997, Ap&SS, 248, 261
Gültekin, K., Richstone, D. O., Gebhardt, K., et al. 2009a, ApJ, 695, 1577
Gültekin, K., Richstone, D. O., Gebhardt, K., et al. 2009b, ApJ, 698, 198
Hao, L., Strauss, M. A., Fan, X., et al. 2005, AJ, 129, 1795
Häring, N. & Rix, H.-W. 2004, ApJ, 604, L89
Hasinger, G. 2008, A&A, 490, 905
Hasinger, G., Miyaji, T., & Schmidt, M. 2005, A&A, 441, 417
Heckman, T. M., Kauffmann, G., Brinchmann, J., et al. 2004, ApJ, 613, 109
Henkel, C., Braatz, J. A., Greenhill, L. J., & Wilson, A. S. 2002, A&A, 394, L23
Hernquist, L. 1989, Nature, 340, 687
Herrnstein, J. R., Moran, J. M., Greenhill, L. J., et al. 1999, Nature, 400, 539
Herrnstein, J. R., Moran, J. M., Greenhill, L. J., & Trotter, A. S. 2005, ApJ, 629, 719
Hewett, P. C., Foltz, C. B., & Chaffee, F. H. 1995, AJ, 109, 1498
Hewett, P. C., Irwin, M. J., Bunclark, P., et al. 1985, MNRAS, 213, 971
Hirschmann, M., Khochfar, S., Burkert, A., et al. 2010, MNRAS, 407, 1016
Ho, L. C. 2007, ApJ, 669, 821
Ho, L. C. 2009, ApJ, 699, 626
Hopkins, P. F. & Hernquist, L. 2009, ApJ, 698, 1550
Hopkins, P. F., Hernquist, L., Cox, T. J., Keres, D., & Wuyts, S. 2009, ApJ, 691, 1424
Hopkins, P. F., Richards, G. T., & Hernquist, L. 2007, ApJ, 654, 731
Hopkins, P. F., Robertson, B., Krause, E., Hernquist, L., & Cox, T. J. 2006, ApJ, 652, 107
Horne, K., Peterson, B. M., Collier, S. J., & Netzer, H. 2004, PASP, 116, 465
Hu, J. 2008, MNRAS, 386, 2242
Hu, J. 2009, arXiv:0908.2028
Inskip, K. J., Jahnke, K., Rix, H., & van de Ven, G. 2011, arXiv:1103.6026
Jaffe, W., Meisenheimer, K., Röttgering, H. J. A., et al. 2004, Nature, 429, 47
Jahnke, K., Bongiorno, A., Brusa, M., et al. 2009, ApJ, 706, L215
Jahnke, K. & Maccio, A. 2010, arXiv:1006.0482
Kaspi, S., Brandt, W. N., Maoz, D., et al. 2007, ApJ, 659, 997
Kaspi, S., Maoz, D., Netzer, H., et al. 2005, ApJ, 629, 61
Kaspi, S., Smith, P. S., Netzer, H., et al. 2000, ApJ, 533, 631
Kauffmann, G. & Haehnelt, M. 2000, MNRAS, 311, 576
Kelly, B. C., Vestergaard, M., Fan, X., et al. 2010, ApJ, 719, 1315
King, A. 2003, ApJ, 596, L27
Kochanek, C. S., Pahre, M. A., Falco, E. E., et al. 2001, ApJ, 560, 566
Koehler, T., Groote, D., Reimers, D., & Wisotzki, L. 1997, A&A, 325, 502
Kormendy, J. & Richstone, D. 1995, ARA&A, 33, 581
Krolik, J. H. 1999, Active galactic nuclei : from the central black hole to the galactic environment, ed. Krolik, J. H.
Krolik, J. H. 2001, ApJ, 551, 72
Kuo, C. Y., Braatz, J. A., Condon, J. J., et al. 2011, ApJ, 727, 20
Labita, M., Decarli, R., Treves, A., & Falomo, R. 2009, MNRAS, 396, 1537
Labita, M., Treves, A., Falomo, R., & Uslenghi, M. 2006, MNRAS, 373, 551
Lamastra, A., Menci, N., Maiolino, R., Fiore, F., & Merloni, A. 2010, MNRAS, 405, 29
Lauer, T. R., Tremaine, S., Richstone, D., & Faber, S. M. 2007, ApJ, 670, 249
Lynden-Bell, D. 1969, Nature, 223, 690
Macchetto, F., Marconi, A., Axon, D. J., et al. 1997, ApJ, 489, 579
Maddox, N., Hewett, P. C., Warren, S. J., & Croom, S. M. 2008, MNRAS, 386, 1605
Magorrian, J., Tremaine, S., Richstone, D., et al. 1998, AJ, 115, 2285
Maiolino, R., Shemmer, O., Imanishi, M., et al. 2007, A&A, 468, 979
Maoz, D. 2007, MNRAS, 377, 1696
Marconi, A., Axon, D. J., Maiolino, R., et al. 2008, ApJ, 678, 693
Marconi, A., Capetti, A., Axon, D. J., et al. 2001, ApJ, 549, 915
Marconi, A. & Hunt, L. K. 2003, ApJ, 589, L21

Marconi, A., Risaliti, G., Gilli, R., et al. 2004, MNRAS, 351, 169
Marshall, H. L. 1987, AJ, 94, 628
Marshall, H. L., Tananbaum, H., Avni, Y., & Zamorani, G. 1983, ApJ, 269, 35
McGill, K. L., Woo, J.-H., Treu, T., & Malkan, M. A. 2008, ApJ, 673, 703
McLeod, K. K. & Bechtold, J. 2009, ApJ, 704, 415
McLeod, K. K. & Rieke, G. H. 1994a, ApJ, 420, 58
McLeod, K. K. & Rieke, G. H. 1994b, ApJ, 431, 137
McLure, R. J. & Dunlop, J. S. 2001, MNRAS, 327, 199
McLure, R. J. & Dunlop, J. S. 2002, MNRAS, 331, 795
McLure, R. J. & Dunlop, J. S. 2004, MNRAS, 352, 1390
McLure, R. J. & Jarvis, M. J. 2002, MNRAS, 337, 109
McLure, R. J., Jarvis, M. J., Targett, T. A., Dunlop, J. S., & Best, P. N. 2006, MNRAS, 368, 1395
McLure, R. J., Kukula, M. J., Dunlop, J. S., et al. 1999, MNRAS, 308, 377
Merloni, A. 2004, MNRAS, 353, 1035
Merloni, A., Bongiorno, A., Bolzonella, M., et al. 2010, ApJ, 708, 137
Merloni, A. & Heinz, S. 2008, MNRAS, 388, 1011
Merloni, A., Rudnick, G., & Di Matteo, T. 2004, MNRAS, 354, L37
Miyaji, T., Hasinger, G., & Schmidt, M. 2000, A&A, 353, 25
Miyoshi, M., Moran, J., Herrnstein, J., et al. 1995, Nature, 373, 127
Mo, H., van den Bosch, F. C., & White, S. 2010, Galaxy Formation and Evolution, ed. Mo, H., van den Bosch, F. C., & White, S.
Narayan, R. & Yi, I. 1994, ApJ, 428, L13
Nenkova, M., Sirocky, M. M., Nikutta, R., Ivezić, Ž., & Elitzur, M. 2008, ApJ, 685, 160
Nesvadba, N. P. H., De Breuck, C., Lehnert, M. D., et al. 2011, A&A, 525, A43+
Netzer, H. 2009, ApJ, 695, 793
Netzer, H., Lira, P., Trakhtenbrot, B., Shemmer, O., & Cury, I. 2007, ApJ, 671, 1256
Netzer, H. & Marziani, P. 2010, ApJ, 724, 318
Neufeld, D. A., Maloney, P. R., & Conger, S. 1994, ApJ, 436, L127+
Neumayer, N., Cappellari, M., Reunanen, J., et al. 2007, ApJ, 671, 1329
Novikov, I. D. & Thorne, K. S. 1973, in Black Holes (Les Astres Occlus), ed. C. Dewitt & B. S. Dewitt, 343–450
Onken, C. A., Ferrarese, L., Merritt, D., et al. 2004, ApJ, 615, 645
Onken, C. A. & Peterson, B. M. 2002, ApJ, 572, 746
Onken, C. A., Valluri, M., Peterson, B. M., et al. 2007, ApJ, 670, 105
Osterbrock, D. E. & Ferland, G. J. 2006, Astrophysics of gaseous nebulae and active galactic nuclei, ed. Osterbrock, D. E. & Ferland, G. J.
Peng, C. Y. 2007, ApJ, 671, 1098
Peng, C. Y., Impey, C. D., Ho, L. C., Barton, E. J., & Rix, H. 2006a, ApJ, 640, 114
Peng, C. Y., Impey, C. D., Rix, H., et al. 2006b, ApJ, 649, 616
Peterson, B. M. 1993, PASP, 105, 247
Peterson, B. M. 1997, An Introduction to Active Galactic Nuclei, ed. Goméz de Castro, A. I. & Franqueira, M.
Peterson, B. M., Ferrarese, L., Gilbert, K. M., et al. 2004, ApJ, 613, 682
Peterson, B. M. & Wandel, A. 2000, ApJ, 540, L13
Raban, D., Jaffe, W., Röttgering, H., Meisenheimer, K., & Tristram, K. R. W. 2009, MNRAS, 394, 1325
Randall, S. W., Forman, W. R., Giacintucci, S., et al. 2011, ApJ, 726, 86
Rees, M. J. 1984, ARA&A, 22, 471
Reid, M. J., Menten, K. M., Genzel, R., et al. 2003, ApJ, 587, 208
Richards, G. T., Deo, R. P., Lacy, M., et al. 2009, AJ, 137, 3884
Richards, G. T., Fan, X., Newberg, H. J., et al. 2002a, AJ, 123, 2945
Richards, G. T., Kruczek, N. E., Gallagher, S. C., et al. 2010, arXiv:1011.2282
Richards, G. T., Strauss, M. A., Fan, X., et al. 2006, AJ, 131, 2766
Richards, G. T., Vanden Berk, D. E., Reichard, T. A., et al. 2002b, AJ, 124, 1
Riechers, D. A., Walter, F., Brewer, B. J., et al. 2008, ApJ, 686, 851
Riechers, D. A., Walter, F., Carilli, C. L., & Lewis, G. F. 2009, ApJ, 690, 463
Robertson, B., Hernquist, L., Cox, T. J., et al. 2006, ApJ, 641, 90
Salpeter, E. E. 1964, ApJ, 140, 796
Salucci, P., Szuszkiewicz, E., Monaco, P., & Danese, L. 1999, MNRAS, 307, 637
Salviander, S., Shields, G. A., Gebhardt, K., & Bonning, E. W. 2007, ApJ, 662, 131
Sargent, W. L. W., Young, P. J., Lynds, C. R., et al. 1978, ApJ, 221, 731
Sarria, J. E., Maiolino, R., La Franca, F., et al. 2010, A&A, 522, L3+
Sarzi, M., Rix, H., Shields, J. C., et al. 2001, ApJ, 550, 65
Schmidt, M. 1968, ApJ, 151, 393
Schmidt, M. & Green, R. F. 1983, ApJ, 269, 352
Schmidt, M., Schneider, D. P., & Gunn, J. E. 1995, AJ, 110, 68
Schödel, R., Ott, T., Genzel, R., et al. 2003, ApJ, 596, 1015
Schramm, M., Wisotzki, L., & Jahnke, K. 2008, A&A, 478, 311
Schwarzschild, M. 1979, ApJ, 232, 236
Shakura, N. I. & Sunyaev, R. A. 1973, A&A, 24, 337
Shankar, F., Bernardi, M., & Haiman, Z. 2009, ApJ, 694, 867
Shankar, F., Salucci, P., Granato, G. L., De Zotti, G., & Danese, L. 2004, MNRAS, 354, 1020
Shapiro, K. L., Cappellari, M., de Zeeuw, T., et al. 2006, MNRAS, 370, 559
Shen, J., Vanden Berk, D. E., Schneider, D. P., & Hall, P. B. 2008a, AJ, 135, 928
Shen, Y., Greene, J. E., Strauss, M. A., Richards, G. T., & Schneider, D. P. 2008b, ApJ, 680, 169
Sheth, R. K., Bernardi, M., Schechter, P. L., et al. 2003, ApJ, 594, 225
Shields, G. A. 1978, Nature, 272, 706
Shields, G. A. 1999, PASP, 111, 661
Shields, G. A., Gebhardt, K., Salviander, S., et al. 2003, ApJ, 583, 124
Shields, G. A., Menezes, K. L., Massart, C. A., & Vanden Bout, P. 2006, ApJ, 641, 683
Sijacki, D., Springel, V., Di Matteo, T., & Hernquist, L. 2007, MNRAS, 380, 877
Silk, J. & Rees, M. J. 1998, A&A, 331, L1
Silverman, J. D., Green, P. J., Barkhouse, W. A., et al. 2008, ApJ, 679, 118
Simpson, C. 2005, MNRAS, 360, 565
Siopis, C., Gebhardt, K., Lauer, T. R., et al. 2009, ApJ, 693, 946
Small, T. A. & Blandford, R. D. 1992, MNRAS, 259, 725
Smith, J. E., Robinson, A., Young, S., Axon, D. J., & Corbett, E. A. 2005, MNRAS, 359, 846
Soltan, A. 1982, MNRAS, 200, 115
Somerville, R. S. 2009, MNRAS, 399, 1988
Thomas, J., Saglia, R. P., Bender, R., et al. 2007, MNRAS, 382, 657
Thomas, J., Saglia, R. P., Bender, R., et al. 2004, MNRAS, 353, 391
Tran, H. D. 1995a, ApJ, 440, 565
Tran, H. D. 1995b, ApJ, 440, 578
Tran, H. D., Tsvetanov, Z., Ford, H. C., et al. 2001, AJ, 121, 2928
Treister, E., Krolik, J. H., & Dullemond, C. 2008, ApJ, 679, 140
Tremaine, S., Gebhardt, K., Bender, R., et al. 2002, ApJ, 574, 740
Treu, T., Woo, J., Malkan, M. A., & Blandford, R. D. 2007, ApJ, 667, 117
Tristram, K. R. W., Meisenheimer, K., Jaffe, W., et al. 2007, A&A, 474, 837
Ueda, Y., Akiyama, M., Ohta, K., & Miyaji, T. 2003, ApJ, 598, 886
Urry, C. M. & Padovani, P. 1995, PASP, 107, 803
van den Bosch, R. C. E. & de Zeeuw, P. T. 2010, MNRAS, 401, 1770
van der Marel, R. P., Cretton, N., de Zeeuw, P. T., & Rix, H. 1998, ApJ, 493, 613
Vanden Berk, D. E., Richards, G. T., Bauer, A., et al. 2001, AJ, 122, 549
Vestergaard, M. 2002, ApJ, 571, 733
Vestergaard, M. 2004, ApJ, 601, 676
Vestergaard, M., Fan, X., Tremonti, C. A., Osmer, P. S., & Richards, G. T. 2008, ApJ, 674, L1
Vestergaard, M. & Osmer, P. S. 2009, ApJ, 699, 800
Vestergaard, M. & Peterson, B. M. 2006, ApJ, 641, 689
Vestergaard, M., Wilkes, B. J., & Barthel, P. D. 2000, ApJ, 538, L103
Walter, F., Carilli, C., Bertoldi, F., et al. 2004, ApJ, 615, L17
Wandel, A., Peterson, B. M., & Malkan, M. A. 1999, ApJ, 526, 579
Wandel, A. & Yahil, A. 1985, ApJ, 295, L1
Wang, R., Carilli, C. L., Neri, R., et al. 2010, ApJ, 714, 699
Warren, S. J., Hewett, P. C., Irwin, M. J., & Osmer, P. S. 1991, ApJS, 76, 1
Warren, S. J., Hewett, P. C., & Osmer, P. S. 1994, ApJ, 421, 412
Welsh, W. F. & Horne, K. 1991, ApJ, 379, 586
Willott, C. J., Albert, L., Arzoumanian, D., et al. 2010, AJ, 140, 546
Willott, C. J., Delorme, P., Omont, A., et al. 2007, AJ, 134, 2435
Wills, B. J. & Browne, I. W. A. 1986, ApJ, 302, 56
Wills, D. & Lynds, R. 1978, ApJS, 36, 317
Wisotzki, L., Koehler, T., Groote, D., & Reimers, D. 1996, A&AS, 115, 227
Wolf, C., Wisotzki, L., Borch, A., et al. 2003, A&A, 408, 499
Woo, J., Treu, T., Barth, A. J., et al. 2010, ApJ, 716, 269
Woo, J., Treu, T., Malkan, M. A., & Blandford, R. D. 2006, ApJ, 645, 900
Woo, J.-H., Treu, T., Malkan, M. A., & Blandford, R. D. 2008, ApJ, 681, 925
Wyithe, J. S. B. & Loeb, A. 2003, ApJ, 595, 614
Yu, Q. & Lu, Y. 2004, ApJ, 602, 603

Yu, Q., Lu, Y., & Kauffmann, G. 2005, ApJ, 634, 901
Yu, Q. & Tremaine, S. 2002, MNRAS, 335, 965
Yu, Z., Yuan, F., & Ho, L. C. 2011, ApJ, 726, 87
Yuan, F. 2007, in Astronomical Society of the Pacific Conference Series, Vol. 373, The Central Engine of Active Galactic Nuclei, ed. L. C. Ho & J.-W. Wang, 95–+
Zakamska, N. L., Schmidt, G. D., Smith, P. S., et al. 2005, AJ, 129, 1212
Zakamska, N. L., Strauss, M. A., Krolik, J. H., et al. 2003, AJ, 126, 2125

Chapter 2

Low redshift AGN in the Hamburg/ESO Survey I. The local AGN luminosity function⋆

Andreas Schulze, Lutz Wisotzki, and Bernd Husemann

Leibniz-Institut für Astrophysik Potsdam (AIP), An der Sternwarte 16, 14482 Potsdam, Germany

ABSTRACT

We present a determination of the local ($z \approx 0$) luminosity function of optically selected type 1 (broad-line) Active Galactic Nuclei. Our primary resource is the Hamburg/ESO Survey (HES), which provides a well-defined sample of more than 300 optically bright AGN with redshifts $z < 0.3$ and blue magnitudes $B \lesssim 17.5$. AGN luminosities were estimated in two ways, always taking care to minimise photometric biases due to host galaxy light contamination. Firstly, we measured broad-band B_J (blue) magnitudes of the objects over small apertures of the size of the seeing disk. Secondly, we extracted Hα and Hβ broad emission line luminosities from the spectra which should be entirely free of any starlight contribution. Within the luminosity range covered by the HES ($-19 \gtrsim M_{B_J} \gtrsim -26$), the two measures are tightly correlated. The resulting AGN luminosity function (AGNLF) is consistent with a single power law, also when considering the effects of number density evolution within the narrow redshift range. We compared our AGNLF with the Hα luminosity function of lower luminosity Seyfert 1 galaxies by Hao et al. (2005) and found a smooth transition between both, with excellent agreement in the overlapping region. From the combination of HES and SDSS samples we constructed a single local AGNLF spanning more than 4 orders of magnitude in luminosity. It shows only mild curvature which can be well described as a double power law with slope indices of -2.0 for the faint end and -2.8 for the bright end. We predicted the local AGNLF in the soft X-ray domain and compared this to recent literature data. The quality of the match depends strongly on the adopted translation of optical to X-ray luminosities and is best for an approximately constant optical/X-ray ratio. We also compared the local AGNLF with results obtained at higher redshifts and find strong evidence for luminosity-dependent evolution, in the sense that AGN with luminosities around $M_B \simeq -19$ are as common in the local universe as they were at $z = 1.5$. This supports the 'AGN downsizing' picture first found from X-ray selected AGN samples.

2.1. Introduction

A good knowledge of the AGN luminosity function (AGNLF) is important for our understanding of the AGN population and its evolution, as well as for gaining insight into the history of black hole growth and galaxy evolution (e.g. Yu & Tremaine 2002; Marconi et al. 2004). Thanks to recent heroic quasar surveys such as the 2dF QSO Redshift Survey (2QZ) and the Sloan Digital Sky Survey (SDSS), large samples of AGN became available, and the optical AGN/QSO luminosity function is today well established over a wide range in redshifts ($0.3 \lesssim z \lesssim 5$) and luminosities (Boyle et al. 2000; Croom et al. 2004; Richards et al. 2006; Bongiorno et al. 2007). However, neither of these surveys reaches below redshifts of $z \sim 0.3$–0.4, because the imposed colour selection criteria, and also the discrimination against extended sources in the 2QZ sample, exclude a large fraction of lower luminosity, 'Seyfert-type' AGN. The *local* AGNLF is therefore much less constrained than at higher redshifts, despite of its importance as a zero-point for quasar evolution.

Approaching this problem from the other end, large spectroscopic galaxy surveys are a powerful way to unravel the AGN content of local galaxy samples (e.g. Huchra & Burg 1992; Ulvestad & Ho 2001; Hao et al. 2005a). When constructing an AGNLF from galaxy surveys, care has to be taken in defining 'AGN luminosity': Simply taking the optical galaxy magnitude will lead to an ill-defined mix of host galaxy and AGN contributions. It is much better to base the AGNLF on the conspicuous broad Balmer emission lines which avoids the host galaxy contamination problem. This approach was recently adopted by Hao et al. (2005a) and Greene & Ho (2007). But since AGN are scarce among galaxies unless the selection is sensitive to very low levels of nuclear activity (Ho et al. 1997), any general galaxy survey has a low yield, and the samples are dominated by weak Seyfert nuclei and rarely reach quasar-like luminosities.

In this paper we study the population statistics of low-redshift quasars and moderately luminous Seyferts. We exploit the Hamburg/ESO Survey (HES; e.g. Wisotzki et al. 2000), a survey which was specifically designed to address the selection of low-redshift AGN with visible host galaxies, and to provide a well-defined, complete, and unbiased sample of the local AGN population. Here, the term 'complete' is meant in a methodological sense, implying that *all* AGN selected by the criteria are included in the sample. Since obscured or heavily reddened AGN are typically not found in the HES, our sample can only claim to be representative of the unobscured 'type 1' AGN with broad emission lines in their spectra. We refrain in this paper from re-

⋆ This chapter is published in *Astronomy & Astrophysics*, 2009, 507, 781.

peatedly recalling this fact, but it should be understood that we always imply this restriction when using the term 'AGN'.

This is the third paper investigating the local AGNLF in the HES. Koehler et al. (1997) used a small sample of 27 objects obtained during the initial period of the survey to construct the first published local LF of quasars and Seyfert 1 galaxies. Wisotzki (2000b) exploited ~ 50 % of the HES to study the evolution of the quasar luminosity function and provided a re-determination of the local LF as a by-product. With the completed HES covering almost 7000 deg^2 of effective area, the AGN samples are doubled in size, as well as augmented by spectroscopic material. Thus a new effort is well justified. In the present paper we go substantially beyond our previous work not only in quantitative, but also in qualitative terms. We first present our data material and our treatment of the spectra. After constructing the standard broad-band AGNLF we investigate the Hα and Hβ emission line luminosity functions. This enables us to compare and combine our data with the recent work by Hao et al. (2005a) based on the SDSS galaxy sample, to obtain a local AGNLF covering several orders of magnitude in luminosities. We discuss our results in the context of other surveys and luminosity functions.

Thoughout this paper we assume a concordance cosmology, with a Hubble constant of $H_0 = 70$ km s^{-1} Mpc^{-1}, and cosmological density parameters $\Omega_\mathrm{m} = 0.3$ and $\Omega_\Lambda = 0.7$ (Spergel et al. 2003).

2.2. Data

2.2.1. The Hamburg/ESO Survey

The Hamburg/ESO Survey (HES) is a wide-angle survey for bright QSOs and other rare objects in the southern hemisphere, utilising photographic objective prism plates taken with the ESO 1 m Schmidt telescope on La Silla. Plates in 380 different fields were obtained and subsequently digitised at Hamburg, followed by a fully automated extraction of the slitless spectra. In total, the HES covers a formal area of ~ 9500 deg^2 in the sky. For each of the $\sim 10^7$ objects extracted, spectral information at 10–15 Å resolution in the range 3200 Å $\lesssim \lambda \lesssim$ 5200 Å is recorded. Details about the survey procedure are provided by Wisotzki et al. (2000).

The relatively rich information content in the HES slitless spectra enabled us to apply a multitude of selection criteria, depending on the object type in question. AGN can be easily recognised from their peculiar spectral energy distributions if they contain a sufficiently prominent nonstellar nucleus, i.e. 'type 1' AGN. The HES picks up quasars with $B \lesssim 17.5$ at redshifts of up to $z \simeq 3.2$. Several precautions ensured that low-redshift, low-luminosity AGN are not systematically missed. For example, both the extraction of spectra and the criteria to select AGN candidates contained a special treatment of extended sources, making the selection less sensitive to the masking of AGN by their host galaxies. This property makes the HES unique among optical survey in that it targets almost the entire local (low-redshift) population of type 1 AGN, from the most luminous quasars to relatively feeble low-luminosity Seyfert galaxies. It is this property which we exploit in the present paper.

2.2.2. Photometry

Photometric calibration in the HES is a two-step process. We first measured internal isophotal broad-band B_J[1] magnitudes in the *Digitized Sky Survey* (DSS) and calibrated these against external CCD photometric sequences. At the start of the HES around 1990, only the *Guide Star Photometric Catalog* (GSPC Lasker et al. 1988) was available which typically provided standard stars with $8 \lesssim B \lesssim 14$, clearly insufficient to obtain reasonably accurate photometry near $B \sim 17 \ldots 18$, the faint limit of the HES. We therefore launched a campaign to obtain our own deeper photometric CCD sequences in as many fields as possible; the results of this campaign will soon be made public (Schulze et al., in preparation). Augmenting these sequences by incorporating also the *Guide Star Photometric Catalog* II (GSPC-II; Bucciarelli et al. 2001), we arrived at a satisfactory photometric calibration of all 380 HES fields.

However, these isophotal DSS magnitudes suffer from a number of drawbacks, the most undesirable one (for our purposes) being the fact that for extended objects, the nuclear AGN contribution tends to be drowned out by the host galaxy. Using isophotal magnitudes would have a detrimental effect on the estimation of a proper AGN luminosity function especially at the low-luminosity end. Other negative properties of the DSS magnitudes include the effects of relatively poor seeing in many fields, boosting the number of undesired blends.

In order to approximate the concept of *nuclear magnitudes*, we optimised the extraction procedure of slitless spectra in the HES digitised data to assume either true point sources or point sources embedded in a diffuse envelope. In other words, the spectra used for the HES candidate selection always refer to an area of the size of the central seeing disk only (note also that the HES spectral plates were typically obtained under much better seeing conditions than the DSS). We then measured 'nuclear magnitudes' by integrating the spectra over the B_J passband, and calibrated these magnitudes against the DSS using hundreds of stars in each field. We demonstrate below (§ 2.4) that this procedure indeed produces measurements that in reasonably good approximation can be taken as basis for nuclear luminosities (see also Figs. 2.5 and 2.6 below).

An additional advantage of our approach lies in the fact that we thus entirely avoid variability bias: Selection criteria and fluxes in each field are all defined for a single dataset.

For the purpose of the present paper, a good knowledge of the survey selection function, and thus of the accurate flux limits is important. In the case of the HES, the flux limit varies considerably between individual fields, mostly due to changes in the seeing and night-sky conditions, but also because of plate quality. Thus, each field maintains its own flux limit, always corresponding to the same limiting signal to noise ratio in the slitless spectra. As long as redshift-dependent selection effects are neglected, the survey selection function is identical to the 'effective area' of the survey, combining the 380 flux limits into single array that provides the total survey area as a function of

[1] B_J is a roughly rectangular passband defined by a red cutoff at 5400 Å (as imposed by the blue-sensitive photographic emulsion Kodak IIIa-J) and a blue cutoff at 3950 Å. For AGN-like spectra, $B \approx B_J + 0.1$, in the Vega system.

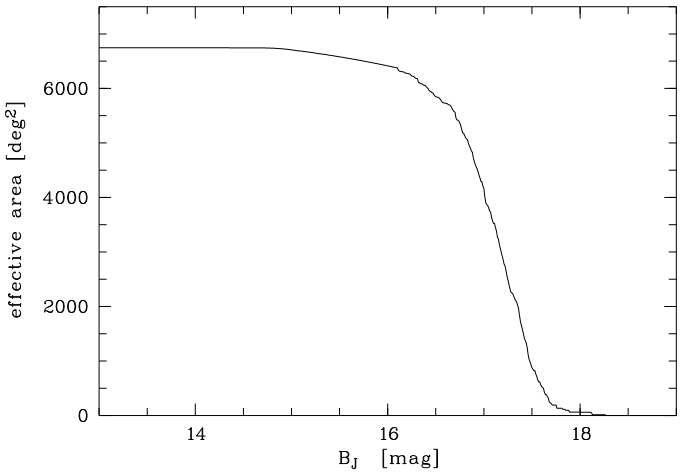

Fig. 2.1. Effective area of the Hamburg/ESO survey as a function of the Galactic extinction corrected B_J magnitude.

magnitude. The effective area of the entire HES is shown in Fig. 2.1. Notice that this array also fully accounts for the losses due to overlapping spectra and images (see the full discussion in Wisotzki et al. 2000).

All magnitudes used in this paper have been corrected for Galactic extinction, using the dust maps of Schlegel et al. (1998) (averaged over each HES field), and the extinction law of Cardelli et al. (1989). Note that for the HES we had previously followed a different extinction correction recipe based on measured column densities of Galactic neutral hydrogen converted into extinction (see Wisotzki et al. 2000). The main result of this change is a slight decrease of the average adopted extinction along most lines of sight.

Figure 2.1 shows that the average extinction-corrected limiting magnitude of the HES is $B_J < 17.3$, but with a dispersion of 0.5 mag between individual fields. There is essentially no bright limit, with 3C 273 recovered as the brightest AGN in the sample.

2.2.3. Spectroscopic data

All AGN and QSO candidates brighter than the flux limit in a given field were subjected to follow-up spectroscopy for confirmation and accurate redshift determination, altogether approximately 2000 targets. These observations were carried out during 23 observing campaigns between 1990 and 2000, using various telescopes and instruments at the ESO La Silla observatory. Known AGN that were recovered by the HES selection criteria were initially not part of the follow-up scheme. However, such objects were often included as backup targets, so that our spectroscopic coverage is almost complete for the entire AGN sample. For some quasars in areas overlapping with the Sloan Digital Sky Survey we could later add spectra from the public SDSS database.

Because of the diversity of telescopes used, the quality of the spectra varied significantly, in signal to noise as well as spectral resolution. We estimated the latter quantity from the width of the night sky O I emission line at 5577 Å. A list of individual observing campaigns with their estimated spectral resolution and the number of AGN from our sample observed is listed in Table 2.1.

Table 2.1. Observing campaigns for follow-up spectroscopy

Date	Telescope	No. of Spectra	Resolution $\lambda/\Delta\lambda$
Dec 1990	3.6 m	4	1020
Apr 1991	3.6 m	1	830
Feb 1992	2.2 m	4	370
Feb 1992	3.6 m	6	900
Sep 1992	3.6 m	4	700
Mar 1993	3.6 m	6	770
Feb 1994	1.5 m	1	1900
Sep 1994	1.5 m	2	1980
Sep 1994	3.6 m	4	680
Nov 1994	1.5 m	11	770
Oct 1995	1.5 m	30	650
Oct 1995	2.2 m	1	300
Mar 1996	1.5 m	19	590
Oct 1996	1.5 m	8	580
Feb 1997	1.5 m	24	600
Oct 1997	1.5 m	19	540
Dec 1997	1.5 m	33	540
Sep 1998	1.5 m	26	670
Nov 1998	1.5 m	23	600
Sep 1999	1.5 m	28	580
Mar 2000	1.5 m	15	540
Sep 2000	1.5 m	36	640
Nov 2000	1.5 m	22	790

Although a formal spectrophotometric calibration was available for all campaigns, the combined dataset is much too heterogeneous to allow for any consistent direct measurement of emission line fluxes. We therefore adjusted all spectra to a common, homogeneous flux scale by computing a synthetic B_J magnitude from each spectrum and matching this to the 'nuclear magnitude' photometry of the HES. This step again also ensured that AGN variability is of no importance.

2.2.4. The sample

For the present investigation of the 'local' AGN population we selected all AGN from the final HES catalogue (Wisotzki et al., in prep.) that belong to the 'complete sample' and that are located at redshifts $z < 0.3$. This sample contains 329 type-1 AGN. For 5 of them we could not obtain spectra of sufficient quality. Thus our sample is $324/329 \approx 98.5$ % complete in terms of spectroscopic coverage.

The HES nuclear fluxes were converted into absolute M_{B_J} magnitudes using the K correction of Wisotzki (2000a). Figure 2.2 shows the distribution of the sample over redshifts and absolute magnitudes. A wide range of nuclear luminosities is covered, ranging from bright quasars with $M_{B_J} \simeq -26$ to low-luminosity Seyfert 1 galaxies of only $M_{B_J} \simeq -18$.

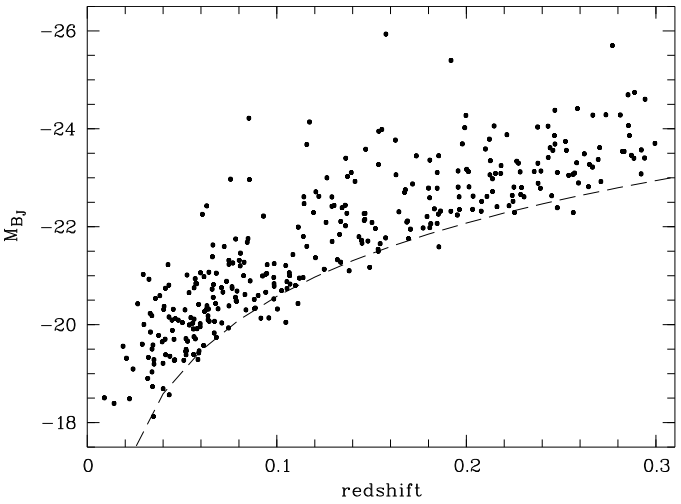

Fig. 2.2. Redshift against absolute magnitude M_{B_J}. The dashed line indicates a constant apparent magnitude of 17.5 mag, approximately the flux limit of the HES.

2.3. Emission line properties

2.3.1. Fitting procedure

As our sample is defined by $z < 0.3$, all objects have Hβ and most also have Hα visible in their spectra. We measured luminosities and line widths of the Hα and Hβ emission lines by fitting the spectral region around each line with a multi-component Gaussian model. Over this short wavelength range we approximated the underlying continuum as a straight line. While the structure of the broad lines is generally complicated, it has repeatedly been demonstrated (e.g. Steidel & Sargent 1991; Ho et al. 1997; Hao et al. 2005b) that in many cases a double Gaussian provides an acceptable fit to the BLR lines. We always started with a single Gaussian per line, which was sometimes already sufficient; otherwise we added a second or third component. At our limited spectral resolution, any possibly present narrow component of a broad line such as Hβ is difficult to detect. We did not include an unresolved narrow component by default and added such a component only when it was clearly demanded by the data.

The Fe II emission complex affecting the red wing of Hβ can be sufficiently approximated by a double Gaussian at wavelength $\lambda\lambda 4924, 5018$ Å for our data. We fixed their positions and also fixed their intensity ratio $\lambda 5018/\lambda 4924$ to 1.28, typical for BLR conditions. Thus only two parameters were allowed to vary, the amplitude and the line width. The [O III] $\lambda\lambda 4959, 5007$ Å lines were also fitted by a double Gaussian with the intensity ratio fixed to the theoretical value of 2.98 (e.g. Dimitrijević et al. 2007). The relative wavelengths of the doublet were fixed as well, but the position of the doublet relative to Hβ was allowed to vary as a whole.

For the Hα line complex, the contributions of [N II], and sometimes also [S II] needed to be taken into account. The latter was mostly well separated and could be ignored, but when required we modelled it as a double Gaussian with fixed positions and same width for both lines. For fitting the [N II] $\lambda\lambda 6548, 6583$ Å doublet we left only the amplitude free. The positions were fixed, the intensity ratio was set to 2.96 (Ho et al. 1997), and the line width was fixed to the width of the narrow [O III] lines.

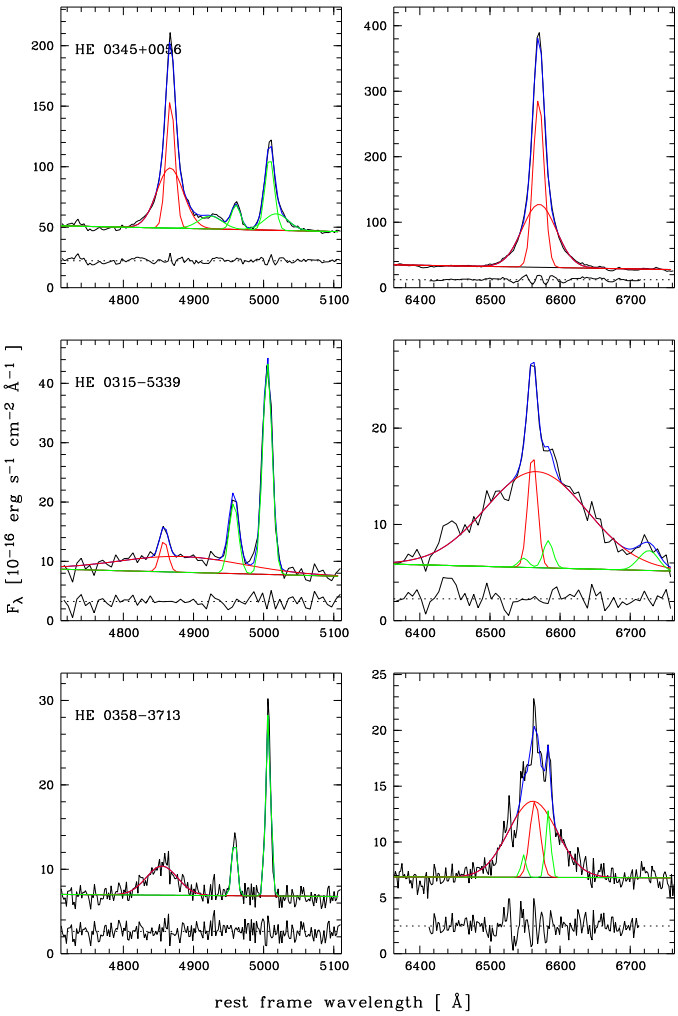

Fig. 2.3. Examples of fits to the spectra, illustrating the quality of the spectroscopic data. The line complex of Hβ is shown on the left side, the corresponding complex around Hα is shown on the right side. The data are represented by black lines, the multi-component Gaussian fits to the Balmer lines are shown in red, other lines are shown green, and the combined model is overplotted in blue. Each panel also shows the fit residuals at the bottom.

With this set of constraints, each spectrum was fitted with a multi-Gaussian plus continuum model. We decided manually which model fits best, neglecting contributions by Fe II, [N II] and [S II] lines if not clearly present. In 6 objects we detected Hα but the S/N was too low to trace Hβ. On the other hand, 21 of our spectra did not reach sufficiently into the red to cover Hα; further 8 spectra were too heavily contaminated by telluric absorption to produce a reliable Hα fit. For these objects, Hβ was readily detected.

Of the 324 spectra of the sample, we thus could obtain reasonable fits for 318 objects in Hβ, and for 295 in Hα. Figure 2.3 shows some example results, illustrating the range of signal to noise ratios and resolutions of the spectral material.

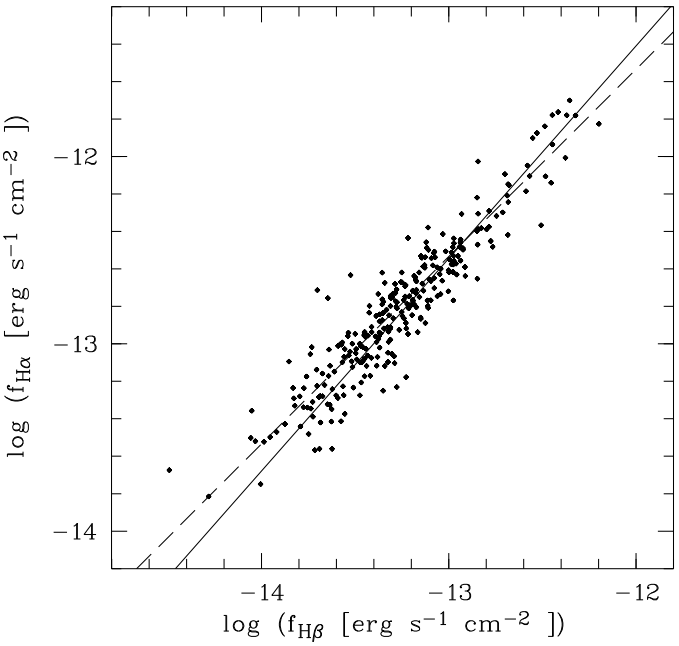

Fig. 2.4. Correlation between the fluxes $f(\mathrm{H}\beta)$ and $f(\mathrm{H}\alpha)$. The solid line shows the regression result using the FITEXY method. The dashed line shows the best fit line with slope of unity.

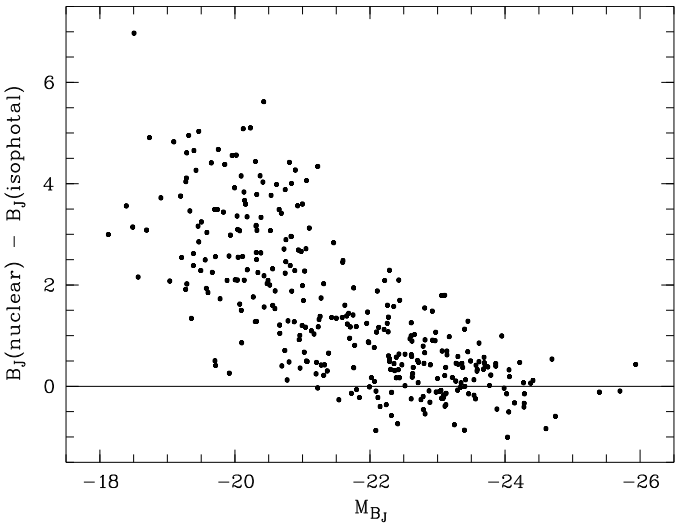

Fig. 2.5. Difference between 'isophotal DSS' and 'nuclear' magnitudes, plotted against absolute nuclear magnitude M_{B_J}.

2.3.2. Line Fluxes

From the fitted model we determined the emission line fluxes of Hα and Hβ as well as the continuum flux at 5100 Å. As said above, a narrow component of the Balmer line was only subtracted if clearly identified in the fit. This happened in 46 cases for Hα and in 34 instances for Hβ. We also measured the line widths of Hα and Hβ, which were then used to estimate the black hole masses for the sample. These results are presented in a companion paper (Schulze & Wisotzki 2010).

In order to estimate realistic errors we constructed artificial spectra for each object, using the fitted model and Gaussian random noise corresponding to the measured S/N. We used 500 realizations for each spectrum. We fitted these artificial spectra as described above, fitting the line and the continuum and measured the line widths and the line flux. The error of these properties was then simply taken as the dispersion between the various realizations. Note that this method provides only a formal error, taking into account fitting uncertainties caused by the noise. Other sources of error may include: A residual Fe II contribution; an intrinsic deviation of the line profile from our multi-Gaussian model, as well as uncertainties in the setting of the continuum level.

2.3.3. Relation between Hβ and Hα fluxes

In order to investigate the distribution of AGN emission line luminosities we focus on Hα and Hβ as the two most prominent recombination lines in our spectra. It is of interest to look at the relation between these two lines. While recent published work on this subject has mostly relied on Hα (Hao et al. 2005a; Greene & Ho 2005), extending similar studies to nonzero redshifts is easier using Hβ. In Fig. 2.4 we plot the fluxes of the two broad lines against each other. As expected, Hα and Hβ are strongly correlated. To quantify this, we applied a linear regression between Hα and Hβ in logarithmic units, using the FITEXY method (Press et al. 1992) which allows for errors in both coordinates. We account for intrinsic scatter in the relation following Tremaine et al. (2002) by increasing the uncertainties until a χ^2 per degree of freedom of unity is obtained. The best-fit relation found for the line fluxes is

$$\log\left(f_{\mathrm{H}\alpha}\right) = (1.14 \pm 0.02)\, \log\left(f_{\mathrm{H}\beta}\right) + (0.46 \pm 0.01) \qquad (2.1)$$

where the fluxes are given in 10^{-13} erg s^{-1} cm^{-2}. The rms scatter around the best fit is 0.15 dex. The relation between Hα and Hβ line flux using the FITEXY method is shown as the solid line in Fig. 2.4. However, a relation with a slope of unity is also consistent with the data (with a scatter of 0.14 dex). When fixing the slope to one, the normalisation corresponds to the relation $f_{\mathrm{H}\alpha} = 2.96\, f_{\mathrm{H}\beta}$, consistent with the Case B recombination value of 3.1 (e.g. Osterbrock 1989). We conclude that the measured Hα and Hβ broad line fluxes give consistent results.

2.4. AGN luminosities

A long-standing issue for the determination of the local AGN luminosity function is the problem of how to disentangle nuclear AGN and host galaxy luminosities. Using total or isophotal photometric measurements will inevitably lead to luminosity- and redshift-dependent biases. For example, the Seyfert luminosity functions determined in some earlier studies (e.g. Huchra & Burg 1992; Ulvestad & Ho 2001) clearly reflected more the distribution of host galaxy luminosities than AGN properties. Ideally, AGN and host light should be properly decomposed object by object; but as this would require high angular resolution data for all objects in a sample, such a route is presently not possible.

As a simplified approach to tackle this problem, we introduced in Sect. 2.2.2 our concept of 'nuclear magnitudes' measured in the HES spectral plates. We did not subtract any host

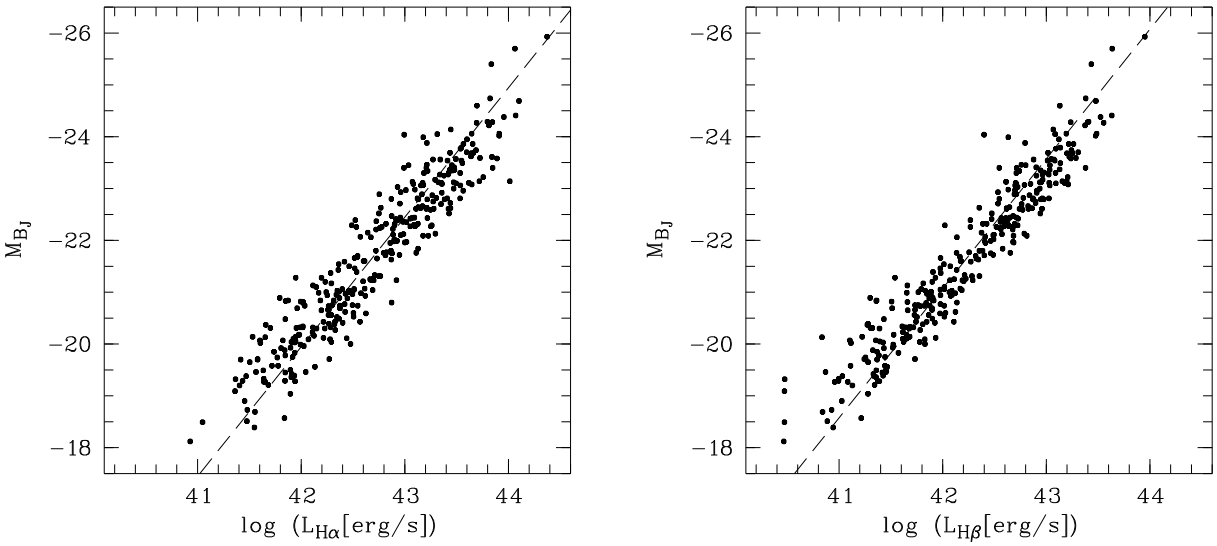

Fig. 2.6. Relation between absolute magnitudes in the B_J band and line luminosities (left: Hα, right: Hβ). A fixed-slope relation $M_{B_J} \propto -2.5 \log L$ is shown as a dashed line in each panel, for illustration purposes only.

galaxy contribution, but we kept it to a minimum by measuring only the flux contribution of a nuclear point source. In Fig. 2.5 we compare these 'nuclear' magnitudes with the more standard isophotal measurements in the DSS direct images. While for high-luminosity quasars (and for all quasars at higher redshifts, not shown in the figure), these two magnitudes give completely consistent results, there is an obvious discrepancy which increases towards lower luminosities. Clearly, the isophotal magnitudes are biased for almost all AGN with nuclear magnitudes fainter than −23, and useless for low-luminosity Seyfert galaxies.

Hence it appears that the HES magnitudes are better estimates of nuclear luminosities than standard isophotal ones; but are they good enough? To investigate this we now compare the HES magnitudes with the luminosities of the broad emission lines. As Hα and Hβ are pure recombination lines, their luminosities should be proportional to the UV continuum (e.g. Yee 1980). In an AGN spectrum, the fluxes of the broad lines are usually conspicuous and can be reasonably well measured even when the host galaxy contribution is strong or dominant. We thus adopt the Balmer emission line luminosities as proxies for the UV continuum luminosity of the AGN, without any host contribution.

In Fig. 2.6 we compare the HES broad band nuclear B_J magnitudes with the luminosities in both Balmer lines. The correlation is excellent and, more importantly, it extends over the entire range of luminosities. To guide the eye, the dashed lines in Fig. 2.6 represent fixed-slope relations $M_{B_J} \propto -2.5 \log L$. We see that the data come very close to a slope of unity in the case of M_{B_J} vs. Hα, while the relation is slightly shallower for Hβ.

If the HES magnitudes were systematically affected by host galaxy contributions we should expect to see a saturation of M_{B_J} values at small L. In fact no clear such trend is visible in the data, except maybe a small excess of a few points above the linear relation in the lower left corner of the right-hand panel. If at all, these few objects appear to be the only ones significantly affected by host galaxy light when described by the HES magnitudes. Overall we conclude that the broad band photometry of the HES is, in good approximation, a measure of the pure AGN luminosities.

2.5. Luminosity functions

2.5.1. Luminosity function parameterisation

The AGN luminosity function (LF) $\phi(L)$ is defined as the number of AGN per unit volume, per unit luminosity. The number of AGN per unit volume and per unit logarithmic luminosity $\Phi(L) = \mathrm{d}\Psi/\mathrm{d}(\log_{10} L)$ is given by $\Phi(L) = (L/\log_{10} e)\phi(L)$, where $\Psi(L)$ is the cumulative luminosity function.

In the following we present the results in two different ways. We first estimate the LF in discrete luminosity bins, expressing it in the logarithmic form $\Phi(L)$ (or in the equivalent form in magnitudes). We then show the results of fitting these binned LFs with simple parametric expressions. As usual, the fit parameters are always expressed in terms of the non-logarithmic form $\phi(L)$.

The most frequently adopted parametric form for the AGN luminosity function is a double power law:

$$\phi(L) = \frac{\phi^*/L_*}{(L/L_*)^{-\alpha} + (L/L_*)^{-\beta}} \,, \tag{2.2}$$

where L_* is a characteristic break luminosity, ϕ^* the normalisation and α and β are the two slopes.

It will be seen that the local AGN LF is close to a single power law, so we will also consider that even simpler form:

$$\phi(L) = \frac{\phi^*}{L_*} \left(\frac{L}{L_*}\right)^{\alpha} \,. \tag{2.3}$$

Expressed in absolute magnitudes these functions have following form:

$$\Phi(M) = \frac{\Phi^*}{10^{0.4(1+\alpha)(M-M_*)} + 10^{0.4(1+\beta)(M-M_*)}} \tag{2.4}$$

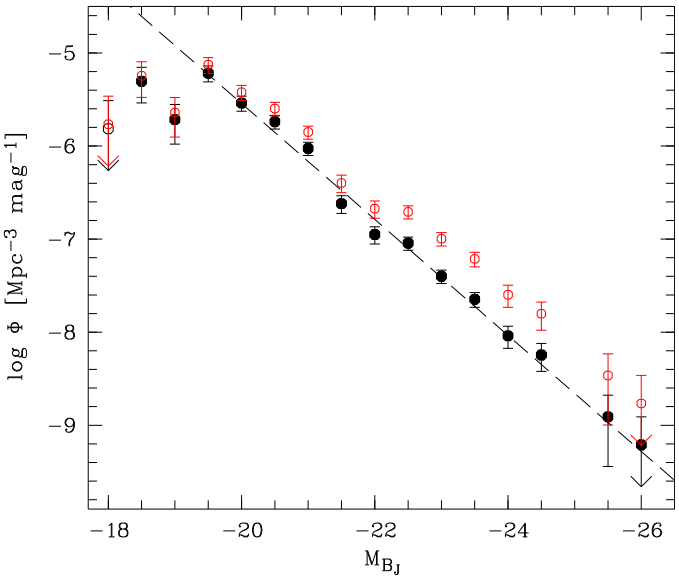

Fig. 2.7. The differential broad band quasar luminosity function of the HES for $0.01 \leq z \leq 0.3$. The error bars are based on Poisson statistics. The arrow indicates a bin with only a single object. The black filled symbols show the luminosity function corrected for evolution using a simple PDE model; red open symbols show the LF not corrected for evolution. The dashed line shows a single power law fit to the data.

for the double power law, and

$$\Phi(M) = \Phi^* 10^{-0.4(1+\alpha)(M-M_*)} \tag{2.5}$$

for the single power law, with $\Phi^* = 0.4\,\phi^* \ln(10)$ for both functions.

2.5.2. Broad band Luminosity Function

We first present the broad band luminosity function, using the full sample of 329 type-1 AGN with $z < 0.3$. This updates the previous work of Wisotzki (2000b), with several improvements: (i) The sample size has doubled. (ii) The quality of the external photometric calibration is improved. (iii) The correction for Galactic extinction has been updated. (iv) We now also include the effects of differential evolution within the redshift range $0 < z < 0.3$ (see below).

We determined the binned luminosity function using the classical $V/V_{\rm max}$ estimator (Schmidt 1968). The luminosity function is then calculated by:

$$\Phi(M) = \frac{1}{\Delta M} \sum_{M-\Delta M/2}^{M+\Delta M/2} \frac{1}{V_{\rm max}^k}\,, \tag{2.6}$$

where ΔM is the bin size and $V_{\rm max}$ is the survey volume in which the object k could have been detected within the flux limit of the survey and the given redshift range. Recall that the dispersion in limiting magnitudes over the 380 HES fields is taken into account by the magnitude dependence of the effective survey area $\Omega_{\rm eff}$ (Fig. 2.1). Thus $V_{\rm max}$ is given by

$$V_{\rm max} = \int_{z_{\rm min}}^{z_{\rm max}} \Omega_{\rm eff}(m) \frac{dV}{dz} dz\,. \tag{2.7}$$

In adopting this form we explicitly assume that the probability of finding an AGN in the HES is independent of redshift. While this would be too strong an assumption for the full quasar sample, it is certainly justified for the restricted low-redshift range $z < 0.3$ considered here. The SEDs of typical type 1 AGN (without host galaxy contributions) at such low redshifts are distinctly blue in the optical/UV, and significant marked variation with redshift occur beyond $z > 0.5$. (Note that we do not consider here the role of 'red' quasars which would be lost in the HES altogether.) If $\mathcal{S}(m, z)$ is the redshift- and magnitude-dependent survey selection function, we can safely marginalise over redshifts and set $\mathcal{S}(m, z) \propto \Omega_{\rm eff}(m)$.

The resulting AGN luminosity function is shown in Fig. 2.7, covering the range $-26 \leq M_{B_J} \leq -18$ in bins of 0.5 mag. It shows remarkably little structure and rises steadily up to the faintest luminosities in the sample. At $M_{B_J} \gtrsim -19$ there appears to be an abrupt break which almost certainly is an artefact, indicating the inevitable onset of severe incompleteness in the HES sample for very low luminosities. For such objects, the host galaxy contribution even to the HES nuclear extraction scheme will be substantial, modifying the slitless spectra in a way that they no longer can be discriminated from normal, inactive galaxies. It is remarkable that this effect plays a role only for the lowest luminosity bins; there is no gradual turnover that might indicate incompleteness already at higher luminosities (alternatively, invoking incompleteness would imply an even steeper LF which would be inconsistent with other results, see below).

If we ignore the lowest luminosity bins affected by incompleteness, the M_{B_J} AGN luminosity function is consistently described by a single power law with slope $\alpha = -2.4$. Fitting instead a double power law to all bins results in the same bright-end slope and a break at $M_{B_J} = -18.75$. A double power law fit to these data is apparently not physically meaningful.

The observation that the local AGNLF is perfectly described by a single power law is in excellent qualitative and quantitative agreement with previous results obtained in the course of the HES (Koehler et al. 1997; Wisotzki 2000b). It is however inconsistent with $z = 0$ extrapolations of the double power law AGNLF obtained at higher redshifts. We will discuss this point in section 2.6.4.

The evolution of comoving AGN space densities with redshift is sufficiently fast that there is a noticeable effect even within the range $0 < z < 0.3$. To derive a truly 'local' ($z = 0$) AGNLF we have to take evolution into account. The $V/V_{\rm max}$ formalism (Schmidt 1968) provides a simple but adequate recipe to do so. If our sample were unaffected by evolution, we would expect to find $\langle V/V_{\rm max}\rangle = 0.5$. Our measured value is $\langle V/V_{\rm max}\rangle = 0.54 \pm 0.02$, implying some evolution. To correct the $z < 0.3$ AGNLF to $z = 0$, we approximate the evolution within this small redshift interval as pure density evolution (PDE), i.e. $\Phi(z) \propto (1+z)^{k_D}$. We varied the density evolution parameter k_D until we reached $\langle V/V_{\rm max}\rangle \approx 0.5$. To increase the leverage we performed the same exercise for a larger redshift range, including quasars from the HES sample up to $z = 0.6$. We found that the evolution within this redshift interval is well described by a PDE model with $k_D = 5$, essentially independent of the exact value of the outer redshift boundary. Notice

Table 2.2. Binned differential luminosity function in the B_J band, corrected for evolution.

M_{B_J}	N	$\log\Phi(M_{B_J})$	$\sigma(\log\Phi)$	
−18.0	1	−5.81	+0.3	−∞
−18.5	6	−5.30	+0.15	−0.24
−19.0	5	−5.72	+0.17	−0.26
−19.5	28	−5.22	+0.08	−0.09
−20.0	30	−5.54	+0.08	−0.09
−20.5	37	−5.74	+0.07	−0.08
−21.0	40	−6.03	+0.07	−0.07
−21.5	23	−6.62	+0.09	−0.10
−22.0	24	−6.95	+0.08	−0.10
−22.5	40	−7.04	+0.06	−0.08
−23.0	38	−7.40	+0.07	−0.08
−23.5	31	−7.65	+0.08	−0.08
−24.0	14	−8.04	+0.10	−0.13
−24.5	9	−8.25	+0.13	−0.17
−25.5	2	−8.91	+0.23	−0.53
−26.0	1	−9.21	+0.3	−∞

Notes. N is the number of objects contributing per bin. The luminosity function is expressed as number density per Mpc^3 per unit magnitude.

that beyond the very local universe, the HES samples only the brightest quasars, and our correction for the most part concerns these high-luminosity bins only. For a single power law, density and luminosity evolution are indistinguishable. Therefore our evolution correction does not critically depend on the choice of the actually adopted model.

We then applied the parameterised density evolution to the HES $z < 0.3$ sample to recompute the evolution-corrected $z = 0$ AGNLF. Note that we used the objects at $z > 0.3$ only to constrain the density evolution index k_D and not for the luminosity function.

We still obtain a relation very close to a single power law, which however is slightly steeper than the uncorrected one. The best fit power law slope is now $\alpha = -2.6$. This evolution-corrected AGNLF is also shown in Fig. 2.7. It is provided in tabulated form in Table 2.2.

2.5.3. Emission Line Luminosity Function

The emission line luminosity function (ELF) – the number of AGN per unit volume per unit logarithmic emission line luminosity – is given by

$$\Phi(L) = \frac{1}{\Delta \log L} \sum_k \frac{1}{V_{\max}^k} \,. \tag{2.8}$$

The selection of AGN in the HES in this redshift range (and up to $z \sim 2.5$) is exclusively based on continuum SED properties and independent of emission line properties (Wisotzki et al. 2000). Thus the selection function is the same as for the broad band luminosity function, and the $V_{\max}$ values needed for the determination of the emission line luminosity function are also the same as for the M_{B_J} luminosity function, except for a correction factor containing the spectroscopic incompleteness. As discussed in § 2.2.4, our sample has an overall spectroscopic completeness of 324/329 ≈ 98.5 %. Of the 324 objects with spectra, 6 do not show Hβ and 29 do not show Hα, due to insufficient spectroscopic coverage or atmospheric absorption. This incompleteness does not affect any particular object types preferentially, and we assumed the losses to be randomly distributed. We therefore adopted the effective survey area as before, multiplied by a factor of 318/329 for Hβ and by 295/329 for Hα, respectively. Unless explicitly stating otherwise, we always refer to the evolution-corrected $V_{\max}$ values, thus providing luminosity functions valid for exactly $z = 0$.

Table 2.3. Binned Hα and Hβ emission line luminosity functions.

	Hα		**Hβ**	
$\log L$	N	$\log\Phi(\mathrm{H}\alpha)$	N	$\log\Phi(\mathrm{H}\beta)$
40.5			4	$-5.19^{+0.2}_{-0.4}$
40.75			3	$-5.7^{+0.24}_{-0.57}$
41.0	2	$-5.26^{+0.23}_{-0.57}$	11	$-5.01^{+0.13}_{-0.2}$
41.25	2	$-5.84^{+0.23}_{-0.55}$	23	$-5.03^{+0.11}_{-0.14}$
41.5	16	$-4.9^{+0.13}_{-0.17}$	26	$-5.19^{+0.09}_{-0.11}$
41.75	23	$-5.04^{+0.11}_{-0.14}$	38	$-5.38^{+0.07}_{-0.09}$
42.0	34	$-5.05^{+0.08}_{-0.11}$	37	$-5.68^{+0.07}_{-0.09}$
42.25	38	$-5.4^{+0.08}_{-0.1}$	25	$-6.26^{+0.09}_{-0.12}$
42.5	35	$-5.72^{+0.09}_{-0.11}$	36	$-6.61^{+0.07}_{-0.09}$
42.75	28	$-6.3^{+0.1}_{-0.12}$	45	$-6.74^{+0.07}_{-0.08}$
43.0	32	$-6.68^{+0.1}_{-0.12}$	35	$-7.16^{+0.07}_{-0.09}$
43.25	34	$-6.9^{+0.09}_{-0.1}$	22	$-7.48^{+0.08}_{-0.11}$
43.5	28	$-7.22^{+0.08}_{-0.1}$	10	$-7.87^{+0.11}_{-0.17}$
43.75	17	$-7.58^{+0.1}_{-0.12}$	2	$-8.59^{+0.23}_{-0.53}$
44.0	6	$-8.04^{+0.15}_{-0.23}$	1	$-8.89^{+0.3}_{-\infty}$

Figure 2.8 displays a very similar behaviour of the ELF when compared to the broad-band LF of Fig. 2.7: It rises nearly as a straight line, i.e. as a single power law, until a sharp cutoff at low luminosities indicates the onset of sample selection incompleteness. Fitting power law relations to the data (again excluding the obviously incomplete lowest luminosity bins) gives slopes of $\alpha_{\mathrm{H}\alpha} = -2.28$ and $\alpha_{\mathrm{H}\beta} = -2.26$, respectively. Fitting a double power law improves the fit quality only marginally. We conclude that a description of the ELF as a single power law, for the luminosity range covered by our data, seems most appropriate.

2.6. Discussion

2.6.1. Low luminosity-AGN: Comparison with SDSS

The sharp cutoff in the binned luminosity functions at nuclear luminosities $M_{B_J} \gtrsim -19$ or $\log L_{H\alpha} \lesssim 42$ clearly signals the onset of incompleteness in our sample. This luminosity approximately marks the limit where AGN cease to be conspicuous in the optical and tend to be masked by their host galaxies. However, deep spectroscopic surveys of galaxies have shown

Table 2.4. Fit parameters for the AGNLF.

AGNLF		ϕ^*, Φ^* [Mpc]$^{-3}$	M_*, log L_*	β	α	χ^2	χ^2/dof
M_{B_J}	$z < 0.3$	1.80×10^{-7}	−22.44	−2.35	–	16.08	1.61
M_{B_J}	$z = 0$	8.36×10^{-8}	−22.46	−2.56	–	14.56	1.46
Hα	$z = 0$	2.18×10^{-7}	42.76	−2.28	–	18.51	2.31
Hβ	$z = 0$	1.07×10^{-7}	42.51	−2.26	–	34.17	3.42
Hα + SDSS	$z = 0$	5.59×10^{-6}	41.58	-2.21	–	97.0	2.85
Hα + SDSS	$z = 0$	1.8×10^{-5}	41.67	-2.58	−1.80	37.32	1.49
M_B (HES+SDSS)	$z = 0$	5.60×10^{-6}	−19.25	−2.40	–	65.5	4.09
M_B (HES+SDSS)	$z = 0$	1.55×10^{-5}	−19.46	−2.82	−2.00	24.4	1.62
log $L_{\rm Bol}$ (HES+SDSS)	$z = 0$	2.54×10^{-5}	44.37	−2.95	−2.17	25.58	1.71

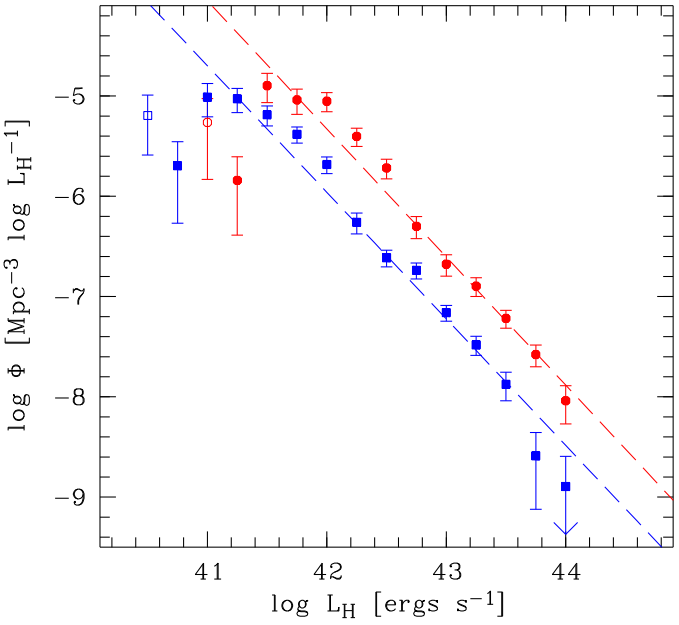

Fig. 2.8. Binned emission line AGN luminosity functions, for Hα (red filled circles) and Hβ (blue squares). Open symbols indicate incompletely filled bins. The dashed lines show the best fit single power law to the Hα and Hβ data, respectively.

that the AGN phenomenon persists down to very low levels (e.g. Ho et al. 1997). In those cases, the only traceable indicator of nuclear activity in the optical are the emission lines, thus the statistics have to be expressed in terms of an ELF. This was recently performed by Hao et al. (2005a, hereafter H05), who selected a set of ∼ 1000 Seyfert 1 galaxies from the Sloan Digital Sky Survey (main galaxy sample) to measure Hα line luminosities and construct the ELF. The redshift range covered in their sample is $0 < z < 0.15$, and the luminosity range is ($10^{38.5}$–10^{43}) erg s^{-1}. H05 found their ELF to be in good agreement with several parametric descriptions, including single and double power laws and also a Schechter function. However, differences between these forms become manifest only at their highest luminosities, for L(Hα) ∼ 10^{42} erg s^{-1} . Over much of the luminosity range, their data suggest a single power law.

Fortunately the *high-luminosity end* of H05 overlaps quite well with the *low-luminosity end* of our Hα ELF, so that a comparison is straightforward. This is shown in Fig. 2.9 where we plot the Seyfert 1 Hα luminosity function of H05 (adapted to our cosmology) together with our Hα LF. The transition from one dataset to the other is remarkably smooth, if the incomplete lowest luminosity bins in the HES sample are ignored. Over the luminosity range in common, both ELFs are fully consistent with each other.

Even more remarkably, the shape of the combined Hα LF – now covering almost 5 orders of magnitude in luminosity – is still close to that of a single power law. Already the fit to the HES Hα LF alone is almost consistent with the H05 LF. Combining both samples, we find a best-fit power law slope of $\alpha \approx -2.2$. This fit is shown as the dashed-dotted line in Fig. 2.9.

However, there is evidence for *some* curvature in the LF, as the H05 LF alone is flatter ($\alpha = -2.02$) than the HES ELF. This is manifest in a 'bulge' around 10^{42} erg s^{-1}, where the space density of the combined LF is above the fitted single power law. A better fit is obtained by a double power law breaking at log $L_\star = 41.67$, with a faint-end slope of $\alpha = -1.8$ describing the SDSS data and a bright-end slope of $\beta = -2.6$ describing the HES. This mildly curved relation, shown by the dashed line in Fig. 2.9, traces the combined data extremely well.

Some caveats are in place regarding the combination of the two datasets. Although H05 determined the narrow Hα components separately, their broad-line ELF does not have this component subtracted, whereas we tried to remove it. As such a removal was possible in only a small number of cases, the different treatment does not make much difference. More relevant might be the possibility of a systematic variation of the narrow Hα contribution to the total Hα flux with luminosity. However, the *narrow* Hα LF published by H05 has also a slope of −1.8, which indicates that there should be no major bias introduced.

Another methodical difference lies in the fact that we corrected our LF for evolution, whereas H05 did not. If we assume that the most luminous objects of H05 lie close to their high-redshift limit of $z < 0.15$ and adopting our simple PDE recipe, then the H05 space densities would have to be corrected downward by a factor of $1.15^5 \approx 2$, i.e. by 0.3 dex; this correction would rapidly decrease towards lower luminosities. The net effect would hardly be visible in Fig. 2.9.

We note that recently, Greene & Ho (2007) (hereafter GH07) derived the AGN Hα LF based on a combined sample of about 9000 broad line AGN from the SDSS. Their space densities are considerably below ours, and the two LFs are highly inconsistent (the same discrepancy exists between the GH07 and

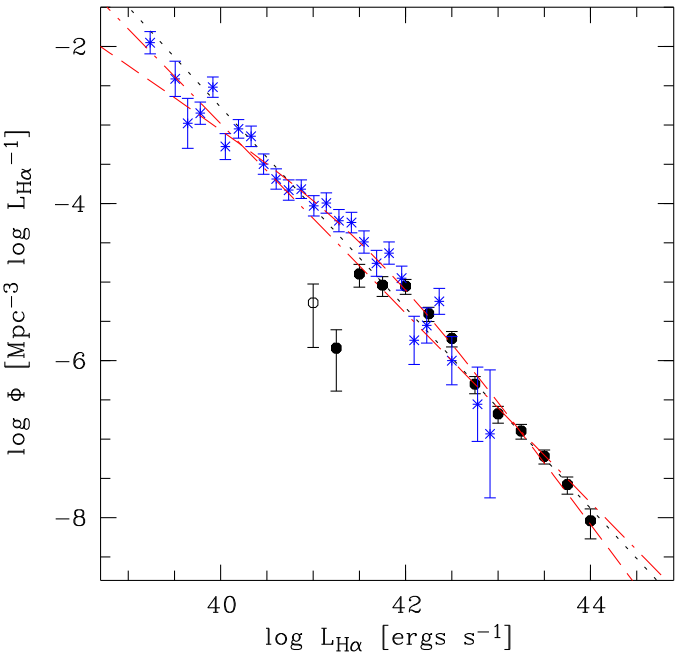

Fig. 2.9. Comparison of the Hα luminosity function derived in this work (black points), with the work of Hao et al. (2005a) (blue asterisks). The black dotted line gives the best fit single power law to our Hα luminosity function. The red dashed dotted line gives the best fit power law to the combined data set, whereas the red dashed line gives the best fit double power law.

H05 results). This inconsistency has been traced back to an error made by GH07 in the determination of their $V/V_{\rm max}$ values (J. Greene, private communication). Therefore the luminosity function as well as the black hole mass function presented in GH07 are incorrect. Removing the error alleviates the discrepancy, and the corrected Hα luminosity function for the low redshift AGN sample from GH07 is consistent with the HES luminosity function presented in this work.

2.6.2. The combined local AGN luminosity function

Given the good agreement of the local HES LF, which traces the bright end, and the SDSS Seyfert 1 LF sampling the faint end, and having the mentioned caveats in mind, it is justified to combine both datasets. Our aim is to present a single best-knowledge local AGNLF in the optical, covering the broadest possible range of luminosities. Because of its robustness against dilution due to host galaxy light, we used the Hα luminosity functions of HES and SDSS. We adopted a bin size of 0.24 dex (0.6 mag) as an integer multiple of the binned values published by H05. We then recomputed the Hα ELF from the HES data for the same bins and merged the two datasets, with weights provided by the inverse statistical variances.

For easy comparison with other AGN luminosity functions, especially at higher redshifts, we converted this combined LF into two common reference systems: (i) absolute magnitudes M_B in the standard Johnson B band; and (ii) bolometric luminosity units. These conversions involve translating the Hα data into broad band or bolometric fluxes. There is a very tight correlation between Hα luminosity and absolute blue magnitude in the HES (Fig. 2.6). The translation relation is $M_B = -2.1\,(\log L(\mathrm{H}\alpha) - 42) - 20.1$. This relation is covered by our data down to $M_B \simeq -19$. In order to incorporate also the lower luminosity SDSS data we now make the somewhat unguarded step of extrapolating the translation of $L_{\rm H\alpha}$ to M_B towards lower L. This certainly introduces additional uncertainties, including the possibility that some of the lowest luminosity AGN could have very different spectral energy distributions (for example, the structure of the accretion disk might change drastically). On the other hand, there is no reason to expect such a change to occur just at the transition luminosity from HES to SDSS, so some degree of extrapolation is most probably justified.

Table 2.5. Combined binned local AGNLF, based on the SDSS broad line galaxy sample (faint end) and the Hamburg/ESO Survey (bright end).

M_B	$\log\Phi(M_B)$	$\log L_{\rm Bol}$	$\log\Phi(L_{\rm Bol})$
−14.2	$-2.60^{+0.11}_{-0.14}$	42.77	$-2.11^{+0.10}_{-0.15}$
−14.8	$-2.95^{+0.12}_{-0.18}$	42.97	$-2.47^{+0.12}_{-0.18}$
−15.4	$-3.00^{+0.08}_{-0.09}$	43.17	$-2.52^{+0.07}_{-0.10}$
−16.0	$-3.49^{+0.07}_{-0.09}$	43.37	$-3.02^{+0.07}_{-0.09}$
−16.6	$-3.63^{+0.08}_{-0.10}$	43.58	$-3.17^{+0.08}_{-0.09}$
−17.2	$-4.10^{+0.08}_{-0.09}$	43.79	$-3.64^{+0.07}_{-0.09}$
−17.8	$-4.26^{+0.08}_{-0.08}$	44.00	$-3.80^{+0.07}_{-0.09}$
−18.4	$-4.44^{+0.08}_{-0.09}$	44.22	$-3.99^{+0.08}_{-0.09}$
−19.0	$-4.69^{+0.07}_{-0.10}$	44.43	$-4.25^{+0.07}_{-0.10}$
−19.6	$-5.04^{+0.09}_{-0.10}$	44.65	$-4.60^{+0.08}_{-0.10}$
−20.2	$-5.46^{+0.06}_{-0.08}$	44.87	$-5.03^{+0.06}_{-0.08}$
−20.8	$-5.78^{+0.07}_{-0.08}$	45.09	$-5.35^{+0.07}_{-0.08}$
−21.4	$-6.36^{+0.09}_{-0.12}$	45.32	$-5.93^{+0.09}_{-0.12}$
−22.0	$-6.85^{+0.09}_{-0.11}$	45.55	$-6.43^{+0.09}_{-0.11}$
−22.6	$-7.19^{+0.08}_{-0.10}$	45.77	$-6.77^{+0.08}_{-0.10}$
−23.2	$-7.40^{+0.08}_{-0.09}$	46.00	$-6.98^{+0.07}_{-0.10}$
−23.8	$-7.87^{+0.10}_{-0.11}$	46.23	$-7.46^{+0.10}_{-0.11}$
−24.4	$-8.20^{+0.12}_{-0.16}$	46.47	$-7.79^{+0.12}_{-0.16}$
−25.0	$-8.76^{+0.20}_{-0.37}$	46.70	$-8.35^{+0.20}_{-0.37}$

The resulting combined local AGN LF is shown in Fig. 2.10, ranging from $M_B \gtrsim -25$ to $M_B \lesssim -15$ (with the above caveat). Also shown as a dotted line is the best fit single power law, and as a solid line the best fit double power law; the fit parameters are provided in Table 2.4. The double power law gives a very good overall description, but the departure from a single power law is not large, albeit statistically significant. There are some minor wiggles in the binned LF that are most probably due to underlying unaccounted for systematics; note however that there is no trace of the HES-SDSS intersection (rather: transition region) around $M_B \sim -20$.

For the convenience of the reader we also provide this LF in tabulated form, both in terms of the B band and as a bolometric LF. For the latter we adopted the luminosity-dependent bolometric corrections of Hopkins et al. (2007). A separate double power law fit to the resulting bolometric LF is also provided

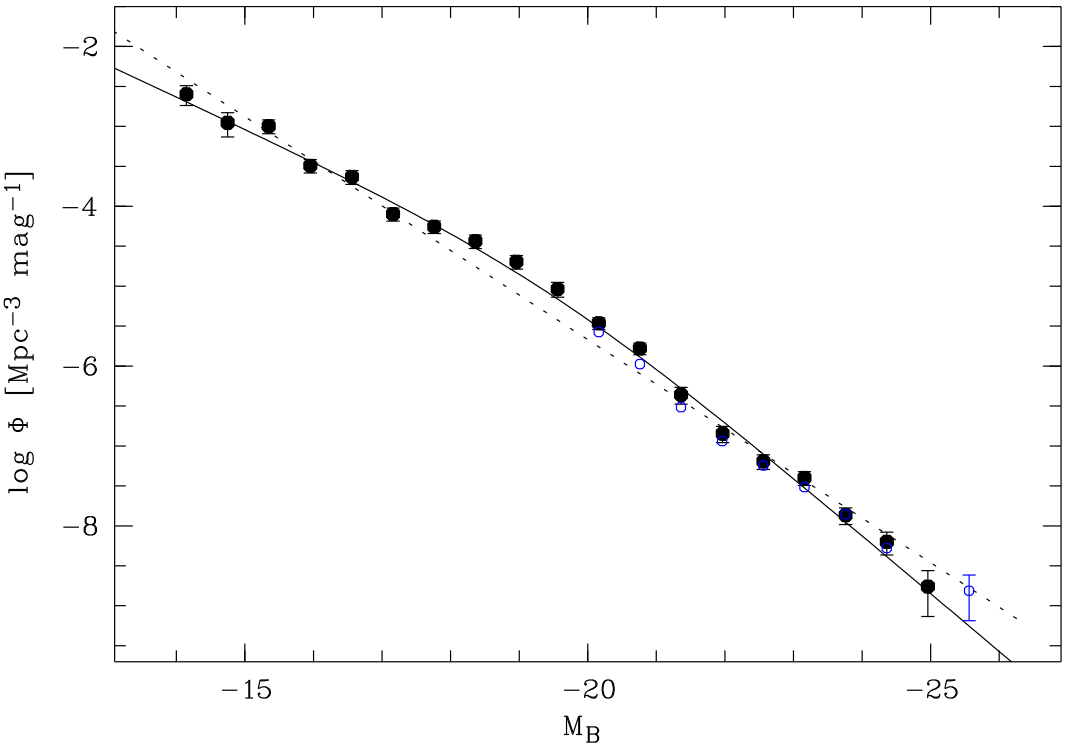

Fig. 2.10. Local AGN luminosity function constructed as a combination of the SDSS broad line AGN LF from Hao et al. (2005a) and our Hα HES bright AGN LF, both converted to the B band. The black solid line and dotted line show the double and single power law fits, respectively. The open blue circles show the directly determined broad band (M_{B_J}) LF for comparison.

in Table 2.4. Recall that this bolometric luminosity function is valid only for broad-line (type 1) AGN, without any accounting for obscuration.

2.6.3. Comparison with X-ray selected samples

X-ray surveys have made a great impact on our understanding of the AGN population, chiefly through their ability to find low-luminosity AGN at all redshifts. However, because of the expensive spectroscopic follow-up, sample statistics are still moderate despite considerable efforts.

The only dedicated effort to estimate an optical local AGNLF from an X-ray selected sample was published by Londish et al. (2000). Their bright-end slope of $\beta = -2.1$ (without evolution correction) is similar to ours, but they obtained a shallow faint end slope of $\alpha = -1.1$, however with considerable error bars. Our new results, in particular in combination with SDSS, show clearly that such a flat slope is ruled out and that the local AGNLF continues to rise towards very faint luminosities.

A local ($z = 0$) luminosity function from an AGN sample selected in the soft X-ray (0.5–2 keV) band was presented by Hasinger et al. (2005). Their sample is restricted to unabsorbed type 1 AGN and is therefore very comparable to ours. To facilitate a comparison, we again used the L-dependent bolometric corrections of Hopkins et al. (2007) to convert our combined optical AGNLF into the soft X-ray domain. In Fig. 2.11 we compare the $z = 0$ XLF of Hasinger et al. (2005) with our prediction. The X-ray points are represented by the filled blue triangles, which are the binned estimate in the redshift shell $z = 0.015 - 0.2$ of Fig. 7 in Hasinger et al. (2005), corrected to redshift zero. The blue dotted line shows their best-fit luminosity-dependent density evolution (LDDE) model for $z = 0$.

For intermediate luminosities, the observed XLF and the prediction based on the optical AGNLF are in good agreement. A modest discrepancy is visible for high-luminosity AGN; but the two LFs disagree strongly at the faint end, with the optical LF predicting more than an order of magnitude higher space densities at given X-ray luminosity compared to the directly determined XLF.

Is there an explanation for these discrepancies? One possibility might be that the adopted conversion from optical to X-ray luminosities has been inadequate. In order to explore this option we alternatively tried a constant optical/X-ray luminosity ratio; the dashed line in Fig. 2.11 shows our double-power law relation converted with such a relation. Evidently, that predicted LF is a very good match to the bright end of the XLF. At the faint end the two LFs still disagree, but the disagreement is now much less. Thus it appears possible that the luminosity dependence of the optical/X-ray ratio is much weaker than usually assumed; if so, it would certainly help to reconcile the two luminosity functions. Another possibility is, of course, incompleteness among the fainter objects in the X-ray sample. We reiterate however that since both samples contain only broad-line AGN, any incompleteness due to obscuration should be irrelevant in this context.

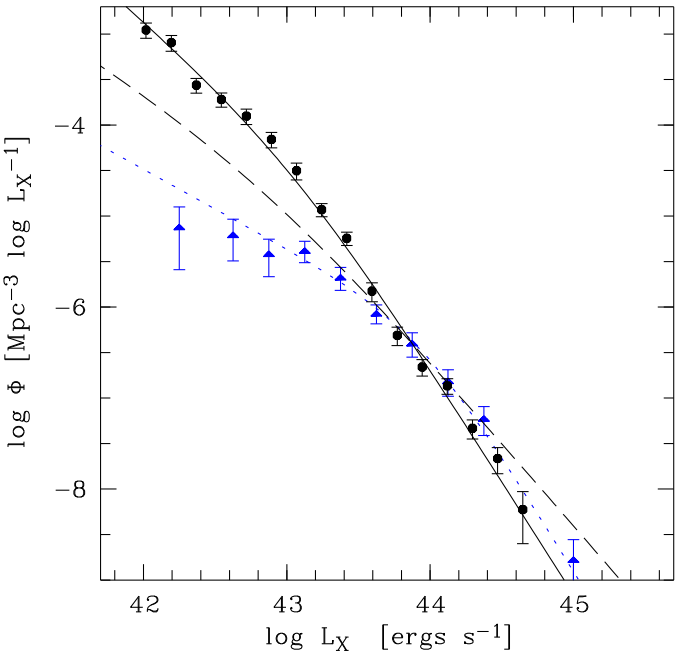

Fig. 2.11. Comparison of the soft X-ray LF of type 1 AGN by Hasinger et al. (2005) with the prediction based on the optical local AGNLF. The filled blue triangles show the binned X-ray (0.5–2 keV) LF within $z = 0.015 - 0.2$, corrected to $z = 0$. The blue dotted line shows the LDDE model of Hasinger et al. (2005) for $z = 0$. The filled black circles and the solid line show the binned data and the double power law fit to the optical HES+SDSS LF, converted to soft X-rays using a luminosity dependent correction. The dashed line shows the same double power law fit, but converted to soft X-rays using a constant correction.

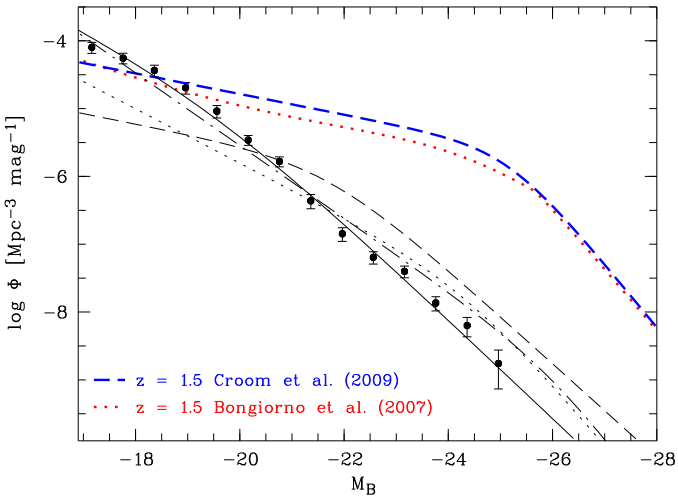

Fig. 2.12. Shape evolution and 'downsizing' of the AGNLF between $z = 1.5$ and $z = 0$. Filled circles and solid line denote our combined HES+SDSS AGNLF at $z = 0$. The blue dashed and red dotted lines show the best fit model to the data of the $z = 1.5$ AGNLF of the 2QZ (Croom et al. 2004) and the VVDS+SDSS (Bongiorno et al. 2007), respectively. The black dashed line shows the PLE model of Croom et al. (2004) extrapolated to redshift zero.

2.6.4. Comparison with higher redshifts: Evidence for 'AGN downsizing'

We now perform a direct comparison of our local AGNLF with luminosity functions based on surveys that probe mainly the higher redshift AGN population. This is interesting not only because a comparison with $z = 0$ provides the longest leverage in redshifts, but also because the local luminosity function can be traced to very faint luminosities and high space densities. A full investigation of the redshift evolution of the AGNLF is outside of the scope of this paper; we limit ourselves to a simple comparison between the $z = 0$ LF determined above and parametric representations of the AGNLF evaluated at $z = 1.5$, the latter chosen as a representative point at moderately high redshift where several surveys have been able to leave their marks.

The results of this comparison are displayed in Fig. 2.12. The datapoints and the solid line show our combined local AGNLF. The thick dashed line shows the $z = 1.5$ fit to optically selected QSOs with $0.4 < z < 2.1$ from the 2dF Redshift Survey (Croom et al. 2004). They found their data to be in good overall agreement with a double power law LF and a pure luminosity evolution (PLE) redshift dependence. The thin dashed line shows the $z = 0$ extrapolation of this PLE model (essentially just a horizontal shift). This extrapolation is clearly a very poor match to the local AGNLF, in several aspects: The observed bright-end slope is flatter and the faint-end slope is much steeper than the extrapolated one, so that the space density of intermediate luminosity AGN is over- and that of low-luminosity AGN is heavily underpredicted.

As a second reference we considered the AGNLF by Bongiorno et al. (2007) (dotted line), derived from a combination of the SDSS at the bright end and the faint type 1 AGN sample from the VVDS (Gavignaud et al. 2006). This sample is noteworthy in that it is certainly the most complete set of low-luminosity AGN at substantial z, as it is purely flux limited and not affected by any colour or morphological preselection. This is manifest in the steeper faint-end slope of the $z = 1.5$ LF.

Nevertheless, comparing the Bongiorno et al. (2007) and the local AGNLF reveals a striking change in the shape of the luminosity function: The pronounced break visible at high z is almost absent in the local LF. In terms of space densities, this implies that while high-luminosity AGN were *much* more frequent at high redshifts, AGN with nuclear luminosities around $M_B \sim -19$ are as common in the local universe as they were at high z. For somewhat fainter AGN this relation might even be reversed, although there are too many uncertainties to make such a claim.

Such a 'downsizing' behaviour of the AGN population was previously detected through X-ray surveys (Ueda et al. 2003; Hasinger et al. 2005); here we demonstrate for the first time that the same phenomenon features very prominently in the optical AGNLF as well. Note that this conclusion does not hinge on our extrapolation of the Hα-M_B relation, as the crossing of the $z = 1.5$ and $z = 0$ LFs occurs at luminosities still covered by the HES.

2.7. Conclusions

We have presented a new determination of the local ($z \approx 0$) luminosity function of broad-line Active Galactic Nuclei. Our sample was drawn from the Hamburg/ESO Survey and contains 329 quasars and Seyfert 1 galaxies with $z < 0.3$, selected from surveying almost 7000 deg^2 in the southern sky. As a central feature, our broad-band magnitudes were measured in the survey data with a point-source matching approach, strongly reducing the contribution of host galaxy flux to the inferred AGN luminosity. Compared to our previous work we have not only substantially increased the statistical basis, but also added a number of methodical improvements.

In the construction of the broad band (B_J) luminosity function, we now included the effects of differential number density evolution within our narrow redshift range, $0 \lesssim z < 0.3$. Since the most luminous AGN tend to be located near the outer edge of that range, ignoring evolution makes the luminosity function appear slightly too shallow. We find that the evolution-corrected local luminosity function within $-19 \lesssim M_{B_J} \lesssim -26$ is well-described by a single power law of slope $\alpha = -2.6$, still significantly shallower than the $z = 0$ extrapolation of the AGNLF measured at higher redshifts.

As a second and independent measure of AGN power we investigated the distribution of Balmer emission line luminosities, in particular the broad Hα and Hβ lines. These lines can be detected and accurately isolated in optical spectra even of low-luminosity AGN where the host galaxy is bright compared to the nucleus. We found a very tight correlation between Hα luminosities and broad band absolute magnitudes M_{B_J} over the entire luminosity range of our sample, confirming that host galaxy contamination to the M_{B_J} magnitudes is unimportant.

We constructed the broad emission line luminosity functions for Hα and Hβ, and found them to agree well with the broad band LF. In particular, there is again no trace of significant curvature over the covered luminosity range, and a single power law is still sufficient to describe the shape of the LF.

We found excellent consistency between our data and the Hα emission line luminosity function of low-luminosity AGN determined from the SDSS by (Hao et al. 2005a). While the two datasets are complementary in luminosity coverage, our low-luminosity end overlaps very well with their high-luminosity end. The SDSS data seamlessly continue the rise of the LF towards the domain of low-luminosity Seyferts. The comparison with SDSS also delineates clearly that below $L(\mathrm{H}\alpha) \sim 10^{42}$ erg s^{-1} (or $M_{B_J} \sim -19$), the HES sample becomes heavily incomplete; this we suspected already from the shape of the HES luminosity function alone.

We combined the HES and SDSS results into a single $z = 0$ AGN luminosity function covering more than 4 orders of magnitude in luminosity. This remedies a long-standing shortcoming of AGN demographics: Despite the heroic survey efforts, there was no really well-determined *local* luminosity function that could serve as anchor for a global take on AGN number density evolution. The combined local AGNLF is still amazingly close to a single power law, but it definitely shows curvature. A good description is provided by a double power law with slopes $\alpha = -2.0$ and $\beta = -2.8$.

Comparing the combined local AGNLF with determinations at higher redshifts, we find strong evidence for luminosity-dependent evolution, in the sense that weak AGN experience a much weaker number density decline, or no decline at all, than powerful quasars. This behaviour is well established from X-ray surveys, where a systematic shift of the peak in comoving space density with luminosity is observed (e.g. Ueda et al. 2003; Hasinger et al. 2005). Known as 'AGN downsizing', it is presumably related to the anti-hierarchical mass dependence of black hole growth (e.g. Heckman et al. 2004; Merloni 2004; Marconi et al. 2004; Merloni & Heinz 2008). The steepening of the faint end slope towards low redshift can be understood in this scenario by the change of quasar lifetime with peak luminosity, and hence black hole mass. The more massive black hole AGN die more quickly than lower mass black hole AGN and are therefore not observable in their decaying stage of their light curve, whereas lower black hole mass AGN are observable in their less luminous stage and contribute significantly to the faint end of the LF (Hopkins et al. 2006; Gavignaud et al. 2008). Thus the faint end of the luminosity function should consist of a mixture of low mass black holes accreting at a high rate and higher mass black holes with low accretion rates. Investigating this question will be the subject of the next chapter.

References

Bongiorno, A., Zamorani, G., Gavignaud, I., et al. 2007, A&A, 472, 443
Boyle, B. J., Shanks, T., Croom, S. M., et al. 2000, MNRAS, 317, 1014
Bucciarelli, B., García Yus, J., Casalegno, R., et al. 2001, A&A, 368, 335
Cardelli, J. A., Clayton, G. C., & Mathis, J. S. 1989, ApJ, 345, 245
Croom, S. M., Smith, R. J., Boyle, B. J., et al. 2004, MNRAS, 349, 1397
Dimitrijević, M. S., Popović, L. Č., Kovačević, J., Dačić, M., & Ilić, D. 2007, MNRAS, 374, 1181
Gavignaud, I., Bongiorno, A., Paltani, S., et al. 2006, A&A, 457, 79
Gavignaud, I., Wisotzki, L., Bongiorno, A., et al. 2008, A&A, 492, 637
Greene, J. E. & Ho, L. C. 2005, ApJ, 630, 122
Greene, J. E. & Ho, L. C. 2007, ApJ, 667, 131
Hao, L., Strauss, M. A., Fan, X., et al. 2005a, AJ, 129, 1795
Hao, L., Strauss, M. A., Tremonti, C. A., et al. 2005b, AJ, 129, 1783
Hasinger, G., Miyaji, T., & Schmidt, M. 2005, A&A, 441, 417
Heckman, T. M., Kauffmann, G., Brinchmann, J., et al. 2004, ApJ, 613, 109
Ho, L. C., Filippenko, A. V., Sargent, W. L. W., & Peng, C. Y. 1997, ApJS, 112, 391
Hopkins, P. F., Hernquist, L., Cox, T. J., et al. 2006, ApJ, 639, 700
Hopkins, P. F., Richards, G. T., & Hernquist, L. 2007, ApJ, 654, 731
Huchra, J. & Burg, R. 1992, ApJ, 393, 90
Koehler, T., Groote, D., Reimers, D., & Wisotzki, L. 1997, A&A, 325, 502
Lasker, B. M., Sturch, C. R., Lopez, C., et al. 1988, ApJS, 68, 1
Londish, D., Boyle, B. J., & Schade, D. J. 2000, MNRAS, 318, 411
Marconi, A., Risaliti, G., Gilli, R., et al. 2004, MNRAS, 351, 169
Merloni, A. 2004, MNRAS, 353, 1035
Merloni, A. & Heinz, S. 2008, MNRAS, 388, 1011
Osterbrock, D. E. 1989, Astrophysics of gaseous nebulae and active galactic nuclei (Research supported by the University of California, John Simon Guggenheim Memorial Foundation, University of Minnesota, et al. Mill Valley, CA, University Science Books, 1989, 422 p.)
Press, W. H., Teukolsky, S. A., Vetterling, W. T., & Flannery, B. P. 1992, Numerical recipes in C. The art of scientific computing (Cambridge: University Press, —c1992, 2nd ed.)
Richards, G. T., Strauss, M. A., Fan, X., et al. 2006, AJ, 131, 2766
Schlegel, D. J., Finkbeiner, D. P., & Davis, M. 1998, ApJ, 500, 525
Schmidt, M. 1968, ApJ, 151, 393
Schulze, A. & Wisotzki, L. 2010, A&A, 516, A87+
Spergel, D. N., Verde, L., Peiris, H. V., et al. 2003, ApJS, 148, 175
Steidel, C. C. & Sargent, W. L. W. 1991, ApJ, 382, 433

Tremaine, S., Gebhardt, K., Bender, R., et al. 2002, ApJ, 574, 740
Ueda, Y., Akiyama, M., Ohta, K., & Miyaji, T. 2003, ApJ, 598, 886
Ulvestad, J. S. & Ho, L. C. 2001, ApJ, 558, 561
Wisotzki, L. 2000a, A&A, 353, 861
Wisotzki, L. 2000b, A&A, 353, 853
Wisotzki, L., Christlieb, N., Bade, N., et al. 2000, A&A, 358, 77
Yee, H. K. C. 1980, ApJ, 241, 894
Yu, Q. & Tremaine, S. 2002, MNRAS, 335, 965

Chapter 3

Low redshift AGN in the Hamburg/ESO Survey II. The active black hole mass function and the distribution function of Eddington ratios⋆

Andreas Schulze and Lutz Wisotzki

Leibniz-Institut für Astrophysik Potsdam (AIP), An der Sternwarte 16, 14482 Potsdam, Germany

ABSTRACT

We estimated black hole masses and Eddington ratios ($L/L_{\rm Edd}$) for a well defined sample of local ($z < 0.3$) broad line AGN from the Hamburg/ESO Survey (HES), based on the Hβ line and standard recipes assuming virial equilibrium for the broad line region. The sample represents the low-redshift AGN population over a wide range of luminosities, from Seyfert 1 galaxies to luminous quasars. From the distribution of black hole masses we derived the active black hole mass function (BHMF) and the Eddington ratio distribution function (ERDF) in the local universe, exploiting the fact that the HES has a well-defined selection function. While the directly determined ERDF turns over around $L/L_{\rm Edd} \sim 0.1$, similar to what has been seen in previous analyses, we argue that this is an artefact of the sample selection. We employed a maximum likelihood approach to estimate the *intrinsic* distribution functions of black hole masses and Eddington ratios simultaneously in an unbiased way, taking the sample selection function fully into account. The resulting ERDF is well described by a Schechter function, with evidence for a steady increase towards lower Eddington ratios, qualitatively similar to what has been found for type 2 AGN from the SDSS. Comparing our best-fit active BHMF with the mass function of inactive black holes we obtained an estimate of the fraction of active black holes, i.e. an estimate of the AGN duty cycle. The active fraction decreases strongly with increasing black hole mass. A comparison with the BHMF at higher redshifts also indicates that, at the high mass end, black holes are now in a less active stage than at earlier cosmic epochs. Our results support the notion of anti-hierarchical growth of black holes, and are consistent with a picture where the most massive black holes grew at early cosmic times, whereas at present mainly smaller mass black holes accrete at a significant rate.

3.1. Introduction

The observed relations between the black hole mass and the properties of the spheroidal galaxy component imply a close connection between the growth of supermassive black holes (SMBH) and the evolution of their host galaxies. For local galaxies a strong correlation between the mass of the SMBH and the luminosity or mass of the bulge component (Magorrian et al. 1998; Marconi & Hunt 2003; Häring & Rix 2004), as well as with the stellar velocity dispersion (e.g. Ferrarese & Merritt 2000; Gebhardt et al. 2000; Tremaine et al. 2002; Gültekin et al. 2009) have been established. Semi-analytical and numerical simulations also show the importance of black hole activity and their corresponding SMBH feedback for galaxy evolution (e.g. Di Matteo et al. 2005; Springel et al. 2005; Croton et al. 2006; Cattaneo et al. 2006; Khalatyan et al. 2008; Booth & Schaye 2009). It became clear that the central SMBH of a galaxy and especially its growth is an important ingredient for our understanding of galaxy formation and evolution.

Therefore a complete census of the black hole population and its properties is required. Active black holes that will be observable as AGN are particularly important to study black hole growth. A useful tool to study the AGN population is the luminosity function (AGNLF). The observed evolution of the AGNLF has been used to gain insight into the growth history of black holes (e.g. Soltan 1982; Yu & Tremaine 2002; Marconi et al. 2004; Merloni 2004; Shankar et al. 2009), and it became clear that most of the accretion occurs during bright QSO phases. But, using the AGNLF alone usually requires some additional assumptions, e.g. for the mean accretion rate, and thus is affected by uncertainties and degeneracies. Disentangling the AGNLF into the underlying distribution functions, namely the active black hole mass function (BHMF) and the distribution function of Eddington ratios (ERDF), is able to provide additional essential constraints on the growth of SMBHs.

To understand the influence of black hole growth on galaxy evolution over cosmic time, first the properties of growing black holes in the local universe have to be well understood. Thus, it is important to derive black hole masses and accretion rates for large, well defined samples of AGN. However, measuring black hole masses is much more difficult than measuring luminosities. Black hole masses for large samples of AGN can not be measured directly, but only estimated, using locally established scaling relations.

The best method to estimate $M_\bullet$ for type 1 AGN is reverberation mapping of the broad line region (Blandford & McKee 1982; Peterson 1993). Assuming virial equilibrium black hole masses can be estimated by $M_{\rm BH} = f R_{\rm BLR} \Delta V^2 / G$, where $R_{\rm BLR}$

⋆ This chapter is published in *Astronomy & Astrophysics*, 2010, 516, A87.

is the size of the broad line region (BLR), ΔV is the broad line width in km/s and f is a scaling factor of order unity, which depends on the structure, kinematics and orientation of the BLR. Although the physics of the BLR is still not well understood and thus a source of uncertainty (e.g. Krolik 2001), the validity of the virial assumption has been shown by the measurement of time lags and line widths for different broad lines in the same spectrum (Peterson & Wandel 2000; Onken & Peterson 2002; Kollatschny 2003).

However, reverberation mapping requires extensive and meticulous observations and thus is not appropriate for large samples. Fortunately, a scaling relationship has been established between $R_{\rm BLR}$ and continuum luminosity of the AGN, $R_{\rm BLR} \propto L^{\gamma}$ (Kaspi et al. 2000, 2005; Bentz et al. 2006). Thus it became possible to estimate $M_\bullet$ from single-epoch spectra for large samples, and has been used extensively in the previous years for large AGN samples (e.g. McLure & Dunlop 2004; Vestergaard 2004; Kollmeier et al. 2006; Netzer & Trakhtenbrot 2007; Shen et al. 2008b; Fine et al. 2008; Gavignaud et al. 2008; Trump et al. 2009).

For the measurement of the line width, different measures are commonly used, and it is unclear if one is superior to the others for estimating black hole masses. Most commonly used is the FWHM, but it has been suggested that the line dispersion $\sigma_{\rm line}$, i.e. the second central moment of the line profile, is a better measure of the line width (Peterson et al. 2004; Collin et al. 2006). The line dispersion is more sensitive to the wings of a line and less to the core, whereas for the FWHM the opposite is the case. An additional measure of line width used is the inter-percentile value (IPV, Fine et al. 2008).

The application of the virial method to large AGN samples allowed the estimation of the active BHMF (McLure & Dunlop 2004; Shen et al. 2008b; Greene & Ho 2007; Vestergaard et al. 2008; Kelly et al. 2009; Vestergaard & Osmer 2009). A dataset that is perfectly suited to study especially low redshift AGN is provided by the Hamburg/ESO Survey (HES). In this paper we use a local AGN sample, drawn from the HES, to estimate their black hole masses and Eddington ratios, and construct the active black hole mass function as well as the distribution function of Eddington ratios.

We first present our data and our treatment of the spectra. We estimate black hole masses and Eddington ratios from the spectra using the virial method. Next, we determine the active BHMF, taking care to account for sample selection effects, inducing a bias on the BHMF. Thereby, we not only constrain the local active BHMF but also put constraints on the intrinsic underlying distribution function of Eddington ratios. Finally, we discuss our results in the context of the local quiescent BHMF as well as that of other surveys.

Thoughout this paper we assume a Hubble constant of $H_0 = 70$ km s^{-1} Mpc^{-1} and cosmological density parameters $\Omega_{\rm m} = 0.3$ and $\Omega_\Lambda = 0.7$.

3.2. The Sample

The sample of low redshift AGN used in this study is drawn from the QSO catalogue of the Hamburg/ESO Survey (Wisotzki et al. 2000). For a more detailed description of the survey and the sample used, see our companion paper (Schulze et al. 2009, hereafter Paper I). Here we only give a short summary.

The HES is a wide-angle, slitless spectroscopy survey, mainly for bright QSOs, carried out in the southern hemisphere, utilising photographic objective prism plates. The HES covers a formal area of ~9500 deg^2 in the sky. After digitisation, slitless spectra in the range 3200 Å $\lesssim \lambda \lesssim$ 5200 Å have been extracted from the plates. From these spectra type 1 AGN have been identified, based on their peculiar spectral energy distribution. Follow-up spectroscopy has been carried out to confirm their QSO nature. The HES picks up quasars with $B \lesssim 17.5$ at redshifts of up to $z \simeq 3.2$.

The Hamburg/ESO Survey yields a well-defined, flux-limited sample with a high degree of completeness. The survey covers a large area on the sky and the quasar candidate selection takes care to ensure that low redshift, low luminosity objects, i.e AGN with prominent host galaxies, are not systematically missed. As in Paper I, we want to use this wide luminosity range at low redshift, which is unique for optical surveys, to study the low-redshift AGN population.

To construct such a local AGN sample we selected all AGN from the final HES catalogue (Wisotzki et al., in prep.) that belong to the 'complete sample' and that are located at redshifts $z < 0.3$. The sample contains 329 type 1 AGN. Spectra are available for most of the objects from the follow-up observations. For five objects, spectra were either missing in our database or they were of such poor quality that they were deemed not usable for our purposes. Thus our sample is 324/329 ≈ 98.5 % complete in terms of spectroscopic coverage.

3.3. Measurement of Emission Line Widths

For the estimation of $M_\bullet$ for our low redshift AGN sample, the broad line width of the Hβ, or alternatively the Hα, emission line has to be determined. For the measurement of the line widths of the Hα and Hβ emission lines we fitted the spectral region around these lines by analytic functions, i.e. by a multi-component Gaussian model plus continuum. Over this short wavelength range we approximated the underlying continuum as a straight line. The Hα and Hβ lines are fitted by one, two or, if required, by up to three Gaussians, based on visual inspection of the fits. Due to the limited resolution of the spectra the narrow line component could only be subtracted for a few lines, if a clear attribution of one fitting component to a narrow line component was possible. Thus a narrow component was only subtracted if clearly identified in the fit. Care has been taken to avoid contamination of the lines by contribution from the [O III] $\lambda\lambda$ 4959,5007 Å lines and the Fe II emission to the Hβ line, as well as from [N II] and [S II] to the Hα line, by fitting them simultaneously with the Balmer lines. For details on the line fitting we refer to Paper I.

We use two different line width measurements, the FWHM and the line dispersion for comparison, because there is at the moment no consensus which is the most appropriate for the estimation of black hole masses. Both can be easily derived from the fit. We then corrected the line widths for the finite resolution of the spectrograph. We measured the continuum flux at 5100 Å from the continuum fit to the Hβ line region. We cor-

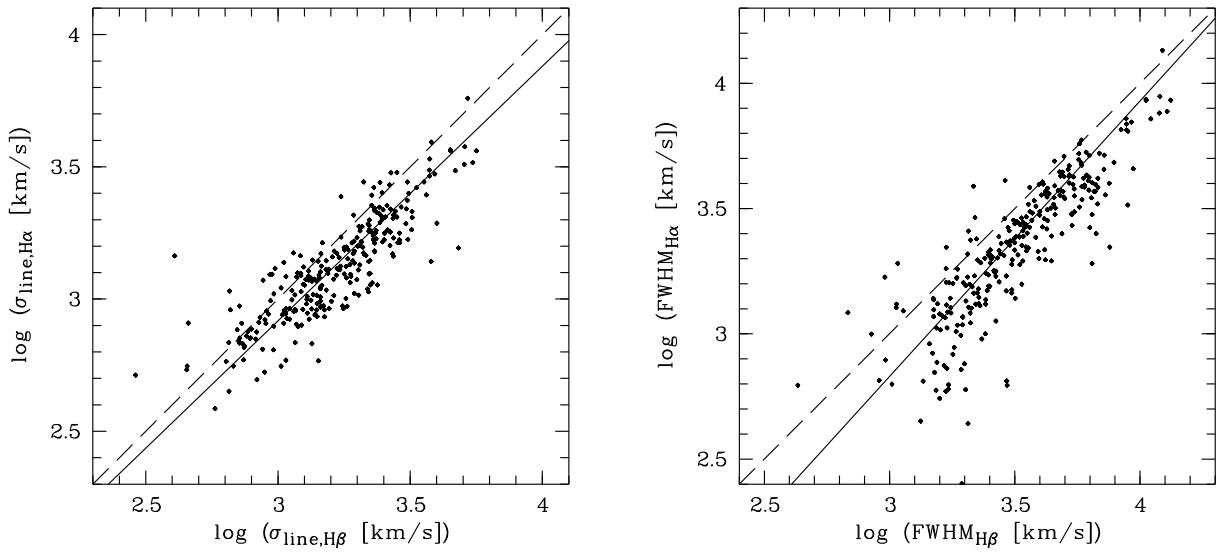

Fig. 3.1. Left panel: Correlation between $\sigma_{\rm line}$(Hβ) and $\sigma_{\rm line}$(Hα). Right panel: Correlation between FWHM(Hβ) and FWHM(Hα). The solid line shows the regression result using the FITEXY method and the dashed line is a one-to-one correspondence.

rected the flux for Galactic extinction, using the dust maps of Schlegel et al. (1998), and the extinction law of Cardelli et al. (1989) and computed the continuum luminosity λL_λ(5100 Å), hereafter L_{5100}.

For the estimation of errors we constructed artificial spectra for each object, using the fitted model and Gaussian random noise, corresponding to the measured S/N. We used 500 realizations for each spectrum. We fitted these artificial spectra, fitting the line and the continuum and measured the FWHM, the line dispersion and the line flux. The error was then simply taken as the dispersion between the various realizations. This method provides a formal error, taking into account fitting uncertainties caused by the noise. Thereby we assume that our multi-Gaussian fitting model provides a sufficiently precise model of the true line shape. Intrinsic deviations of the line shape from the model will increase the error. A remaining Fe II contribution at Hβ might also increase the error.

For a subsample of 21 AGN also included in the SDSS Data Release 5 (DR5; Adelman-McCarthy et al. 2007), we compared our results to the higher resolution SDSS spectra. We fitted the SDSS spectra in the same manner as the HES spectra. The correlation for $\sigma_{\rm line}$ is tight (we found a scatter of 0.07 dex for Hβ), whereas the scatter in the measurement of the FWHM is significantly larger (0.18 dex for Hβ). This is at least partially caused by the narrow component that can be disentangled better in the SDSS spectra. In contrast, $\sigma_{\rm line}$ is less susceptible to the narrow line contribution and thus provides a more precise width measurement for our sample. We also see evidence for an small underestimation of the line width compared to the SDSS spectrum, especially for narrower lines, with a mean deviation of 0.03 dex. This might be caused by the lower resolution of the HES spectra compared to the SDSS spectra and therefore the stronger influence of the resolution correction.

A comparison of the continuum luminosity, FWHM and black hole mass with the quasar sample of Shen et al. (2008b) is in general agreement with our values for the few objects in common.

The line dispersion is more sensitive to the wings of a line, thus to the subtraction of the contaminating lines, i.e. Fe II and [O III] for Hβ and [N II] and [S II] for Hα. On the other hand, the FWHM is more susceptible to the line core, thus to a proper subtraction of the narrow component (see Denney et al. 2009). For our data the latter seems to exhibit the larger uncertainty. Together with the indication that $\sigma_{\rm line}$ is a preferable width estimate over the FWHM (Peterson et al. 2004; Collin et al. 2006), we decided to use $\sigma_{\rm line}$ to estimate black hole masses, and only give the results using the FWHM for comparison.

3.3.1. Relations between Hβ and Hα Line Widths

We see a well-defined correlation between the line widths (both FWHM and $\sigma_{\rm line}$) of the Hβ and Hα emission lines, as shown in Fig. 3.1. To quantify this relation, we applied a linear regression between Hα and Hβ in logarithmic units, using the FITEXY method (Press et al. 1992), that accounts for errors in both coordinates. We accounted for intrinsic scatter in the relation following Tremaine et al. (2002) by increasing the uncertainties until a χ^2 per degree of freedom of unity was obtained.

We found the following relations for the line widths:

$$\log \sigma_{\rm H\alpha} = 0.96 \log \sigma_{\rm H\beta} - 0.08 \,, \tag{3.1}$$

$$\log {\rm FWHM}_{\rm H\alpha} = 1.10 \log {\rm FWHM}_{\rm H\beta} - 0.17 \,. \tag{3.2}$$

The rms scatter around the best fits are 0.11 dex for $\sigma_{\rm line}$ and 0.16 dex for the FWHM respectively. The relations between Hα and Hβ line properties using the FITEXY method are shown in Fig. 3.1.

The relation obtained for the FWHM slightly deviates from the relations obtained by Greene & Ho (2005) and Shen et al. (2008a), showing a stronger deviation from a one-to-one correlation. This might be due to the lower resolution of our data, thus the resolution correction has a stronger effect on the line width. This is supported by the slightly larger scatter for our relation. The scatter in the relation between the line dispersions

is lower than between the FWHMs, again favouring $\sigma_{\rm line}$over FWHM for our data.

The Hβ lines are on average broader than Hα with $\langle$FWHM(Hβ)/FWHM(Hα)$\rangle$ = 1.54 and $\langle\sigma_{\rm line}$(Hβ)/$\sigma_{\rm line}$(Hα)$\rangle$ = 1.29 respectively. This is larger than found in other samples (e.g. Osterbrock & Shuder 1982; Greene & Ho 2005) but in general agreement with the physical expectation of an increasing density or ionisation parameter of the BLR with decreasing radius.

3.4. Results

3.4.1. Estimation of Black Hole Masses

We estimated black hole masses for the AGN using the common scaling relationship. The sample of quasars analysed is well inside the ranges in redshift, with $z < 0.3$, and in luminosity, with $10^{42} \leq L_{5100} \leq 10^{46}$ erg s^{-1}, over which the scaling relationship based on reverberation mapping has been established. So the estimated black hole masses do not suffer from an extrapolation of this relationship outside the range for which it is observationally tested.

For the scaling relationship between BLR size and continuum luminosity we use the values of Bentz et al. (2009):

$$\log R_{\rm BLR} = -21.3 + 0.519 \log(L_{5100}) \,, \qquad (3.3)$$

with L_{5100} given in erg s^{-1} and $R_{\rm BLR}$ in light days.
The black hole mass is thus computed by

$$M_{\rm BH} = 6.7 \cdot f \left(\frac{L_{5100}}{10^{44}\,{\rm ergs^{-1}}}\right)^{0.52} \left(\frac{\Delta V}{\rm km/s}\right)^2 M_\odot \qquad (3.4)$$

where f is the scale factor and ΔV the line width used, i.e. the FWHM or $\sigma_{\rm line}$. We computed black hole masses based on both width measurements. We prefer the black hole masses using the line dispersion and give the FWHM based black hole masses as a reference. For the line dispersion we used a scale factor $f = 3.85$, following Collin et al. (2006). This factor has been determined by setting the black hole masses, computed from the mean spectrum of the reverberation mapping sample and using the line dispersion, to the local $M_{\rm BH} - \sigma_*$ relation for quiescent galaxies, similar to the work of Onken et al. (2004). For the FWHM we used the common scale factor $f = 3/4$ (e.g. Netzer et al. 1990) appropriate for a spherical BLR.

We have not corrected our continuum luminosities L_{5100} for their host galaxy contribution. This might lead to an overestimation of $M_\bullet$ for lower luminosity AGN, where the host contribution becomes significant. To disentangle the host contribution high resolution HST imaging is required, which is not available for our sample. However, the narrow slit used for the spectroscopy and the AGN selection technique already reduce the expected host contribution. Thus, the bias introduced by host galaxy contamination is expected to be small, but will lead to a systematic effect.

To estimate the degree of galaxy contribution to our AGN spectra we used the equivalent width (EW) of the Ca II K line at 3934 Å, because this is the only prominent galaxy absorption feature not confused by AGN emission features within our spectral range. As this feature is only prominent in evolved stellar populations, the contribution from a very young stellar population might be neglected. However, low luminosity AGN hosts are known to have not particularly blue colours and generally do not show extremely young stellar populations, but rather indications for post starbursts (Vanden Berk et al. 2006; Davies et al. 2007).

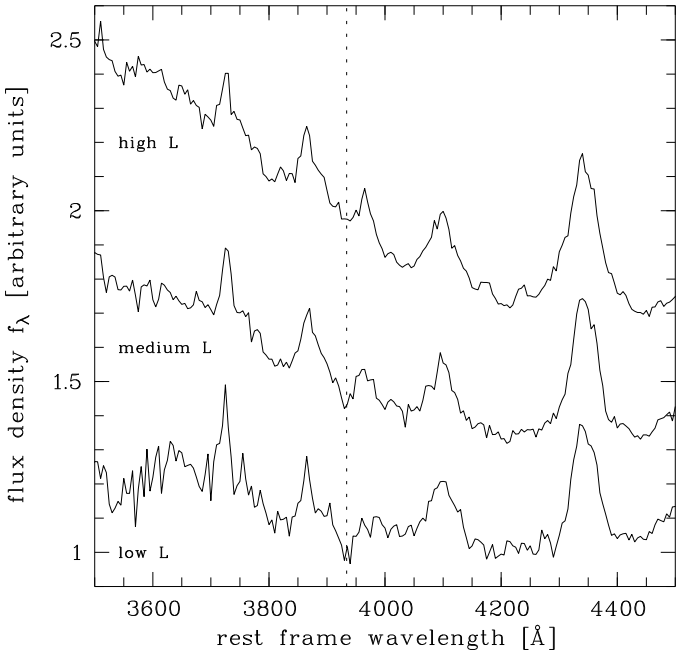

Fig. 3.2. Median composite spectra for 3 luminosity bins, showing the Ca II K line region. The upper composite shows the high luminosity bin ($\log L_{5100} > 44.5$), the middle composite is for the medium luminosity bin ($43.6 < \log L_{5100} < 44.5$) and the lower composite spectrum shows the low luminosity bin ($\log L_{5100} < 43.6$). The Ca II K line at 3934 Å is indicated as the dashed line.

Since the mean signal-to-noise in our spectra is not sufficient to accurately measure the Ca II EW in individual spectra, we constructed composite spectra for three luminosity bins, depending on L_{5100}, shown in Fig. 3.2. While no Ca II absorption is detected for the highest luminosity composite ($\log L_{5100} > 44.5$), it is clearly present in the lower luminosity composites. We measure EWs of 0.8 Å in the medium luminosity ($43.6 < \log L_{5100} < 44.5$) and of 2.0 Å in the low luminosity ($\log L_{5100} < 43.6$) median composite spectrum, respectively.

To estimate the corresponding galaxy contribution, we used model spectra from single stellar population models with different ages and metallicities (Bruzual & Charlot 2003). The low luminosity AGN, which will show the strongest host contribution, are preferentially spiral galaxies. We modeled them by stellar populations with ages between 900 Myr and 2.5 Gyr. We added various constant AGN contributions to the spectra and measured the resulting EWs of the AGN+galaxy spectra. To derive the galaxy contribution at 5100 Å we assumed a flux ratio of the AGN of $f_{5100}/f_{3934} = 0.64$. An EW of 2.0 Å, as measured for our low luminosity subsample, corresponds to a host contribution to L_{5100} of $35-40$ %. This would reduce our black hole mass estimate by $0.10-0.12$ dex. The upper limit we can put on the host contribution is $\sim$ 50 %, implying 0.16 dex for

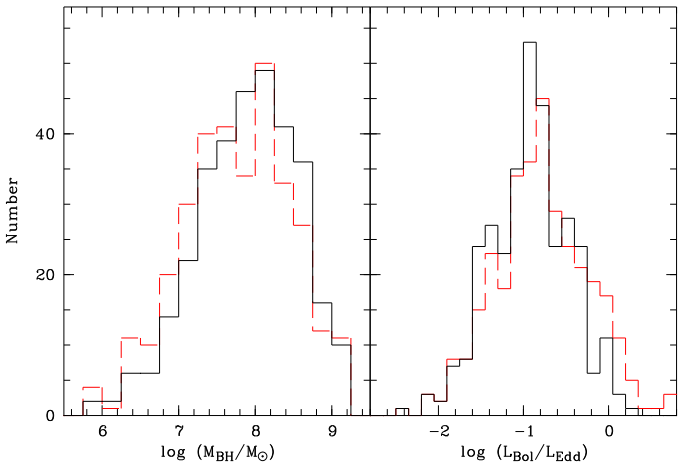

Fig. 3.3. Left panel: Distribution of black hole masses. The black solid histogram shows the distribution of black hole masses estimated from $\sigma_{\rm line}$, the red dashed histogram shows $M_{\rm BH}$ estimated using the FWHM (and a constant scale factor of $f = 0.75$). Right panel: Distribution of Eddington ratios. The histograms are the same as in the left panel.

the $M_\bullet$ estimation. The medium luminosity subsample shows an average host contribution of 15 – 20 %, corresponding to an overestimation of $M_\bullet$ by 0.04 – 0.05 dex.

We used these estimates to apply average host corrections to the continuum luminosities and thus to the black hole masses. Although these corrections might be wrong in individual cases, for the sample as a whole the host contribution is thereby accounted for as good as possible for these data. We verified that our results are not qualitatively affected by applying or neglecting this correction. The quantitative change in the results is certainly very small.

The distributions of black hole masses using the FWHM and the line dispersion are shown in Fig. 3.3. The usage of the FWHM instead of $\sigma_{\rm line}$ slightly shifts the distribution to lower values, with $\langle \log M_{\rm BH} \rangle$ decreasing from 7.90 to 7.77, and also broadens the distribution, with the standard deviation changing from 0.65 dex for $\sigma_{\rm line}$ to 0.70 dex for FWHM.

In the following we will only refer to the black hole masses using $\sigma_{\rm line}$. This width estimate provides a more reliable width measurement for our data compared to the FWHM, as discussed in Section 3.3. We have verified that our results are fully consistent when using the FWHM instead.

3.4.2. Eddington ratios

To compute the Eddington ratio $\lambda = L_{\rm bol}/L_{\rm Edd}$, which can be understood as a normalised accretion rate, we estimated the bolometric luminosity from the optical continuum luminosity $L_{\rm bol} = f_L L_{5100}$, applying a bolometric correction factor of $f_L = 9$, as proposed by Kaspi et al. (2000). The mean bolometric correction factor is still somewhat uncertain, ranging from 7 (e.g. Netzer & Trakhtenbrot 2007) to values around 10 (e.g. Richards et al. 2006a; Marconi et al. 2004), and also seems to be dependent on luminosity (Marconi et al. 2004; Hopkins et al. 2007), black hole mass (Kelly et al. 2008) or Eddington ratio (Vasudevan & Fabian 2009; Lusso et al. 2010). However, assuming a constant value f_L at 5100 Å is a good approximation. The value of $f_L = 9$ is also in general agreement with the value obtained by integrating over the mean SED presented by Richards et al. (2006a). The Eddington luminosity is given by $L_{\rm Edd} \cong 1.3 \cdot 10^{38}\,(M/M_\odot)$ erg s^{-1}.

The distribution of Eddington ratios, using the FWHM and $\sigma_{\rm line}$, are shown in the right panel of Fig. 3.3. The mean Eddington ratio of this sample is $\langle \log \lambda \rangle = -0.92$ with standard deviation of 0.46 dex using $\sigma_{\rm line}$, and $\langle \log \lambda \rangle = -0.79$ with 0.56 dex deviation for FWHM.

This dispersion is higher than that found by other authors in higher redshift and higher luminosity samples (Kollmeier et al. 2006; Shen et al. 2008b). Indeed, the shape of the observed distribution does depend on the underlying distribution function and the selection function of the survey. Thus the observed distribution of Eddington ratios is affected by the flux limitation of the survey and is not a quantity independent of the specific survey. The Eddington ratio distribution will change in mean and dispersion with luminosity (Babić et al. 2007; Hopkins & Hernquist 2009) due to this selection effect. Usually it will broaden with decreasing typical luminosity.

This trend is also clearly visible in the sample of SDSS AGN presented by Shen et al. (2008b). A redshift dependence is also indicated by their data. For their whole sample, covering the range $0.1 \lesssim z \lesssim 4.5$, they found a typical dispersion of ~ 0.3 dex, similar to the sample of Kollmeier et al. (2006) that covers a similar redshift range and includes relatively high luminosity objects. Restricting the sample of Shen et al. (2008b) to $z \lesssim 0.3$ gives a deviation of 0.43 dex, similar to our results, but a lower mean Eddington ratio of -1.17 in logarithmic units. This trend is also present in deeper surveys that cover a wide redshift range. In the VVDS a value for the dispersion of ~ 0.33 dex has been found (Gavignaud et al. 2008), while in the COSMOS survey a dispersion of ~ 0.4 dex has been observed (Trump et al. 2009), in agreement with our low redshift result. We will discuss this issue further in Section 3.6.

In Fig. 3.4 we plot black hole mass, Eddington ratio and bolometric luminosity against each other. The first thing we have to be aware of when interpreting these plots are the implicit underlying correlations between these quantities. What we effectively always show is a combination of continuum luminosity L_{5100} and line width $\sigma_{\rm line}$. Their underlying relation is shown in Fig. 3.5. There is only some week correlation present between L_{5100} and line width.

Physically these plots can be understood from the shape of the underlying black hole mass function and distribution function of Eddington ratios in combination with the selection function of the survey, as we will explicitly show in Section 3.6. The Eddington ratio λ spans the range $0.01 < \lambda < 1$, similar to other optical studies (Woo & Urry 2002; Kollmeier et al. 2006; Greene & Ho 2007; Shen et al. 2008b). At high values, observations have shown that the Eddington rate represents an approximate upper boundary to the Eddington ratio distribution, implying a steep decrease of the Eddington ratio distribution function toward Super-Eddington values. At low λ the sample suffers from incompleteness due to the selection effects of the survey. This can explain the observed range of Eddington ratios

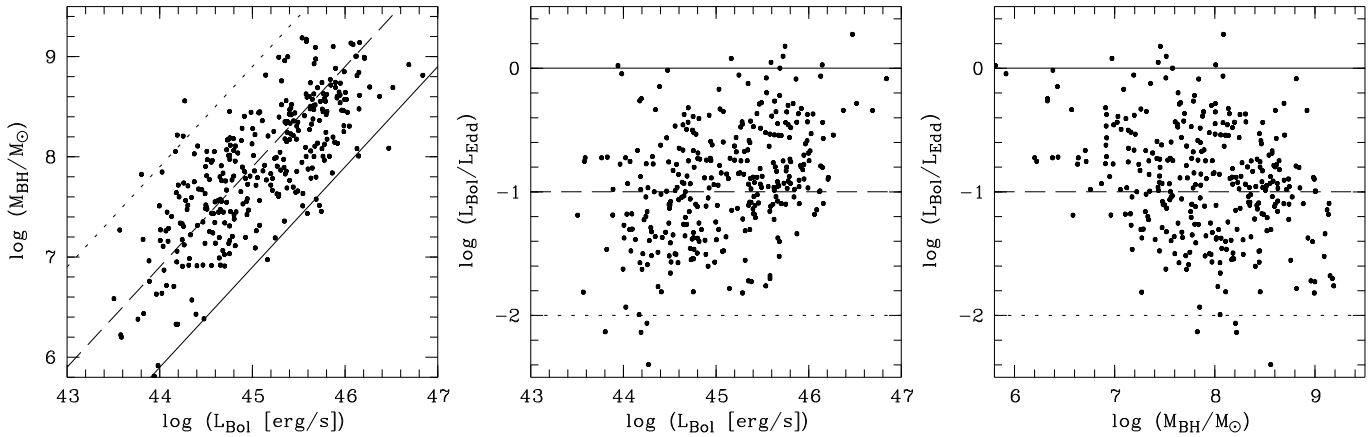

Fig. 3.4. Left panel: Black hole mass versus bolometric luminosity. Middle panel: Eddington ratio versus bolometric luminosity. Right panel: Eddington ratio versus black hole mass. The three lines indicate Eddington ratios of 1 (solid), 0.1 (dashed) and 0.01 (dotted).

and the rough correlation between $M_\bullet$ and $L_{\rm bol}$, shown in the left panel of Fig. 3.4.

No strong correlation is seen between λ and $L_{\rm bol}$ for this low redshift sample. There is a lack of objects in the lower right corner of the middle panel of Fig. 3.4, thus a lack of objects with low-λ and high luminosity. These objects would have $M_\bullet > 2 \cdot 10^9 M_\odot$ and are rare objects due to the steep decrease of the black hole mass function at the high mass end (see Section 3.5.1 and 3.6.2). Thus it is not surprising to see a lack of these objects in the sample. The same applies to the lack of objects seen in the upper right corner of the right panel of Fig. 3.4. These would be objects with relative high $M_\bullet$ and high Eddington ratio. This lack is also caused by the rarity of these objects, due to the steep decrease of the black hole mass function in combination with the decrease of the Eddington ratio distribution function toward the Eddington rate. Therefore, in the local universe massive black holes, accreting close to the Eddington limit, are exceedingly rare.

In the right panel of Fig. 3.4, there is an absence of objects in the lower left corner, i.e. objects with low black hole mass and low Eddington ratio. These objects are victims of the survey selection. They would have low luminosities and therefore only the closest would be detectable in a flux limited sample. An additional effect is that the AGN selection in the HES inevitably becomes incomplete at $M_{B_J} \gtrsim -19$, because the contribution of the host galaxy light even to the HES nuclear extraction scheme will become substantial, and the object will no longer be distinguished from a normal galaxy, due to a more galaxy like SED or due to a no longer detectable broad emission line. Therefore, no AGN with $M_{B_J} \gtrsim -18$ are detected in the survey, and the range $-18 \gtrsim M_{B_J} \gtrsim -19$ is already seriously affected by this survey selection effect. Note that lines of equal luminosities in the right panel of Fig. 3.4 are diagonals from the upper left to the lower right. This selection effect explains the absence of observed objects in this region and results in the apparent anti-correlation between Eddington ratio and black hole mass, also seen in other samples (e.g. McLure & Dunlop 2004; Netzer & Trakhtenbrot 2007).

In Section 3.6 we will explicitly show by Monte Carlo simulations how the observed distributions arise from an assumed underlying BHMF and Eddington ratio distribution function under consideration of the survey selection criteria.

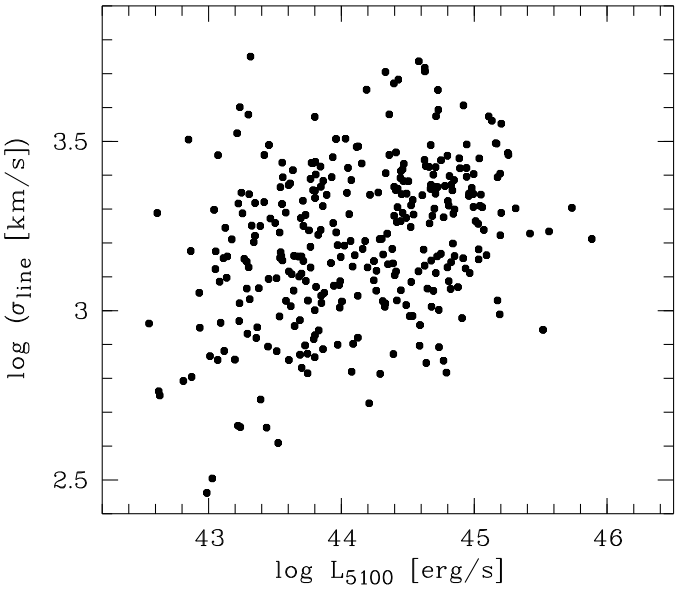

Fig. 3.5. Distribution of the Hβ line width ($\sigma_{\rm line}$) with continuum luminosity L_{5100}. There is only little correlation seen between line width and L_{5100}.

3.5. Black hole mass function and Eddington ratio distribution function

3.5.1. The local active black hole mass function

The BHMF of quiescent galaxies in the local universe can be estimated, based on the relation between $M_\bullet$ and bulge properties (e.g. Salucci et al. 1999; Yu & Tremaine 2002; Shankar et al. 2004; Marconi et al. 2004). Only a small fraction of local black holes are currently in an active state, accreting at a significant level and appearearing as an AGN. However, AGN do not accrete at a single value of λ, but rather show a wide distribution of Eddington ratios (e.g. Heckman et al. 2004; Yu et al. 2005; Merloni & Heinz 2008; Ho 2009; Kauffmann & Heckman

2009). Therefore it is not obvious what exactly to call an *active* black hole. A pragmatic definition is to use a lower limit for the Eddington ratio. A natural choice for such a lower Eddington ratio for optical type 1 AGN samples would be $\lambda \simeq 0.01$, as this is approximately the observed lower value.

By this definition, our sample suffers from incompleteness at low black hole masses, because some low mass and low λ AGN will be fainter than the flux-limit. The sample is not selected on black hole mass or Eddington ratio but on AGN flux. As already mentioned, the sample becomes incomplete at $M_{B_J} \gtrsim -19$. Thus, at low black hole mass only the AGN above this luminosity limit will be detected. This introduces a selection effect on the black hole mass distribution that needs to be taken into account for the determination of the BHMF. In the following, we will refer to this selection effect on the black hole mass and the Eddington ratio distribution as sample censorship, to distinguish it from more direct, for example redshift dependent, selection effects on the AGN luminosity distribution.

It is in principle possible to correct for this sample censorship by proper use of the respective selection function. If applying the usual selection function, which is a function of luminosity, and is appropriate for the determination of the luminosity function, to the determination of the black hole mass function, incompleteness is introduced because it has not properly accounted for active black holes below the flux limit (Kelly et al. 2009). Instead, the selection function has to be derived as a function of black hole mass and this selection function has to be applied to the construction of the BHMF. However, to do so would require knowledge of the, a priori unknown, Eddington ratio distribution function. Thus this approach is not feasible without additional assumptions. Nevertheless, it can be useful as a consistency check, as we will show in Section 3.6.3. To avoid such additional assumptions, we used a different approach to determine the intrinsic underlying active BHMF from our data, taking into account the effect of sample censorship. These results are presented in Section 3.6.

However, in this section we first determine the active BHMF, ignoring the effect of sample censorship on the data. We construct the BHMF using the usual selection function also used for the determination of the AGN luminosity function. However, it must be kept in mind that in this case we ignore active black holes with luminosities below the flux limit of the survey, even if their Eddington ratio is high enough to call it active by the above definition. Thus, this determined BHMF suffers from incompleteness at low mass caused by the sample censorship. Nevertheless, this exercise is worthwhile, because it does not require any assumptions on the shape of the mass function or any information about the Eddington ratio distribution function. While the low mass end clearly will be affected by sample censorship, the high mass end is already well determined by this approach, providing important information on this mass range. Also, this uncorrected BHMF can be better compared with previous estimates on the BHMF that usually have not properly accounted for the sample censorship.

We constructed this active BHMF, not corrected for sample censorship, in an equivalent manner as for the determination of a luminosity function (see Paper I). We made use of the classical $1/V_{\rm max}$ estimator (Schmidt 1968) to construct a binned BHMF. The differential BHMF (space density per $\log M_\bullet$) is thus given by:

$$\Phi(M_\bullet) = \frac{1}{\Delta \log M_\bullet} \sum_k \frac{1}{V^k_{\rm max}} \,, \tag{3.5}$$

where $V_{\rm max}$ is the maximal accessible volume in which the object, with given magnitude could have been found, given the flux-limit of the survey and the redshift bin used. The AGN sample used has been selected based on UV excess measured in the slitless spectra and no selection based on the presence of emission lines is applied. Thus, the $V_{\rm max}$ values used are equal to the ones used for the determination of the AGN luminosity function, presented in Paper I. We lack usable spectra for 5 objects, and for an additional 7 objects we could not fit Hβ due to poor quality of the spectra in this region and/or due to a low Hβ contribution. Therefore we could not estimate $M_\bullet$ for 12 objects. We took this into account in the survey selection function by multiplying the effective area by a factor of 317/329. The exclusion of the 7 objects without proper Hβ measurement may potentially bias our results. Therefore we estimated the Hβ width from the Hα measurement, using Equation 3.1, and then estimated $M_\bullet$ for these 7 objects. Including these objects results in a consistent BHMF. Thus, the in- or exclusion of these objects makes no difference.

To derive the local ($z = 0$) BHMF we corrected for evolution within our narrow redshift bin, $0 < z < 0.3$, as described in Paper I. We applied a simple pure density evolution model within the redshift bin, i.e. $\rho(z) = (1+z)^{k_D}$ with $k_D = 5$, thus adjusting our BHMF to redshift zero. This specific value ensures a result of the $V/V_{\rm max}$ test consistent with $\langle V/V_{\rm max}\rangle = 0.5$, as would be expected in the case of no evolution.

The differential active BHMF of the HES is computed for bins of $\Delta \log M_\bullet = 0.25$ dex in the range $10^6 \le M_\bullet \le 10^{9.5}$. The resulting differential local BHMF, not corrected for sample censorship, is shown in Fig. 3.6.

We used the following functional forms to fit the BHMF. A double power law, given by:

$$\phi(M_\bullet) = \frac{\phi^*/M_*}{(M_\bullet/M_*)^{-\alpha} + (M_\bullet/M_*)^{-\beta}} \,, \tag{3.6}$$

where M_* is a characteristic break mass, ϕ^* the normalisation and α and β are the two slopes. A Schechter (1976) function, given by:

$$\phi(M_\bullet) = \frac{\phi^*}{M_*} \left(\frac{M_\bullet}{M_*}\right)^{\alpha} \exp\left(-\frac{M_\bullet}{M_*}\right) \,. \tag{3.7}$$

is also used.

We additionally used a functional form, motivated by the quiescent BHMF. The quiescent BHMF is given as a convolution of a Schechter function with a Gaussian and can be parameterised by the following function (e.g. Aller & Richstone 2002; Shankar et al. 2004):

$$\phi(M_\bullet) = \frac{\phi^*}{M_*} \left(\frac{M_\bullet}{M_*}\right)^{\alpha} \exp\left(-\left[\frac{M_\bullet}{M_*}\right]^{\beta}\right) \,. \tag{3.8}$$

This basically corresponds to an ad-hoc modification of the Schechter function with an extra parameter β. A value $\beta > 1$ corresponds to a decrease stronger than exponential and $\beta < 1$ corresponds to a milder than exponential decrease. For $\beta = 1$

Table 3.1. Fitting results for the local active black hole mass function, corrected for evolution but not for sample censorship.

Function	$\phi_\bullet^*$ in Mpc^{-3}	$\log M_*$	α	β	χ^2	χ^2/d.o.f.
DPL	2.86×10^{-6}	7.86	−0.74	−3.11	7.29	0.81
Schechter	2.73×10^{-6}	8.06	−0.84	–	15.47	1.55
mod. Schechter	4.96×10^{-6}	6.97	−0.25	0.51	13.64	1.52
DPL (FWHM)	9.95×10^{-7}	8.21	−1.16	−3.62	11.66	1.30
Schechter (FWHM)	1.37×10^{-6}	8.19	−1.08	–	16.40	1.64
mod. Schechter (FWHM)	5.15×10^{-6}	6.81	−0.59	0.32	15.33	1.70

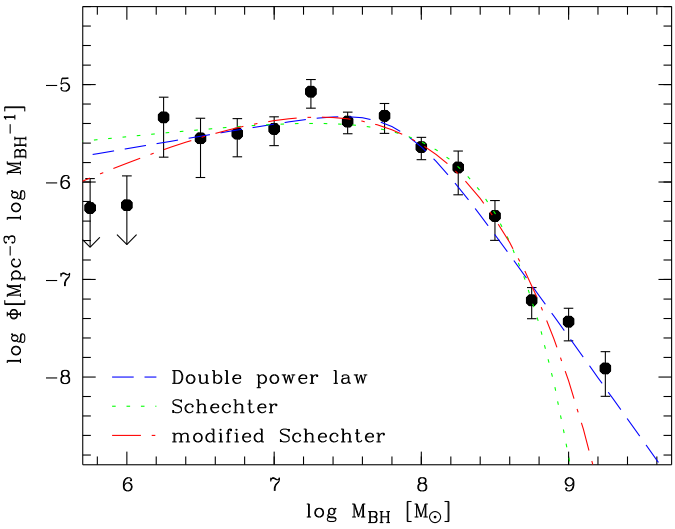

Fig. 3.6. The differential active black hole mass function for $z = 0$, not corrected for sample censorship. Filled black symbols show the BHMF using the line dispersion to estimate the black hole mass. The dashed line shows the double power law fit to the BHMF, the dotted line gives the Schechter function fit and the dashed dotted line represents the fit using a modified Schechter function.

this function turns into the usual Schechter function. In the following we refer to it as the modified Schechter function.

These BHMFs are connected to the expression in logarithmic units by $\Phi(M_\bullet) = (M_\bullet / \log_{10} e)\phi(M_\bullet)$. The resulting fitting parameters of these three functions to our binned BHMF are listed in Table 3.1. All give acceptable fits, while the Schechter function performs poorly at the highest black hole masses. However, the BHMF is less well constrained at high $M_\bullet$ due to the small number of objects in these bins.

The shape of the BHMF is described by a steep decrease of the space density towards higher $M_\bullet$ with $\beta \approx -3$ in the double power law, and a significant flattening at $M_\bullet \approx 10^8 M_\odot$ toward lower $M_\bullet$. The high mass regime is not affected by the already mentioned sample censorship, while the low mass flattening is partially caused by the systematic underrepresentation of low λ objects at low mass.

3.5.2. The local Eddington ratio distribution function

Given the estimates of the Eddington ratio λ for our sample, we can analogously determine the local Eddington ratio distribution function (ERDF) for the HES, equivalent to the BHMF.

Table 3.2. Binned black hole mass function, not corrected for sample censorship. N gives the number of objects in each bin, $\log \phi$ and $\Delta \log \phi$ gives the space density per unit logarithmic black hole mass in solar masses and its 1σ error respectively.

	$\sigma_{\rm line}$		FWHM	
$\log M_{\rm BH}$	N	$\log \Phi_M$	N	$\log \Phi_M$
5.75	1	$-6.27^{+0.31}_{-\infty}$	4	$-5.75^{+0.20}_{-0.36}$
6.00	1	$-6.24^{+0.30}_{-\infty}$	0	
6.25	4	$-5.34^{+0.21}_{-0.40}$	6	$-5.33^{+0.20}_{-0.41}$
6.50	5	$-5.55^{+0.20}_{-0.40}$	8	$-5.49^{+0.19}_{-0.33}$
6.75	6	$-5.50^{+0.15}_{-0.24}$	11	$-5.29^{+0.15}_{-0.22}$
7.00	20	$-5.45^{+0.12}_{-0.18}$	28	$-5.34^{+0.11}_{-0.15}$
7.25	27	$-5.07^{+0.12}_{-0.17}$	35	$-5.15^{+0.12}_{-0.16}$
7.50	38	$-5.38^{+0.10}_{-0.12}$	42	$-5.65^{+0.09}_{-0.12}$
7.75	47	$-5.32^{+0.13}_{-0.18}$	33	$-5.45^{+0.15}_{-0.22}$
8.00	42	$-5.64^{+0.10}_{-0.13}$	45	$-5.63^{+0.13}_{-0.19}$
8.25	42	$-5.85^{+0.17}_{-0.28}$	36	$-5.78^{+0.15}_{-0.24}$
8.50	45	$-6.35^{+0.16}_{-0.25}$	32	$-6.37^{+0.16}_{-0.27}$
8.75	21	$-7.21^{+0.13}_{-0.19}$	23	$-7.20^{+0.13}_{-0.18}$
9.00	13	$-7.43^{+0.13}_{-0.20}$	8	$-7.62^{+0.17}_{-0.29}$
9.25	5	$-7.91^{+0.17}_{-0.29}$	6	$-7.83^{+0.16}_{-0.25}$

This determination also does not take into account the effect of sample censorship. We computed the local ERDF in bins of $\Delta \log \lambda = 0.25$ dex in the range $-2.25 \leq \log \lambda \leq 0.25$. The resulting differential local ERDF is shown in Fig. 3.7.

The uncorrected AGN space density declines at high as well as at low λ , showing a peak around $\log \lambda \approx -1.0$. We fitted the ERDF by a Schechter function, neglecting the lowest λ point. The resulting best fit values are $\phi_\lambda{}^* = 6.66 \times 10^{-6}$ Mpc^{-3}, $\log \lambda_* = -1.01$ and $\alpha_\lambda = -0.05$ with a value of χ^2 per degree of freedom of 1.9.

However, also this ERDF is strongly affected by sample censorship. While at the highest Eddington ratios ($\log \lambda > -1$) the majority of AGN will be detected by the survey, at low Eddington ratio ($\log \lambda < -1$) a significant number of objects will have a too low luminosity to be detected. Therefore the space density at low λ will be underestimated by the derived ERDF. In the next section we will reconstruct the intrinsic underlying ERDF as well as the intrinsic BHMF.

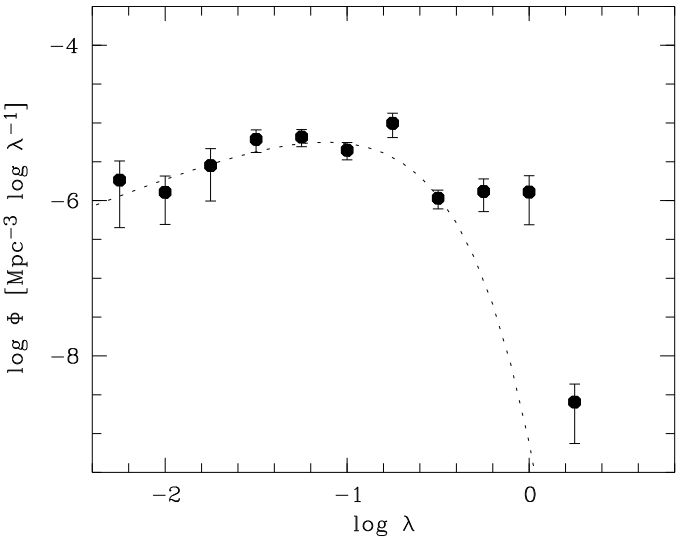

Fig. 3.7. The differential Eddington ratio distribution function for $z = 0$, not corrected for sample censorship. The dashed line shows the best Schechter function fit.

3.6. Reconstruction of the intrinsic BHMF and ERDF

3.6.1. Method

As already noted, the BHMF presented so far is basically luminosity limited and thus incomplete at low mass in terms of an accretion rate limited active BHMF. We now want to constrain the intrinsic active BHMF by our observations, correcting for this sample censorship. We use $\log\lambda = -2$ as the lower limit for the Eddington ratio; for $\log\lambda = -2$ we call black holes 'active'.

The selection function of the survey is a function of luminosity, and thus of the product of $M_\bullet$ and λ. Therefore, the reconstruction of the active BHMF also requires the knowledge of the ERDF. Both distribution functions cannot be determined independently from each other. In Section 3.6.3, as a consistency test, we will determine the active BHMF assuming a specific ERDF. But without such an assumption both distribution functions have to be determined at the same time. This is the approach we will follow in this section.

Knowing both distribution functions, the AGN luminosity function is directly given as a convolution of the two:

$$\Phi(L) = \int_{M_{\bullet,\min}}^{\infty} P_\lambda(\lambda)\Phi_\bullet(M_\bullet)\,\mathrm{d}\log M_\bullet\,, \tag{3.9}$$

where we adopt $\log M_{\bullet,\min} = 6$. With P_λ we define the normalised ERDF, thus:

$$P_\lambda(\lambda) = \frac{\Phi_\lambda(\lambda)}{\int \Phi_\lambda(\lambda)\,\mathrm{d}\log\lambda}\,. \tag{3.10}$$

We determined the BHMF and ERDF together, performing a maximum likelihood fit to the data (e.g. Marshall et al. 1983). We consider the joint Poisson probability distribution of black hole mass and Eddington ratio. We minimise the function $S = -2\ln\mathcal{L}$, with $\mathcal{L}$ being the likelihood of finding the observed data, given the respective model. Thus, S is given by:

$$S = -2\sum_{i=1}^{N}\ln p(M_{\bullet,i},\lambda_i) + 2\iint p(M_\bullet,\lambda)\mathrm{d}\log\lambda\,\mathrm{d}\log M_\bullet\,. \tag{3.11}$$

The sum is over the observed objects and the integral is equal to the expected number of objects, given the assumed BHMF and ERDF. The probability distribution $p(M_\bullet,\lambda)\mathrm{d}\log\lambda\,\mathrm{d}\log M_\bullet$ gives the probability of finding an AGN with black hole mass between $\log M_\bullet$ and $\log M_\bullet + \mathrm{d}\log M_\bullet$ and Eddington ratio between $\log\lambda$ and $\log\lambda + \mathrm{d}\log\lambda$ in an observed sample. The total number of objects N is then given by integration of $p(M_\bullet,\lambda)$ over $M_\bullet$ and λ.

We will now briefly motivate the used probability distribution $p(M_\bullet,\lambda)$ for our sample. The observed number of objects in a sample is given by:

$$N = \iint \Omega_{\mathrm{eff}}(m,z)\,\Phi_L(\log L,z)\,\frac{\mathrm{d}V}{\mathrm{d}z}\,\mathrm{d}\log L\,\mathrm{d}z\,, \tag{3.12}$$

where $\Phi_L(\log L)$ is the AGN luminosity function and Ω_{eff} is the effective survey area as a function of apparent magnitude and redshift, thus the selection function for our flux-limited survey. This can be understood as a selection function depending on z, $M_\bullet$ and λ, thus $\Omega_{\mathrm{eff}}(m,z) = \Omega_{\mathrm{eff}}(L,z) = \Omega_{\mathrm{eff}}(M_\bullet,\lambda,z)$. For the Hamburg/ESO Survey the selection function within our covered redshift range is almost independent of redshift. Thus, as discussed in Paper I, we can marginalise over redshift. For details on the selection function of the HES see Wisotzki et al. (2000).

Apart from the flux limit, our sample is incomplete at the lowest luminosities $M_{B_J} > -19$. For low luminosity AGN the host galaxy contribution becomes an important factor and the objects might no longer be classified as an AGN, due to the SED being dominated by starlight. As shown in Paper I, the sample is highly complete brighter than $M_{B_J} \approx -19$. Thus, we adopted a luminosity limit of $M_{B_J} < -19$ in the selection function, Ω_{eff}. We also restricted the observed sample to this lower luminosity for the comparison of the sample properties.

The AGN luminosity function $\Phi_L(\log L)$ is related to the BHMF and the ERDF via Equation 5.12. For the redshift evolution, we assumed the simple pure density evolution model of Section 3.5.1. In this case the black hole mass function is separable into a function of $M_\bullet$ and a function of z, $\Phi(M_\bullet,z) = \Phi(M_\bullet)\rho(z) = \Phi(M_\bullet)(1+z)^{k_D}$, with $k_D = 5$.

The expected number of objects for a given survey and an assumed BHMF and ERDF is then given by:

$$N = \iiint \Omega_{\mathrm{eff}}\,P_\lambda(\lambda)\Phi_\bullet(M_\bullet)\,(1+z)^{k_D}\frac{\mathrm{d}V}{\mathrm{d}z}\mathrm{d}\log\lambda\,\mathrm{d}\log M_\bullet\mathrm{d}z\,. \tag{3.13}$$

Thus, the bivariate probability distribution of black hole mass and Eddington ratio is given by:

$$p(M_\bullet,\lambda) = \int \Omega_{\mathrm{eff}}\,P_\lambda(\lambda)\Phi_\bullet(M_\bullet)\,(1+z)^{k_D}\frac{\mathrm{d}V}{\mathrm{d}z}\mathrm{d}z\,. \tag{3.14}$$

Given this bivariate distribution for an assumed BHMF and ERDF, we minimise the likelihood function S (Equation 3.11) using a downhill simplex algorithm (Nelder & Mead 1965). As a lower limit for the fitting we employed a black hole mass of

$M_{\rm min} = 10^6 M_\odot$ and an Eddington ratio of $\lambda_{\rm min} = 10^{-2}$. The HES sample was restricted to these limits accordingly.

For the BHMF we assumed three different models. Firstly we used a double power law with the high mass slope fixed to the value $\beta_{\rm BH} = -3.01$, determined from the uncorrected BHMF in Section 3.5.1. This lowers the required number of free parameters and is justified, because the high mass region in the uncorrected BHMF is only weakly affected by incompleteness. Secondly we also used a double power law, but leaving the high mass slope as a free parameter, to be determined in the fit. As third model we used the function given by Equation 3.8, thus a modified Schechter function. The starting values for the minimisation algorithm are taken from the fit to the uncorrected BHMF.

We decided to model the ERDF by a Schechter function, corresponding to an exponential cutoff close to the Eddington limit and a wide power law-like distribution at low Eddington ratio. This parameterisation differs from the often assumed log-normal distribution. However, a log-normal distribution is only motivated by the *observed* distribution, not accounting for any selection effects. Also, a log-normal distribution enforces a maximum and a turnover at low λ. A Schechter function is more flexible, allowing for a turnover at low values, but not enforcing it. In particular, it allows an increase of the space density at low λ. This shape would be consistent with observations of type 2 AGN (Yu et al. 2005; Hopkins & Hernquist 2009; Kauffmann & Heckman 2009), with estimates for the total AGN population (Merloni & Heinz 2008) as well as with model expectations of AGN lightcurves from self-regulated black hole growth (Yu & Lu 2008; Hopkins & Hernquist 2009). Aside from the Schechter function parameterisation of the ERDF, we additionally tested a log-normal ERDF as functional form. Together with the Schechter function it covers a wide range of possible parameterisations for the ERDF.

From our data we are not able to constrain a dependence of the ERDF on $M_\bullet$, so we assumed the ERDF to be independent of $M_\bullet$, already implicitly assumed in Equation 5.12. The normalisation of the ERDF is fixed by the condition that the BHMF and ERDF have to predict the same space density of AGN. This leaves two free parameters for the ERDF, the break λ_* and the low-λ slope α_λ for the Schechter function, or the mean λ_* and the width σ_λ for the log-normal distribution. However, these two parameters in both cases are not independent from each other, because the data by construction needs to be consistent with the observed luminosity function (LF). Thus, for a given BHMF and a fixed value for λ_*, α_λ is given by the condition that the LF derived from the BHMF and ERDF by Equation 5.12 has to be consistent with the observed LF. Our approach automatically ensures the consistency of the BHMF and the ERDF with the observed LF.

To assess the goodness of fit for the individual models we used two different methods. This is required because the maximum likelihood method does not provide its own assessment of the goodness of fit. First, we used a two-dimensional K-S test (Fasano & Franceschini 1987) on the unbinned data. Second, we employed a χ^2 test, binning the data in bins of 0.5 dex in $M_\bullet$ and λ respectively. The results are given with the best fit parameters in Table 3.3.

3.6.2. Results

The first model consists of a double power law BHMF, with the high mass slope fixed to $\beta = -3.11$, and a Schechter function ERDF. The best fit distribution functions are shown as black dashed line in Fig. 3.8 and their fit parameters are given in Table 3.3. The BHMF shows a steep high mass slope with $\alpha_{\rm BH} \approx -2$ and the break is consistent with the uncorrected BHMF. The ERDF is increasing towards low λ down to the applied limit of $\lambda = 0.01$.

This function provides a good fit to the high mass end of the uncorrected BHMF, which is only little affected by sample censorship. At the low mass end the uncorrected BHMF strongly underpredicts the active black hole space density, compared to the reconstructed underlying active BHMF. This also holds true for all other applied functional forms for the BHMF and the ERDF. The same also applies to the uncorrected ERDF. The uncorrected ERDF is strongly biased and underestimates the BH space density. The best fit to the *uncorrected* BHMF and to the ERDF is clearly rejected by the maximum likelihood approach with high confidence. They are not able to produce the observed distributions of $M_\bullet$ and λ and are not consistent with the AGN LF. This clearly shows that the usual approach used to construct an uncorrected BHMF and ERDF is strongly biased.

We briefly want to illustrate how the maximum likelihood approach is able to reject certain models for the BHMF and ERDF and favour others. To compute the expected distributions within a grid of free parameters, we restricted the number of parameters to two. We fixed the break and normalisation of the BHMF. Thus, with the high mass slope already fixed, the only free parameter for the BHMF is the low mass slope $\alpha_{\rm BH}$. For the ERDF there are two free parameters, the break and the low-λ slope of the Schechter function. However, one of these is fixed by the constraint to recover the observed AGN LF. We took α_λ as a free parameter and determined the break by a χ^2 minimisation of the LF computed via Equation 5.12 to the observed LF. The normalised *observed* distribution of $\log M_\bullet$ and $\log\lambda$ are given by:

$$p(\log M_\bullet) = \frac{1}{N}\int p(M_\bullet, \lambda)\,{\rm d}\log\lambda \qquad (3.15)$$

$$p(\log\lambda) = \frac{1}{N}\int p(M_\bullet, \lambda)\,{\rm d}\log M_\bullet\,. \qquad (3.16)$$

For illustration, in Fig. 3.9 we compare these expected distributions with the observed ones within a grid of free parameter $\alpha_{\rm BH}$ and α_λ. For a too steep BHMF the number of low mass objects is larger than observed, while for a too flat BHMF the number of low mass objects is lower than observed. A steep ERDF corresponds to a break of the ERDF close to the Eddington limit, thus more objects above the Eddington limit and less at low λ are predicted, compared to the observations. For a too flat ERDF, the break needs to be at a low value of λ and thus not enough objects close to the Eddington limit are predicted.

We also carried out Monte Carlo simulations for a grid of free parameters $\alpha_{\rm BH}$ and α_λ, using the same assumptions as above, as well as for the best fit model of the maximum likelihood estimation. Here we proceeded as follows: First each AGN gets assigned a redshift, then its black hole mass is drawn from

Table 3.3. Fitting results for the active black hole mass function and the Eddington ratio distribution function. The first column indicates the function used for the BHMF. 'DPL' is for a double power law, with β indicating the fixing of the high mass slope and 'mS' is for a modified Schechter function. The second column indicates the ERDF. 'S' is for a Schechter function and 'ln' stands for a log-normal distribution.

BHMF	ERDF	$\phi^*_\bullet$ [Mpc^{-3}]	$\log M_*$	$\alpha_{\rm BH}$	$\beta_{\rm BH}$	$\log \lambda_*$	$\alpha_\lambda/\sigma_\lambda$	$D_{\rm KS}$	$p_{\rm KS}$	χ^2/d.o.f.	p_{χ^2}	$\rho_{\rm act}$ [$M_\odot$Mpc^{-3}]
DPL(β)	S	2.97×10^{-6}	7.97	−2.11	−3.11	−0.57	−1.90	0.100	2.8e−2	61.3/25	4.2e−5	1621
DPL	S	2.86×10^{-6}	8.01	−2.10	−3.21	−0.56	−1.94	0.101	2.6e−2	63.4/25	2.1e−5	1687
mS	S	2.75×10^{-6}	8.11	−2.11	0.50	−0.55	−1.95	0.094	4.8e−2	56.8/25	1.8e−4	1767
mS	ln	2.36×10^{-6}	8.07	−2.12	0.48	−1.83	0.49	0.081	1.2e−1	50.8/25	1.1e−3	1388

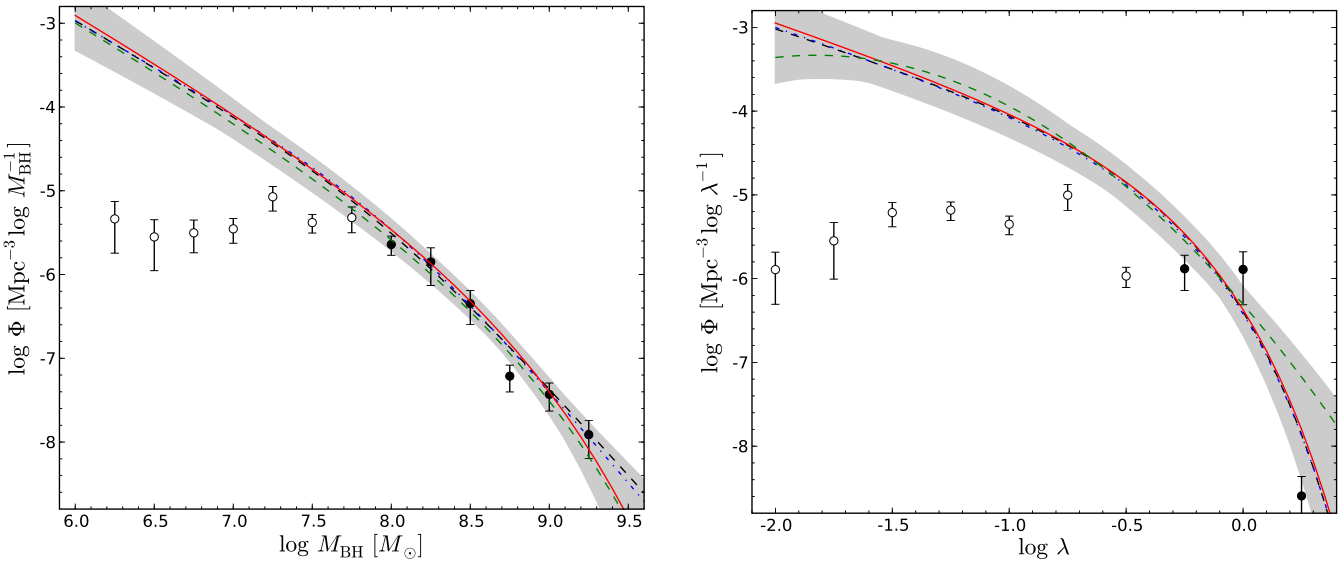

Fig. 3.8. Results for the reconstructed BHMF and ERDF. The left panel gives the BHMF and the right panel the ERDF respectively. The black points show the binned uncorrected distribution function, with filled circles representing bins that do not suffer significantly from sample censorship and open circles represent bins, biased by sample censorship. They are shown for comparison with the reconstructed BHMF and ERDF. The black dashed line shows a double power law BHMF with fixed high mass slope $\beta = -3.11$ and Schechter ERDF, the blue dashed dotted line is for a free double power law BHMF and Schechter ERDF, the red solid line represents a modified Schechter BHMF and Schechter ERDF and the green dashed line is for a modified Schechter BHMF and log-normal ERDF. The gray areas show the 1σ confidence regions of both distribution functions, taking into account all 4 parametric models.

the assumed BHMF, and finally an Eddington ratio is drawn from the ERDF. From these values absolute and apparent B_J magnitudes are computed, applying a bolometric correction. By means of the apparent magnitude B_J it is decided if the object is selected by the survey or not, taking into account the flux-limit.

We ran Monte Carlo simulations for a wide range of $\alpha_{\rm BH}$ and α_λ and found results consistent with what we discussed above and what is shown in Fig. 3.9. The Monte Carlo simulations are clearly able to discriminate between models that are consistent with the data and those that are not. The best matching solutions of the Monte Carlo simulations are consistent with the best fit from the maximum likelihood method, although 'best matching' is not as well defined in this case.

In Fig. 3.10 we show the mean of 10 Monte Carlo realizations of this best fit model. We show the observed distributions for the sample for this model as well as the uncorrected BHMF and ERDF, as well as the M_{B_J}-LF and bolometric LF that would be determined from an 'observed' sample. To construct such an 'observed' sample we again limited the simulated sample to $M_{B_J} < -19$. In the middle panels of Fig. 3.10, we then compare these expected distribution functions with the uncorrected BHMF and ERDF determined with the same restriction applied (shown as open red symbols). The distributions as well as the constructed distribution functions are consistent with the observed distributions and distribution functions. For models that are found to be not consistent with the observations based on the maximum likelihood approach, the Monte Carlo samples also provide a poor match to the observed distributions and distribution functions, and thus can also be rejected based on the Monte Carlo simulations.

These Monte Carlo simulations show that the observed distribution of objects between $L_{\rm Bol}$, $M_\bullet$ and λ, as shown in the plots of Fig. 3.4, are well understood by the underlying BHMF and ERDF and the selection function of the HES. These results

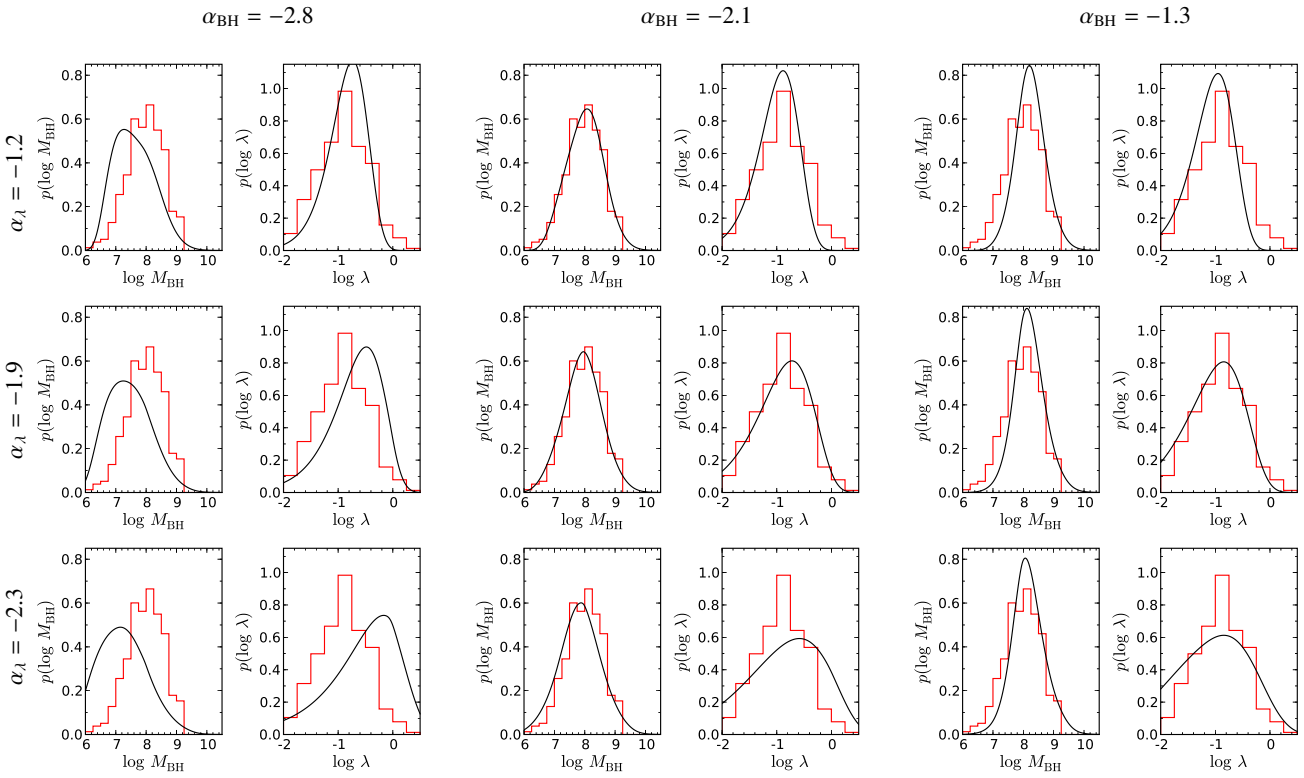

Fig. 3.9. Comparison of the expected distribution of $M_\bullet$ and λ (solid lines) with their distribution in the HES sample (red histogram) for 9 different combinations of the two free parameter $\alpha_{\rm BH}$ and α_λ. The central panel is close to our best fit solution.

do not qualitatively change using a different functional form for the BHMF or ERDF.

As a second model we again used a double power law, but included the high mass slope as an additional free parameter to be determined in the maximum likelihood fit. The result is shown as blue dashed dotted lines in Fig. 3.8. The BHMF is highly consistent with the previous result, with a mild steepening of the high mass slope when this parameter is allowed to change in the fit.

Third, we also used the function given by Equation 3.8, thus a modified Schechter function. The best fit result is consistent with the double power law fit over most of the mass range and only decreases stronger at the high mass end. All three models are good representations of the observed data and therefore span the range of acceptable distribution functions. Formally, the modified Schechter function has the lowest value of S and the highest probability both in the KS-test as well as in the χ^2-test and we will use it in the following as our reference model.

Apart from the Schechter function for the ERDF, we additionally tested a log-normal distribution. This distribution function also provides a good representation of the data. In Table 3.3 and Fig. 3.8 we give a model with a log-normal distribution for the ERDF and a modified Schechter function for the BHMF. While the BHMF is nearly unchanged, the ERDF deviates from the Schechter ERDF at the highest and lowest values, while being consistent over a wide range in between. When enforcing a turnover in the ERDF, using a log-normal distribution, the data are consistent with such a turnover at low λ ($\log \lambda \approx -1.8$). However, there is no evidence for a turnover at higher λ, where the maximum in the *observed* Eddington ratio distribution is present ($\log \lambda \approx -1$).

The log-normal fit indicates rather a flattening of the ERDF at the low-λ end then a real turnover, because it is cut off before the turnover, enforced by a log-normal fit, becomes evident. However, the low-λ regime is dominated by high mass black holes. If there is a mass dependence in the ERDF and the ERDF flattens towards high $M_\bullet$, this would be most prominent at low λ. Such a flattening would also be consistent with Hopkins & Hernquist (2009), who found evidence for a mass dependence in the ERDF of type 2 AGN, with a flatter low λ slope at high $M_\bullet$.

We take into account the log-normal ERDF in the uncertainty range of the determination of the BHMF and ERDF. Formally it has a higher probability in the applied statistical tests than the Schechter function. However, as mentioned, the main deviation compared to the Schechter function is above the Eddington limit and close to the lower limit at $\lambda = 0.01$. The number statistics in this regions are low and thus a clear discrimination between the two models is not possible. Thus, the Schechter function and log-normal distributions indicate the range of acceptable ERDFs.

We derived uncertainties in the BHMF and ERDF by randomly modifying the best fit parameters for each model and computing the likelihood function S. Using $\Delta S = S - S_{\rm min}$ for each random realization, we converted ΔS into confidence values assuming a χ^2 distribution (Lampton et al. 1976; Press et al. 1992). For all models within a certain confidence interval the BHMF and ERDF is computed and these functions then span

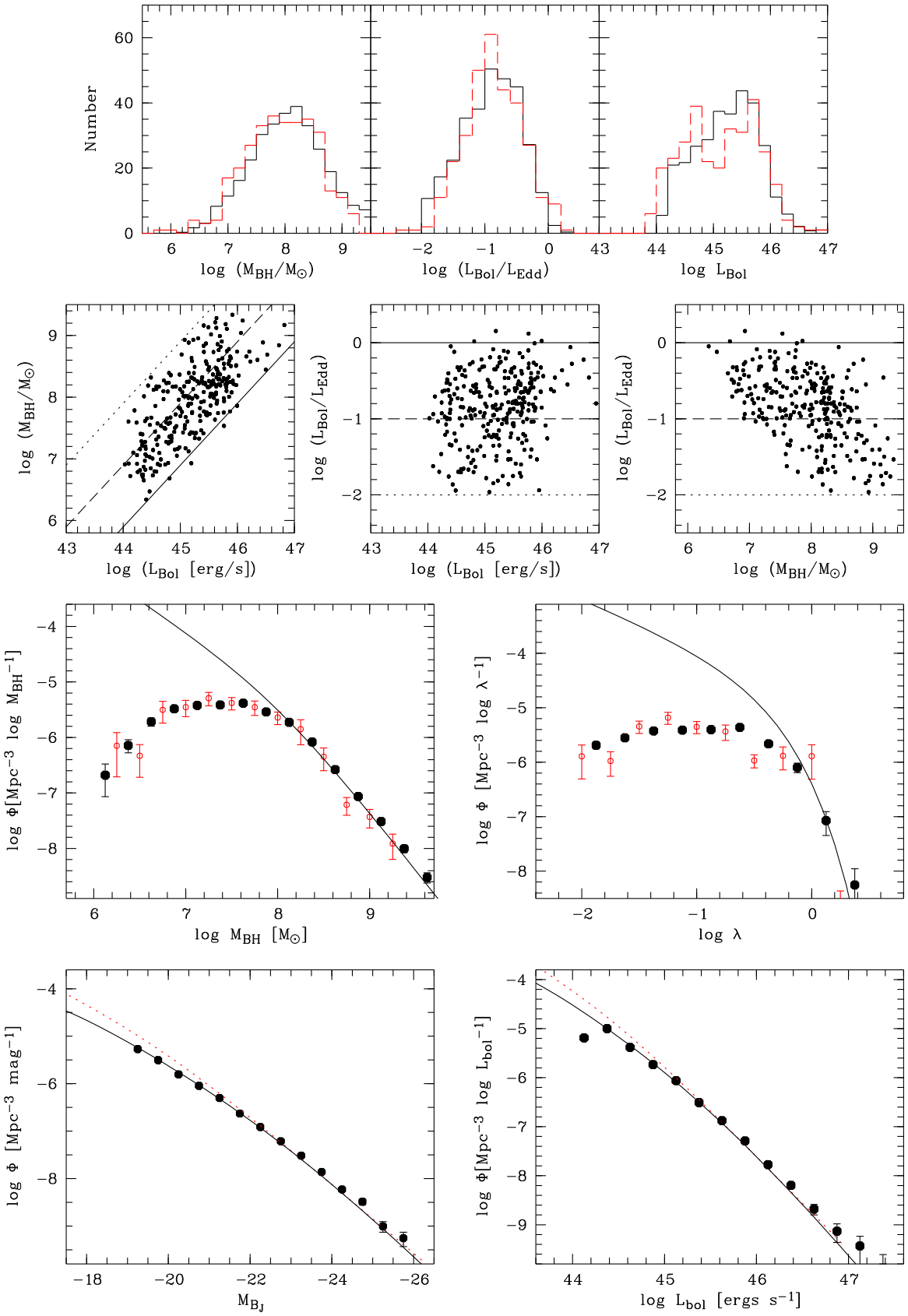

Fig. 3.10. Results of 10 Monte Carlo realizations for the best fit model with an assumed double power law with fixed high mass slope for the BHMF and a Schechter function parameterisation of the ERDF. Upper panels: Comparison of the distributions of $M_\bullet$, λ and $L_{\rm bol}$ between simulated sample (black, solid histogram) and observed sample (red, dashed histogram). Middle panels: Same as Fig. 3.4, but for one simulated sample. Lower panels: uncorrected BHMF and ERDF, M_{B_J} luminosity function and bolometric luminosity function. The results for the simulated sample are shown as filled black points. The solid black line shows the true input function and the dotted lines show the best fit to the uncorrected distribution functions of the observed sample. The open red circles in the BHMF and ERDF plot indicate the individual bins for the observed uncorrected BHMF and ERDF with a restriction of $M_{B_J} < -19$ applied.

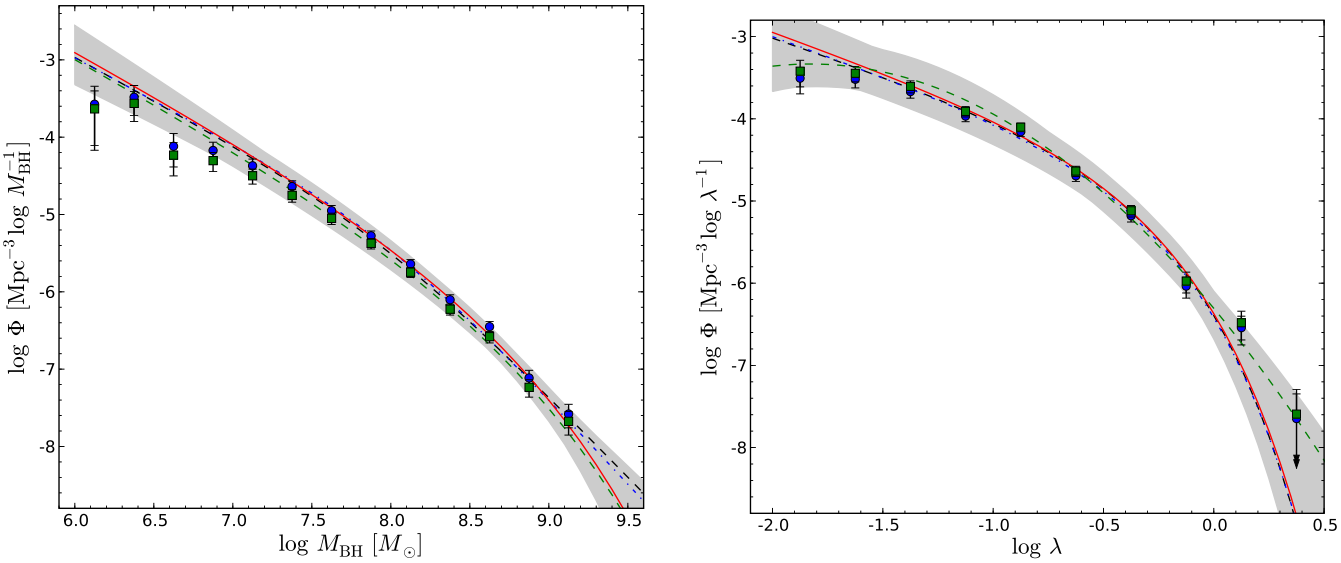

Fig. 3.11. Same as Fig. 3.8 with the constraints from the $1/V_{\rm max}$ method added (see Section 3.6.3). The binned results for the BHMF (left panel) were derived assuming the ERDF of the best fit solutions for the 4 models given in Table 3.3. Shown are only the two distinct models, the Schechter function (blue circles) and the log-normal distribution (green squares). Analogously, the binned results for the ERDF were derived assuming the BHMF of these 4 models. Shown are again only the two distinct models, the double power law (blue circles) and the modified Schechter function (green squares). The binned results for the different models are consistent with each other, as well as with the results of Section 3.6.2, shown as lines and by the shaded area.

the confidence range of the two distribution functions. The total uncertainty of the BHMF or ERDF is then the sum of the confidence ranges of the individual models. In Fig. 3.8, we show this sum of the 1σ confidence values for the two distribution functions as the gray shaded areas.

So far, we assumed the estimated black hole mass to be equal to the true black hole mass. However, this is probably an oversimplification. It is known that there is a considerable uncertainty in $M_\bullet$ estimates using the virial method, probably of order 0.4 dex (Vestergaard & Peterson 2006). Accounting for this uncertainty might change the reconstructed BHMF and ERDF in shape as well as in normalisation. We will investigate this important point in detail in future work.

3.6.3. BHMF and ERDF from the $1/V_{\rm max}$ method

As mentioned in Section 3.5.1, there is also a different approach to determine the intrinsic BHMF and ERDF, namely using the $1/V_{\rm max}$ method, but directly accounting for the selection effects in terms of black hole mass or Eddington ratio completeness imposed on the sample by the AGN luminosity selection. In this case, the BHMF and ERDF cannot be determined jointly. When using the $1/V_{\rm max}$ method the selection effects need to be accounted for in the determination of the accessible volume of the individual AGN, given by:

$$V_{\rm max} = \int_{z_{\rm min}}^{z_{\rm max}} \Omega_{\rm eff} \frac{{\rm d}V}{{\rm d}z} {\rm d}z \,, \qquad (3.17)$$

where $\Omega_{\rm eff}$ is the effective survey area as a function of apparent magnitude, thus the selection function for our flux-limited survey, depending on z, $M_\bullet$ and λ, is $\Omega_{\rm eff}(m) = \Omega_{\rm eff}(L, z) = \Omega_{\rm eff}(M_\bullet, \lambda, z)$. While for the determination of the luminosity function the proper selection function to compute $V_{\rm max}$ is given by $\Omega_{\rm eff}(L, z)$, using it for the determination of the BHMF (as we did in Section 3.5.1) will lead to the presence of sample selection effects, and thus to the observed underestimation of the space density at low mass.

This bias on the determined BHMF can be avoided by using a black hole mass selection function, given by:

$$\Omega_{\rm eff}(M_\bullet, z) = \int_{\lambda_{\rm min}}^{\infty} P_\lambda(\lambda) \Omega_{\rm eff}(M_\bullet, \lambda, z) {\rm d}\log\lambda \,, \qquad (3.18)$$

where $P_\lambda(\lambda)$ is the normalised ERDF, given by Equation 3.10. However, this approach requires knowledge of the ERDF as prior information, which is not present a priori.

Likewise, the ERDF can be derived in an unbiased way by using the Eddington ratio selection function for the survey, given by:

$$\Omega_{\rm eff}(\lambda, z) = \int_{M_{\rm min}}^{\infty} P_{\rm BH}(M_\bullet) \Omega_{\rm eff}(M_\bullet, \lambda, z) {\rm d}\log M_\bullet \,, \qquad (3.19)$$

where $P_{\rm BH}(M_\bullet)$ is the normalised BHMF, similar to $P_\lambda(\lambda)$, defined by:

$$P_{\rm BH}(M_\bullet) = \frac{\Phi_\bullet(M_\bullet)}{\int \Phi_\bullet(M_\bullet) \, {\rm d}\log M_\bullet} \,. \qquad (3.20)$$

This reqires knowledge of the BHMF, which is also unknown beforehand. Thus this approach is usually not feasible for the determination of the intrinsic BHMF and ERDF directly from the data.

However, this approach has the advantage that no prior assumptions on the shape on the ERDF are required for their determination, once we fixed the assumed BHMF. The same is equally true for the determination of the BHMF. The only necessary information beforehand is on the shape of the ERDF. The

problem is that one distribution function needs to be known to determine the other one.

Nevertheless, first we can use it as a consistency test, constructing the BHMF from the constraints on the ERDF from Section 3.6.2 and vice versa. The resulting binned BHMFs and ERDFs using the 4 best fit models are shown as filled symbols in Fig. 3.11 together with the best fit solutions to the active BHMF and the ERDF, as determined in Section 3.6.2. These binned BHMFs as well as the binned ERDFs for all 4 models are fully consistent with our previous constraints and also consistent with each other.

On the other hand, this approach is useful to verify the assumptions on the shape of the distribution functions used in Section 3.6.2. This is especially worthwhile for the ERDF, because the shape of the BHMF is relatively well determined at the high mass end, with the main uncertainty in the low mass slope, while the shape of the ERDF is poorly determined. Therefore, we assumed the double power law with fixed high mass slope parameterisation of the BHMF. As shown above, the shape of the binned ERDF is consistent for all four assumed BHMFs, based on the 4 best fit models. Thus it is justified to use one of these for the investigation of the ERDF shape.

We again fix the break of the double power law and thus the only free parameter left is the low mass slope $\alpha_{\rm BH}$. We determined the Eddington ratio selection function, using Equation 3.19 for a variety of values for $\alpha_{\rm BH}$, covering the whole range of acceptable values. We use $\alpha_{\rm BH} = -0.7$ as lower limit, taken from the uncorrected BHMF, and $\alpha_{\rm BH} = -3.2$ as upper limit, corresponding to a single power law BHMF. The fitting results on these ERDFs with a Schechter function are given in Table 3.6.3. While the normalisation of these ERDFs changes significantly for different assumed values of $\alpha_{\rm BH}$, the shape is not strongly affected and is consistent with our previous constraints thoughout the whole range. In particular, the ERDF is well described by a Schechter function. While there is an indication for a flattening at the low λ end, no indication for a real turnoff of the ERDF is present, as also shown in the right panel of Fig. 3.11. A log-normal distribution is also appropriate, but needs to be cut off close to the maximum of the distribution. Thus it does not indicate a turnover, but only a flattening of the ERDF. We again want to emphasise that no prior assumptions on the ERDF are used here, we just modified the selection function using an assumed BHMF over a wide range of possible parameters. This strongly confirms our previous results for the shape of the ERDF, in that it shows that a Schechter function provides a good representation of the data.

Table 3.4. Fitting results for the ERDF, determined using an appropriate Eddington ratio selection function, assuming different values for the low mass slope $\alpha_{\rm BH}$ of the BHMF.

$\alpha_{\rm BH}$	α_λ	$\log \lambda_*$	χ^2/d.o.f.
−0.7	−1.51	−0.63	1.81
−1.2	−1.50	−0.66	1.77
−1.7	−1.51	−0.69	1.73
−2.0	−1.55	−0.70	1.73
−2.2	−1.59	−0.71	1.75
−2.2	−1.59	−0.71	1.75
−2.7	−1.79	−0.73	1.92
−3.0	−1.94	−0.72	2.02
−3.2	−2.04	−0.71	2.02

3.7. Discussion

3.7.1. Active fraction of local black holes

For a census of active black holes, the derived mass function of active black holes should be compared to the local mass function of quiescent black holes. Because the number of dynamically measured black hole masses is still very low and the sample is inhomogeneous, the quiescent black hole mass function has to rely on the known $M_\bullet$ - bulge property relations, thus converting galaxy luminosity or velocity functions into a black hole mass function. This approach has been used by several authors to derive a local BHMF (e.g. Salucci et al. 1999; Yu & Tremaine 2002; Shankar et al. 2004; Marconi et al. 2004). However, there is still some uncertainty in the estimation (Tundo et al. 2007). We compare our active BHMF to the BHMF presented by Marconi et al. (2004), shown as the solid line in Fig. 3.12. Our best fit model of the reconstructed active BHMF, derived above, is indicated as dashed line in Fig. 3.12.

At this point we need to recall that our operational definition of 'active' black holes only includes type 1 AGN. We are not able to distinguish between a true quiescent black hole and an AGN not selected due to obscuration. By dividing our active BHMF by the quiescent BHMF we thus get the fraction of black holes in an active stage, not hidden to our survey by obscuration, and thus a lower limit to the true active fraction.

The lower panels in Fig. 3.12 show the fraction of local black holes in an active stage as a function of the black hole mass, thus the black hole duty cycle.

As circles we give the active fraction, or duty cycle, derived from the binned uncorrected BHMF, presented in Section 3.5.1, where open symbols indicate bins that are affected by sample censorship. The estimate of the active fraction for the intrinsic BHMF is shown as dashed line, thus showing the intrinsic underlying black hole duty cycle. A clear decrease of the active fraction with increasing $M_\bullet$ is visible, being close to a power law with slope $\alpha_{\rm AF} \approx -0.86$ over the whole covered mass range.

Using a very different approach, Shankar et al. (2009) predicted the black hole duty cycle. They used simple black hole growth models, based on the local quiescent BHMF and the bolometric AGN luminosity function. They made the simplified assumption of a single constant accretion rate, in contrast to the wide accretion rate distribution we assumed. Their active fraction also refers to the whole AGN population, while we are restricted to type 1 AGN. Nevertheless, when comparing their low z duty cycle with our results, we find an excellent agreement between both. However, taking into account the large differences between the simple model of Shankar et al. (2009) and our empirical determination, this agreement might even be a coincidence.

In the right panels of Fig. 3.12 we split our sample into two subsamples, based on the Eddington ratio λ, at $\log \lambda = -1$.

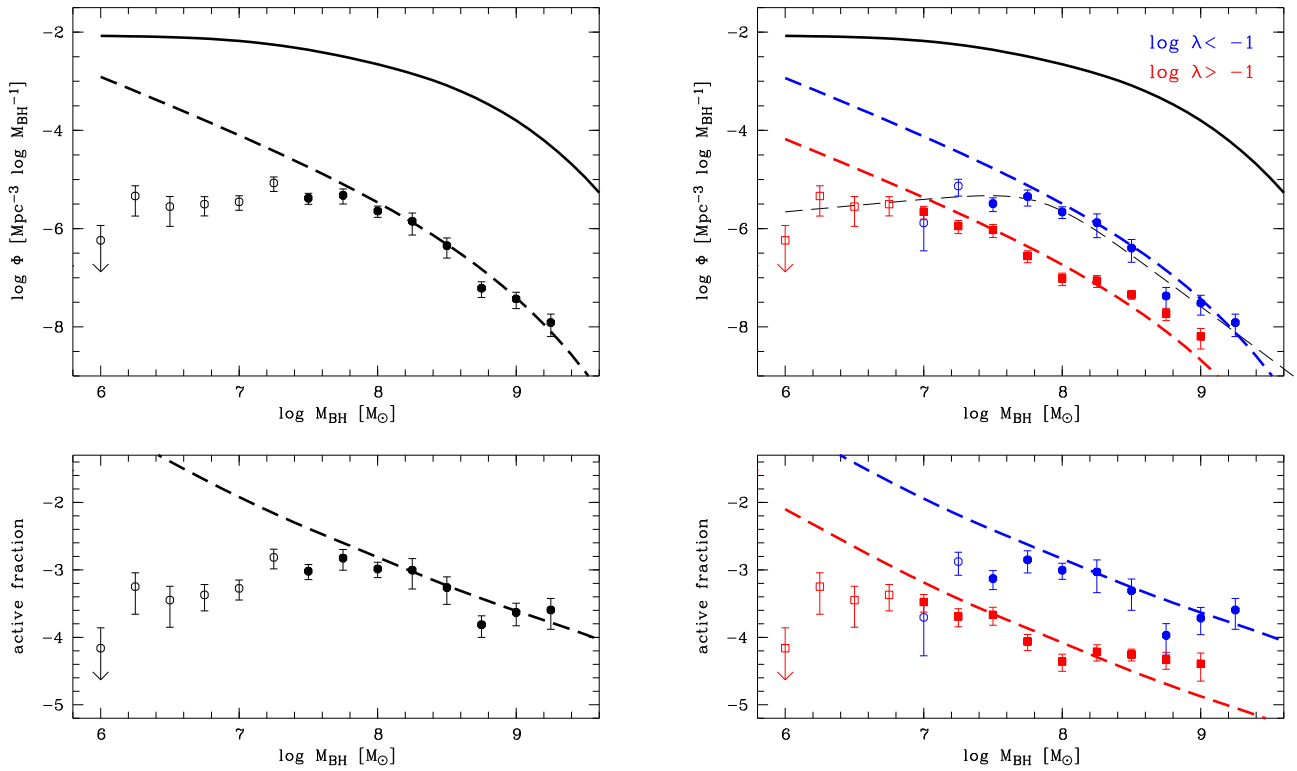

Fig. 3.12. Comparison of our active black hole mass function with the inactive BHMF of Marconi et al. (2004) (solid line in upper panels). The circles show the uncorrected binned data, where open symbols correspond to bins that suffer from selection effects. In the lower panels the active fraction of black holes in the local universe is shown in logarithmic units. In the left panel the active BHMF and active fraction for the whole sample are shown. In the right panel the active BHMF and the corresponding active fraction are shown for two Eddington ratio bins (above and below $\log\lambda = -1$). The BHMF and active fraction for the best fit model of the intrinsic BHMF and ERDF are shown as dashed lines, in the left panel for the whole sample and in the right panel for the two λ bin subsamples. There is a decrease in the active fraction with increasing black hole mass, in agreement with the cosmic downsizing picture. This decrease is already visible in the high λ subsample (red squares).

For both subsamples we computed the uncorrected BHMF and the active fraction. The uncorrected BHMF and the uncorrected active fraction for the low λ subsample are shown as blue circles, while the blue dashed line shows the active fraction derived from the reconstructed BHMF (best fit modified Schechter function). Incompleteness sets in around $10^8\,M_\odot$ and is dominant below $10^7\,M_\odot$, therefore no information on the behaviour of the active fraction can be gained from these low λ black holes.

The high λ subsample is shown as red squares, while the red dashed line shows the active fraction derived from the reconstructed BHMF, with the normalisation derived from the fraction of objects above $\log\lambda = -1$. The subsample is almost complete up to $\sim 10^7\,M_\odot$, where the low λ subsample is already heavily incomplete. Above $10^7\,M_\odot$ the binned active fraction is in good agreement with the reconstructed intrinsic active fraction. This provides a consistency test for the reconstructed BHMF and ERDF estimate. But even without this comparison there is a clear trend present for the high λ subsample with a decrease of the active fraction with increasing black hole mass, directly verifying our previous result from the uncorrected binned data. Thus, far more low mass black holes in the local universe are in an active state than high mass black holes.

This result is in general agreement with the picture of anti-hierarchical growth of black holes (e.g. Merloni 2004; Merloni & Heinz 2008), where the most massive black holes grew at early cosmic times and are preferentially in a less active stage in the present universe, and at present mainly smaller mass black holes grow at a significant rate, also known as cosmic downsizing. Our results strongly support this anti-hierarchical black hole growth scenario. This is in general agreement with previous findings on low redshift AGN (Heckman et al. 2004; Greene & Ho 2007; Goulding et al. 2010) that also report a decrease of the active fraction for the most massive black holes, as well as with results at higher redshifts (Vestergaard & Osmer 2009).

3.7.2. The active black hole mass density

We now want to estimate the black hole mass density of active type 1 AGN in the local universe

$$\rho_{\rm act} = \int_{M_{\rm min}}^{\infty} M_\bullet \phi(M_\bullet) {\rm d}M_\bullet \,, \qquad (3.21)$$

with $M_{\rm min} = 10^6 M_\odot$, using our results for the active BHMF. A lower limit on the local mass density of active black holes is given by the BHMF without a correction for sample censorship. We derived a lower limit of $\rho_{\rm act} = 277\,M_\odot\,{\rm Mpc}^{-3}$. Using

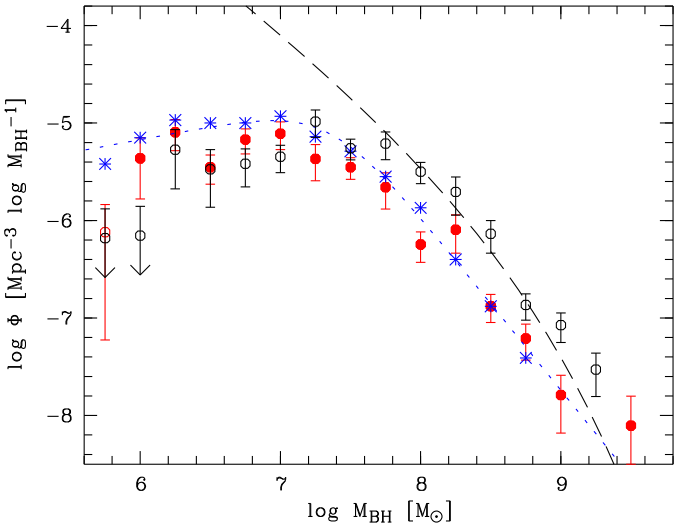

Fig. 3.13. Comparison of the local BHMF of the HES with the BHMF presented in Greene & Ho (2009). The blue asterisks and the blue dotted line show the BHMF from Greene & Ho (2007) (corrected in Greene & Ho (2009)). The open, black circles show our BHMF, not corrected for evolution and sample censorship, while the filled, red circles show our BHMF, with the black hole mass estimated as in Greene & Ho (2007). The dashed line indicates our reconstructed BHMF for reference.

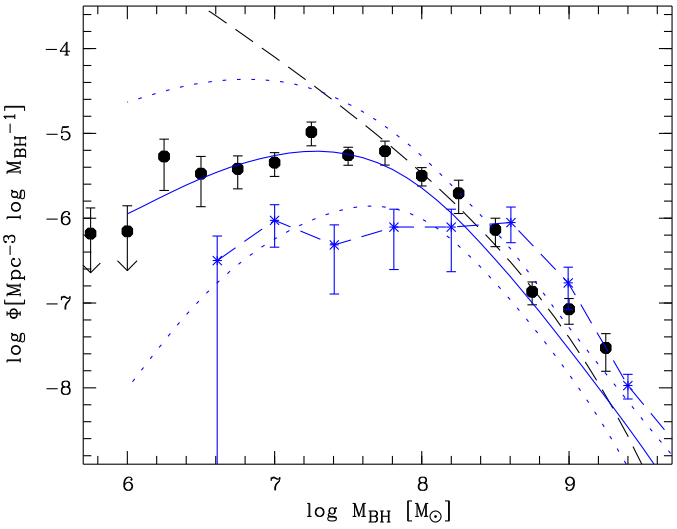

Fig. 3.14. Comparison of our local active BHMF (filled circles for uncorrected and dashed line for intrinsic BHMF) with the BHMF of the BQS, as determined directly as binned estimate by Vestergaard & Osmer (2009)(blue asterisks) and as determined by a Bayesian approach by Kelly et al. (2009)(blue solid line for median and dashed lines for 1σ uncertainty).

our reconstructed BHMF, the local mass density of active black holes with $\log\lambda > -2$ is then $\rho_{\rm act} \approx 1700\,M_\odot\,{\rm Mpc}^{-3}$, a factor of 6 higher then derived from the uncorrected active BHMF. The results for the individual models are given in Table 3.3.

The observational estimate of the integrated mass density of the total black hole population in the local universe is $\rho_{\rm tot} = (3.2 - 5.4) \times 10^5\,M_\odot\,{\rm Mpc}^{-3}$ (Shankar et al. 2009; Graham & Driver 2007; Yu & Lu 2008). Using a value of $4.6 \times 10^5\,M_\odot\,{\rm Mpc}^{-3}$, as presented by Marconi et al. (2004), results in a fraction of $\sim 4 \times 10^{-3}$ of the black hole mass that is currently actively accreting at a rate larger that 1% of the Eddington limit ($\sim 6 \times 10^{-4}$ for the uncorrected BHMF).

3.7.3. Comparison with other surveys

Greene & Ho (2007) presented a determination of the active black hole mass function for $z < 0.352$, using the SDSS DR4 main galaxy sample as well as the QSO sample. They constructed their sample based on spectroscopic confirmation of broad Hα lines, ending up with 8728 objects. For these they computed black hole masses from the Hα FWHM and line luminosity.

As already mentioned in Paper I, an error has been discovered in the determination of the $V_{\rm max}$ values in the work of Greene & Ho (2007) (J. Greene, private communication), resulting into an erroneous luminosity function as well as BHMF. This error has recently been resolved (Greene & Ho 2009). Thus we caution not to use the original active BHMF from Greene & Ho (2007). In Fig. 3.13 the active BHMF by Greene & Ho (2009) from their SDSS sample is shown as blue asterisks.

Greene & Ho (2007) have not taken into account the selection effects caused by the use of the luminosity selection function and thus underestimate the number of active black holes at low masses, due to the discussed sample censorship. They also do not correct for evolution within their z range. However, a direct comparison with the mass function from Greene & Ho (2009) can be made using our BHMF, without correction for evolution and sample censorship.

For consistency, we also re-estimated the black hole masses of our sample, using the same formula as Greene & Ho (2007), using Hα FWHM and Hα line luminosity. For our sample, the black hole mass distribution is shifted by 0.54 dex towards lower mass in the mean. Compared to the FWHM based $M_\bullet$ this shift is 0.42 dex, thus $\sim$ 0.1 dex can be attributed to the difference between the FWHM and $\sigma_{\rm line}$based $M_\bullet$. The main reason for the remaining difference originates from a different relation of Hα luminosity to L_{5100} found for our sample compared to the one given in Greene & Ho (2005). This difference leads to an offset of 0.31 dex. The remaining offset can be attributed to the different $R_{\rm BLR} - L$ scaling relation as well as to scatter in the relation between the FWHMs, as shown in Fig. 3.1.

The resulting BHMF of the HES is shown as filled circles in Fig. 3.13. Both BHMFs are fully consistent with each other, especially at the high mass end, where different survey selection effects are not important. At the low mass end the SDSS BHMF seems to exhibit similar survey selection effects as our HES sample, resulting in a consistent uncorrected BHMF, even at the biased low mass end.

Recently, Vestergaard & Osmer (2009) presented the binned local active BHMF of the Bright Quasar Survey (BQS, Schmidt & Green 1983), in the redshift interval $z = 0 - 0.5$. In Fig. 3.14 we compare their derived BHMF with our binned BHMF, not corrected for evolution and sample censorship (filled black circles), and our reconstructed intrinsic BHMF (dashed black line). We also show the local BHMF of the BQS as blue solid

line, but determined using a Bayesian approach (Kelly et al. 2009).

The most direct comparison between the BQS and the HES is with the binned estimates. At the high mass end, both binned estimates are in reasonable agreement. However, the BQS does not cover exactly the same redshift range as our HES sample. This might also cause some difference between both BHMFs, due to evolution of the BHMF, which has the largest effect at the high mass end. Because the BQS is not as deep as the HES, incompleteness sets in at higher $M_\bullet$ in the binned BHMF. Also it is known that the BQS suffers from both incompleteness (Goldschmidt et al. 1992; Koehler et al. 1997) as well as over-completeness (Wisotzki et al. 2000). Thus, the HES is superior to the BQS for a determination of the local active BHMF.

Recently, Kelly et al. (2009) presented a determination of the active BHMF from the BQS using a Bayesian method, taking also into account scatter in $M_\bullet$ and accounting for black holes below the flux limit of the survey. Their approach aims at correcting their BHMF for sample selection effects caused by the flux-limit, as we did in Section 3.6. However, they modeled the BHMF with a combination of Gaussian functions and also enforced a log normal distribution for the ERDF, while we mainly used a Schechter function description without a specific maximum and with a high fraction of objects at low λ. In Fig. 3.14 we compare their posterior median BHMF (blue solid line) with our intrinsic BHMF (black dashed line). While both mass functions are consistent at the high mass end, there is a clear disagreement at the low mass end. Their BHMF is rather consistent with our uncorrected BHMF. We speculate that the reason for this disagreement might lie in the different assumptions on the shape of the BHMF and ERDF. This emphasises the importance of the assumed ERDF for the determination of the underlying BHMF. An important constraint on the ERDF is provided by the condition to recover the observed luminosity function as a convolution of BHMF and ERDF, as we have ensured by construction.

So far, little observational results exist on the distribution function of Eddington ratios from AGN surveys. Yu et al. (2005) used a sample of type 2 AGN from the SDSS (Kauffmann et al. 2003; Heckman et al. 2004) to determine the ERDF. Their results have recently been compiled by Hopkins & Hernquist (2009). They also fitted the ERDF by a Schechter function and found an average slope of $\alpha_\lambda \approx -1.6$. [1] Our constraints on the local type 1 ERDF presented here are consistent with this average slope of the ERDF of type 2 AGN. This might indicate a similar accretion behaviour of type 1 and type 2 AGN, as expected from the standard unification model (e.g. Antonucci 1993).

3.7.4. Evolution of the active fraction

Vestergaard et al. (2008) presented a determination of the BHMF in the redshift range $0.3 \leq z \leq 5$. They used a well-defined, homogeneous sample of 15180 quasars from the SDSS DR3, already used by Richards et al. (2006b) for the construction of the luminosity function. They found a high-mass decline

[1] See also Fig. 1.8 for their results on the type 2 AGN ERDF (this note was added for the thesis).

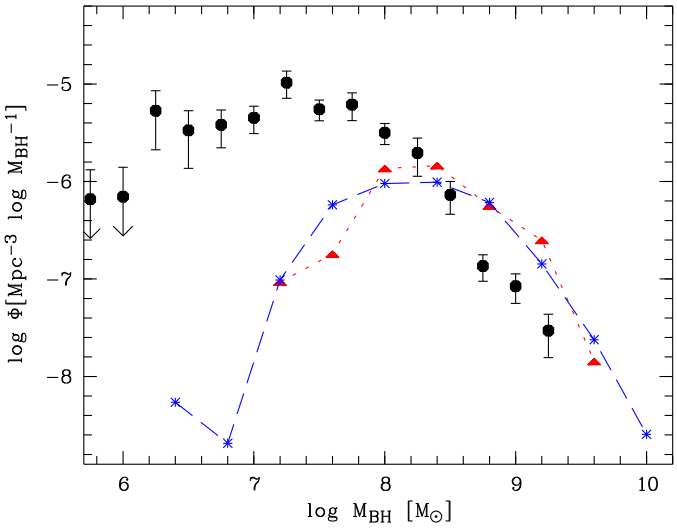

Fig. 3.15. Comparison of our uncorrected $z \leq 0.3$ BHMF (filled circles) with the active BHMF within $0.3 \leq z \leq 0.7$ from the SDSS (Vestergaard et al. 2008), shown as the blue dashed line and asterisks, and the active BHMF of the LBQS within $0.2 \leq z \leq 0.5$ (Vestergaard & Osmer 2009), shown as the red dotted line and triangles.

with constant slope $\beta \approx -3.3$ at all epochs. Our high-mass slope of $\beta = -3.1$ for $z \leq 0.3$ (when not corrected for evolution) is consistent with their higher-z result within the uncertainties.

We compare our $z \leq 0.3$ BHMF, not corrected for evolution within the z-bin and for sample censorship, with the lowest redshift bin ($0.3 \leq z \leq 0.68$) BHMF of Vestergaard et al. (2008), shown in Fig. 3.15. We also show the active BHMF of the Large Bright Quasar Survey (LBQS; e.g. Hewett et al. 2001) in the redshift bin $z = 0.2 - 0.5$ (Vestergaard & Osmer 2009) as triangles. Both SDSS and LBQS BHMFs are in general agreement, even though they do not cover exactly the same redshift range. The decline of the space density at the lowest $M_\bullet$ in both BHMFs is mainly due to incompleteness in this mass range in the SDSS QSO sample as well as in the LBQS QSO sample. At the high mass end the BHMF shows a similar slope but a larger space density than our HES BHMF. This seems to indicate evolution of the BHMF between these redshift bins. Because the mass function of the total supermassive black hole population will only decrease at the high mass end toward higher z, we can use the local quiescent BHMF as an upper limit for the mass function at $0.3 \leq z \leq 0.68$. This then implies an increase of the active fraction at the high mass end towards higher redshift, exactly as would be expected in the cosmic downsizing scenario. Thus, the number of the most massive black holes being in an active stage in the present universe seems to be lower than at earlier cosmic epochs.

3.8. Conclusions

We have presented a study of the low-redshift active black hole population, residing in broad-line active galactic nuclei. We estimated black hole masses and Eddington ratios, and from it estimated the local active black hole mass function and the Eddington ratio distribution function. Our sample was drawn

from the Hamburg/ESO Survey and contains 329 quasars and Seyfert 1 galaxies with $z < 0.3$, selected from surveying almost 7000 deg^2 in the southern sky.

We estimated black hole masses from single-epoch spectra, measuring the line dispersion of the broad Hβ line and the continuum luminosity at 5100 Å L_{5100}, using the common virial method. We took care to avoid contamination of the line measurement by neighbouring emission lines and roughly estimated the degree of host galaxy contribution to L_{5100}. This has been found to be negligible for the most luminous AGN and not dominant even at the low luminosity end of our sample. We applied a rough statistical correction to the continuum luminosities to take into account the host contribution. The bolometric luminosity and thus the Eddington ratio λ, has been estimated from L_{5100}.

The observed black hole masses cover a range $10^6 - 2 \cdot 10^9\, M_\odot$ and the Eddington ratio is roughly confined between $0.01 - 1$. The observed distributions of these quantities are understood by the underlying distribution functions of black hole mass and Eddington ratio, in combination with the survey selection function, as we explicitly demonstrated by Monte Carlo simulations.

We made an attempt to determine these two distribution functions in an unbiased way. First of all, when we want to determine the *active* BHMF, we have to make clear what we mean by an *active* black hole, due to the wide distribution of accretion rates. We used a lower Eddington ratio cut of $\log \lambda = -2$, in agreement with the observed range of Eddington ratios. Using a different cut for λ will preserve the shape of the BHMF, but change their normalisation, due to our assumption of an uncorrelated BHMF and ERDF. This is already shown in the left panel of Fig.3.12. The normalisation and therefore the space density clearly depend of the chosen definition of an active black hole.

Next we have to be aware that our sample is selected on AGN luminosity, not on black hole mass. Therefore, we have to make sure that we properly account for active black holes below the flux limit of the survey. We presented a method that determines the active BHMF as well as the ERDF at the same time, by a maximum likelihood fit. Here, the bivariate probability distribution of black hole mass and Eddington ratio is fitted to the observations. This probability distribution is given by an assumed BHMF, ERDF and the selection function of the survey. We also corrected for evolution within our redshift range, transforming the distribution functions to $z = 0$. This maximum likelihood method also ensures the consistency of the derived BHMF and ERDF with the AGN luminosity function. We were able to put tight constraints on both the active black hole mass function and the Eddington ratio distribution function.

The Eddington ratio distribution function is well described by a Schechter function with low λ slope $\alpha_\lambda \approx -1.9$. The data are consistent with no decrease of the ERDF at low λ, within the constrained range. Using a log-normal distribution, we found a maximum at $\log \lambda = -1.8$, what can be taken as an upper limit for a potential turnover in the ERDF. Our results clearly show a wide distribution of Eddington ratios, in contrast to a single value or to a narrow log-normal distribution, which is based on the observed distribution, without accounting for the underlying selection effects. While we also observe a narrow log-normal distribution of Eddington ratios, this is in agreement with the constrained Schechter function or wide log-normal distribution for the Eddington ratio distribution function, when survey selection effects are properly accounted for, because low-λ objects will be systematically missed in flux limited samples.

The active BHMF is well described by different analytic models. In general, it strongly decreases at the high mass end and follows a power law at the low mass end with slope of $\alpha \approx -2$. A good fit to the data is achieved by a function similar to a Schechter function, but modified by an extra parameter that determines the steepness of the high mass decrease. We found no evidence for a decrease of the BHMF toward low mass, as indicated by Greene & Ho (2007) for $M_\bullet \lesssim 10^{6.5} M_\odot$. However, our sample is not very sensitive in this low mass range.

We compared our local active BHMF with the local quiescent BHMF from Marconi et al. (2004), determining the active fraction, or duty cycle, of local black holes. This active fraction is decreasing with increasing black hole mass, consistent with a power law with slope ~ -0.86. Thus, the most massive black holes in the present universe are less active than their lower mass companions. At the highest $M_\bullet$ only 10^{-4} of all black holes are currently in an active stage, i.e. accreting above 0.01 of the Eddington rate. This supports the general picture of anti-hierarchical growth of black holes. This mass dependence of the active fraction indicates that our assumption of an uncorrelated BHMF and ERDF cannot be sustained up to low values of λ and thus we caution to extrapolate the distribution functions into the low λ regime. Investigating a mass dependence of the ERDF would especially require a wider luminosity coverage of the sample.

By comparing our low z BHMF with the BHMF of a higher z-bin, presented by Vestergaard et al. (2008) and Vestergaard & Osmer (2009), we found an indication that the most massive black holes are currently in a less active stage than at earlier cosmic times, also in general agreement with anti-hierarchical black hole growth.

Recently, Marconi et al. (2008) proposed a modified method to estimate $M_\bullet$, taking into account the effect of radiation pressure. So far, it is still unknown if radiation pressure has an important effect on the BLR or not (see e.g. Netzer 2009). If we take into account radiation pressure and apply their $M_\bullet$ estimation formula to our sample, the major effect is an increase of $M_\bullet$ especially for the low $M_\bullet$ objects. In total, the dispersion of the $M_\bullet$ distribution decreases from 0.65 dex to 0.63 dex. In the BHMF the space density at median $M_\bullet$ increases, while at high $M_\bullet$ the space density slightly decreases. This would strengthen even further the evidence for anti-hierarchical black hole growth. On the other hand it would change our observed $M_\bullet$, and especially our λ, distributions, and thereby our constrained BHMF and the Eddington ratio distribution function.

Our work strengthens the scenario of anti-hierarchical growth of black holes, also seen in other studies (Merloni 2004; Heckman et al. 2004; Greene & Ho 2007; Shankar et al. 2009; Vestergaard & Osmer 2009), at least at low redshift. The observation of 'cosmic downsizing' in the X-ray luminosity function (e.g. Ueda et al. 2003; Hasinger et al. 2005), as well as in the optical, radio and IR luminosity function (e.g. Hunt et al. 2004;

Cirasuolo et al. 2005; Matute et al. 2006; Croom et al. 2009), i.e. the flattening of the faint end slope of the luminosity function towards higher redshift, is explained by the shift of the typical black hole mass of an active accreting black hole toward lower mass.

The presented local active black hole mass function and Eddington ratio distribution function serve as a local anchor for future studies of both distribution functions. These will provide further information on the cosmic history of growth and activity of supermassive black holes.

References

Adelman-McCarthy, J. K., Agüeros, M. A., Allam, S. S., et al. 2007, ApJS, 172, 634
Aller, M. C. & Richstone, D. 2002, AJ, 124, 3035
Antonucci, R. 1993, ARA&A, 31, 473
Babić, A., Miller, L., Jarvis, M. J., et al. 2007, A&A, 474, 755
Bentz, M. C., Peterson, B. M., Netzer, H., Pogge, R. W., & Vestergaard, M. 2009, ApJ, 697, 160
Bentz, M. C., Peterson, B. M., Pogge, R. W., Vestergaard, M., & Onken, C. A. 2006, ApJ, 644, 133
Blandford, R. D. & McKee, C. F. 1982, ApJ, 255, 419
Booth, C. M. & Schaye, J. 2009, MNRAS, 398, 53
Bruzual, G. & Charlot, S. 2003, MNRAS, 344, 1000
Cardelli, J. A., Clayton, G. C., & Mathis, J. S. 1989, ApJ, 345, 245
Cattaneo, A., Dekel, A., Devriendt, J., Guiderdoni, B., & Blaizot, J. 2006, MNRAS, 370, 1651
Cirasuolo, M., Magliocchetti, M., & Celotti, A. 2005, MNRAS, 357, 1267
Collin, S., Kawaguchi, T., Peterson, B. M., & Vestergaard, M. 2006, A&A, 456, 75
Croom, S. M., Richards, G. T., Shanks, T., et al. 2009, MNRAS, 399, 1755
Croton, D. J., Springel, V., White, S. D. M., et al. 2006, MNRAS, 365, 11
Davies, R. I., Sánchez, F. M., Genzel, R., et al. 2007, ApJ, 671, 1388
Denney, K. D., Peterson, B. M., Dietrich, M., Vestergaard, M., & Bentz, M. C. 2009, ApJ, 692, 246
Di Matteo, T., Springel, V., & Hernquist, L. 2005, Nature, 433, 604
Fasano, G. & Franceschini, A. 1987, MNRAS, 225, 155
Ferrarese, L. & Merritt, D. 2000, ApJ, 539, L9
Fine, S., Croom, S. M., Hopkins, P. F., et al. 2008, MNRAS, 390, 1413
Gavignaud, I., Wisotzki, L., Bongiorno, A., et al. 2008, A&A, 492, 637
Gebhardt, K., Bender, R., Bower, G., et al. 2000, ApJ, 539, L13
Goldschmidt, P., Miller, L., La Franca, F., & Cristiani, S. 1992, MNRAS, 256, 65P
Goulding, A. D., Alexander, D. M., Lehmer, B. D., & Mullaney, J. R. 2010, MNRAS, 406, 597
Graham, A. W. & Driver, S. P. 2007, MNRAS, 380, L15
Greene, J. E. & Ho, L. C. 2005, ApJ, 630, 122
Greene, J. E. & Ho, L. C. 2007, ApJ, 667, 131
Greene, J. E. & Ho, L. C. 2009, ApJ, 704, 1743
Gültekin, K., Richstone, D. O., Gebhardt, K., et al. 2009, ApJ, 698, 198
Häring, N. & Rix, H.-W. 2004, ApJ, 604, L89
Hasinger, G., Miyaji, T., & Schmidt, M. 2005, A&A, 441, 417
Heckman, T. M., Kauffmann, G., Brinchmann, J., et al. 2004, ApJ, 613, 109
Hewett, P. C., Foltz, C. B., & Chaffee, F. H. 2001, AJ, 122, 518
Ho, L. C. 2009, ApJ, 699, 626
Hopkins, P. F. & Hernquist, L. 2009, ApJ, 698, 1550
Hopkins, P. F., Richards, G. T., & Hernquist, L. 2007, ApJ, 654, 731
Hunt, M. P., Steidel, C. C., Adelberger, K. L., & Shapley, A. E. 2004, ApJ, 605, 625
Kaspi, S., Maoz, D., Netzer, H., et al. 2005, ApJ, 629, 61
Kaspi, S., Smith, P. S., Netzer, H., et al. 2000, ApJ, 533, 631
Kauffmann, G. & Heckman, T. M. 2009, MNRAS, 397, 135
Kauffmann, G., Heckman, T. M., White, S. D. M., et al. 2003, MNRAS, 341, 54
Kelly, B. C., Bechtold, J., Trump, J. R., Vestergaard, M., & Siemiginowska, A. 2008, ApJS, 176, 355
Kelly, B. C., Vestergaard, M., & Fan, X. 2009, ApJ, 692, 1388
Khalatyan, A., Cattaneo, A., Schramm, M., et al. 2008, MNRAS, 387, 13
Koehler, T., Groote, D., Reimers, D., & Wisotzki, L. 1997, A&A, 325, 502
Kollatschny, W. 2003, A&A, 407, 461
Kollmeier, J. A., Onken, C. A., Kochanek, C. S., et al. 2006, ApJ, 648, 128
Krolik, J. H. 2001, ApJ, 551, 72
Lampton, M., Margon, B., & Bowyer, S. 1976, ApJ, 208, 177
Lusso, E., Comastri, A., Vignali, C., et al. 2010, A&A, 512, A34+
Magorrian, J., Tremaine, S., Richstone, D., et al. 1998, AJ, 115, 2285
Marconi, A., Axon, D. J., Maiolino, R., et al. 2008, ApJ, 678, 693
Marconi, A. & Hunt, L. K. 2003, ApJ, 589, L21
Marconi, A., Risaliti, G., Gilli, R., et al. 2004, MNRAS, 351, 169
Marshall, H. L., Tananbaum, H., Avni, Y., & Zamorani, G. 1983, ApJ, 269, 35
Matute, I., La Franca, F., Pozzi, F., et al. 2006, A&A, 451, 443
McLure, R. J. & Dunlop, J. S. 2004, MNRAS, 352, 1390
Merloni, A. 2004, MNRAS, 353, 1035
Merloni, A. & Heinz, S. 2008, MNRAS, 388, 1011
Nelder, J. A. & Mead, R. A. 1965, Computer Journal, 7, 308
Netzer, H. 2009, ApJ, 695, 793
Netzer, H., Maoz, D., Laor, A., et al. 1990, ApJ, 353, 108
Netzer, H. & Trakhtenbrot, B. 2007, ApJ, 654, 754
Onken, C. A., Ferrarese, L., Merritt, D., et al. 2004, ApJ, 615, 645
Onken, C. A. & Peterson, B. M. 2002, ApJ, 572, 746
Osterbrock, D. E. & Shuder, J. M. 1982, ApJS, 49, 149
Peterson, B. M. 1993, PASP, 105, 247
Peterson, B. M., Ferrarese, L., Gilbert, K. M., et al. 2004, ApJ, 613, 682
Peterson, B. M. & Wandel, A. 2000, ApJ, 540, L13
Press, W. H., Teukolsky, S. A., Vetterling, W. T., & Flannery, B. P. 1992, Numerical recipes in C. The art of scientific computing (Cambridge: University Press, —c1992, 2nd ed.)
Richards, G. T., Lacy, M., Storrie-Lombardi, L. J., et al. 2006a, ApJS, 166, 470
Richards, G. T., Strauss, M. A., Fan, X., et al. 2006b, AJ, 131, 2766
Salucci, P., Szuszkiewicz, E., Monaco, P., & Danese, L. 1999, MNRAS, 307, 637
Schechter, P. 1976, ApJ, 203, 297
Schlegel, D. J., Finkbeiner, D. P., & Davis, M. 1998, ApJ, 500, 525
Schmidt, M. 1968, ApJ, 151, 393
Schmidt, M. & Green, R. F. 1983, ApJ, 269, 352
Schulze, A., Wisotzki, L., & Husemann, B. 2009, A&A, 507, 781
Shankar, F., Salucci, P., Granato, G. L., De Zotti, G., & Danese, L. 2004, MNRAS, 354, 1020
Shankar, F., Weinberg, D. H., & Miralda-Escudé, J. 2009, ApJ, 690, 20
Shen, J., Vanden Berk, D. E., Schneider, D. P., & Hall, P. B. 2008a, AJ, 135, 928
Shen, Y., Greene, J. E., Strauss, M. A., Richards, G. T., & Schneider, D. P. 2008b, ApJ, 680, 169
Soltan, A. 1982, MNRAS, 200, 115
Springel, V., Di Matteo, T., & Hernquist, L. 2005, ApJ, 620, L79
Tremaine, S., Gebhardt, K., Bender, R., et al. 2002, ApJ, 574, 740
Trump, J. R., Impey, C. D., Kelly, B. C., et al. 2009, ApJ, 700, 49
Tundo, E., Bernardi, M., Hyde, J. B., Sheth, R. K., & Pizzella, A. 2007, ApJ, 663, 53
Ueda, Y., Akiyama, M., Ohta, K., & Miyaji, T. 2003, ApJ, 598, 886
Vanden Berk, D. E., Shen, J., Yip, C., et al. 2006, AJ, 131, 84
Vasudevan, R. V. & Fabian, A. C. 2009, MNRAS, 392, 1124
Vestergaard, M. 2004, ApJ, 601, 676
Vestergaard, M., Fan, X., Tremonti, C. A., Osmer, P. S., & Richards, G. T. 2008, ApJ, 674, L1
Vestergaard, M. & Osmer, P. S. 2009, ApJ, 699, 800
Vestergaard, M. & Peterson, B. M. 2006, ApJ, 641, 689
Wisotzki, L., Christlieb, N., Bade, N., et al. 2000, A&A, 358, 77
Woo, J.-H. & Urry, C. M. 2002, ApJ, 579, 530
Yu, Q. & Lu, Y. 2008, ApJ, 689, 732
Yu, Q., Lu, Y., & Kauffmann, G. 2005, ApJ, 634, 901
Yu, Q. & Tremaine, S. 2002, MNRAS, 335, 965

Chapter 4

Accounting for scatter in virial black hole masses in the AGN distribution function determination⋆

Andreas Schulze and Lutz Wisotzki

Leibniz-Institut für Astrophysik Potsdam (AIP), An der Sternwarte 16, 14482 Potsdam, Germany

ABSTRACT

We here present further, but preliminary results on the active black hole mass function and Eddington ratio distribution function. In Chapter 3 we determined the active black hole mass function (BHMF) and the Eddington ratio distribution function (ERDF) at $z < 0.3$ from the Hamburg/ESO Survey (HES). However, we treated the estimated masses as the true values, ignoring the intrinsic uncertainty $\sigma_{\rm VM}$ in the virial method. Here, we present results that properly take the uncertainty in the virial method into account. We present the extension of our maximum likelihood method to incorporate measurement uncertainties. We demonstrate the effect of the correction on the distribution functions for different values of $\sigma_{\rm VM}$. Finally, we investigate whether our method is able to put constraints on the size of the intrinsic scatter in the virial method and present an independent assessment on the size of the intrinsic scatter.

4.1. Including scatter in the maximum likelihood approach

The maximum likelihood method presented in section 3.6.1 determines the BHMF and ERDF jointly. Both distribution functions can be combined in a bivariate distribution function of black hole mass and Eddington ratio

$$\Psi(M_\bullet, \lambda, z) = P_\lambda(\lambda)\,\Phi_\bullet(M_\bullet, z)\,. \tag{4.1}$$

Here $M_\bullet$ is the black hole mass, λ is the Eddington ratio ($\lambda = L_{\rm bol}/L_{\rm Edd}$), $\Phi_\bullet$ is the BHMF and P_λ is the normalised ERDF, defined by Equation (3.10). BHMF and ERDF are just different projections of this general bivariate distribution function.

The bivariate probability distribution is then:

$$p(M_\bullet, \lambda) = \int \Omega_{\rm eff}(M_\bullet, \lambda, z)\,\Psi(M_\bullet, \lambda, z)\frac{{\rm d}V}{{\rm d}z}{\rm d}z\,, \tag{4.2}$$

where $\Omega_{\rm eff}$ is the selection function of the specific survey, as a function of $M_\bullet$, λ and z, The probability distribution $p(M_\bullet, \lambda)$ predicts the observed distribution of objects in the $M_\bullet$-λ plane and is directly compared to the observations via a minimisation of the likelihood function, Equation (3.11).

We account for the uncertainty in the black hole mass and Eddington ratio estimates by convolving Ψ with the measurement uncertainty before comparing to the data

$$\Psi_{\rm o}(M_{\bullet,{\rm o}}, \lambda_{\rm o}, z) = \int g(M_{\bullet,{\rm o}}, \lambda_{\rm o} \mid M_\bullet, \lambda)\,\Psi(M_\bullet, \lambda, z)\,{\rm d}M_\bullet\,{\rm d}\lambda\ . \tag{4.3}$$

We assume a log-normal scatter distribution in $M_\bullet$ as well as in $L_{\rm bol}$,

$$g(M_{\bullet,{\rm o}}, \lambda_{\rm o} \mid M_\bullet, \lambda) = \frac{1}{2\pi\sigma_{\rm VM}\sigma_{\rm bol}} \exp\left\{-\frac{(\mu_{\rm o}-\mu)^2}{2\sigma^2_{\rm VM}} - \frac{(l_{\rm o}-l)^2}{2\sigma^2_{\rm bol}}\right\}, \tag{4.4}$$

where $\mu = \log M_\bullet$ is the black hole mass and $l = \log M_\bullet + \log\lambda + 38.11$ is the bolometric luminosity. For the uncertainty in the bolometric correction $\sigma_{\rm bol}$ we assumed a scatter of 0.05 dex (Marconi et al. 2004). The statistical scatter in $M_\bullet$ was varied. Thus the 2D scatter distribution in the $M_\bullet$-λ plane is represented by an ellipse with axes $\sigma_{\rm bol}$ and $\sigma_{\rm VM}$. The respective probability distribution, computed via Equation (4.2), is then used for the maximum likelihood fit, constraining the underlying BHMF and ERDF in the presence of measurement uncertainties, equivalent to Chapter 3.

4.2. Effect of scatter in virial black hole masses on the AGN distribution functions

We applied this method to our sample of 329 type 1 AGN with $z < 0.3$ from the HES. The uncertainty in the virial method is not well established. Usually a value of ~ 0.4 dex is adopted (Vestergaard & Peterson 2006), but there is also evidence that it may be smaller (Fine et al. 2008; Steinhardt & Elvis 2010; Kelly et al. 2010). Neglecting or underestimating the intrinsic scatter in the virial method will bias the resulting BHMF and ERDF. But if $\sigma_{\rm VM}$ is overestimated, the resulting BHMF and ERDF will be biased likewise. Therefore, we corrected for scatter in the virial mass estimates using different values for the uncertainty ($\sigma_{\rm VM} = 0.1$, 0.2, 0.3 and 0.4 dex), spanning a range of reasonable values. Our aim at this point is only to demonstrate the effect of accounting for $\sigma_{\rm VM}$ on the derived AGN distribution functions. In Table 4.1 we give the best fit parameters using the presented maximum likelihood approach for a BHMF modeled by a modified Schechter function and an ERDF modeled by a Schechter function. As in Chapter 3, we provide an assessment of the goodness of fit my means of a two-dimensional K-S test (Fasano & Franceschini 1987) and by a χ^2 test. In Fig. 4.1

⋆ This chapter may lead or contribute to a future publication.

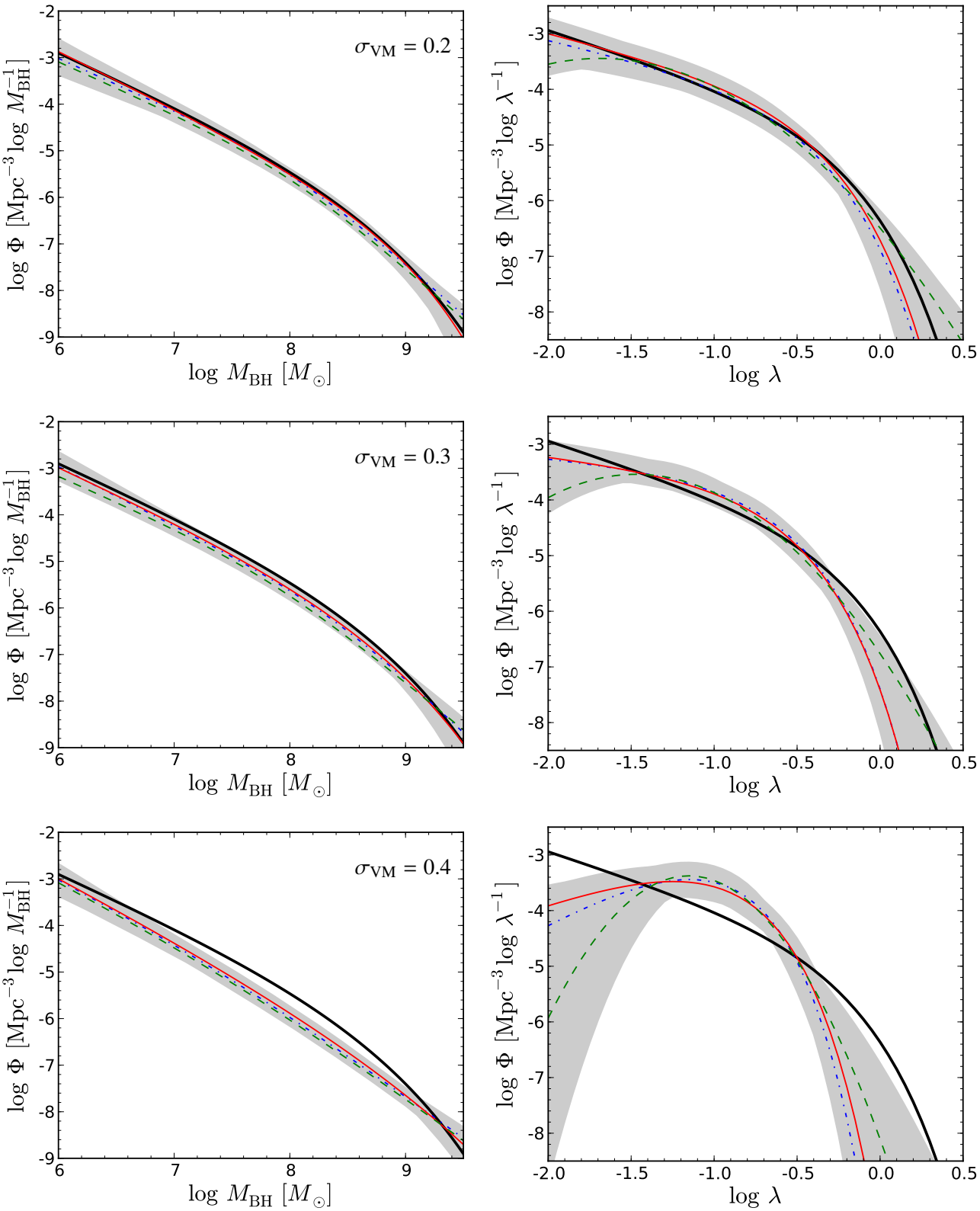

Fig. 4.1. Reconstructed BHMF (left) and ERDF (right) when accounting for uncertainty in virial black hole mass estimates. Three assumed values for the uncertainty $\sigma_{\rm VM}$ are used. Uncertainties of $\sigma_{\rm VM}$ = 0.2, 0.3 and 0.4 are assumed in the upper panels, middle panels and lower panels, respectively.. The blue dashed dotted line corresponds to a model with double power law BHMF and Schechter ERDF, the red solid line is for a modified Schechter BHMF and Schechter ERDF and the green dashed line is for a modified Schechter BHMF and a log-normal ERDF. The thick solid black line shows the BHMF or ERDF without accounting for $\sigma_{\rm VM}$, for reference (The model with modified Schechter function for the BHMF and Schechter function for the ERDF is displayed).

Table 4.1. Fitting results for the active black hole mass function and the Eddington ratio distribution function for a modified Schechter function BHMF and Schechter ERDF for different values of the intrinsic scatter in the virial method $\sigma_{\rm VM}$.

$\sigma_{\rm VM}$	$\phi^*_\bullet$ [Mpc^{-3}]	$\log M_*$	$\alpha_{\rm BH}$	$\beta_{\rm BH}$	$\log \lambda_*$	α_λ	$D_{\rm KS}$	$p_{\rm KS}$	χ^2/d.o.f.	p_{χ^2}	$\rho_{\rm act}$ [$M_\odot$ Mpc^{-3}]
0.00	2.75×10^{-6}	8.11	−2.11	0.50	−0.55	−1.95	0.094	4.8e−2	56.8/25	1.8e−4	1767
0.10	2.70×10^{-6}	8.10	−2.12	0.49	−0.62	−1.87	0.086	8.5e−2	61.5/25	3.9e−5	1742
0.15	2.44×10^{-6}	8.12	−2.12	0.51	−0.67	−1.82	0.087	8.1e−2	61.5/25	4.0e−5	1702
0.20	5.47×10^{-7}	8.49	−2.22	0.64	−0.72	−1.74	0.086	8.5e−2	60.6/25	5.3e−5	1700
0.30	3.02×10^{-6}	7.99	−2.11	0.45	−0.91	−1.34	0.094	4.5e−2	72.6/25	8.6e−7	1386
0.40	1.91×10^{-6}	7.94	−2.27	0.32	−1.29	0.10	0.109	1.3e−2	83.6/25	1.6e−8	1004

we show the reconstructed BHMF and ERDF for $\sigma_{\rm VM} = 0.2$, $\sigma_{\rm VM} = 0.3$ and $\sigma_{\rm VM} = 0.4$.

The best fit solution for $\sigma_{\rm VM} = 0.2$ only slightly deviates from our previous estimate, neglecting the effect of intrinsic scatter in virial black hole masses. While the BHMF is nearly unchanged, in the ERDF the space density of objects above the Eddington limit decreases and the low λ slope of the ERDF flattens. This trend is strongly enhanced for $\sigma_{\rm VM} = 0.3$ and even more for $\sigma_{\rm VM} = 0.4$. The break of the ERDF is shifted to a lower value and α_λ flattens significantly. The ERDF for $\sigma_{\rm VM} = 0.4$ even shows a maximum and a turnover towards low λ also for the Schechter function parameterisation.

On the other hand, the shape of the BHMF is affected little. The BHMF, accounting for measurement uncertainty, is basically consistent with the previous results. Only the normalisation, i.e. the total space density, decreases.

A change of the shape is expected, because accounting for measurement uncertainties narrows the intrinsic observed distribution of $M_\bullet$ and λ, corresponding to less objects at low and high values. Therefore, also in the reconstructed distribution functions, the space density at low and high values should be reduced. The effect is much stronger for the ERDF, because their observed distribution is already narrower than the $M_\bullet$ distribution. The BHMF is almost not affected. For a large value of $\sigma_{\rm VM}$, the BHMF at the low mass end is only poorly constrained by the observations. In this mass range, only objects with high λ are observable in the survey. However, due to the steep decrease of the ERDF toward the Eddington rate, very few objects are expected in this region. Thus, it is more likely that the objects observed with low mass and high λ have intrinsically a higher mass and therefore lower Eddington ratio and are only scattered into this region of the $M_\bullet$-λ plane. Therefore, the low mass end of the BHMF is less well constrained if measurement uncertainties become significant. The same is true for the low-λ end of the ERDF.

The decrease of the normalisation is a result of the change of the shape of the ERDF. Because the number of objects at low λ is reduced, there are less objects with low luminosity that would be missed by the survey. Thus, the observed number of objects corresponds to a lower corrected number of objects and hence to a lower space density and to a lower normalisation.

4.3. Can we constrain the statistical scatter?

Without any further knowledge on the size of the intrinsic scatter $\sigma_{\rm VM}$, our uncertainty on the active BHMF and especially on the ERDF increases significantly, as indicated by the range of solutions in Fig. 4.1. However, we can ask the question if all of these solutions provide equally good fits to the observations.

In Fig. 4.2 we show the effect of increasing the assumed $\sigma_{\rm VM}$ on the predicted observed distributions. We also show the $\sigma_{\rm VM} = 0$ distributions as dashed blue line. The observed mass distribution is broadened with increasing intrinsic scatter. This is a consequence of the almost invariance in shape of the best fit BHMF when convolved with $\sigma_{\rm VM}$, as discussed in the previous section. On the other hand, the best fit ERDF changes significantly while the observed distribution of λ, after convolution with the intrinsic scatter, has a comparable width as for $\sigma_{\rm VM} = 0$ or is even narrower. The main effect is a shift of the peak of the observed distribution to lower λ, but still consistent with the observed distribution of the HES sample. However, from the observed distribution of $M_\bullet$ it is already conspicuous that the best fit solution for $\sigma_{\rm VM} = 0.4$ provides a less well fit to the observations as the best fit solution for $\sigma_{\rm VM} = 0.2$. The results of the two-dimensional KS-test and χ^2-test support this suspection. The mismatch can be properly quantified by the maximum likelihood fit.

While the maximum likelihood method does not have its own assessment of the goodness-of-fit, it provides an estimate of the confidence level for the free model parameters via the distribution of S, where $S = -2 \ln \mathcal{L}$ is the likelihood for the model. We computed $\Delta S = S - S_{\rm min}$ within a range of assumed $\sigma_{\rm VM}$ values and converted it into confidence values assuming a χ^2 distribution (Press et al. 1992). In Fig. 4.3 we show the resulting ΔS for three model parameterisations. We again take the modified Schechter BHMF and Schechter ERDF parameterisation as our reference model. The minimum of the ΔS distribution lies at $\sigma_{\rm VM} \approx 0.15$. The confidence contours suggest constraints of $\sigma_{\rm VM} < 0.21$ at 1σ confidence, and $\sigma_{\rm VM} < 0.30$ at 3σ confidence.

The crucial question is now whether these constraints are reliable, i.e. whether this method is actually able to constrain the intrinsic scatter. Currently, we have to leave the answer to this question open. A possible way to test this is by performing extensive Monte Carlo simulations and inspect if the assumed input value of $\sigma_{\rm VM}$ is recovered. We started on this approach, but

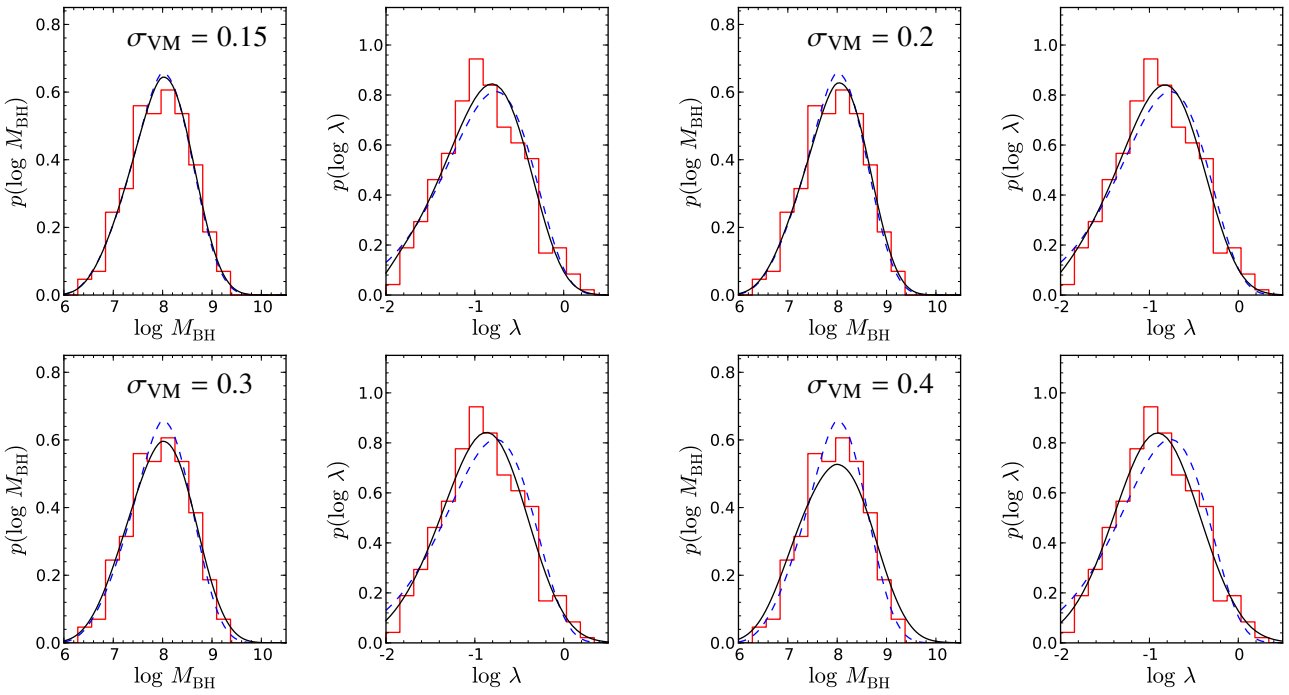

Fig. 4.2. Comparison of the model observable distributions of black hole mass and Eddington ratio (black curve) with the observations (red histograms) for different assumed values of the intrinsic scatter $\sigma_{\rm VM}$. As blue dashed line the model distributions without correction for $\sigma_{\rm VM}$ are given for reference.

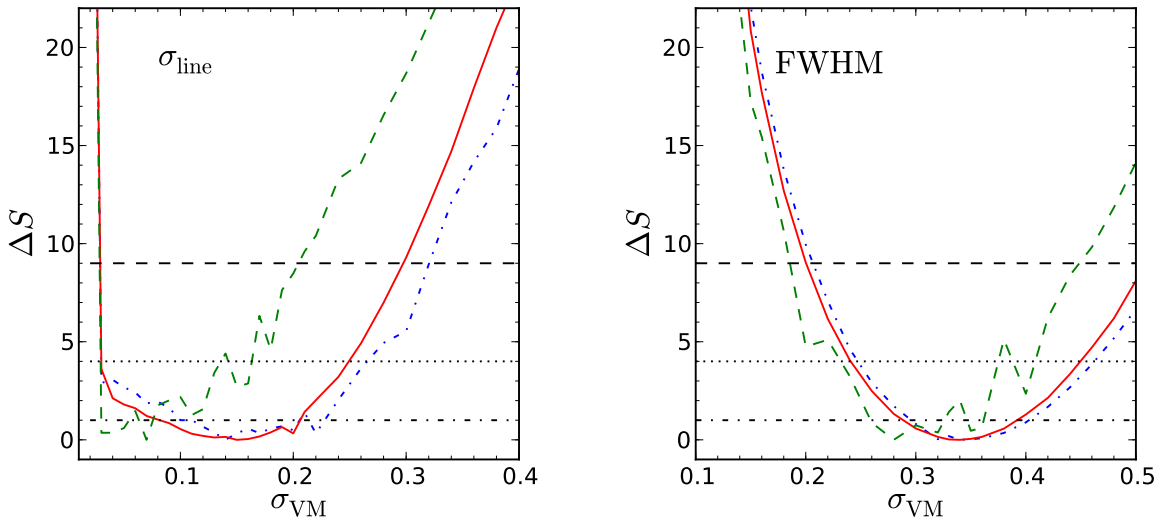

Fig. 4.3. ΔS distribution as a function of the applied intrinsic scatter in the virial method. The lines indicate different models, with the red solid line for a modified Schechter BHMF and Schechter ERDF, the blue dashed-dotted line for a double-power law BHMF and Schechter ERDF and the green dashed line for a modified Schechter BHMF and a log-normal ERDF. The black horizontal lines indicate 1σ, 2σ and 3σ confidence levels, corresponding to ΔS = 1, 4 and 9 respectively. Left panel: For black hole masses based on the line-dispersion. Right panel: For black hole masses based on the FWHM.

so far the results are inconclusive. Further work on this subject is required. Therefore, we here only report tentative evidence for a small intrinsic scatter in the virial method.

Nevertheless, the constraints we would get from our data only strictly refers to our method for estimating $M_\bullet$, which is based on the Hβ line, and uses the line dispersion $\sigma_{\rm line}$ as measure of the broad line width. This variant of the virial method probably exhibits the smallest intrinsic scatter (Collin et al. 2006), as it is directly tied to reverberation mapping, while other variants require an additional cross-calibration of single-epoch spectra against the reverberation mapped masses (e.g. Vestergaard & Peterson 2006; McGill et al. 2008; Wang et al.

2009; Rafiee & Hall 2011). In Chapter 3 we not only used $\sigma_{\rm line}$ to estimate $M_\bullet$, but also the full width half maximum (FWHM). While our results do not change qualitatively using the FWHM instead of $\sigma_{\rm line}$, we consider the FWHM based mass estimates as less reliable (see section 3.3). Thus, we would expect a larger value for the scatter in the virial black hole masses using the FWHM. We tested this expectation by again computing the likelihood of the BHMF and ERDF fit for a range of $\sigma_{\rm VM}$, but using $M_\bullet$ and λ from the FWHM. The results are shown in the right panel of Fig. 4.3. We obtained $\sigma_{\rm VM} = 0.35 \pm 0.05$, i.e. it is suggested that the FWHM based mass estimates exhibit a significant additional uncertainty of ~ 0.3 dex, compared to the mass estimates from $\sigma_{\rm line}$, as qualitatively expected. This at least shows consistency in the $\sigma_{\rm VM}$ estimates we derive from the maximum likelihood fit.

We further note that it would be interesting to have a direct constraint on $\sigma_{\rm VM}$ for our sample, because it covers the same range in redshift and luminosity as the reverberation mapping sample and also uses Hβ. Thus, it does not suffer from uncertainties due to the extrapolation of the virial method, as it is the case for other studies (Fine et al. 2008; Steinhardt & Elvis 2010; Kelly et al. 2010).

4.4. Intrinsic scatter budget for the virial method

If reliable, our constraints on $\sigma_{\rm VM}$ suggest a smaller intrinsic scatter in the virial method for the Hβ line dispersion than usually adopted. We now check whether such a small scatter is realistic at all, based on the scatter budget in the virial method. In particular, we are interested in putting lower and upper limits on $\sigma_{\rm VM}$.

Virial black hole masses are given by

$$\log M_\bullet = \log f + \gamma \log L + 2 \log \Delta V + C \,, \qquad (4.5)$$

where in C all remaining constants are absorbed. The intrinsic scatter is thus given by:

$$\sigma^2_{\rm VM} = \sigma^2_{\log f} + \sigma^2_R + \sigma^2_{\rm var} \,. \qquad (4.6)$$

Here, $\sigma_{\log f}$ is the uncertainty in the f factor that will also affect reverberation mapping (RM) masses, σ_R is the scatter in the $R_{\rm BLR} - L$ relation and $\sigma_{\rm var}$ contains the uncertainty in line width from using single-epoch spectra instead of line widths from RM campaigns. We briefly discuss all of these contributions.

Uncertainty in the f factor affects both, reverberation mapping and single-epoch black hole masses. The intrinsic scatter in the f factor is probably caused by the difference in inclination and geometry of the AGN broad line region. The average value for f is derived by scaling RM masses to the local $M_\bullet - \sigma_*$ relationship of quiescent galaxies, assuming they follow the same relation (Onken et al. 2004; Collin et al. 2006; Woo et al. 2010). The scatter in the f factor adds to the intrinsic scatter in the $M_\bullet - \sigma_*$ relation. This intrinsic scatter is of order 0.3 – 0.44 dex (Tremaine et al. 2002; Gültekin et al. 2009). For the RM sample, the intrinsic scatter around the $M_\bullet - \sigma_*$ relationship is $\sigma_{\rm int} = 0.44 \pm 0.07$ (Woo et al. 2010). This implies a constraint on the intrinsic scatter in $\log f$ of $0 < \sigma_{\log f} < 0.32$.

For the RM sample, Bentz et al. (2009) found a value of $\sigma_R = 0.15$ dex for the intrinsic scatter in the $R_{\rm BLR} - L$ scaling relationship, using the FITEXY method (Press et al. 1992). However, there is evidence that the measurement errors for some time delays from low-quality data are underestimated. Peterson (2010) report an intrinsic scatter of only 0.11 dex, when restricting the RM sample to objects with reliable time delay measurements. Denney et al. (2010) found an improved agreement with the $R_{\rm BLR} - L$ relation for objects with previously unreliable time delays, when using new accurate reverberation mapping measurements. These results suggest that the scaling relation and thus the virial method is better than usually assumed and only better, high precision reverberation data are required to improve on this relation. We assume here $0.11 < \sigma_R < 0.15$.

Denney et al. (2009) presented a comprehensive analysis of uncertainties in black hole mass estimates from single epoch spectra, based on the Seyfert 1 galaxy NGC 5548 and the quasar PG 1229+204. For the uncertainty in the estimated black hole mass due to variability they found about 0.12 dex for Seyferts and 0.05 dex for quasars, which we simply take as upper and lower limit for the contribution of variability to the intrinsic scatter.

For the full scatter budget on the intrinsic scatter in the virial method, using the Hβ line and the line dispersion, we then get an estimate of $0.12 < \sigma_{\rm VM} < 0.37$. Thus, a low estimate for $\sigma_{\rm VM}$, as suggested by our BHMF and ERDF determination, is at least not unreasonable. Further support comes from the determination of the $M_\bullet - \sigma_*$ relation for virial black-hole masses (Greene & Ho 2006; Bennert et al. 2011), finding a scatter of 0.4 dex, similar to the value for the RM sample and quiescent galaxies. The $M_\bullet - L_{\rm Bulge}$ relation for a sample of black holes with virial mass estimates seems to have a scatter comparable to direct mass measurements as well (Kim et al. 2008).

4.5. Conclusions

We presented an extension of our maximum likelihood method to determine the active BHMF and ERDF, presented in Chapter 3, to account for the intrinsic scatter $\sigma_{\rm VM}$ in the virial method to estimate black hole masses. We corrected our BHMF and ERDF estimates from Chapter 3 for this scatter and made an attempt to constrain $\sigma_{\rm VM}$ from our data. We found evidence for a small value of $\sigma_{\rm VM}$. However, we have not rigorously verified the reliablity of this result yet. Therefore, in the spirit of presenting preliminary results, we currently refrain from drawing a firm conclusion on the size of $\sigma_{\rm VM}$. However, we argue that a small value of $\sigma_{\rm VM}$ is not unreasonable and consistent with independent direct estimates of $\sigma_{\rm VM}$.

References

Bennert, V. N., Auger, M. W., Treu, T., Woo, J., & Malkan, M. A. 2011, ApJ, 726, 59

Bentz, M. C., Peterson, B. M., Netzer, H., Pogge, R. W., & Vestergaard, M. 2009, ApJ, 697, 160

Collin, S., Kawaguchi, T., Peterson, B. M., & Vestergaard, M. 2006, A&A, 456, 75

Denney, K. D., Peterson, B. M., Dietrich, M., Vestergaard, M., & Bentz, M. C. 2009, ApJ, 692, 246

Denney, K. D., Peterson, B. M., Pogge, R. W., et al. 2010, ApJ, 721, 715
Fasano, G. & Franceschini, A. 1987, MNRAS, 225, 155
Fine, S., Croom, S. M., Hopkins, P. F., et al. 2008, MNRAS, 390, 1413
Greene, J. E. & Ho, L. C. 2006, ApJ, 641, L21
Gültekin, K., Richstone, D. O., Gebhardt, K., et al. 2009, ApJ, 698, 198
Kelly, B. C., Vestergaard, M., Fan, X., et al. 2010, ApJ, 719, 1315
Kim, M., Ho, L. C., Peng, C. Y., et al. 2008, ApJ, 687, 767
Marconi, A., Risaliti, G., Gilli, R., et al. 2004, MNRAS, 351, 169
McGill, K. L., Woo, J.-H., Treu, T., & Malkan, M. A. 2008, ApJ, 673, 703
Onken, C. A., Ferrarese, L., Merritt, D., et al. 2004, ApJ, 615, 645
Peterson, B. M. 2010, in IAU Symposium, Vol. 267, IAU Symposium, 151–160
Press, W. H., Teukolsky, S. A., Vetterling, W. T., & Flannery, B. P. 1992, Numerical recipes in C. The art of scientific computing, ed. Press, W. H., Teukolsky, S. A., Vetterling, W. T., & Flannery, B. P.
Rafiee, A. & Hall, P. B. 2011, arXiv:1104.1828
Steinhardt, C. L. & Elvis, M. 2010, MNRAS, 406, L1
Tremaine, S., Gebhardt, K., Bender, R., et al. 2002, ApJ, 574, 740
Vestergaard, M. & Peterson, B. M. 2006, ApJ, 641, 689
Wang, J.-G., Dong, X.-B., Wang, T.-G., et al. 2009, ApJ, 707, 1334
Woo, J., Treu, T., Barth, A. J., et al. 2010, ApJ, 716, 269

Chapter 5

Selection effects in the black hole-bulge relations and its evolution*

Andreas Schulze and Lutz Wisotzki

Leibniz-Institut für Astrophysik Potsdam (AIP), An der Sternwarte 16, 14482 Potsdam, Germany

ABSTRACT

The observed tight correlation between black hole masses and their host galaxies' spheroid properties and especially the redshift evolution of this correlation contains important information on the coevolution of black holes and galaxies. Observational studies on the evolution in these relations are affected by sample selection effects. These need to be understood and taken into account, to distinguish a real evolutionary trend from a selection bias. Here, we discuss in detail the issue of selection effects on type 1 AGN samples. Apart from the well known luminosity bias, we identify additional sources of biases. If for a black hole the probability to be in an active stage directly depends on the black hole mass, a bias is induced on the active black hole subsample. Furthermore, an evolutionary signal in the black hole - bulge relations may be superimposed by the evolutionary behaviour of the AGN population itself, as evident from the evolution of the AGN luminosity function, which affects the expected sample bias. We present a general framework to investigate these biases, based on the bivariate probability distribution of galaxy property and black hole mass, and show predictions for luminosity limited and flux limited samples. We discuss these predictions in the context of current observations. Additionally, we comment on the effect of measurement uncertainties in black hole masses and spheroid properties on the bias. Our work emphasises the importance and complexity of sample selection effects for observational studies on the black hole - bulge relations and their evolution.

5.1. Introduction

Supermassive black holes appear to be ubiquitous in the centers of massive galaxies (Kormendy & Richstone 1995). Furthermore, they show tight correlations with the properties of the galaxies' spheroidal components, e.g. with the stellar velocity dispersions (Ferrarese & Merritt 2000; Gebhardt et al. 2000; Tremaine et al. 2002; Gültekin et al. 2009), bulge luminosity and mass (Magorrian et al. 1998; Marconi & Hunt 2003; Häring & Rix 2004; Sani et al. 2011) or concentration index (Graham et al. 2001). These relations have been established by direct dynamical measurement of the black hole mass in a few dozens of local, inactive galaxies, mainly using stellar dynamics (e.g. van der Marel et al. 1998; Emsellem et al. 1999; Gebhardt et al. 2003) or gas dynamics (e.g. Ferrarese et al. 1996; Marconi et al. 2001; Dalla Bontà et al. 2009).

Nevertheless, significant uncertainties in these relations persist. The high mass and the low mass regimes are still poorly constrained. There even may be systematic effects on the determined masses. Not accounting for triaxiality of the galaxy (van den Bosch & de Zeeuw 2010) or not including a dark matter halo in the dynamical models (Gebhardt & Thomas 2009; Schulze & Gebhardt 2011) can bias the dynamical measurement. Also the intrinsic scatter in these relations is still not well established (Gültekin et al. 2009). Furthermore, there is evidence that late-type galaxies and in particular pseudobulges do not follow the same relationships as early-type galaxies (Hu 2008; Graham 2008; Greene et al. 2010; Kormendy et al. 2011).

The black hole - bulge relations contain important information, as they imply a connection between the growth of a black hole and the evolution of its host galaxy. A common picture invokes AGN feedback to shut down star formation and self-regulate black hole accretion. This scenario is able to reproduce the local black hole - bulge relations in numerical simulations (Di Matteo et al. 2005; Sijacki et al. 2007; Booth & Schaye 2009), and semi-analytic models (Kauffmann & Haehnelt 2000; Cattaneo et al. 2005; Croton et al. 2006; Bower et al. 2006; Somerville et al. 2008; Marulli et al. 2008). On the other hand, a correlation between black hole mass and host galaxy mass will also be tightened or may even be generated natural within a merger driven galaxy evolution framework (Peng 2007; Hirschmann et al. 2010; Jahnke & Maccio 2010).

Essential constraints on the origin of the black hole - bulge relation can be inferred from their redshift evolution. There are several theoretical predictions, based on numerical simulations (Robertson et al. 2006; Hopkins et al. 2007; Di Matteo et al. 2008; Johansson et al. 2009; Booth & Schaye 2011) as well as on semi-analytic models (Wyithe & Loeb 2003; Croton 2006; Malbon et al. 2007; Hopkins et al. 2009; Lamastra et al. 2010). Although the details are still far from being settled, they tend to predict an increase in the $M_\bullet/M_{\rm Bulge}$ ratio with redshift, while only a weak or even negative evolution in the $M_\bullet - \sigma_*$ relation is implied.

These models need to be confronted with observations. Several different approaches have been followed in the last

* A version of this chapter will be submitted to *Astronomy & Astrophysics*

years to observationally constrain the evolution in the black hole - bulge relations. These range from more indirect arguments, to direct estimates of $M_\bullet$ and the respective bulge property. Constraints on integrated quantities can be gained from the black hole mass function (Merloni et al. 2004; Hopkins et al. 2006; Shankar et al. 2009; Somerville 2009; Kisaka & Kojima 2010). Bluck et al. (2011) studied X-ray selected AGN, employing Eddington ratio arguments, to constrain black hole - bulge coevolution.

A direct dynamical determination of $M_\bullet$ is not feasible outside of the local universe. Therefore, the most direct approach resorts to broad line AGN, for which the black hole mass is easily accessible through the 'virial estimator' (e.g., McLure & Jarvis 2002; Vestergaard & Peterson 2006). The main challenge for the determination of the $M_\bullet$−bulge relationship from AGN samples is the determination of the bulge properties, hampered by the bright nuclear point source of the AGN, which may well outshine the entire galaxy.

The $M_{\rm BH} - \sigma_*$ relation has been studied, measuring either the stellar velocity dispersion directly (Woo et al. 2006, 2008; Shen et al. 2008) or using the width of narrow emission lines as surrogates for σ_* (Shields et al. 2003, 2006; Salviander et al. 2007). The $M_\bullet - M_{\rm Bulge}$ relation has been investigated by measuring QSO host galaxy luminosities (Peng et al. 2006a,b; Treu et al. 2007; McLeod & Bechtold 2009; Decarli et al. 2010; Bennert et al. 2010), by directly estimating the stellar masses utilising colour information (Schramm et al. 2008; Jahnke et al. 2009; Merloni et al. 2010), or by dynamical mass measurements (Inskip et al. 2011). Also obscured AGN with detectable broad lines have been used (Sarria et al. 2010; Nesvadba et al. 2011), for which the determination of stellar masses is less problematic. McLure et al. (2006) determined the $M_\bullet - M_{\rm Bulge}$ ratio up to $z = 2$, matching distributions of radio-loud QSOs and radio galaxies. At the highest redshifts, CO rotation curves have been used to determine dynamical masses for a few individual objects (Walter et al. 2004; Riechers et al. 2008, 2009; Wang et al. 2010). All these methods have their own advantages and drawbacks. Nevertheless, there seems to be increasing evidence for evolution in the relations, with more massive SMBHs at given bulge mass than in the local universe.

On the other hand, observations of sub-mm selected galaxies (SMGs) appear to imply a lower $M_\bullet/M_{\rm Bulge}$ ratio at high redshifts (Borys et al. 2005; Alexander et al. 2008). However, these samples are limited to strongly star forming galaxies, which tend to be biased towards massive stellar systems (Lamastra et al. 2010).

But, selection effects may also play an important role for observations of broad line AGN. One of these selection effects is related to the AGN luminosity. AGN samples preferentially select luminous AGN, which on average tend to have more massive black holes. The intrinsic scatter in the $M_\bullet - M_{\rm Bulge}$ relation then generates a bias towards a higher $M_\bullet/M_{\rm Bulge}$ ratio. This bias has been pointed out by several authors (Adelberger & Steidel 2005; Fine et al. 2006; Salviander et al. 2007), but received major attention by the work of Lauer et al. (2007), who discussed it in more detail (but see also Peng 2010). However this AGN luminosity bias may not be the only important selection effect and thus restricting the discussion to this single point falls short. For example, previous studies usually assume that AGN are a random subset of the supermassive black hole population. As they are per definition *active* black holes, this is not necessarily true, which can potentially introduce an additional selection effect. This effect did not receive much attention so far, and we discuss it in more detail below. A further effect has been discussed by Shen & Kelly (2010), caused by the uncertainty in virial black hole mass estimates in connection with the steep decease of the active black hole mass function (BHMF). We also comment on this effect below. Overall, previous studies tend to be focused on a single selection effect. We here present a general framework to investigate a variety of effects at large.

In this paper we study and quantify selection effects on observations of the $M_\bullet - M_{\rm Bulge}$ relation and discuss their implications for studies on evolution in this relation. In section 5.2 we present the general framework in which we investigate the consequences of selection effects and show a first application to the quiescent black hole sample. Section 5.3 discusses several selection effects for AGN samples and their ramifications for the black hole-bulge relations. In section 5.4, we take into account redshift evolution effects. We discuss the implications of our results on observational studies in section 5.5. We finally conclude in section 5.6. For the cosmological parameters we assume $H_0 = 70$ km s^{-1} Mpc^{-1}, $\Omega_{\rm m} = 0.3$ and $\Omega_\Lambda = 0.7$.

5.2. The local $M_\bullet - M_{\rm Bulge}$ relation

We start with some general thoughts on the $M_\bullet - M_{\rm Bulge}$ relation and selection effects, discussing the special aspect of AGN samples in the next section. We here focus on the $M_\bullet - M_{\rm Bulge}$ relation, but the argument equally holds for the $M_\bullet - \sigma_*$ relation. We do not imply one relation to be more fundamental than the other. We refer to the bulge property as s with $s = \log \sigma_*$ or $s = \log M_{\rm Bulge}$, respectively and to the black hole mass as $\mu = \log M_\bullet$.

The distribution of objects in the $\mu - s$ diagram is given by the bivariate distribution function of bulge mass and black hole mass $\Psi(s, \mu)$. Thus $\Psi(s, \mu)\mathrm{d}\mu\mathrm{d}s$ gives the number of objects per Mpc^3 with galaxy property between s and $s + \mathrm{d}s$ and black hole mass between μ and $\mu + \mathrm{d}\mu$. We assume the following parameterisation for most of the paper,

$$\Psi(s, \mu) = g(\mu \,|\, s)\, \Phi_s(s)\,, \tag{5.1}$$

where $\Phi_s(s)$ is the spheroid distribution function, e.g. the spheroid mass function, and $g(\mu \,|\, s)$ gives the probability of finding the black hole mass μ given s. If s and μ are correlated, as suggested by the observations, then $g(\mu \,|\, s)$ corresponds to this correlation. In the following we assume a linear relation $\mu = a + bs$ with log-normal intrinsic scatter σ, i.e.

$$g(\mu \,|\, s) = \frac{1}{\sqrt{2\pi}\sigma} \exp\left\{-\frac{(\mu - a - bs)^2}{2\sigma^2}\right\}\,. \tag{5.2}$$

This parameterisation for the bivariate distribution function is not the only one possible. We comment on the its observational justification as well as on alternative parameterisations and their implications in the Appendix of this Chapter. While our quantitative results depend on the adopted parameterisation, most of

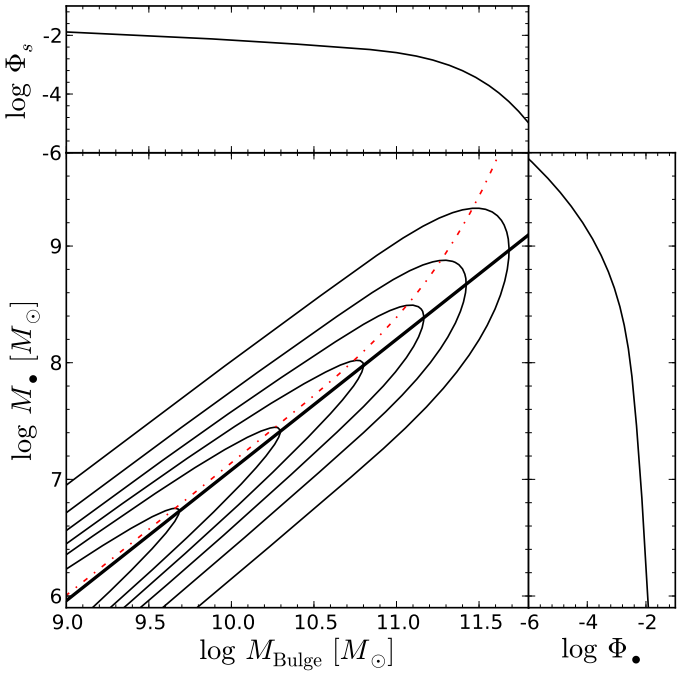

Fig. 5.1. Bivariate probability distribution function of bulge mass and black hole mass with no selection effects. The contours indicate decreasing probability in logarithmic units. The thick black line shows the input $M_\bullet - M_{\rm Bulge}$ relation from Häring & Rix (2004). The red dashed dotted line shows the mean galaxy property for a given black hole mass. The upper panel shows the projection of the bivariate distribution function to the bulge mass, i.e. the spheroid mass function. The right panel shows the projection to black hole mass, i.e the quiescent black hole mass function.

our qualitative results are independent of the specific choice of $\Psi(s,\mu)$.

The corresponding distribution functions for s and μ are given by marginalisation over the other variable.

$$\Phi_s(s) = \int \Psi(s,\mu)\,\mathrm{d}\mu = \Phi_s(s) \tag{5.3}$$

$$\Phi_\bullet(\mu) = \int \Psi(s,\mu)\,\mathrm{d}s = \int g(\mu\,|\,s)\,\Phi_s(s)\,\mathrm{d}s \tag{5.4}$$

The integration over μ simply returns the spheroid mass function. The integration over s returns the quiescent black hole mass function (BHMF), equivalent to the common approach for its determination (e.g. Yu & Lu 2004; Marconi et al. 2004; Merloni 2004). The first equality in Equations (5.3) and (5.4) is independent of the special choice of $\Psi(s,\mu)$. In particular, as the galaxy distribution function is an observable, Equation (5.3) sets a constraint on the bivariate distribution $\Psi(s,\mu)$. Note that the specific shape of $\Psi(s,\mu)$ has direct consequences for the quiescent black hole mass function.

Fig. 5.1 shows $\Psi(s,\mu)$, $\Phi_s(s)$ and $\Phi_\bullet(\mu)$ for the local universe, employing our parameterisation. We estimated the spheroid mass function from the early type and late type stellar mass functions from Bell et al. (2003), selected from the SDSS. We computed the spheroid mass function as sum of the early type mass function and the mass function of the bulge component of the late type galaxies. Since the bulge fraction in disk galaxies is still somehow uncertain, we simply assumed an average value of $B/T = 0.3$ to convert the late type mass function into a bulge mass function, consistent with current observations (e.g. Graham & Worley 2008; Gadotti 2009). This value also produces a black hole mass function that is consistent with determinations from the $M_\bullet - \sigma_*$ and $M_\bullet - L$ relations (Marconi et al. 2004). For the $M_\bullet - M_{\rm Bulge}$ relation, we used the relation by Häring & Rix (2004) and an intrinsic scatter of $\sigma = 0.3$ dex. We keep this value for the intrinsic scatter fixed for most of the paper and comment on the consequences of changing it when appropriate.

The distribution shown in Fig. 5.1 would be obtained for a volume limited sample of galaxies with $M_{\rm Bulge}$ and $M_\bullet$ measurements. In practise, the distribution will be affected by selection effects of the sample construction. This is accounted for by the selection function, defined as the probability of observing an object of a given bulge mass, black hole mass and potentially further selection criteria, such as for instance redshift or AGN luminosity. We define a selection function $\Omega(s,\mu,\theta)$, where θ refers to the set of additional parameters present as selection criteria. The observed bivariate distribution is then given by

$$\Psi_{\rm o}(s,\mu) = \int \Omega(s,\mu,\theta)\,\Psi(s,\mu)\,p_\theta(\theta)\,\mathrm{d}\theta\,, \tag{5.5}$$

where $p_\theta(\theta)$ is a set of normalised distribution functions of the parameters θ. Depending on Ω, the observed $M_\bullet - M_{\rm Bulge}$ relation can be significantly biased if the selection effects are not taken into account. However, this requires a proper knowledge of the selection function.

The bivariate distribution $\Psi_{\rm o}(s,\mu)$, when normalised to one, represents the full probability distribution of the expected $M_\bullet - M_{\rm Bulge}$ relation. However, we may be not mainly interested in the full distribution, but only in the mean relation. This is given by the mean black hole mass at a given bulge property

$$\langle\mu\rangle(s) = \frac{\int \mu\,\Psi_{\rm o}(s,\mu)\,\mathrm{d}\mu}{\int \Psi_{\rm o}(s,\mu)\,\mathrm{d}\mu}\,. \tag{5.6}$$

If no selection effects are present then $\langle\mu\rangle(s)$ will be identical to the input $M_\bullet$–bulge relation, $\langle\mu\rangle = a + bs$. Alternatively, the mean bulge property at a given black hole mass can be used

$$\langle s\rangle(\mu) = \frac{\int s\Psi_{\rm o}(s,\mu)\,\mathrm{d}s}{\int \Psi_{\rm o}(s,\mu)\,\mathrm{d}s}\,. \tag{5.7}$$

Even without any selection effects $\langle s\rangle(\mu)$ does not simply correspond to the inverse relation but deviates from it at the high mass end where the space density in the galaxy distribution function is decreasing. This is illustrated as red dashed-dotted line in Fig. 5.1 and was already discussed by Lauer et al. (2007). This is not an observational bias but just a direct consequence of the different projection chosen and the decrease of the galaxy distribution function. In general, under the presence of selection effects $\langle s\rangle(\mu)$ may be modified as well.

In observational studies on the evolution of the $M_\bullet$–bulge relation, the sample is often compared to the local relation in

terms of a single value, the offset from the local relation. The sample bias on this offset is given by

$$\langle \Delta\mu \rangle = \frac{\iint (\mu - a - bs)\, \Psi_{\rm o}(s,\mu)\, {\rm d}\mu {\rm d}s}{\iint \Psi_{\rm o}(s,\mu)\, {\rm d}\mu {\rm d}s} \,. \tag{5.8}$$

Alternatively, the mean offset of the galaxy property from the local relation is given by

$$\langle \Delta s \rangle = \frac{\iint (s - \alpha - \beta\mu)\, \Psi_{\rm o}(s,\mu)\, {\rm d}\mu {\rm d}s}{\iint \Psi_{\rm o}(s,\mu)\, {\rm d}\mu {\rm d}s} = -\frac{1}{b} \langle \Delta\mu \rangle \,, \tag{5.9}$$

where we use the inverse relation $s = \alpha + \beta\mu$ with $\alpha = -a/b$ and $\beta = 1/b$. This directly leads to $\langle \Delta s \rangle = -1/b\, \langle \Delta\mu \rangle$, without any specific assumption on $\Psi_{\rm o}(s,\mu)$. Thus the bias in $\langle \Delta\mu \rangle$ and $\langle \Delta s \rangle$ should always be directly proportional to each other.

To a certain extend, also the observed sample of a few dozen quiescent black holes will be affected by selection effects. However, this sample is inhomogeneous, i.e. it does not posses a well defined selection function, which hampers a proper investigation of potential selection effects. Yu & Tremaine (2002) and Bernardi et al. (2007) reported on a possible bias in the quiescent black hole mass sample through finding a discrepancy in the $\sigma_* - L$ relation compared to the SDSS. Furthermore, Gültekin et al. (2009) discussed a bias induced by culling the sample based on the resolution of the black hole's sphere of influence. Before discussing selection effects on AGN samples in detail, we want to investigate this bias to illustrate the general applicability of Equation (5.5).

5.2.1. Bias by sphere of influence resolution

Dynamical black hole mass determinations need to spatially resolve the region of gravitational influence of the central black hole on the stellar velocity distribution. The size of this region is commonly estimated by the sphere of influence, with radius $R_{\rm inf} = G M_\bullet \sigma_*^{-2}$. It has been argued (e.g. Ferrarese & Ford 2005) that dynamical black hole masses are unreliable for $R_{\rm inf}/d_{\rm res} < 1$ and therefore should be excluded from the sample. Here $d_{\rm res}$ is the spatial resolution of the observations. Gültekin et al. (2009) demonstrated that this procedure leads to a bias in the $M_\bullet$–bulge relations, simply because galaxies below a line $M_\bullet \propto \sigma_*^2$ are rejected. Batcheldor (2010) pointed out that it would even be possible to artificially generate a $M_\bullet - \sigma_*$ correlation via this selection effect. Gültekin et al. (2009) argued against culling the sample based on the sphere of influence to avoid this bias. However, even without an active rejection this effect may be present, either due to an implicit target selection or through the mere ability to detect a black hole. The condition $R_{\rm inf}/d_{\rm res} \geq 1$ is no strict limit for the reliability of black hole detection, but it is clear that for $R_{\rm inf}/d_{\rm res} \ll 1$ no black hole can be detected dynamically.

We now illustrate the results of this bias. We assume that we can detect all black holes above a certain threshold in resolution of the sphere of influence, $R_{\rm inf}/d_{\rm res} > r_{\rm min}$. We keep the spatial resolution of our survey fixed at $0.1''$. Thus the selection function is given by

$$\Omega(s,\mu,d) = \begin{cases} 1 & \text{for} \quad R_{\rm inf}/d_{\rm res} > r_{\rm min} \\ 0 & \text{else} \end{cases} \tag{5.10}$$

where d is the distance to the galaxy. The observed bivariate probability distribution is then given by

$$\Psi_{\rm o}(s,\mu) = \frac{3}{d_2^3 - d_1^3} \int_{d_1}^{d_2} \Omega(s,\mu,d)\, \Psi(s,\mu)\, d^2\, {\rm d}d \,. \tag{5.11}$$

For the purpose of illustration, we again use the $M_\bullet - M_{\rm Bulge}$ diagram. We convert bulge mass into velocity dispersion, assuming a fixed mass-to-light ratio for the r-band and using the $\sigma_* - L_r$ relation from Bernardi (2007). We cover the distance range from 1 to 30 Mpc. In Fig. 5.2 we show the $M_\bullet - M_{\rm Bulge}$ diagram for two thresholds in the sphere of influence resolution, $r_{\rm min} = 1$ and $r_{\rm min} = 0.1$. We additionally plot the 'observed' mean $M_\bullet - M_{\rm Bulge}$ relation $\langle \mu \rangle (s)$ for both cases as thick black solid line and the 'observed' mean relation $\langle s \rangle (\mu)$ as red dashed-dotted line. The bias induced by the resolution of the black hole's sphere of influence leads to a flatter slope, a higher normalisation and a smaller intrinsic scatter, as already shown by Gültekin et al. (2009). See also their work for an extensive Monte Carlo investigation of this bias.

While a significant bias is induced only for a high cutoff in $r_{\rm min}$, the probability distribution is affected even for a low threshold, most severely at the low mass end. Also the relation $\langle s \rangle (\mu)$ is biased in both cases. The selection along lines of $M_\bullet \propto \sigma_*^2$ is clearly visible in the probability contours. However, the degree of the bias caused by this selection effect on the actually used sample of quiescent black holes is hard to quantify, due to the inhomogeneous character of the sample. Here, we only emphasize that selection effects are a concern in general, thus also for dynamical black hole mass measurements.

5.3. Biases of broad line AGN samples

Selection effects are a major concern for samples selected as broad line AGN. For these objects the black hole mass can be easily estimated using the virial method. This makes them so valuable for studies of the evolution in the $M_\bullet$–bulge relations, as at high redshift black hole masses cannot be determined by means of direct dynamical observations. We first discuss general issues of selection effects, also inherent in low-z AGN samples. The application to higher redshifts will be covered in section 5.4.

Samples of non-active galaxies are basically drawn from the galaxy luminosity function. In contrast, AGN samples are effectively drawn from the broad line AGN luminosity function. This can induce non-trivial selection effects on the sample, as already pointed out by Lauer et al. (2007). Firstly, there will be a luminosity bias. Flux limited AGN surveys will on average contain more luminous objects then an 'ideal' volume-limited sample. Thus, the AGN will on average have more massive black holes. The intrinsic scatter in the black hole-bulge relations, together with the steep decrease of the spheroid distribution function, causes a Malmquist type bias towards more massive black holes at a given spheroid mass. The strength of the bias depends on the luminosity limit, the shape of the spheroid distribution function, the intrinsic scatter in the $M_\bullet$–bulge relation, and the distribution of Eddington ratios. We will further discuss and illustrate these details below.

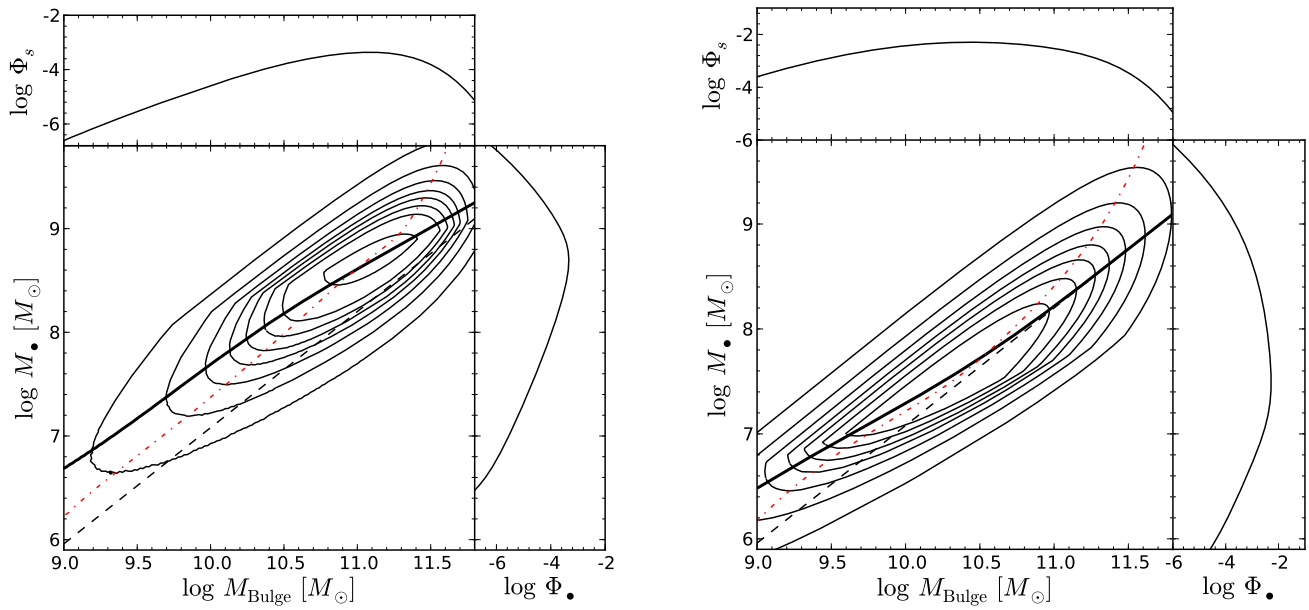

Fig. 5.2. The bivariate probability distribution function and its projections for a quiescent black hole sample under the presence of a sample selection on the resolution of the black hole's sphere of influence. A threshold of $R_{\rm inf}/d_{\rm res} > 1$ (left panel) or $R_{\rm inf}/d_{\rm res} > 0.1$ (right panel) is applied to the sample. The dashed black line shows the input $M_\bullet - M_{\rm Bulge}$ relation, the thick black solid line highlights the 'observed' relation $\langle\mu\rangle(s)$, and the red dashed dotted line indicates the 'observed' relation $\langle s\rangle(\mu)$

.

A second effect, so far not discussed, may be an active fraction bias. For a sample of broad line AGN, their black holes are per definition active, and therefore not a random representation of the entire black hole population. Only a minority of all black holes is active, described by the active fraction or duty cycle. If this active fraction is a function of $M_\bullet$ then the intrinsic scatter in the $M_\bullet - M_{\rm Bulge}$ relation will induce an additional bias as shown below. If the active fraction is decreasing with increasing black hole mass, then for a given spheroid mass it will be more probable to find a smaller mass black hole in an AGN sample, causing a bias towards a lower $M_\bullet/M_{\rm Bulge}$ ratio. Conversely, for an increasing active fraction we expect a positive bias, while for a constant ($M_\bullet$ independent) active fraction no bias will occur. Thus, this bias can work in both directions, depending on the black hole mass dependence of the active fraction. It will add to the luminosity bias.

5.3.1. Luminosity limited samples

We now show analytically how these selection effects influence the $M_\bullet$–bulge diagram. Broad line AGN are drawn from the AGN luminosity function $\Phi_L(l)$, with $l \equiv \log L_{\rm bol}$. The luminosity of an AGN is produced by mass accretion onto a SMBH, thus it is determined by the black hole mass and the mass accretion rate. The latter is expressed in normalised units by the Eddington ratio $\lambda = L_{\rm bol}/L_{\rm Edd}$. The Eddington luminosity is proportional to $M_\bullet$, thus the bolometric luminosity is given by $l = \log\lambda + \mu + 38.1$. The AGN luminosity function $\Phi_L(l)$ (in logarithmic units) is then given by

$$\Phi_L(l) = \int p_\lambda(l-\mu)\,\Phi_{\bullet,a}(\mu)\,{\rm d}\mu\,. \qquad (5.12)$$

By $\Phi_{\bullet,a}(\mu)$ we define the *active* BHMF, where active black holes are those that contribute to the corresponding AGN luminosity function. Thus, when restricting the AGN sample to type 1 AGN (showing broad lines), the active BHMF includes only these type 1 AGN. The distribution function $p_\lambda(l-\mu)$ gives the probability of finding a black hole with mass μ given an AGN luminosity l, i.e. it corresponds to the normalised distribution function of Eddington ratios λ. We implicitly assume that the Eddington ratio distribution function is independent of black hole mass, i.e. $p_\lambda(\mu\,|\,l) = p_\lambda(l-\mu) = p_\lambda(\log\lambda)$. Type 1 AGN are observed to have Eddington ratios in the range $0.01 < L_{\rm bol}/L_{\rm Edd} < 1$. When applying a lower threshold to the Eddington ratio, not all black holes are currently in an active state. The active fraction is defined as the ratio between the active and the total black hole population, estimated as

$$p_{\rm ac}(\mu) = \Phi_{\bullet,a}(\mu)/\Phi_{\bullet,q}(\mu)\,; \qquad (5.13)$$

with $\Phi_{\bullet,a}(\mu)$ and $\Phi_{\bullet,q}(\mu)$ as the active and quiescent BHMF, respectively. Therefore, the AGN luminosity function can be expressed as

$$\Phi_L(l) = \iint p_\lambda(l-\mu)\,p_{\rm ac}(\mu)\,g(\mu\,|\,s)\,\Phi_s(s)\,{\rm d}s{\rm d}\mu\,. \qquad (5.14)$$

There is thus a connection between the bulge property and the AGN luminosity, which is however smeared out by convolution with a set of additional distribution functions.

Following Equation (5.5), the bivariate black hole-bulge distribution function for a luminosity limited sample is given by

$$\Psi_{\rm o}(s,\mu) = \int \Omega(s,\mu,l)\,p_\lambda(l-\mu)\,g(\mu\,|\,s)\,\Phi_s(s)\,{\rm d}l\,. \qquad (5.15)$$

If we assume a fixed lower luminosity limit $l_{\rm lim}$, the selection function is

$$\Omega(s,\mu,l) = \begin{cases} p_{\rm ac}(\mu) & \text{for} \quad l \geq l_{\rm lim} \\ 0 & \text{else} \end{cases} \qquad (5.16)$$

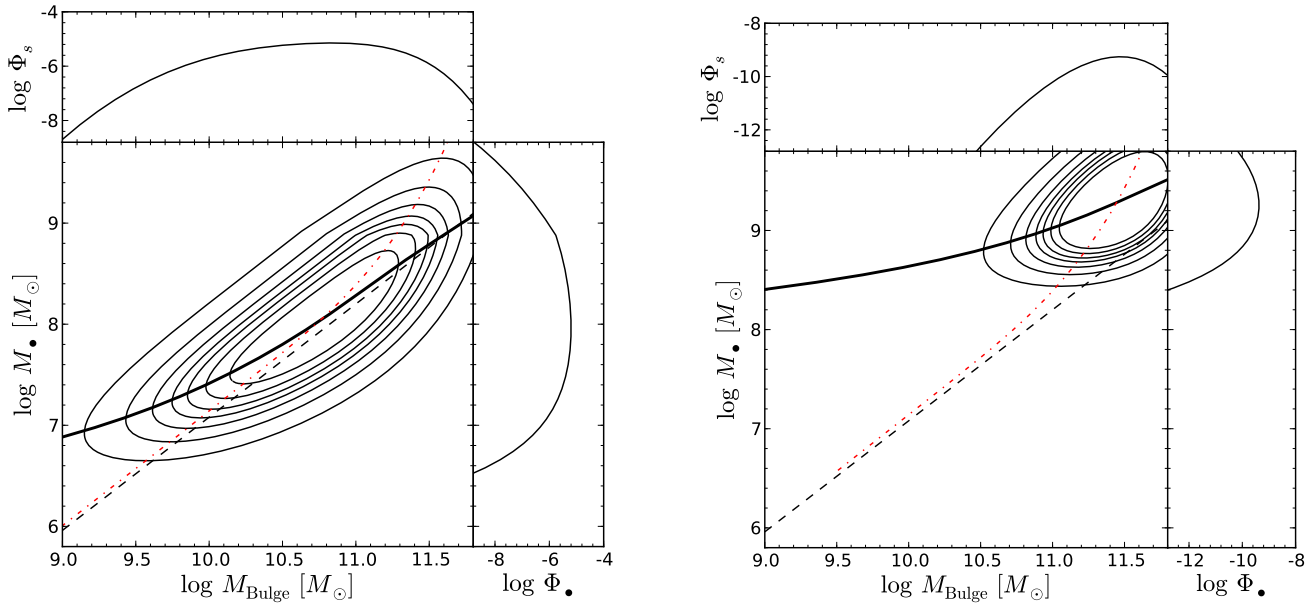

Fig. 5.3. Bivariate probability distribution function and its projections for a local type 1 AGN sample under the presence of a lower luminosity limit. The dashed black line again shows the input relation, the thick black solid line the observed relation $\langle\mu\rangle(s)$, and the red dashed dotted line indicates the 'observed' relation $\langle s\rangle(\mu)$ of this sample. A lower luminosity limit of $\log L_{\rm bol} > 45$ (left panel) and $\log L_{\rm bol} > 47$ (right panel) is applied, respectively.

The bivariate distribution function is then

$$\Psi_{\rm o}(s,\mu) = p_{\rm ac}(\mu)\, g(\mu\,|\,s)\, \Phi_s(s) \int_{l_{\rm lim}}^{\infty} p_\lambda(l-\mu)\,{\rm d}l\,. \qquad (5.17)$$

So, $\Phi_L(l)$ and $\Psi_{\rm o}(s,\mu)$ are just different projections of a multivariate distribution function $\Psi_{\rm o}(s,\mu,l)$. The non-trivial difference between $\Psi(s,\mu)$ and $\Psi_{\rm o}(s,\mu)$ is the source of the bias. It is controlled by the three probability distributions, $p_{\rm ac}(\mu)$, $p_\lambda(l-\mu)$, and $g(\mu\,|\,s)$. The distribution of $p_{\rm ac}(\mu)$ regulates the active fraction bias, $p_\lambda(l-\mu)$ rules the luminosity bias and $g(\mu\,|\,s)$ controls the overall strength of the bias.

In Equation (5.17) we can combine the parts governing the AGN selection, by defining the selection function, integrated over the AGN luminosity,

$$\Omega(\mu) = p_{\rm ac}(\mu) \int_{l_{\rm lim}}^{\infty} p_\lambda(l-\mu)\,{\rm d}l\,. \qquad (5.18)$$

and thus $\Psi_{\rm o}(s,\mu) = \Omega(\mu)\Psi(s,\mu)$.

The mean relations obtained from such a sample, affected by an AGN luminosity limit, are

$$\langle\mu\rangle(s) = \frac{\int \mu\,\Psi_{\rm o}(s,\mu)\,{\rm d}\mu}{\int \Psi_{\rm o}(s,\mu)\,{\rm d}\mu} = \frac{\int \mu\Omega(\mu) g(\mu\,|\,s){\rm d}\mu}{\int \Omega(\mu) g(\mu\,|\,s)\,{\rm d}\mu}\,; \qquad (5.19)$$

$$\langle s\rangle(\mu) = \frac{\int s\Psi_{\rm o}(s,\mu)\,{\rm d}s}{\int \Psi_{\rm o}(s,\mu)\,{\rm d}s} = \frac{\int s g(\mu\,|\,s)\Phi_s(s)\,{\rm d}s}{\int g(\mu\,|\,s)\Phi_s(s){\rm d}s}\,. \qquad (5.20)$$

The relation $\langle\mu\rangle(s)$ is independent of the galaxy distribution function, but it is affected by the selection function. Therefore, $\langle\mu\rangle(s) \neq a + bs$, as would be the case without selection effects. On the other hand $\langle s\rangle(\mu)$ is already intrinsically affected by the galaxy distribution function, but it is independent of the selection function. Therefore, $\langle s\rangle(\mu)$ contains information on the intrinsic relation, unaffected by the AGN luminosity bias and active fraction bias. This is an interesting fact, as it provides a potential route to study the evolution in the $M_\bullet$–bulge relations without accounting for AGN selection effects. However, even if $\langle s\rangle(\mu)$ is not biased by the selection effects, the mean offset $\langle\Delta s\rangle$ is biased, as shown by Equation (5.9), because we have to integrate over the entire observed black hole mass distribution.

We now first illustrate the AGN bias in the $M_\bullet$–bulge plane, and then investigate it in terms of a simple offset from the input relation. For this purpose, we need to know all the underlying distribution functions, for which we here adopt the local values. For $\Phi_s(s)$, we again use the above estimated spheroid mass function. For $g(\mu\,|\,s)$, we assume a log-normal distribution with intrinsic scatter $\sigma = 0.3$ dex around the relation from Häring & Rix (2004). These then define the quiescent BHMF via Equation (5.4). If we further know the active BHMF, the active fraction is given by Equation (5.13). The active BHMF and the Eddington ratio distribution function (ERDF) $p_\lambda(l-\mu)$ for type 1 AGN in the local universe were determined by Schulze & Wisotzki (2010, hereafter SW10), and we use those values, assuming a modified Schechter function for the BHMF and a Schechter function for the ERDF. The SW10 active BHMF implies a decrease of the active fraction with increasing black hole mass, thus the active fraction bias will work towards a lower $M_\bullet/M_{\rm Bulge}$ ratio, opposite to the luminosity bias. Note that this parameterisation by construction ensures the consistency with the broad line AGN luminosity function via Equation (5.14).

In Fig. 5.3 we show the $M_\bullet - M_{\rm Bulge}$ diagram for a luminosity limited local AGN sample, for two lower luminosity limits, $l_{\rm min} = 45$ and $l_{\rm min} = 47$. For $z \sim 0$ the latter case is rather unrealistic, as we are limited to the most luminous QSOs. However, as further discussed below, it is of importance for higher z observations, where only the brightest QSOs can be detected. The luminosity limit of $l_{\rm min} = 47$ roughly corresponds to the SDSS

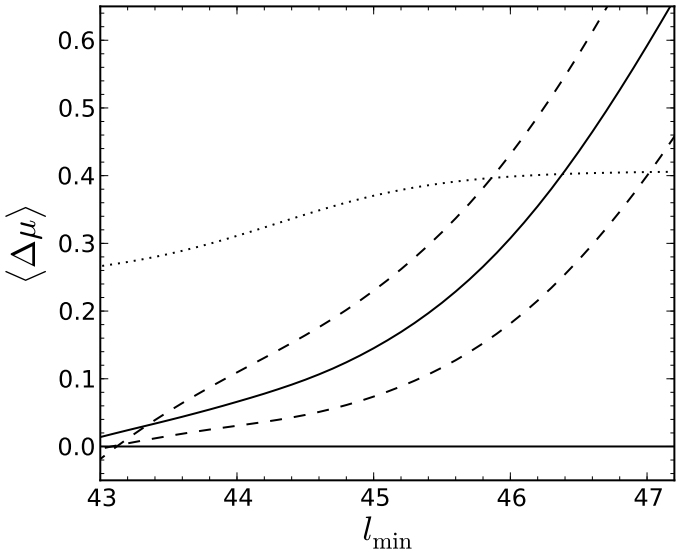

Fig. 5.4. Predicted bias for a luminosity limited local type 1 AGN sample as a function of the low luminosity limit (in logarithmic units). The solid line shows our prediction for $\sigma = 0.3$. The dashed lines show the predictions for $\sigma = 0.4$ (upper line) and $\sigma = 0.2$ (lower line). The dotted line gives the prediction from Lauer et al. (2007), based on the local AGN luminosity function; see text for an explanation of the differences.

magnitude limit of $i \simeq 19$ at $z \simeq 3$ and to the SDSS high-z limit of $i = 20.2$ at $z \simeq 6$.

For both luminosity limits the $M_\bullet - M_{\rm Bulge}$ relation is biased towards larger black hole masses at a given spheroid mass. This is already true for $l_{\rm min} = 45$, but is greatly enhanced for the high luminosity limit. The dashed line again shows the mean black hole mass for a given spheroid mass (computed via Equation (5.6)), i.e. the $M_\bullet - M_{\rm Bulge}$ relation obtained for the given sample. It is clearly visible that in general the bias is strongest at the low mass end rather than at the high mass end. Specifically, it is strongest close to the luminosity limit of the survey, on average corresponding to lower mass black holes. The red dashed dotted line again shows the mean spheroid mass for a given black hole mass (computed via Equation (5.7)). As noted, this relation is unaffected by the AGN selection and is identical to the one shown in Fig. 5.1. However, it is not identical to the intrinsic relation, as it turns upwards at the high mass end due to the decrease in the spheroid mass function. Therefore, an integration over $\langle s \rangle(\mu)$ with a stronger weight on the high mass end will lead to a bias for the mean offset from the local relation, i.e for the total sample bias.

The sample bias is enhanced for a bright luminosity limit. The steep decrease of the spheroid mass function and the intrinsic scatter in the relation itself induce an increase in the bias compared to the flat section of the spheroid mass function. This is shown in Fig. 5.4, where the mean offset from the input relation for the whole AGN sample, $\langle \Delta\mu \rangle$ (computed via Equation (5.8)), is plotted for a range of bolometric AGN luminosity limits, assuming the local distribution functions. Here, we assumed our reference value for the intrinsic scatter, $\sigma = 0.3$ dex, but we also indicate the dependence of the bias on the intrinsic scatter. A smaller intrinsic scatter also leads to a smaller sample bias, while a larger scatter causes a larger bias. As dotted line, we additionally show the bias predicted by Lauer et al. (2007), using their Equation (25) and the local bolometric type 1 AGN luminosity function from Schulze et al. (2009). The main difference between their result and ours is that we not only use the AGN luminosity function, but the whole set of underlying distribution functions. In particular, we also take into account the active fraction bias that reduces the total bias, due to the decrease of the active fraction towards higher black hole masses. As a caveat we note that for very high luminosities, our knowledge of the underlying distributions (active and passive BHMFs, AGN luminosity function and $M_\bullet - M_{\rm Bulge}$ relation) are observationally poorly determined.

We provide an additional illustration of these selection effects by Monte Carlo Simulations. We generated a large galaxy sample drawn from the spheroid mass function, and attributed black hole masses drawn from a log-normal distribution with mean from the Häring & Rix (2004) relation. We decided if the black hole is in an active state based on the probability $p_{\rm ac}(\mu)$. If so, an Eddington ratio was drawn from the SW10 Eddington ratio distribution function, which also sets the bolometric luminosity of the AGN. Now specific selection criteria were applied to this sample, with the results presented in Fig. 5.5. It is notable that for a bright luminosity limit most, if not all, AGN lie above the input $M_\bullet - M_{\rm Bulge}$ relation, while they are intrinsically drawn from it. The applied luminosity limit effectively corresponds to a smoothed low black hole mass limit. At the same time also many massive black holes are excluded that accrete only at low rates. For low spheroid masses only positive outliers from the relation can be detected, while for increasing spheroid masses also black holes on the relation and for further increasing spheroid masses even strongly negative outliers can be still detected. This causes the bias at low $M_{\rm Bulge}$.

In a realistic AGN sample there may be additional selection effects that affect the distribution of $M_{\rm Bulge}$. For example, usually a minimum host-to-nucleus ratio is required for the AGN host galaxy to be detected. This will correspond to some sort of cutoff in $M_{\rm Bulge}$, excluding low mass hosts. This additional selection effect will decrease the average bias for the sample, as the excluded objects are the most biased. However, this will only be of importance if objects are actively eliminated during the sample construction based on these considerations. Therefore, it is important to model the selection effects as precisely as possible for a realistic prediction of the average bias of the given sample.

5.3.2. On a black hole mass bias

Shen & Kelly (2010) discussed an additional black hole mass bias that will affect AGN samples with virial mass estimates. This Malmquist type bias should arise due to the steep decrease of the active BHMF and the intrinsic scatter in the virial method. They argue that this is independent of the luminosity bias discussed by Lauer et al. (2007) and thus adds an additional bias to the observations. In our framework we are directly sampling from the active BHMF, thus we are already taking this effect into account. If we introduce an uncertainty in the mass esti-

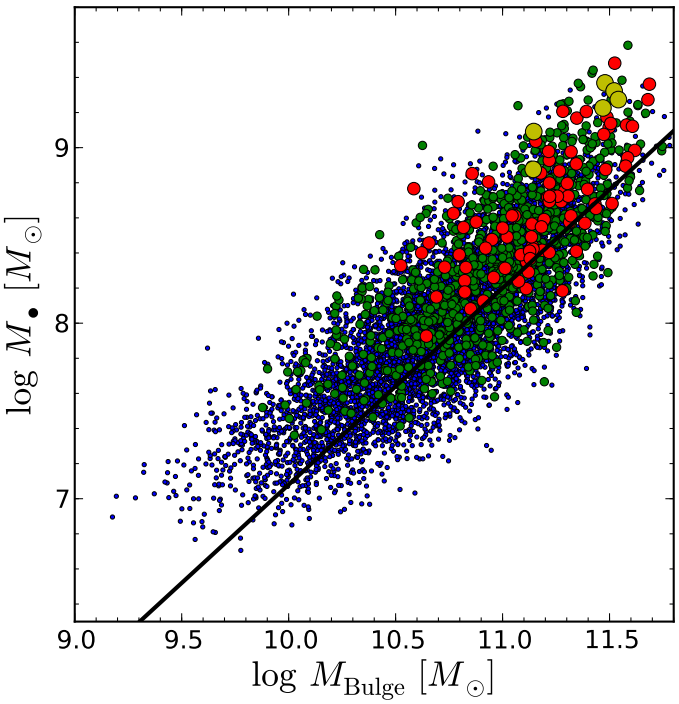

Fig. 5.5. $M_\bullet - M_{\rm Bulge}$ diagram for a Monte Carlo simulation of a local AGN sample. The different sized and coloured symbols correspond to different luminosity limits, applied to the sample. Blue, green, red, and yellow symbols show the sample when culled at a bolometric luminosity of $l_{\rm min} = 45$, 45.5, 46, and 46.5 in logarithmic units. The solid black line shows the input relation for the sample from Häring & Rix (2004).

mates this will only increase the scatter, but it will not affect the mean relation $\langle\mu\rangle(s)$ or $\langle\Delta\mu\rangle$. This can again be illustrated by the Monte Carlo simulations. Adding a virial mass scatter does not affect our sample selection, as it is by construction based on luminosities, which can be measured with relatively high precision. Thus we are just shifting the black hole masses symmetrically to lower or higher values, without affecting the mean.

It is also straightforward to see this from the distribution function $\Psi_{\rm o}(s,\mu)$. We assume that the virial mass estimate (the observed mass $\mu_{\rm o}$) is given by a log-normal probability distribution with mean μ and dispersion $\sigma_{\rm vm}$, the uncertainty in the virial mass estimate,

$$g(\mu_{\rm o}\,|\,\mu) = \frac{1}{\sqrt{2\pi}\sigma_{\rm vm}} \exp\left\{-\frac{(\mu_{\rm o}-\mu)^2}{2\sigma_{\rm vm}^2}\right\} . \tag{5.21}$$

The bivariate distribution function for bulge property and virial black hole mass is then

$$\Psi_{\rm o}(s,\mu_{\rm o}) = \int g(\mu_{\rm o}\,|\,\mu)\,\Psi_{\rm o}(s,\mu)\,{\rm d}\mu\,. \tag{5.22}$$

The mean relation is

$$\langle\mu_{\rm o}\rangle(s) = \frac{\iint \mu_{\rm o}\, g(\mu_{\rm o}\,|\,\mu)\,\Psi_{\rm o}(s,\mu)\,{\rm d}\mu{\rm d}\mu_{\rm o}}{\iint g(\mu_{\rm o}\,|\,\mu)\,\Psi_{\rm o}(s,\mu)\,{\rm d}\mu{\rm d}\mu_{\rm o}} = \frac{\int \mu\,\Psi_{\rm o}(s,\mu)\,{\rm d}\mu}{\int \Psi_{\rm o}(s,\mu)\,{\rm d}\mu}\,, \tag{5.23}$$

when integrating over $\mu_{\rm o}$. This is identical to Equation (5.6), so no additional bias is introduced by the virial mass uncertainty.

The conceptual difference between our results and the work by Shen & Kelly (2010) is, firstly, that we do not treat the black hole mass bias independently, but within the total bias budget. Secondly, we are effectively not sampling directly from the true BHMF, but rather from the luminosity limited BHMF. This suffers from incompleteness at the low mass end, due to the luminosity limit, and therefore turns over towards low $M_\bullet$ (see SW10 for a detailed discussion).

In Fig. 5.6 we show the result for a luminosity limit of $l_{\rm min} = 47$, assuming $\sigma_{\rm vm} = 0.3$ dex. While the black hole mass distribution is broadened, the mean relation is unchanged.

5.3.3. On a spheroid bias

At least, at high redshifts, not only the estimated black hole mass is significantly uncertain, but also the spheroid property. Several times, the emission line width of [O III] has been used as surrogate of σ_*. However, this is at best reliable on average and exhibits a dispersion of probably ~ 0.2 dex (Nelson 2000). Also spheroid masses estimated for AGN host galaxies suffer from several uncertainties, among them are a proper AGN-host decomposition, a decomposition of the galaxies' bulge and disk components, and the conversion of host luminosities into stellar masses, using either a fixed mass-to-light ratio or colour information. These uncertainties accumulate to a total error of at least similar magnitude or more. Therefore, the observationally determined galaxy properties will be similarly uncertain as the black hole mass estimates. In that case, again a Malmquist type bias is possible.

We model the observed spheroid property $s_{\rm o}$ by a log-normal probability distribution with mean s and dispersion σ_s, analog to Equation (5.21). The bivariate distribution function is then

$$\Psi_{\rm o}(s_{\rm o},\mu) = \int g(s_{\rm o}\,|\,s)\,\Psi_{\rm o}(s,\mu)\,{\rm d}s\,, \tag{5.24}$$

and the mean relation is

$$\langle\mu\rangle(s_{\rm o}) = \frac{\iint \mu\, g(s_{\rm o}\,|\,s)\,\Psi_{\rm o}(s,\mu)\,{\rm d}s{\rm d}\mu}{\iint g(s_{\rm o}\,|\,s)\,\Psi_{\rm o}(s,\mu)\,{\rm d}s{\rm d}\mu}\,. \tag{5.25}$$

The total sample bias $\langle\Delta\mu\rangle$ is not affected by the uncertainty, as can easily be verified. However, the predicted $M_\bullet$–bulge relation is affected, as shown in Fig. 5.7. At the low mass end the mean $M_\bullet$ increases compared to the prediction without scatter, while at the high mass end it decreases. To understand this trend we have to recall that we are sampling from the luminosity limited AGN host galaxy spheroid mass function. Due to the luminosity limit the space density decreases at the low mass end, similarly to the BHMF. Because of this steep decrease at the low mass end more objects are scattered from slightly larger masses to lower masses than the other way around. This produces an excess of higher true s at a given observed $s_{\rm o}$. This leads to an increase in the average μ at the given $s_{\rm o}$. At the high mass end the reverse happens. Due to the steep decrease towards higher masses, more black holes are scattered to higher $s_{\rm o}$, having on average a lower μ, as they intrinsically have a lower s than observed. In total, the observed $M_\bullet$–bulge relation flattens, without changing its normalisation. As for AGN the bulge property

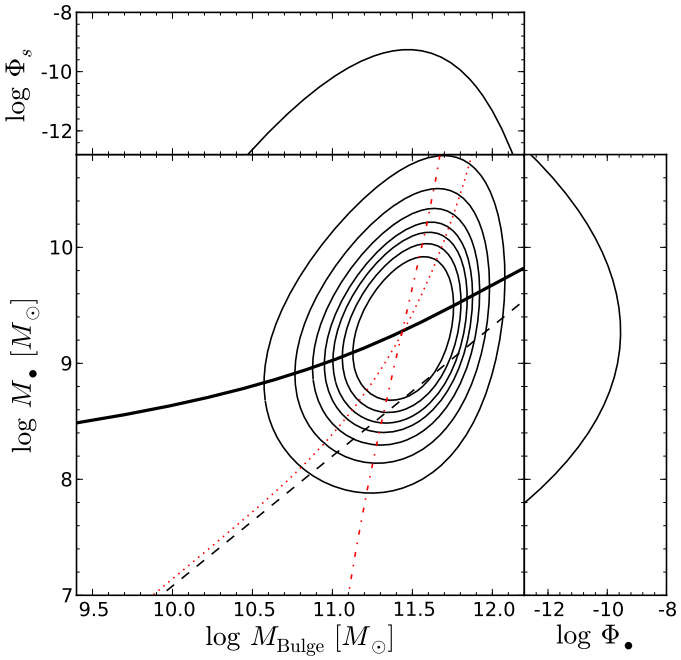

Fig. 5.6. Predicted $M_\bullet - M_{\rm Bulge}$ diagram and its projections for a type 1 AGN sample, with luminosity limit of $l_{\rm min} = 47$ (as the right panel of Fig. 5.3). For the black hole masses an uncertainty of 0.3 dex is assumed, representing the intrinsic uncertainty in the virial method. A thick solid line shows the observed $M_\bullet - M_{\rm Bulge}$ relation for the observed $M_\bullet$, which is identical to the relation without uncertainty in the virial mass. Only the scatter in the relation is increased. The red dashed dotted line shows the mean relation $\langle s \rangle(\mu_{\rm o})$, while the dotted red line gives the mean relation $\langle s \rangle(\mu)$, i.e. without measurement uncertainty in the black hole mass.

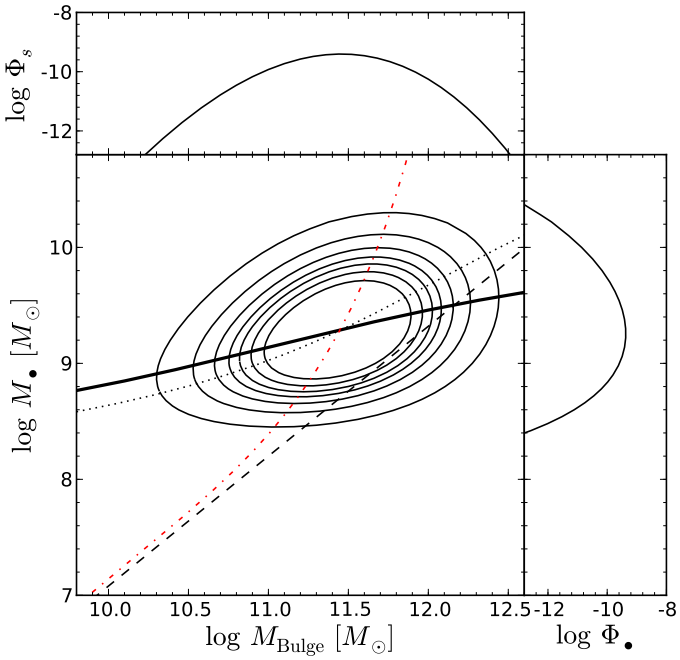

Fig. 5.7. Same as Fig. 5.6, but with measurement uncertainty of 0.2 dex in the spheroid mass and no uncertainty in the black hole mass. The thick solid line shows the $M_\bullet - M_{\rm Bulge}$ relation for the observed $M_{\rm Bulge}$ and the dotted is the $M_\bullet - M_{\rm Bulge}$ relation for the true $M_{\rm Bulge}$, i.e. if there where no measurement uncertainty. The sample bias is not affected, but the slope of the $M_\bullet - M_{\rm Bulge}$ relation flattens due to uncertainties in $M_{\rm Bulge}$. The red dashed dotted line shows the mean relation $\langle s_{\rm o} \rangle(\mu)$, which is not affected by uncertainties in $M_{\rm Bulge}$.

is usually determined with larger uncertainty than for quiescent galaxies, this effect could contribute to the flatter slope observed several times in the $M_\bullet$–bulge relation of AGN (Greene & Ho 2006; Kim et al. 2008; Bentz et al. 2009b; Woo et al. 2010).

For the mean spheroid mass at a given black hole mass the opposite effect happens. Uncertainties in the spheroid masses does not change the mean relation $\langle s_{\rm o} \rangle(\mu)$, but uncertainties in the black hole masses can strongly affect the mean relation $\langle s \rangle(\mu_{\rm o})$, causing a steepening of the observed relation. This is indicated by the red lines in Figures 5.6 and 5.7.

Finally, we note that in general the convolution with the uncertainty has to be with $\Psi(s, \mu)$ rather than with $\Psi_{\rm o}(s, \mu)$, i.e. before applying the selection criteria. In our case of a purely luminosity limited sample, the selection function does not depend on $s_{\rm o}$ or $\mu_{\rm o}$. Therefore, our approach is justified and no additional bias is introduced for the sample in total. In case of a more complicated selection function that depends on $s_{\rm o}$ or $\mu_{\rm o}$ this might no longer be the case. An additional bias by the measurement uncertainty then becomes possible which will depend on the details of the selection function.

5.3.4. Flux limited samples

So far, we have discussed purely luminosity limited samples. This approximation is valid for samples spanning small ranges in redshift. More generally, we have to consider flux limited samples. There may be additional luminosity limits present, because the AGN need to be identified as such, requiring them not to be outshined by their host galaxies. We first define the multivariate distribution function $\Psi_{\rm o}(s, \mu, l, z)$, as

$$\Psi_{\rm o}(s, \mu, l, z) = \Omega(l, z)\, p_{\rm ac}(\mu, z)\, p_\lambda(l - \mu, z)\, g(\mu \mid s, z)\, \Phi_s(s, z) \frac{{\rm d}V}{{\rm d}z}\,. \tag{5.26}$$

The bivariate distribution function for a flux limited sample is then

$$\Psi_{\rm o}(s, \mu) = \frac{1}{\Delta V_c} \iint \Psi_{\rm o}(s, \mu, l, z)\, {\rm d}z{\rm d}l \tag{5.27}$$

where ΔV_c is the comoving volume within the redshift range.

At this place, we ignore possible redshift dependencies of the individual distribution functions and postpone their discussion to section 5.4.2. We further assume that the selection function is purely defined by an AGN luminosity limit and an AGN flux limit, i.e. we neglect any dependence of the selection function on the bulge property s. The selection function Ω is then defined as

$$\Omega(l, z) = \begin{cases} 1 & \text{for} \quad l \geq l_{\rm min} \;\&\; f \geq f_{\rm min} \\ 0 & \text{else} \end{cases}\,, \tag{5.28}$$

where f is the bolometric flux $f = l - \log(4\pi d_l^2)$ in logarithmic units.

At high redshift and for a narrow z range, this is almost identical to the luminosity limited case. However, it is the more general case for realistic observations, also able to describe a wider z range and the low z regime. Its application to low z AGN samples is illustrated in the next subsection. Its consequences at higher z are discussed in section 5.4.

5.3.5. Application to the reverberation mapping AGN sample

As demonstrated above, even the low z population will be affected by selection effects. The main difference compared to high z is that the AGN in the local universe are so close that the luminosity limit is low and therefore the bias is less severe. Nevertheless, it is present, and as a test case we will briefly estimate its influence on the AGN sample with black hole masses determined via reverberation mapping.

The technique of reverberation mapping (e.g. Blandford & McKee 1982; Peterson 1993) provides the most precise black hole mass estimates for type 1 AGN. It builds the foundation for the virial method through the establishment of a scaling relationship between the size of the broad line region and the continuum luminosity (Kaspi et al. 2000, 2005; Bentz et al. 2009a). However, currently this method only provides a measurement of $M_\bullet$ that is uncertain up to a scale factor depending on the (largely unknown) geometry and dynamics of the broad line region. The usual approach to determine this scale factor and thus fix the virial mass scale is to scale the reverberation mapped black hole masses of galaxies with stellar velocity dispersion measurements to the local $M_\bullet - \sigma_*$ relation of quiescent galaxies (Onken et al. 2004; Woo et al. 2010). However, this implicitly assumes that the reverberation mapping (RM) sample follows the same relation as quiescent galaxies. If its $M_\bullet - \sigma_*$ relation is biased by selection effects than this bias will propagate into the absolute calibration of the virial mass estimates.

Properly defining the selection function for the RM sample is difficult, due to the inhomogeneous selection of the objects. Thus, it does not represent a well defined sample. Nevertheless, to estimate potential systematics that may be inherent in the sample, we assume a first order approximation to the selection function. The sample covers a wide range in luminosity, from bright quasars to moderate-luminosity Seyfert galaxies. Especially for the Seyfert galaxies there is no clear AGN luminosity dependence for the selection. However, there must be an implicit limit on the AGN luminosity and also on the AGN flux. First of all, the AGN has to be luminous enough to classify the galaxy as harbouring an active nucleus. Furthermore, the continuum and broad lines have to be sufficiently bright to enable the measurement of a reliable time lag. For simplicity, we relate the low luminosity limit to the faintest AGN in the sample of Bentz et al. (2009a), NGC 4051, with $\log \lambda L_{\lambda,\mathrm{AGN}}(5100\,\text{Å}) = 41.9$. This approximately corresponds to $\log L_{\mathrm{bol}} = 42.8$, We adopt a redshift range of $0.003 \le z \le 0.15$, which contains the majority of the RM AGN. We also tested the effect of extending the range to $z \le 0.3$, including the full RM sample, and provide the results as well.

If we only assume a luminosity limit, the total sample bias $\langle \Delta\mu \rangle$ predicted by our model would be negligible (see Fig 5.4). Indeed, when omitting the flux limit we find $\langle \Delta\mu \rangle = 0.003$, as a lower limit to the bias. However, the luminosity limit is only important for $z \lesssim 0.008$. At higher z the flux limit dominates the selection function. Incorporating the flux limit, we get $\langle \Delta\mu \rangle = 0.09$ for $z \le 0.15$ ($\langle \Delta\mu \rangle = 0.12$ for $z \le 0.3$). If we relax our conservative flux limit, the expected sample bias would decrease slightly. Decreasing our assumed luminosity limit has almost no effect, as we are dominated by the flux limit. Increasing the luminosity limit will slightly increase the bias.

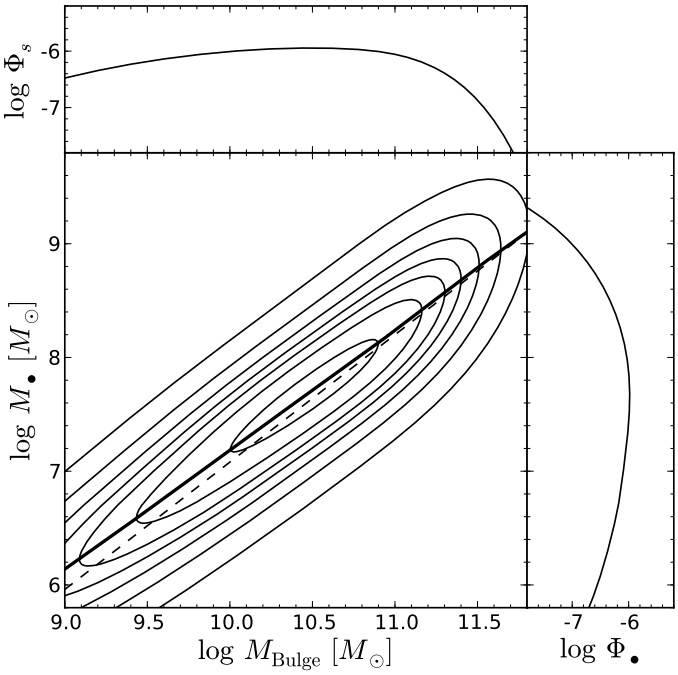

Fig. 5.8. Predicted $M_\bullet - M_{\mathrm{Bulge}}$ diagram and its projections for a local type 1 AGN sample, simulating the reverberation mapping sample. A flux limit in the redshift interval $(0.003, 0.15)$ and a luminosity limit are applied to the sample, based on the observed range for the reverberation mapping AGN. In this sample a mild bias of 0.09 dex is present.

In Fig. 5.8, we show the predicted $M_\bullet - M_{\mathrm{Bulge}}$ diagram. At the high mass end no bias is expected, whereas a mild bias at low masses is present. Thus, the $M_\bullet - M_{\mathrm{Bulge}}$ relation is slightly affected.

We further tested this result with Monte Carlo simulations. We restricted our Monte Carlo sample to the same luminosity limit and flux limit and fitted the culled sample with a maximum likelihood method (see e.g. Gültekin et al. 2009), with slope b, normalisation a and intrinsic scatter σ as free parameters. From the restricted sample, we fitted 1000 random subsamples of 100 objects each. The distribution of the free parameters are shown in Fig. 5.9. We found mean values of $a = 8.31$, $b = 1.12$ and $\sigma = 0.29$, compared to input values of $a = 8.2$, $b = 1.12$ and $\sigma = 0.3$, i.e we recover the predicted mean offset and confirm that the slope and scatter are not strongly affected.

Therefore, based on our model assumptions, we estimate that the reverberation mapping sample may be biased towards a high $M_\bullet / M_{\mathrm{Bulge}}$ ratio by ~ 0.1 dex. This would correspond to an underestimation of the virial method by the same amount, when using the scale factor normalised to the quiescent $M_\bullet -$

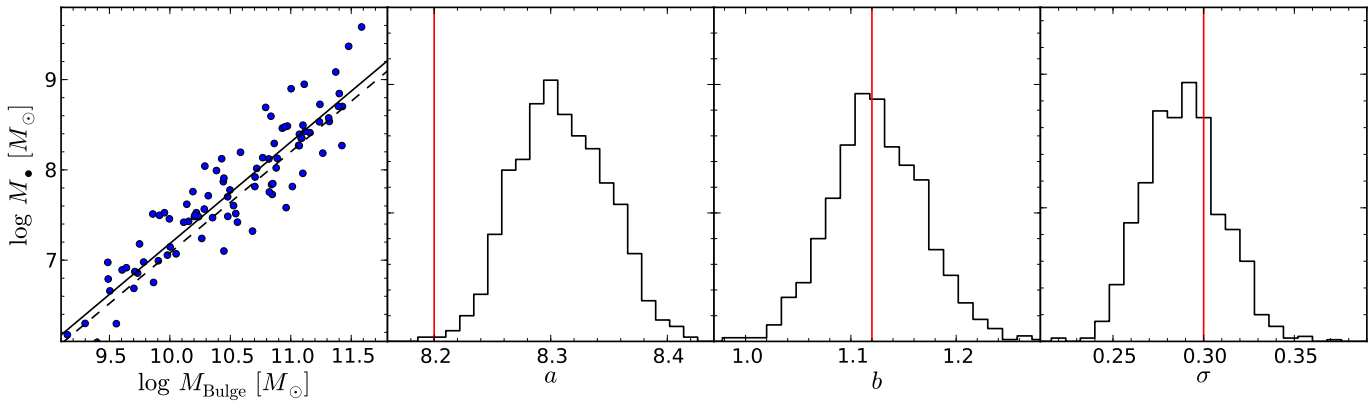

Fig. 5.9. Results of Monte Carlo simulations of the reverberation mapping AGN sample. Panels from left to right: (1) $M_\bullet - M_{\rm Bulge}$ relation for a Monte Carlo realisation of 100 objects. The dashed line shows the input relation, the solid line the mean best fit for 1000 realisations. (2) Distribution of recovered zero points of the $M_\bullet - M_{\rm Bulge}$ relation. The horizontal line shows the input. (3) same for the slope of the relation. (4) same for the intrinsic scatter in the relation. There is an offset in the zero point of ~ 0.1 dex. The slope and intrinsic scatter are not strongly affected.

σ_* relation (Onken et al. 2004; Woo et al. 2010). However, due to the poorly defined selection function of the RM sample this can only be taken as a qualitative evaluation of possible selection effects.

5.4. Evolution in the $M_\bullet - M_{\rm Bulge}$ relation

5.4.1. Evolution in a flux limited sample

How will selection effects bias studies that test for redshift evolution in the black hole-bulge relations? If at higher z exactly the same sample selection criteria are applied as for a local comparison sample, no bias will be present, at least to first order (see section 5.4.2). A change in the $M_\bullet$–bulge relations could then be seen as evidence for their evolution. However, usually this simple situation is not the case. The local comparison is commonly provided either directly by the quiescent relation, or by a local type 1 AGN comparison sample. While the former clearly possesses different selection criteria, also the latter is not automatically selected in the same manner. This has to be considered when comparing low and high redshift results.

To illustrate this case we derive the sample bias for a flux limited sample at a given redshift. The sample bias at a given redshift z is

$$\langle \Delta\mu \rangle (z) = \frac{\iiint (\mu - a - bs)\, \Psi_{\rm o}(s, \mu, l, z)\, {\rm d}l\, {\rm d}\mu\, {\rm d}s}{\iiint \Psi_{\rm o}(s, \mu, l, z)\, {\rm d}l\, {\rm d}\mu\, {\rm d}s} \,, \qquad (5.29)$$

with the multivariate distribution function $\Psi_{\rm o}(s, \mu, l, z)$ given by Equation (5.26). This is equivalent to the bias for a luminosity limited sample, with a redshift dependent luminosity limit.

Instead of using a bolometric flux limit as before, we now assume an optical flux limit in the B band. For simplicity, we assume a simple power law K-correction with spectral index $\alpha = -0.44$ (Vanden Berk et al. 2001). The B band luminosity is converted to bolometric luminosity using the bolometric corrections of Marconi et al. (2004). In Fig. 5.10 we provide the expected sample bias at a given z for different apparent magnitude limits. The deeper the respective survey, the lower is the expected bias. For a fixed flux limit, the expected bias increases

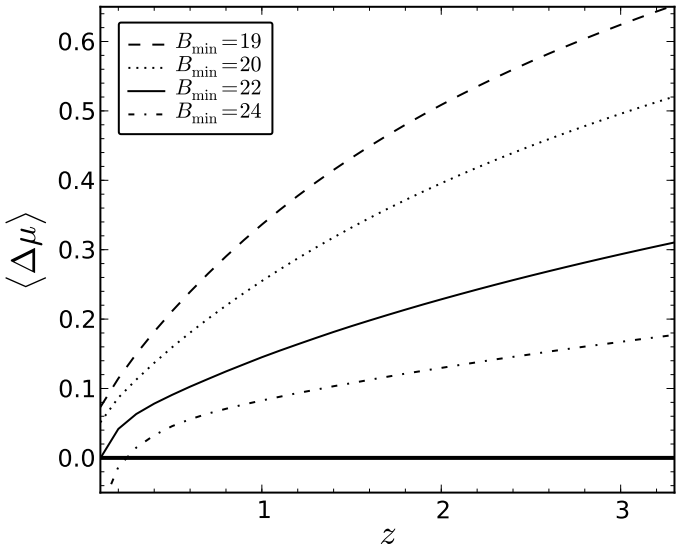

Fig. 5.10. Redshift evolution of the selection bias for a magnitude limited AGN sample, assuming the local distribution functions. The dashed, dotted, solid, and dashed dotted lines show B band magnitude limits of 19, 20, 22, and 24 mag, respectively.

with redshift, which can mimic an evolutionary trend if taken for granted.

Furthermore, to have a comparable bias between a local sample with $B_{\rm min} \approx 19$ mag and a sample at $z \approx 2$, the high redshift sample has to be complete for $B_{\rm min} \approx 24$ mag. The use of a local AGN sample as comparison sample for higher z studies is already an improvement over the use of the quiescent black hole sample, but it does not ensure the absence of a selection bias. Ideally, the local comparison sample should be matched in AGN luminosity to the high z sample.

On the other hand, if the selection function of the respective sample at high z is known, the predicted bias can be computed and a clear offset from this prediction can be interpreted as evidence for evolution in the $M_\bullet$–bulge relations. However, unfortunately even this approach is not fully unbiased.

5.4.2. AGN evolution biases

So far, we have ignored any possible explicit redshift dependence of the underlying distribution functions in Equation (5.26). However, at least some of them must evolve with redshift. The stellar mass function, and thus also the spheroid mass function, are certainly evolving with z (e.g. Bundy et al. 2005; Franceschini et al. 2006; Pozzetti et al. 2007; Ilbert et al. 2010). Furthermore, it is well known that the AGN population itself is strongly changing between $z = 0$ and $z \approx 2$, apparent in the evolution of the AGN luminosity function (e.g. Ueda et al. 2003; Hasinger et al. 2005; Richards et al. 2006; Bongiorno et al. 2007; Croom et al. 2009). Not only the normalisation and typical luminosity changes with z but also the shape of the luminosity function. At low z the faint end of the QSO luminosity function steepens, known as "AGN cosmic downsizing". While in the local universe the QSO luminosity function shows only a mild break (Schulze et al. 2009), at high z a prominent break is present in the luminosity function. This directly implies evolution in the active black hole mass function, the Eddington ratio distribution function, or most probably in both. This will lead to a change of the predicted bias with redshift, even for a fixed luminosity limit. It is not straightforward to judge if an observed evolution in the $M_\bullet$-bulge relations may be caused by evolution in the intrinsic relations, or whether it is a result of evolution in the distribution functions.

A prediction of the sample bias at given redshift requires, apart from a well defined selection function, also knowledge about these underlying distribution functions, the spheroid mass function, active BHMF and ERDF. At low redshift they are at least reasonably well established (SW10), but for the high redshift universe currently the situation is not so good. The velocity dispersion function is essentially unknown beyond the local universe (Sheth et al. 2003). The total stellar mass function is observed up to $z \approx 4$ (Fontana et al. 2006), but galaxy mass functions for different morphological types have been determined only up to $z \approx 1.4$ (Bundy et al. 2005; Franceschini et al. 2006; Ilbert et al. 2010). The spheroid mass function itself is unknown for higher z. To enable the illustration of how evolution influences the biases, we derive rough estimates of these distribution functions. A more detailed investigation is beyond the scope of the current paper.

An upper limit on the spheroid mass function is given by the total stellar mass function. We use the parametric fit to the stellar mass function from Fontana et al. (2006) for this purpose. A lower limit is given by the elliptical galaxy mass function. To derive this mass function at arbitrary z we assume the same elliptical-to-total ratio as for the local mass function from Bell et al. (2003), and apply this correction to the total mass function at higher redshift. This is clearly an oversimplification, as the relative contribution of elliptical galaxies seems to decrease with increasing z, at least to $z \sim 1$ (e.g. Bundy et al. 2005). However, at higher redshifts the low mass end that is most affected by this correction is not well determined and may be underestimated, due to the distribution of galaxy mass-to-light ratios. Thus, we assume that our simple approximation serves as a reasonable lower limit of the spheroid mass function for the purpose of this work. As our reference spheroid mass function we use the local spheroid-to-total ratio, derived above from the Bell et al. (2003) local mass function.

There has been significant progress in the determination of the active BHMF and Eddington ratio distribution function at high redshifts in the last years (Vestergaard et al. 2008; Vestergaard & Osmer 2009; Kelly et al. 2010). But these results mainly cover the bright end of the luminosity function and thus the high mass end of the BHMF, while the low mass end is still poorly determined; also the systematics are not fully understood. Here we restrict ourselves to the use of a mass function that is consistent with current observations.

We use the local active BHMF and ERDF as well as the redshift evolution of the type 1 AGN luminosity function (LF) as constraints to predict the distribution functions at higher redshift. To achieve a smooth redshift evolution of the BHMF and ERDF we explored several arbitrary, but reasonable evolution models for these distribution functions. We fixed the zero point of the two distribution functions to their local values (SW10), and fit their redshift evolution to the optical LF (employing Equation 5.12). For the LF we use the luminosity dependent density evolution model from Bongiorno et al. (2007), utilising the SDSS at the bright end and the VVDS at the faint end. Optical B band magnitudes are converted to bolometric luminosity using the bolometric corrections from Marconi et al. (2004). We also directly fitted the BHMF and ERDF in individual redshift bins. This approach does not change our qualitative conclusions, but introduces artifacts into the redshift evolution.

Purely based on the LF, there is a degeneracy between evolution in the BHMF and evolution in the ERDF, while probably both are present. Therefore, we explore two extreme cases. First, we assume a constant ERDF and let the BHMF change with z. Second, we fix the active BHMF and let the ERDF evolve with z.

The first case, a non-evolving ERDF, serves as an upper limit to the expected AGN evolution bias. The downsizing of the AGN LF directly corresponds to a downsizing in the active BHMF. In Fig. 5.11 we show the best fit BHMF, ERDF, and the respective AGN LF, for a few representative redshifts. Here, we assume a mass dependent density evolution model, following the LDDE model used by Bongiorno et al. (2007) to parameterise the evolution in the AGN LF. To reproduce the observed AGN LF, the space density at the high-mass end has to increase. Thus, the mass dependence of the active fraction is flattened, changing the active fraction bias. This leads to an increase of the expected sample bias compared to the local case. This is illustrated in Fig. 5.12, where we show the expected sample bias $\langle \Delta\mu \rangle$ as a function of the applied lower luminosity limit for various redshifts.

The second case, a fixed BHMF and evolving ERDF, provides a lower limit to the expected AGN evolution bias. In this case, the active fraction is only mildly evolving with z, through the evolution of the spheroid mass function. Furthermore, the ERDF needs to evolve strongly, with an increasing average $\log \lambda$, to satisfy the constraints from the evolving AGN LF. For a higher average $\log \lambda$ the same luminosity limit corresponds to a lower average black hole mass limit, thus reducing the expected bias. Therefore, this assumption will predict the lowest sample bias. However, the best fit model enforces an

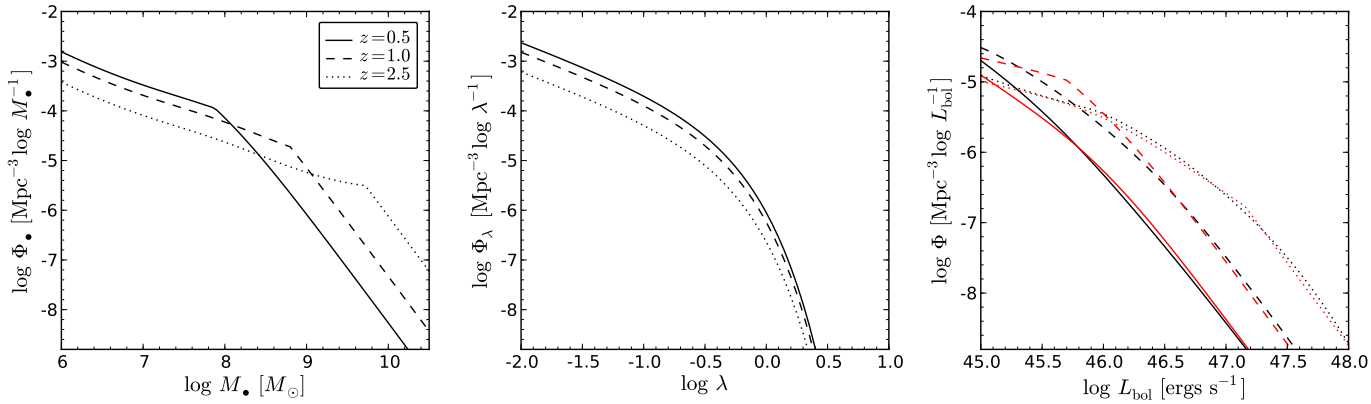

Fig. 5.11. Reconstructed AGN distribution functions at three representative redshift derived from fitting the observed AGN luminosity function to a redshift evolution model for the BHMF and ERDF. For the BHMF a mass dependent density evolution model is used, and no evolution in the ERDF is assumed. Left panel: Best fit active black hole mass function. Middle panel: Eddington ratio distribution function. The shape has been fixed, the normalisation is determined by the space density of the black hole mass function. Left panel: AGN luminosity function. The red lines show the type 1 AGN luminosity functions from Bongiorno et al. (2007), the black lines are our best fit to them.

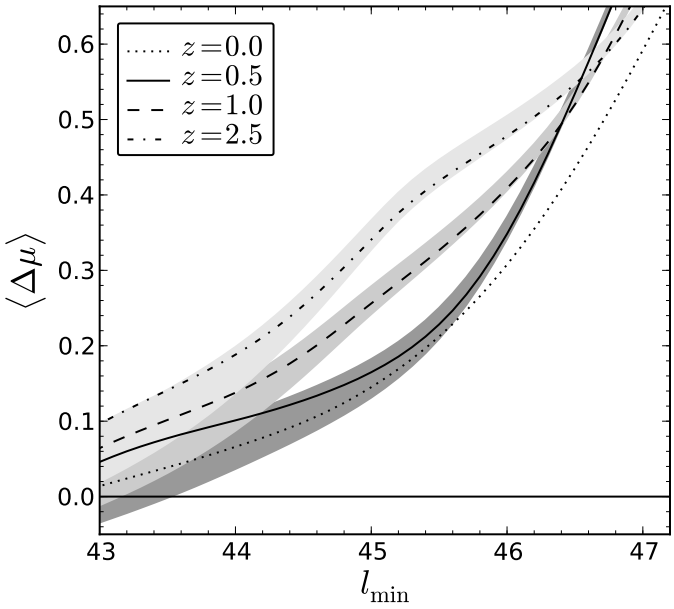

Fig. 5.12. Expected sample bias as a function of the lower luminosity limit for the same representative redshifts as in Fig. 5.11. The dotted line shows the local prediction, the other lines show predictions at higher z. The shaded area incorporates the uncertainty on the spheroid mass function, by using the total mass function as upper limit and an estimate of the elliptical mass function as lower limit.

unreasonably high space density of objects accreting at super Eddington rates and also provides a poorer fit to the AGN LF. Furthermore, it disagrees with the picture of anti-hierarchical black hole growth (Marconi et al. 2004; Merloni 2004; Merloni & Heinz 2008). Thus, this case is not physically plausible. We also experimented with intermediate evolution scenarios, where a mild evolution of the ERDF balances the increasing bias through the evolution of the BHMF to some degree. For all physically plausible scenarios, we found at least some increase of the bias compared to the local case. Thus we argue that the expected sample bias for the local universe is a lower limit for high z samples.

In Fig. 5.13 we show the expected bias at a fixed magnitude limit as a function of redshift, equivalent to Fig. 5.10, but now assuming an evolving active BHMF and a constant ERDF (our case 1 above). As discussed, the resulting bias can be seen as an upper limit. Only observations that show a clear excess on top of this prediction constitute evidence for real evolution in the $M_\bullet$−bulge relations. However, due to the limitations of our model these results should only be taken as a qualitative estimate.

While the evolution is usually thought of as evolution in the normalisation of the relation, also evolution in the intrinsic scatter is possible (Merloni et al. 2010). The strength of the sample bias is strongly affected by the size of the intrinsic scatter in the $M_\bullet$−bulge relations. Therefore, an offset of the $M_\bullet/M_{\rm bulge}$ ratio on top of the expected selection bias can equally be interpreted as being caused by an increased bias due to an increased intrinsic scatter, rather than as a true offset in the zero point of the respective $M_\bullet$−bulge relation. To illustrate this effect, we assume an arbitrary redshift evolution model for the intrinsic scatter $\sigma(z) = \sigma_{z=0}(1+z)^{0.5}$ with $\sigma_{z=0} = 0.3$, which gives approximately $\sigma(z=2) \approx 0.5$. In Fig. 5.14 we show the resulting redshift evolution of the bias for fixed magnitude limits. The predicted scatter is strongly enhanced in this case, especially at high redshift.

An increase in the intrinsic scatter is also some kind of evolution in the relations. However, its interpretation is of course different from a change in the zero point. Whereas the latter would suggest a phase where black holes grow stronger than galaxies, or the other way around, the former would be consistent with a true coeval growth on average, in which the correlation is tightened from a rather loose one to the tight correlation we observe today. Indeed, such an evolution in scatter towards a tight relation is expected in various models (e.g. Peng 2007; Volonteri & Natarajan 2009; Lamastra et al. 2010).

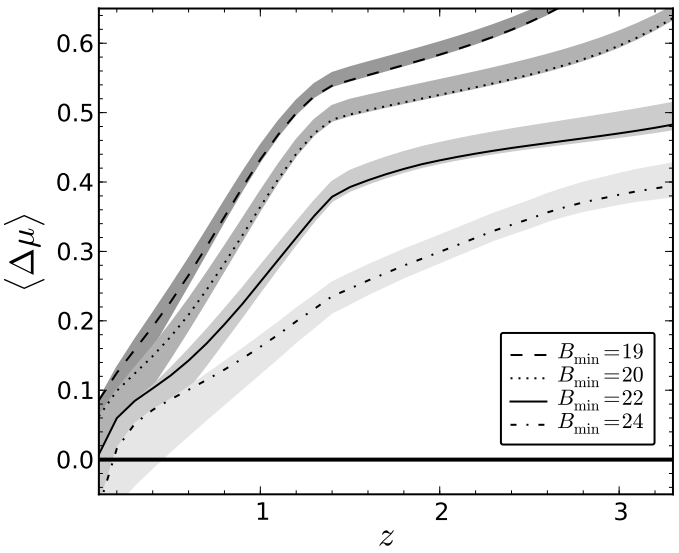

Fig. 5.13. Redshift evolution of the selection bias for a magnitude limited AGN sample, assuming our estimate of the z evolution of the underlying distribution functions, as discussed in the text. The shaded regions incorporate the uncertainty on the spheroid mass function.

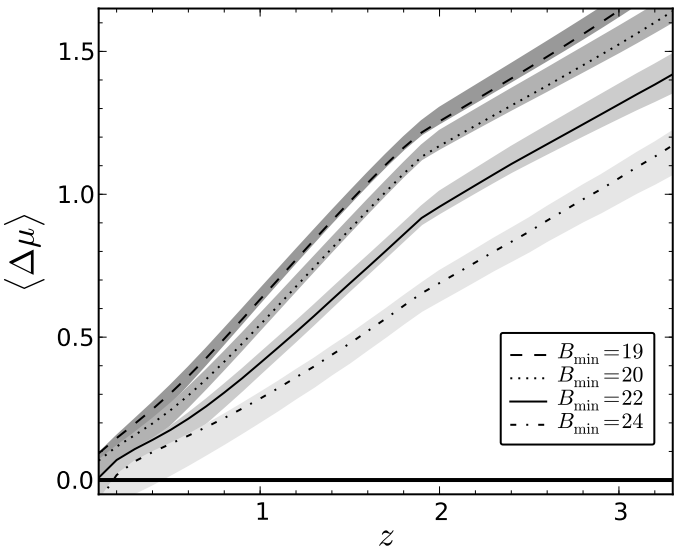

Fig. 5.14. Same as Fig. 5.13, but assuming an evolution of the intrinsic scatter in the $M_\bullet - M_{\rm Bulge}$ relation of $\sigma(z) = 0.3(1+z)^{0.5}$.

5.5. Discussion

Several observational studies on type 1 AGN samples found tentative evidence for an increase in the $M_\bullet/M_{\rm Bulge}$ ratio with redshift. This increase is often parametrised as an evolutionary behaviour $M_\bullet/M_{\rm Bulge} \propto (1+z)^\gamma$, with values for γ up to 2.1 reported (McLure et al. 2006). As discussed in this paper, these observational studies are invariably affected by selection effects. We now apply our formalism to a few published studies. We estimate approximate distribution functions and the resulting sample biases. We do not aim at deriving detailed corrections, or presenting a full discussion of the literature, but we want to highlight the magnitude of possible systematic biases.

Specifically, we explore two scenarios for the distribution functions that serve as upper and lower limits for the magnitude of our predicted selection bias.

- *Model 1:* We use the local distribution functions presented in section 5.3.1 throughout the entire redshift range, i.e. ignoring any effect of redshift evolution. As discussed above, even if this scenario is unrealistic, it serves as a lower limit to the expected bias.
- *Model 2:* Here, we incorporate redshift evolution in the underlying distribution functions, in particular in the AGN population. We use the model discussed in section 5.4.2, assuming a mass dependent density evolution for the BHMF and a non-evolving ERDF. This model provides an approximate upper limit to the selection bias.

5.5.1. Merloni et al. (2010)

A relatively large, well-defined sample has been employed by Merloni et al. (2010). They used an I band limited sample drawn from zCOSMOS (Lilly et al. 2007) in the redshift range $z = [1.06, 2.19]$, with $I_{\rm AB} < 22.5$. We modelled their sample selection using these restrictions and explore our two models for the distribution functions. The results are shown in Fig. 5.15, together with the data from Merloni et al. (2010). While for the observations the offset from the local relation is $\langle \Delta\mu \rangle_{\rm obs} = 0.34$, we found values for the sample bias of $\langle \Delta\mu \rangle_{\rm M1} = 0.17$ and $\langle \Delta\mu \rangle_{\rm M2} = 0.36$, for our model 1 and 2, respectively. As dashed-dotted line in the right panel of Fig. 5.15 we additionally indicate our sample offset prediction for an evolution of the form $(1+z)$, i.e $\gamma = 1$, for our model 1, serving as lower limit to the bias. A stronger evolution is barely consistent with the observations. When only considering the mean sample offset from the local relation, the data are fully consistent with the null hypothesis of no evolution.

Alternatively, the mean stellar mass at given black hole mass can be inspected for this sample, as this quantity is to first order unaffected by the AGN selection bias. We show the predicted relation as red dashed-dotted line in Fig. 5.15. As a rough approximation of the observed mean relation $\langle s \rangle(\mu)$ we bin the data in black hole mass and show the mean stellar mass in the middle panel of Fig. 5.15 as open red triangles. While the binned relation is consistent with the prediction at the low mass end, it deviates at the high mass end, being suggestive of evolution. This evolution can be interpreted in two ways. Firstly, the normalisation at the high mass end may increase with redshift, with $\gamma \approx 1$, while the low mass end may evolve weaker, as suggested by some semianalytic models (Lamastra et al. 2010). Secondly, the intrinsic scatter in the relations may increase, with $\sigma \approx 0.5$ at $z > 1$. Also a mixture of both scenarios is possible. Our results are qualitatively consistent with the conclusions from Merloni et al. (2010).

5.5.2. Jahnke et al. (2009)

Jahnke et al. (2009) studied the $M_\bullet - M_*$ relation for a sample of 10 AGN from COSMOS (Hasinger et al. 2007). Their

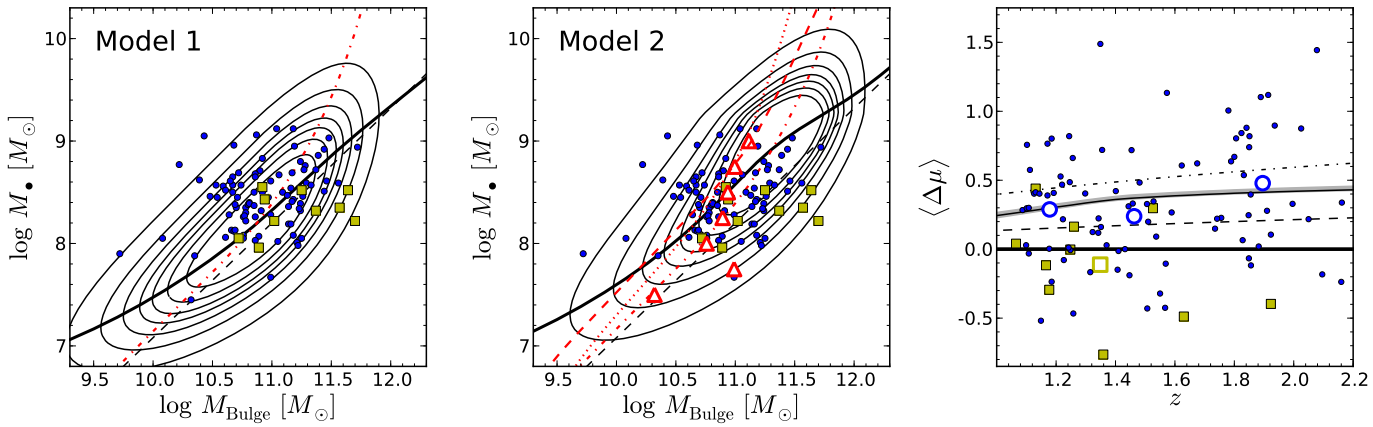

Fig. 5.15. Left panel: Predicted $M_\bullet - M_{\rm Bulge}$ probability distribution for the sample of Merloni et al. (2010), using our model 1 (local distribution functions). The black dashed line shows $\langle\mu\rangle(s)$, the red dashed-dotted line shows $\langle s\rangle(\mu)$. The blue symbols show the data from Merloni et al. (2010), the yellow squares are for the sample of Jahnke et al. (2009). Middle panel: same, but for model 2 (evolving distribution functions). Additionally, the red open triangles give the mean stellar mass for the data from Merloni et al. (2010) binned in black hole mass. We also indicate $\langle s\rangle(\mu)$ for evolution in the normalisation, with $\gamma = 1$ (red dashed line), and for evolution in the intrinsic scatter, with $\sigma = 0.5$ (red dotted line). Right panel: redshift evolution of the sample bias. The blue circles show the data from Merloni et al. (2010), the large, open circles show the mean offset in three redshift bins. The yellow squares give the data from Jahnke et al. (2009), the large, open square is their mean. The dashed line shows our prediction for model 1, the solid line with the shaded area shows our prediction for model 2, including the uncertainties on the spheroid mass function. The dashed-dotted line is for model 1, but assuming evolution in the $M_\bullet - M_{\rm Bulge}$ relation $M_\bullet/M_{\rm Bulge} \propto (1+z)$. This serves as an upper limit to the evolution in the relation.

sample is X-ray selected, but the spectroscopic follow-up requirement leads to a similar optical flux limit as for the work by Merloni et al. (2010) (see Trump et al. 2009). As the covered redshift range is very similar as well, we simply add the results from Jahnke et al. (2009) to Fig. 5.15. As already discussed in Jahnke et al. (2009), their data are fully consistent with the local relation. Accounting for selection effects, would rather imply a negative evolution. It is interesting to note that also the small, X-ray selected sample by Sarria et al. (2010), covering a similar redshift range finds no, or even a negative evolution. However, notice that both studies (and also Merloni et al. 2010) target the black hole - *total* galaxy mass relation instead of the black hole - *bulge* mass relation.

5.5.3. Salviander et al. (2007)

Next, we investigate the study by Salviander et al. (2007). They studied the $M_\bullet - \sigma_*$ relation in the redshift range $0 < z < 1.2$, using the [O III] line width as surrogate of σ_* for $z < 0.8$, and the [O II] line width for $0.4 < z < 1.2$. Their sample is drawn from the Sloan Digital Sky Survey Data Release 3 (SDSS DR3; Abazajian et al. 2005), which does not constitute a well-defined sample (see e.g. Richards et al. 2006). Furthermore, they excluded a large fraction of objects based on quality cuts. To model their sample, we assumed the flux limit of the SDSS main quasar sample, $i < 19.1$ (Richards et al. 2002). In Fig 5.16 we show our predicted redshift evolution for the sample bias, adopting this flux limit and again exploring our two models, and compare them to the observations. For $z < 0.7$, their results are broadly consistent with no evolution, given the current uncertainties. At $z > 0.7$, an evolutionary trend is indicated, consistent with $\gamma \lesssim 1$.

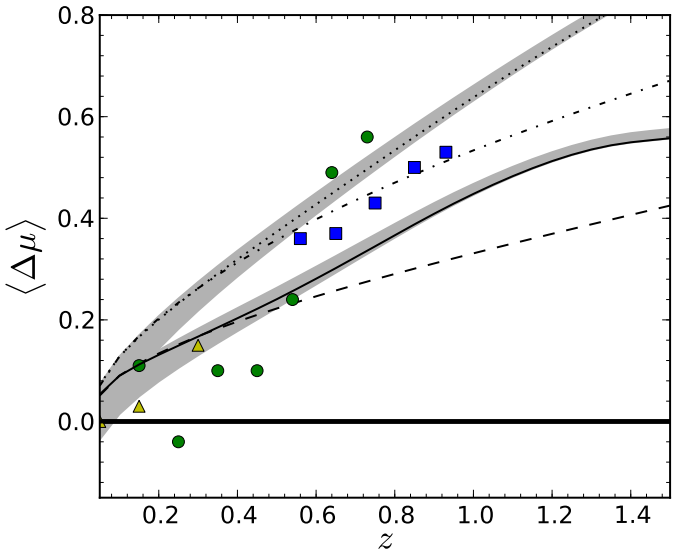

Fig. 5.16. Predicted redshift evolution of the sample bias for the SDSS. The dashed and solid lines shows our model 1 and model 2, respectively, assuming no intrinsic evolution in the $M_\bullet - \sigma_*$ relation. The dashed-dotted and dotted lines give the predicted sample offsets for an evolution with $\gamma = 1$ for model 1 and model 2, respectively. The green circles show the observational results from Salviander et al. (2007), using the [O III] line width as surrogate of σ_*, the blue squares show their results using [O II], and the yellow triangles show the results from Shen et al. (2008).

Salviander et al. (2007) already extensively discussed the influence of selection effects on their results, attributing ~

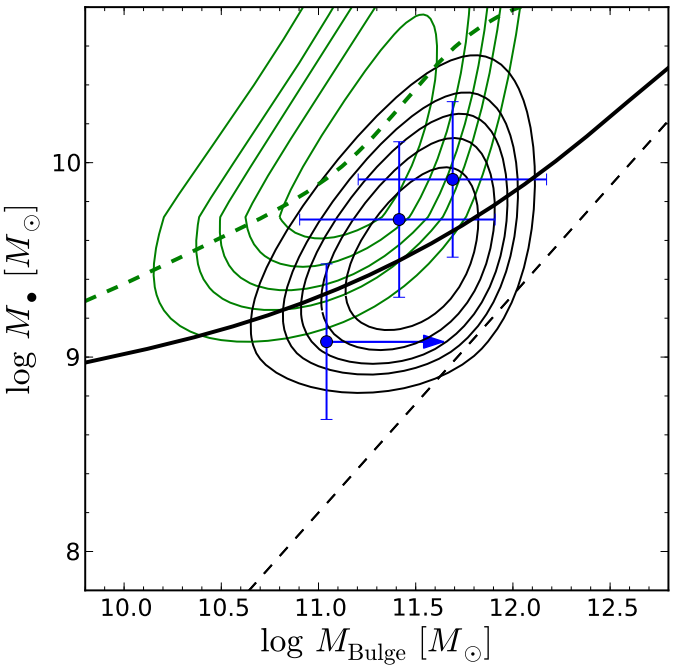

Fig. 5.17. Predicted $M_\bullet - M_{\rm Bulge}$ probability distribution for the sample of Schramm et al. (2008), using our model 2. The blue symbols show the data from Schramm et al. (2008). The black contours show the case of no evolution in the $M_\bullet - M_{\rm Bulge}$ relation, and the green contours show our prediction for evolution of the form $(1+z)^2$.

0.25 dex of their offset to selection effects. They also discussed an additional bias, caused by their signal-to-noise requirement for the narrow lines, which may accumulate to ~ 0.15 dex at high z. This bias may at least contribute to the offset in $\langle\Delta\mu\rangle$ in the data compared to our no-evolution predictions. Therefore, the null hypothesis of no evolution is not clearly rejected.

5.5.4. High redshift, bright QSO samples

The largest offset from the local $M_\bullet$−bulge relations observed so far are for high redshift samples, $z \gtrsim 3$. However, these samples suffer from a bright luminosity limit and therefore are strongly affected by selection effects. We illustrate this effect on the small sample by Schramm et al. (2008). They used a sample of three luminous quasars in the range $z = [2.6, 3.0]$, drawn from the Hamburg/ESO Survey (Wisotzki et al. 2000), with a magnitude limit of $B_j \lesssim 18$ mag. We modelled the sample, employing these restrictions and our model 2. In Fig. 5.17 we show our prediction, together with the sample from Schramm et al. (2008). The vast majority of objects is predicted above the local relation, although the local relation is still assumed as input. The three objects from Schramm et al. (2008) are consistent with this prediction. We additionally show the probability distribution for evolution of the form $(1+z)^2$, barely consistent with the observations, while the data are fully consistent with $\gamma \approx 1$.

The general trend discussed on this example is applicable to other bright QSO, high z studies. In particular, this sample at $z \sim 3$ has a similar luminosity limit as the $z \sim 6$ SDSS main quasar sample (Fan et al. 2001). Therefore, the large offset from the local relations found in high-z studies (e.g. Walter et al. 2004; Wang et al. 2010) is at least partially, if not fully, due to these selection effects. A quantitative assessment of this bias is currently hampered by our poor knowledge of the underlying distribution functions at such high redshift.

5.6. Conclusions

We investigated the ramifications of sample selection effects for the observed black hole - bulge relations. Our starting point is the bivariate probability distribution of galaxy bulge properties and black hole masses, providing the true underlying relation. However, for realistic observations this probability distribution is inevitably modified. The only way to avoid this is to obtain a complete volume limited sample with measured galaxy properties and black hole masses. We incorporate the modification of the bivariate distribution function by the use of a selection function. While the true $M_\bullet$−bulge relations are recovered from the original bivariate probability distribution, this is generally not the case for the observed one, i.e. in the presence of selection effects. We presented a qualitative framework to predict the expected bias on the $M_\bullet$−bulge relations.

Also the probability distribution for the sample of normal galaxies with dynamical black hole mass measurements, which defines the reference for the $M_\bullet$−bulge relations, is changed by selection effects. We illustrated one potential effect, namely a selection effect against objects for which the black hole's sphere of influence is not well resolved, which may bias the local $M_\bullet$−bulge relations, even without active rejection of objects.

For the main part of this paper we investigated in detail selection effects for type 1 AGN samples. These samples are essential as probes for redshift evolution in the $M_\bullet$−bulge relations. We identified a variety of selection effects that can work in both directions:

- *Active fraction bias:* If the probability for a black hole to be in an active (type 1 AGN) stage directly depends on the black hole mass, the selection from the quiescent BHMF is affected. For an active fraction decreasing with black hole mass, low mass black holes have a higher probability to be in an active stage and thus a bias towards a low $M_\bullet/M_{\rm Bulge}$ ratio is produced. For an increasing active fraction the opposite is the case. If the active fraction is independent of, or constant with black hole mass, no bias is introduced. This bias has not been discussed before.
- *Luminosity bias:* As AGN are selected based on their luminosity, we expect to find on average higher mass black holes when we restrict our sample to a brighter luminosity limit. The steep decrease of the galaxy distribution function and the intrinsic scatter in the $M_\bullet$−bulge relations generates a bias which is strongly enhanced for a bright luminosity limit. The magnitude of the bias depends on the underlying distribution functions and the size of the intrinsic scatter. This bias has already been extensively discussed before (e.g. Salviander et al. 2007; Lauer et al. 2007).
- *AGN evolution bias:* The AGN distribution functions that regulate the magnitude of the bias are evolving themselves as a function of redshift, as implied by the evolution of the

AGN luminosity function. This evolution will change the expected sample bias with redshift.

These effects modify the bivariate probability distribution and can alter the conclusion drawn from observational studies. It is important to distinguish what is meant by saying the $M_\bullet-$bulge relations are biased, as, due to the intrinsic scatter, there are different quantities to represent these relations. (1) The most comprehensive approach would be to investigate the bivariate distribution of galaxy property and black hole mass. However, the bivariate distribution is modified by the AGN selection, and is thus biased. (2) The most basic approach is to simply compute the mean offset from the local relation for the entire sample. We showed that this quantity is equally biased by the AGN selection. (3) An intermediate way is to look at the respective $M_\bullet-$bulge relation, defined as the mean black hole mass for a given galaxy property. This relation is also biased by the AGN selection, as some black holes are excluded from the sample during the selection process. (4) Alternatively, one can inspect the relation of mean galaxy property for a given black hole mass. While, for our parameterisation of the bivariate distribution, this quantity deviates from the true relation even without any selection effects, it is not affected by the three AGN selection effects outlined above. Therefore it is unbiased, as long as no additional selection on the host galaxy properties exists.

The first three quantities above are biased by the AGN selection. To properly model and correct these for the effects introduced onto an AGN sample it is necessary to know the underlying distribution functions. These are the spheroid distribution function, the active fraction, or alternatively the active black hole mass function, and the Eddington ratio distribution function. These are at least reasonably well known for the local universe, but only poorly established at high z. This current uncertainty in the high z distribution functions prevents an exact correction for the above selection effects. Thus, resolving this issue is essential for the determination of the $M_\bullet-$bulge relations at high redshifts. Furthermore, the selection function of the studied sample needs to be known, which demands a well-defined observational sample. An ill-defined sample lowers the ability to properly account for the selection effects.

The fourth quantity, inspecting the mean relation of galaxy property at a given black hole mass, may provide a possible route to circumvent some of these issues. However, it does also not directly yield the intrinsic relation. Reconstructing the intrinsic relation from the observed mean relation of galaxy property at a given black hole mass also requires knowledge of the spheroid distribution function and the intrinsic scatter in the respective $M_\bullet-$bulge relation, which is of particular importance at the high mass end. Furthermore, measurement uncertainties in the black hole mass will introduce a dependence of the AGN selection into this quantity, as a chosen black hole mass bin is contaminated by neighbouring mass bins. This contamination is not symmetric, but depends on the active black hole mass function from which the masses are sampled.

There are several sources of uncertainties to our knowledge of the $M_\bullet-$bulge relations at high redshifts. All of them need to be understood and incorporated to make progress in this field. Firstly, there are statistical uncertainties, simply caused by the limited sample size of the observations. These uncertainties can be reduced in the future by increasing the sample size. Secondly, there are measurement uncertainties, i.e. how well can we determine the black hole mass and spheroid property from the observations, and are there systematic effects in their determination? If the measurement error is symmetric this is not a crucial concern, but systematic effects can bias the conclusions if they are not properly understood. Finally, there are selection effects present, which are the topic of this paper. These regulate the composition of the observed samples and may modify the apparent $M_\bullet-$bulge relations in these observations.

To reach a definite conclusion on the presence or absence of redshift evolution in the $M_\bullet-$bulge relations it is essential to improve on all of these aspects. Being confronted with all these issues it may appear to be hard to say anything about the presence of evolution. However, we are indeed able to make a statement on evolution in the $M_\bullet-$bulge relations from observations, even in the presence of selection effects, as we demonstrated in section 5.5. However, to do so, it is essential to properly incorporate these effects into the analysis.

We employed our method to predict the $M_\bullet-$bulge probability distribution and the the bias for a few representative observational studies. Firstly, we inspected the reverberation mapping sample. This is essential, as this sample serves as absolute calibration of the virial method. We found evidence for a bias in this sample by ~ 0.1 dex. A precise prediction is hampered by the inhomogeneous selection of the reverberation mapping sample. Most studies that test for evolution show a clear intrinsic offset from the local $M_\bullet - M_{\rm Bulge}$ relation at higher z, but at least a part of it is caused by sample selection effects. We found tentative evidence for a mild evolution in the $M_\bullet - M_{\rm Bulge}$ relation and in the $M_\bullet - \sigma_*$ relation in the works of Merloni et al. (2010) and Salviander et al. (2007), respectively, in line with the conclusions in these studies. From our approximate assessment of the selection effects we found for both relations consistency with the observations within the range $0 \lesssim \gamma \lesssim 1$ for the redshift evolution parameter.

Our work emphasises the importance and complexity of sample selection effects for observational studies on the $M_\bullet-$bulge relations and their evolution. Several studies already took these effects into account (Salviander et al. 2007; Merloni et al. 2010; Bennert et al. 2010; Lamastra et al. 2010), however sometimes with simplifying assumptions. Our work goes beyond these attempts and provides a common framework in which all kinds of selection effects on the $M_\bullet-$bulge relations can be investigated. With future improvements in observational sample sizes, the estimation of black hole masses and galaxy properties, and the determination of the underlying distribution functions, an answer to the question of evolution in the $M_\bullet-$bulge relations seems to be within reach.

Appendix 5.A: Validation of the bivariate probability distribution

O ur chosen parameterisation of the bivariate probability distribution $\Psi(s,\mu)$, given by Equation (5.1), follows common practise, but is not the only possible solution. In particular, this parameterisation predicts an upturn in the distribution at high values of the galaxy property, where their space density is decreas-

ing. Thus, it is worthwhile to first test if this parameterisation is consistent with current observations, and second inspect a more general parameterisation and their consequences for our presented work.

Firstly, in Fig. 5.18 we compare our intrinsic bivariate probability distribution $\Psi(s,\mu)$ with the quiescent black hole sample from dynamical black hole mass measurements, employing the $M_\bullet - \sigma_*$, the $M_\bullet - M_K$ and $M_\bullet - M_{\rm bulge}$ relations. For the $M_\bullet - \sigma_*$ relation we use the stellar velocity dispersion distribution function from Sheth et al. (2003) and the observational sample from Gültekin et al. (2009). For the $M_\bullet - M_K$ relation we employ the 2MASS K-band luminosity function from Kochanek et al. (2001) and the sample from Hu (2009), and for the $M_\bullet - M_{\rm bulge}$ relation we use our estimate for the spheroid mass function, based on galaxy mass functions from Bell et al. (2003), and show the sample from Häring & Rix (2004). The observations do not directly follow the probability contours, as they suffer from selection effects. However, especially at the high mass end they should allow a fair assessment of the true distribution. We found that our used bivariate probability distribution $\Psi(s,\mu)$ is consistent with the current observations of this bivariate distribution for all three relations, supporting our assumption for the quiescent black hole population and their host galaxies.

The bivariate distribution of active black holes and their host galaxies will not directly resemble that of quiescent black holes, because active black holes are a non-random subpopulation of the total black hole population. This can be incorporated by multiplying $\Psi(s,\mu)$ by an active fraction term that in general may depend on black hole mass and galaxy property $p_{\rm ac}(s,\mu)$ (in this paper we made the simplifying assumption $p_{\rm ac}(s,\mu) = p_{\rm ac}(\mu)$). Additionally, AGN luminosity selection will modify $\Psi_{\rm o}(s,\mu)$. In Fig 5.19, we compare a local prediction for $\Psi_{\rm o}(s,\mu)$ with local observations of type 1 AGN samples. For the $M_\bullet - \sigma_*$ and $M_\bullet - M_{\rm bulge}$ relations the high mass end is currently poorly covered by observations, which inhibits us to draw firm conclusions. Nevertheless, they seem to be consistent with our parameterisation. The $M_\bullet - L_{\rm Bulge}$ relation seems to disagree with our bivariate probability distribution at the high mass end. This may reveal a problem with our assumption or it may just indicate that the $M_\bullet - L_V$ is not the same for normal galaxies and AGN host galaxies. In particular, host galaxies of high luminosity AGN have on average younger stellar populations (e.g. Kauffmann et al. 2003; Jahnke et al. 2004; Vanden Berk et al. 2006) compared to normal galaxies. Thus, if they obey the same $M_\bullet - M_{\rm bulge}$ relation, they should deviate in the $M_\bullet - L_{\rm Bulge}$ relation.

To summarise, the bivariate distribution used in this work is consistent with the local quiescent black hole sample and is therefore a proper choice for the intrinsic bivariate distribution. The comparison with local AGN samples is yet inconclusive, but our used bivariate distribution is at least not inconsistent with current observations. The $M_\bullet - L_{\rm Bulge}$ relation seems to deviate, but this may be simply caused by the difference in the average stellar population in elliptical galaxies between normal galaxies and AGN host galaxies.

Nevertheless, we can also think about other parameterisation for $\Psi(s,\mu)$. However, in any case they need to satisfy the constraints on the two distribution functions:

$$\Phi_s(s) = \int \Psi(s,\mu)\,\mathrm{d}\mu \tag{5.30}$$

$$\Phi_\bullet(\mu) = \int \Psi(s,\mu)\,\mathrm{d}s \tag{5.31}$$

As the BHMF is not known observationally and only inferred from the galaxy LF, this means that we have to satisfy the constraint on the galaxy distribution function. Furthermore, we require two additional assumptions to be fulfilled. First, there is a linear mean relation $y = a + bx$. Second, there is intrinsic scatter on this relation in the s direction and in the μ direction, i.e. s is drawn from a probability distribution with mean x and μ is drawn from a probability distribution with mean y. These three assumptions lead to the following general bivariate distribution function

$$\Psi(s,\mu) = \int g(\mu\,|\,x) g(s\,|\,x)\,\Phi_x(x)\,\mathrm{d}x \tag{5.32}$$

Here x is the position on the linear relation, $g(\mu\,|\,x)$ and $g(s\,|\,x)$ are the two probability distributions that account for the intrinsic scatter in both directions and $\Phi_x(x)$ is an arbitrary distribution function (without physical correspondence) to satisfy the galaxy distribution function constraint. Indeed, we find for the distribution functions

$$\Phi_s(s) = \int g(s\,|\,x)\,\Phi_x(x)\,\mathrm{d}x \tag{5.33}$$

$$\Phi_\bullet(\mu) = \int g(\mu\,|\,x)\,\Phi_x(x)\,\mathrm{d}x \tag{5.34}$$

Once we choose a specific $g(s\,|\,x)$ Equation (5.33) defines the function $\Phi_x(x)$. This parametrisation is able to cover the full range of possibilities to divide the intrinsic scatter between μ and s. If we attribute no scatter to s, i.e. we assume $g(s\,|\,x)$ to be a δ-function we get the case discussed in this work $\Psi(s,\mu) = g(\mu\,|\,s)\,\Phi_s(s)$. As other extreme case, if we assume $g(\mu\,|\,x)$ to be a δ-function, we get $\Psi(s,\mu) = g(s\,|\,\mu)\,\Phi_\bullet(\mu)$. This case is excluded observationally. It would require the galaxy luminosity function to be a convolution of the BHMF with the intrinsic scatter and in order to achieve this, the BHMF would need to decrease strongly above $\sim 10^8\,M_\odot$. This is in conflict with the observations of higher masses of dormant black holes as well as in AGN, and also with the *active* BHMF (SW10).

We can also define an intermediate case where the intrinsic scatter is distributed symmetrically. This is achieved by additionally requiring the conditional probabilities $p(\mu\,|\,s)$ and $p(s\,|\,\mu)$ to be equal. These conditional probabilities are defined by

$$p(\mu\,|\,s) = \frac{\Psi(s,\mu)}{\int \Psi(s,\mu)\,\mathrm{d}\mu} \tag{5.35}$$

$$p(s\,|\,\mu) = \frac{\Psi(s,\mu)}{\int \Psi(s,\mu)\,\mathrm{d}s} \tag{5.36}$$

Thus, we require $\Phi_s(s) = \Phi_\bullet(a+bs)$. We assume log-normal distributions for $g(\mu\,|\,x)$ and $g(s\,|\,x)$, with means given by $a+bx$ and x, respectively, and dispersions σ_μ and σ_s. When we assume a total intrinsic scatter of σ, the condition $p(\mu\,|\,s) = p(s\,|\,\mu)$ requires $\sigma_\mu = \sigma/\sqrt{2}$ and $\sigma_s = \sigma/(\sqrt{2}b)$. The function $\Phi_x(x)$ is

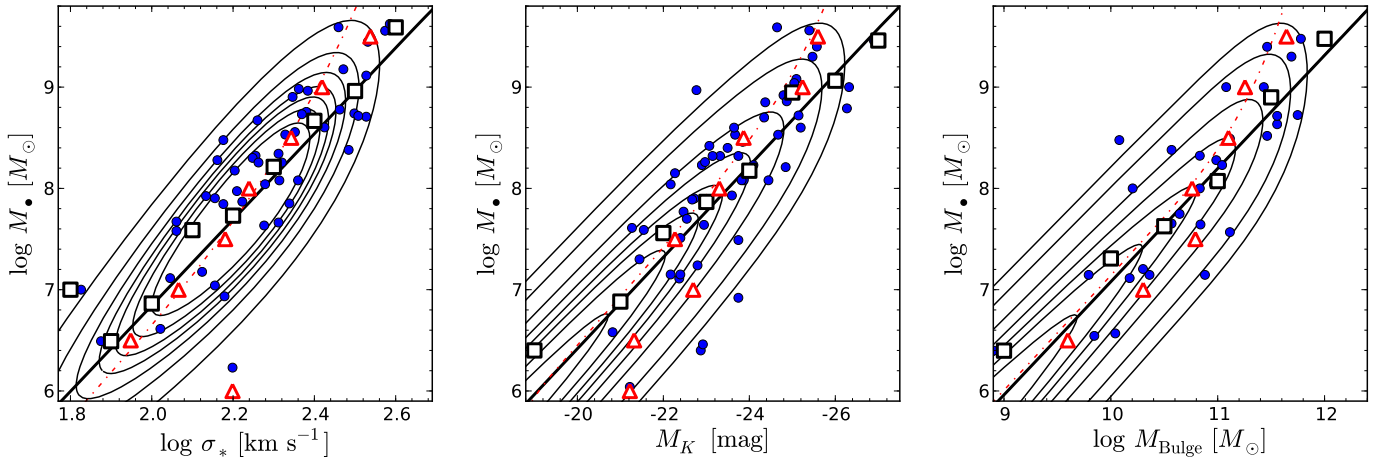

Fig. 5.18. Comparison of our bivariate probability distribution $\Psi(s,\mu)$ (contours) with observational data of dormant black holes (blue circles). The thick black line shows the mean relation $\langle\mu\rangle(s)$, the red dashed dotted line shows $\langle s\rangle(\mu)$. The black open squares gives the mean μ binned in s from the observations (an estimate of $\langle\mu\rangle(s)$) and the red open triangles gives s binned in μ (an estimate of $\langle s\rangle(\mu)$). Left panel: $M_\bullet - \sigma_*$ sample from Gültekin et al. (2009). Middle panel: $M_\bullet - M_K$ sample from Hu (2009). Right panel: $M_\bullet - M_{\rm bulge}$ sample from Häring & Rix (2004).

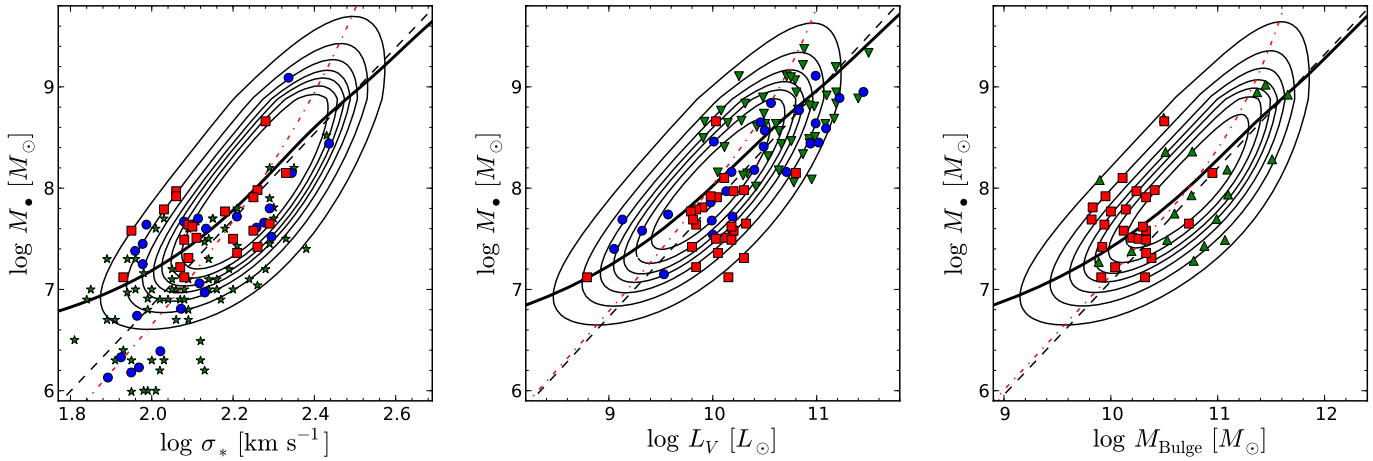

Fig. 5.19. Comparison of our bivariate probability distribution $\Psi(s,\mu)$ (contours), for active black holes with an arbitrary AGN luminosity limit of $\log L_{\rm bol} = 10^{45}$ ergs s^{-1}, with observational data of local active black holes. The thick black line shows the mean relation $\langle\mu\rangle(s)$, the red dashed dotted line shows $\langle s\rangle(\mu)$. Left panel: $M_\bullet - \sigma_*$ relation. We show stellar velocity dispersion measurements for the reverberation mapping sample (blue circles, Woo et al. 2010), a local SDSS sample (green stars, Greene & Ho 2006) and the sample from Bennert et al. (2011, red squares). Middle panel: $M_\bullet - L_V$ relation for the reverberation mapping sample (blue circles, Bentz et al. 2009b), a local QSO host galaxy sample (green triangles, Kim et al. 2008) and the sample from Bennert et al. (2011, red squares). Right panel: $M_\bullet - M_{\rm bulge}$ relation for the sample from Bennert et al. (2011, red squares) and a $z < 0.2$ AGN sample from Schramm et al. (in prep., green triangles)

determined via Equation (5.33). We show the bivariate probability distribution $\Psi(s,\mu)$ in Fig. 5.20, symmetric around the intrinsic linear relation $y = a + bx$. We also show the mean relations $\langle\mu\rangle(s)$ and $\langle s\rangle(\mu)$, computed via Equations (5.6) and (5.7), both symmetrically deviating from the intrinsic relation at the high mass end. The general result that the two mean relations do not give the same answer is caused by the decrease of the galaxy distribution function and the intrinsic scatter in the relations. It cannot be avoided as long as consistency with the observed galaxy distribution function is enforced. Furthermore, this bivariate distribution is in worse agreement with the observations of quiescent black holes, while it does not improve the consistency with the AGN observations. Thus, we prefer the bivariate distribution defined by Equation (5.1) for the intrinsic probability distribution.

The here presented more general case can be easily incorporated into the main paper by replacing $\Psi(s,\mu) = g(\mu\,|\,s)\,\Phi_s(s)$ by Equation (5.32). While the details of our work depend on our choice of $\Psi(s,\mu)$, our general results are still valid assuming a different bivariate distribution, as long as we satisfy the three general assumptions above.

Currently, the bivariate distribution of galaxy property and black hole mass $\Psi(s,\mu)$ is not well established. This is particularly true for AGN, as only few measurements of stellar velocity dispersions and spheroid masses at high values, where the galaxy space density is decreasing, are available so far. A bet-

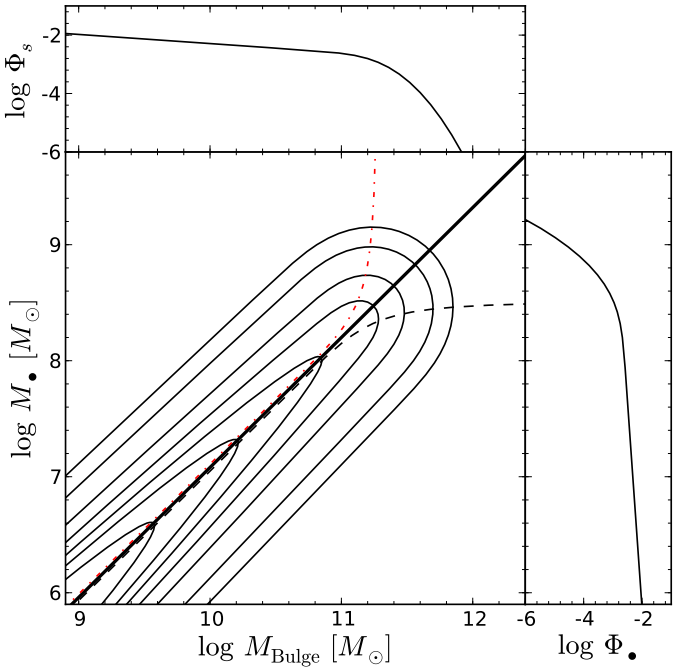

Fig. 5.20. Bivariate probability distribution function (assuming Equation (5.32)) which is constructed as symmetric around the intrinsic linear relation. The black dashed line shows the relation binned in galaxy property, i.e. $\langle\mu\rangle(s)$. The red dashed dotted line shows the relation binned in black hole mass, i.e. $\langle s\rangle(\mu)$. The galaxy distribution function constraint it satisfied by construction.

ter determination of this bivariate distribution will improve our understanding of galaxy-black hole coevolution and is important for a proper assessment of the evolution in the $M_\bullet$−bulge relations.

References

Abazajian, K., Adelman-McCarthy, J. K., Agüeros, M. A., et al. 2005, AJ, 129, 1755
Adelberger, K. L. & Steidel, C. C. 2005, ApJ, 627, L1
Alexander, D. M., Brandt, W. N., Smail, I., et al. 2008, AJ, 135, 1968
Batcheldor, D. 2010, ApJ, 711, L108
Bell, E. F., McIntosh, D. H., Katz, N., & Weinberg, M. D. 2003, ApJS, 149, 289
Bennert, V. N., Auger, M. W., Treu, T., Woo, J., & Malkan, M. A. 2011, ApJ, 726, 59
Bennert, V. N., Treu, T., Woo, J., et al. 2010, ApJ, 708, 1507
Bentz, M. C., Peterson, B. M., Netzer, H., Pogge, R. W., & Vestergaard, M. 2009a, ApJ, 697, 160
Bentz, M. C., Peterson, B. M., Pogge, R. W., & Vestergaard, M. 2009b, ApJ, 694, L166
Bernardi, M. 2007, AJ, 133, 1954
Bernardi, M., Sheth, R. K., Tundo, E., & Hyde, J. B. 2007, ApJ, 660, 267
Blandford, R. D. & McKee, C. F. 1982, ApJ, 255, 419
Bluck, A. F. L., Conselice, C. J., Almaini, O., et al. 2011, MNRAS, 410, 1174
Bongiorno, A., Zamorani, G., Gavignaud, I., et al. 2007, A&A, 472, 443
Booth, C. M. & Schaye, J. 2009, MNRAS, 398, 53
Booth, C. M. & Schaye, J. 2011, MNRAS, 243
Borys, C., Smail, I., Chapman, S. C., et al. 2005, ApJ, 635, 853
Bower, R. G., Benson, A. J., Malbon, R., et al. 2006, MNRAS, 370, 645
Bundy, K., Ellis, R. S., & Conselice, C. J. 2005, ApJ, 625, 621
Cattaneo, A., Blaizot, J., Devriendt, J., & Guiderdoni, B. 2005, MNRAS, 364, 407
Croom, S. M., Richards, G. T., Shanks, T., et al. 2009, MNRAS, 399, 1755
Croton, D. J. 2006, MNRAS, 369, 1808
Croton, D. J., Springel, V., White, S. D. M., et al. 2006, MNRAS, 365, 11
Dalla Bontà, E., Ferrarese, L., Corsini, E. M., et al. 2009, ApJ, 690, 537
Decarli, R., Falomo, R., Treves, A., et al. 2010, MNRAS, 402, 2453
Di Matteo, T., Colberg, J., Springel, V., Hernquist, L., & Sijacki, D. 2008, ApJ, 676, 33
Di Matteo, T., Springel, V., & Hernquist, L. 2005, Nature, 433, 604
Emsellem, E., Dejonghe, H., & Bacon, R. 1999, MNRAS, 303, 495
Fan, X., Narayanan, V. K., Lupton, R. H., et al. 2001, AJ, 122, 2833
Ferrarese, L. & Ford, H. 2005, Space Sci. Rev., 116, 523
Ferrarese, L., Ford, H. C., & Jaffe, W. 1996, ApJ, 470, 444
Ferrarese, L. & Merritt, D. 2000, ApJ, 539, L9
Fine, S., Croom, S. M., Miller, L., et al. 2006, MNRAS, 373, 613
Fontana, A., Salimbeni, S., Grazian, A., et al. 2006, A&A, 459, 745
Franceschini, A., Rodighiero, G., Cassata, P., et al. 2006, A&A, 453, 397
Gadotti, D. A. 2009, MNRAS, 393, 1531
Gebhardt, K., Bender, R., Bower, G., et al. 2000, ApJ, 539, L13
Gebhardt, K., Richstone, D., Tremaine, S., et al. 2003, ApJ, 583, 92
Gebhardt, K. & Thomas, J. 2009, ApJ, 700, 1690
Graham, A. W. 2008, ApJ, 680, 143
Graham, A. W., Erwin, P., Caon, N., & Trujillo, I. 2001, ApJ, 563, L11
Graham, A. W. & Worley, C. C. 2008, MNRAS, 388, 1708
Greene, J. E. & Ho, L. C. 2006, ApJ, 641, L21
Greene, J. E., Peng, C. Y., Kim, M., et al. 2010, ApJ, 721, 26
Gültekin, K., Richstone, D. O., Gebhardt, K., et al. 2009, ApJ, 698, 198
Häring, N. & Rix, H.-W. 2004, ApJ, 604, L89
Hasinger, G., Cappelluti, N., Brunner, H., et al. 2007, ApJS, 172, 29
Hasinger, G., Miyaji, T., & Schmidt, M. 2005, A&A, 441, 417
Hirschmann, M., Khochfar, S., Burkert, A., et al. 2010, MNRAS, 407, 1016
Hopkins, P. F., Hernquist, L., Cox, T. J., Keres, D., & Wuyts, S. 2009, ApJ, 691, 1424
Hopkins, P. F., Hernquist, L., Cox, T. J., Robertson, B., & Krause, E. 2007, ApJ, 669, 45
Hopkins, P. F., Robertson, B., Krause, E., Hernquist, L., & Cox, T. J. 2006, ApJ, 652, 107
Hu, J. 2008, MNRAS, 386, 2242
Hu, J. 2009, arXiv:0908.2028
Ilbert, O., Salvato, M., Le Floc'h, E., et al. 2010, ApJ, 709, 644
Inskip, K. J., Jahnke, K., Rix, H., & van de Ven, G. 2011, arXiv:1103.6026
Jahnke, K., Bongiorno, A., Brusa, M., et al. 2009, ApJ, 706, L215
Jahnke, K., Kuhlbrodt, B., & Wisotzki, L. 2004, MNRAS, 352, 399
Jahnke, K. & Maccio, A. 2010, arXiv:1006.0482
Johansson, P. H., Burkert, A., & Naab, T. 2009, ApJ, 707, L184
Kaspi, S., Maoz, D., Netzer, H., et al. 2005, ApJ, 629, 61
Kaspi, S., Smith, P. S., Netzer, H., et al. 2000, ApJ, 533, 631
Kauffmann, G. & Haehnelt, M. 2000, MNRAS, 311, 576
Kauffmann, G., Heckman, T. M., Tremonti, C., et al. 2003, MNRAS, 346, 1055
Kelly, B. C., Vestergaard, M., Fan, X., et al. 2010, ApJ, 719, 1315
Kim, M., Ho, L. C., Peng, C. Y., et al. 2008, ApJ, 687, 767
Kisaka, S. & Kojima, Y. 2010, MNRAS, 405, 1285
Kochanek, C. S., Pahre, M. A., Falco, E. E., et al. 2001, ApJ, 560, 566
Kormendy, J., Bender, R., & Cornell, M. E. 2011, Nature, 469, 374
Kormendy, J. & Richstone, D. 1995, ARA&A, 33, 581
Lamastra, A., Menci, N., Maiolino, R., Fiore, F., & Merloni, A. 2010, MNRAS, 405, 29
Lauer, T. R., Tremaine, S., Richstone, D., & Faber, S. M. 2007, ApJ, 670, 249
Lilly, S. J., Le Fèvre, O., Renzini, A., et al. 2007, ApJS, 172, 70
Magorrian, J., Tremaine, S., Richstone, D., et al. 1998, AJ, 115, 2285
Malbon, R. K., Baugh, C. M., Frenk, C. S., & Lacey, C. G. 2007, MNRAS, 382, 1394
Marconi, A., Capetti, A., Axon, D. J., et al. 2001, ApJ, 549, 915
Marconi, A. & Hunt, L. K. 2003, ApJ, 589, L21
Marconi, A., Risaliti, G., Gilli, R., et al. 2004, MNRAS, 351, 169
Marulli, F., Bonoli, S., Branchini, E., Moscardini, L., & Springel, V. 2008, MNRAS, 385, 1846
McLeod, K. K. & Bechtold, J. 2009, ApJ, 704, 415
McLure, R. J. & Jarvis, M. J. 2002, MNRAS, 337, 109
McLure, R. J., Jarvis, M. J., Targett, T. A., Dunlop, J. S., & Best, P. N. 2006, MNRAS, 368, 1395
Merloni, A. 2004, MNRAS, 353, 1035

Merloni, A., Bongiorno, A., Bolzonella, M., et al. 2010, ApJ, 708, 137
Merloni, A. & Heinz, S. 2008, MNRAS, 388, 1011
Merloni, A., Rudnick, G., & Di Matteo, T. 2004, MNRAS, 354, L37
Nelson, C. H. 2000, ApJ, 544, L91
Nesvadba, N. P. H., De Breuck, C., Lehnert, M. D., et al. 2011, A&A, 525, A43+
Onken, C. A., Ferrarese, L., Merritt, D., et al. 2004, ApJ, 615, 645
Peng, C. Y. 2007, ApJ, 671, 1098
Peng, C. Y. 2010, in IAU Symposium, Vol. 267, IAU Symposium, 161–171
Peng, C. Y., Impey, C. D., Ho, L. C., Barton, E. J., & Rix, H. 2006a, ApJ, 640, 114
Peng, C. Y., Impey, C. D., Rix, H., et al. 2006b, ApJ, 649, 616
Peterson, B. M. 1993, PASP, 105, 247
Pozzetti, L., Bolzonella, M., Lamareille, F., et al. 2007, A&A, 474, 443
Richards, G. T., Fan, X., Newberg, H. J., et al. 2002, AJ, 123, 2945
Richards, G. T., Strauss, M. A., Fan, X., et al. 2006, AJ, 131, 2766
Riechers, D. A., Walter, F., Brewer, B. J., et al. 2008, ApJ, 686, 851
Riechers, D. A., Walter, F., Carilli, C. L., & Lewis, G. F. 2009, ApJ, 690, 463
Robertson, B., Hernquist, L., Cox, T. J., et al. 2006, ApJ, 641, 90
Salviander, S., Shields, G. A., Gebhardt, K., & Bonning, E. W. 2007, ApJ, 662, 131
Sani, E., Marconi, A., Hunt, L. K., & Risaliti, G. 2011, MNRAS, 443
Sarria, J. E., Maiolino, R., La Franca, F., et al. 2010, A&A, 522, L3+
Schramm, M., Wisotzki, L., & Jahnke, K. 2008, A&A, 478, 311
Schulze, A. & Gebhardt, K. 2011, ApJ, 729, 21
Schulze, A. & Wisotzki, L. 2010, A&A, 516, A87+
Schulze, A., Wisotzki, L., & Husemann, B. 2009, A&A, 507, 781
Shankar, F., Bernardi, M., & Haiman, Z. 2009, ApJ, 694, 867
Shen, J., Vanden Berk, D. E., Schneider, D. P., & Hall, P. B. 2008, AJ, 135, 928
Shen, Y. & Kelly, B. C. 2010, ApJ, 713, 41
Sheth, R. K., Bernardi, M., Schechter, P. L., et al. 2003, ApJ, 594, 225
Shields, G. A., Gebhardt, K., Salviander, S., et al. 2003, ApJ, 583, 124
Shields, G. A., Menezes, K. L., Massart, C. A., & Vanden Bout, P. 2006, ApJ, 641, 683
Sijacki, D., Springel, V., Di Matteo, T., & Hernquist, L. 2007, MNRAS, 380, 877
Somerville, R. S. 2009, MNRAS, 399, 1988
Somerville, R. S., Hopkins, P. F., Cox, T. J., Robertson, B. E., & Hernquist, L. 2008, MNRAS, 391, 481
Tremaine, S., Gebhardt, K., Bender, R., et al. 2002, ApJ, 574, 740
Treu, T., Woo, J., Malkan, M. A., & Blandford, R. D. 2007, ApJ, 667, 117
Trump, J. R., Impey, C. D., Elvis, M., et al. 2009, ApJ, 696, 1195
Ueda, Y., Akiyama, M., Ohta, K., & Miyaji, T. 2003, ApJ, 598, 886
van den Bosch, R. C. E. & de Zeeuw, P. T. 2010, MNRAS, 401, 1770
van der Marel, R. P., Cretton, N., de Zeeuw, P. T., & Rix, H. 1998, ApJ, 493, 613
Vanden Berk, D. E., Richards, G. T., Bauer, A., et al. 2001, AJ, 122, 549
Vanden Berk, D. E., Shen, J., Yip, C., et al. 2006, AJ, 131, 84
Vestergaard, M., Fan, X., Tremonti, C. A., Osmer, P. S., & Richards, G. T. 2008, ApJ, 674, L1
Vestergaard, M. & Osmer, P. S. 2009, ApJ, 699, 800
Vestergaard, M. & Peterson, B. M. 2006, ApJ, 641, 689
Volonteri, M. & Natarajan, P. 2009, MNRAS, 400, 1911
Walter, F., Carilli, C., Bertoldi, F., et al. 2004, ApJ, 615, L17
Wang, R., Carilli, C. L., Neri, R., et al. 2010, ApJ, 714, 699
Wisotzki, L., Christlieb, N., Bade, N., et al. 2000, A&A, 358, 77
Woo, J., Treu, T., Barth, A. J., et al. 2010, ApJ, 716, 269
Woo, J., Treu, T., Malkan, M. A., & Blandford, R. D. 2006, ApJ, 645, 900
Woo, J.-H., Treu, T., Malkan, M. A., & Blandford, R. D. 2008, ApJ, 681, 925
Wyithe, J. S. B. & Loeb, A. 2003, ApJ, 595, 614
Yu, Q. & Lu, Y. 2004, ApJ, 602, 603
Yu, Q. & Tremaine, S. 2002, MNRAS, 335, 965

Chapter 6

Accounting for selection effects in the black hole-bulge relations and its evolution⋆

Andreas Schulze and Lutz Wisotzki

Leibniz-Institut für Astrophysik Potsdam (AIP), An der Sternwarte 16, 14482 Potsdam, Germany

ABSTRACT

We present preliminary results on a further investigation of the issue of selection effects in the black hole mass-bulge relations. We build on the ideas and methods developed in Chapter 5, and present an alternative route to reconstruct the intrinsic black hole-bulge relations from a sample affected by selection effects. The method employs a maximum likelihood fit to the conditional probability distributions of black hole mass and galaxy properties. Two different probability distributions are used. Firstly, the probability distribution for a black hole mass at given galaxy property, redshift and Eddington ratio. Secondly, the probability distribution for a galaxy property for a given black hole mass. Both provide independent constraints on the intrinsic relation. This approach restricts prior knowledge of the underlying distribution functions to a minimum and thus tries to avoid some of the issues discussed in Chapter 5. Furthermore, it allows a quantitative assessment of the confidence for or against evolution in the black hole-bulge relations. We present Monte Carlo tests for this method, discuss their modifications in the presence of measurement uncertainties in black hole masses and galaxy properties and present a first application of the method to observational data.

6.1. Introduction

In Chapter 5 we showed that observational studies on the $M_\bullet-$bulge relations naturally suffer from selection effects. If these are not considered, the observed $M_\bullet-$bulge relations will inevitably be biased. However, a full assessment of the selection effects and potential inherent biases requires knowledge of the underlying distribution functions, such as the galaxy distribution function, the active black hole mass function and the Eddington ratio distribution function. While at least for the local universe these distribution functions are reasonably well established, at higher z they are only poorly known. This is a problem for observational studies that test for evolution in the $M_\bullet-$bulge relations. If the associated biases are not properly understood and accounted for, it is hard to judge if an observed evolutionary trend is real or not. Here we present a simple fitting method to determine the intrinsic black hole-bulge relations, restricting prior knowledge of the underlying distribution functions to a minimum.

6.2. Maximum likelihood fit

In Chapter 5 we discussed the full probability distribution of s and μ (with $s = \log\sigma_*$ or $s = \log M_{\rm Bulge}$ and $\mu = \log M_\bullet$). However, we are interested in the $M_\bullet-$bulge relation, represented by the relations of black hole mass at a given galaxy property or galaxy property at a given black hole mass. These quantities are given by the conditional probabilities

$$p(\mu\,|\,s) = \frac{\Psi_{\rm o}(s,\mu)}{\int \Psi_{\rm o}(s,\mu)\,{\rm d}\mu} \tag{6.1}$$

$$p(s\,|\,\mu) = \frac{\Psi_{\rm o}(s,\mu)}{\int \Psi_{\rm o}(s,\mu)\,{\rm d}s}\,, \tag{6.2}$$

where $p(\mu\,|\,s)$ gives the probability of finding a black hole of mass μ in a galaxy with property s and $p(s\,|\,\mu)$ is the probability of finding a galaxy with s for a black hole with mass μ. The function $\Psi_{\rm o}(s,\mu)$ is the bivariate distribution function of μ and s for the observed sample, as defined in section 5.2. If there are no selection effects present $\Psi_{\rm o}(s,\mu) = \Psi(s,\mu)$. When we further assume the same bivariate distribution as we did in Chapter 5 (given by Equation (5.1)), in this case it follows that $p_{\rm int}(\mu\,|\,s) = g(\mu\,|\,s)$, i.e. the intrinsic underlying relation is directly recovered. For the conditional probability of spheroid mass for given black hole mass it follows in the absence of any selection effects

$$p_{\rm int}(s\,|\,\mu) = \frac{g(\mu\,|\,s)\,\Phi_s(s)}{\int g(\mu\,|\,s)\,\Phi_s(s){\rm d}s}\,, \tag{6.3}$$

already deviating from the intrinsic relation $g(\mu\,|\,s)$.

In general, selection effects will be present. These modify the bivariate distribution, i.e. $\Psi_{\rm o}(s,\mu) \neq \Psi(s,\mu)$, and therefore also affect the conditional probabilities, i.e. $p(\mu\,|\,s) \neq g(\mu\,|\,s)$. However, if the relation between the conditional probability and the intrinsic $M_\bullet-$bulge relation is known, the latter can be reconstructed from observations of the former. So lets assume we know the conditional probability distribution up to some free parameters that represent the respective intrinsic $M_\bullet-$bulge relation, and we have an observational sample, with observed black hole mass, galaxy property, redshift, Eddington ratio, etc.. In this case, we can fit our model for the conditional probability distribution to the observations. The parameters of the

⋆ This chapter may lead or contribute to a future publication.

$M_\bullet$−bulge relation are then obtained from the best fit solution. A reliable and simple method is to employ the maximum likelihood technique. This method aims at minimising the likelihood function $S = -2 \ln \mathcal{L}$, with $\mathcal{L} = \prod_i l_i$ being the product of the likelihoods for the individual measurements. For the study of the $M_\bullet$−bulge relations, the individual likelihoods are given by the conditional probabilities for the observed data.

There are two independent options to study the $M_\bullet$−bulge relations. The first one utilises the conditional probability of black hole mass at a given galaxy property, i.e. $l_i = p(\mu \,|\, s)$, as defined by Equation (6.1). In the absence of selection effects $p(\mu \,|\, s) = g(\mu \,|\, s)$, i.e we are directly fitting the data to the underlying relation. This is identical to the common maximum likelihood fit to the $M_\bullet$−bulge relations (e.g. Gültekin et al. 2009). However, in the presence of selection effects the conditional probability is modified, as given below. The second possibility uses the conditional probability of galaxy property at a given black hole mass, i.e. $l_i = p(s \,|\, \mu)$, as defined by Equation (6.2). In the following we discuss the special case of an AGN sample, but the approach is applicable to any sample affected by selection effects.

For an AGN sample with well defined selection function $\Omega(\mu, \lambda\,, z)$ that describes the AGN flux limit of the sample, the multivariate probability distribution $\Psi_\mathrm{o}(s, \mu, \lambda\,, z)$ of galaxy property, black hole mass, Eddington ratio and redshift is given by

$$\Psi_\mathrm{o}(s, \mu, \lambda\,, z) = \Omega(\mu, \lambda\,, z)\, p_\mathrm{ac}(\mu, z)\, p_\lambda(\lambda\,, z)\, g(\mu \,|\, s, z)\, \Phi_s(s, z) \frac{\mathrm{d}V}{\mathrm{d}z}\,. \tag{6.4}$$

This is equivalent to Equation (5.26), we only expressed the probability distribution as a function of the Eddington ratio λ instead of logarithmic AGN luminosity l. The conditional probability then follows as

$$\begin{aligned} p(\mu \,|\, s, \lambda\,, z) &= \frac{\Psi_\mathrm{o}(s, \mu, \lambda\,, z)}{\int \Psi_\mathrm{o}(s, \mu, \lambda\,, z)\, \mathrm{d}\mu} \\ &= \frac{\Omega\, p_\mathrm{ac}(\mu, z)\, g(\mu \,|\, s, z)}{\int \Omega\, p_\mathrm{ac}(\mu, z)\, g(\mu \,|\, s, z)\, \mathrm{d}\mu}\,. \end{aligned} \tag{6.5}$$

The dependencies on the Eddington ratio distribution function (ERDF) $p_\lambda(\lambda\,)$ and the galaxy distribution function $\Phi_s(s)$ cancel out. The conditional probability only depends on the selection function, the mass dependence of the active fraction and the true $M_\bullet$−bulge relation. This has the advantage that we do not need to know these other distribution functions, and we also do not have to assume that the sample is randomly drawn from them, as long as the selection function is well defined. Nevertheless, knowledge of the selection function of the sample and the mass dependence of the active fraction is required. For the fit, we then minimise

$$S = -2 \sum_{i=1}^{N} \ln p(\mu_i \,|\, s_i, \lambda_i, z_i)\,. \tag{6.6}$$

The intrinsic $M_\bullet$−bulge relation $g(\mu \,|\, s)$ is inferred from the best fit solution of $p(\mu \,|\, s, \lambda\,, z)$ to their free parameters. Thus, when accounting for the selection function in the fit, we are able to recover the true relation, even if the location of the data points indicate a clear apparent offset from the true relation.

For the second option, the conditional probability is given by

$$\begin{aligned} p(s \,|\, \mu, \lambda\,, z) &= \frac{\Psi_\mathrm{o}(s, \mu, \lambda\,, z)}{\int \Psi_\mathrm{o}(s, \mu, \lambda\,, z)\, \mathrm{d}s} \\ &= \frac{g(\mu \,|\, s)\, \Phi_s(s)}{\int g(\mu \,|\, s)\, \Phi_s(s) \mathrm{d}s}\,, \end{aligned} \tag{6.7}$$

identical to the case without AGN selection effects (Equation (6.3)). We already discussed this fact in Chapter 5, but we can use this result here to recover the intrinsic relation by the maximum likelihood fit, fully unaffected by AGN selection effects. The only quantity that has to be known is the galaxy distribution function.

Both options tackle the $M_\bullet$−bulge relations from different directions and require different prior knowledge. Thus, they can put independent constraints on the relations and it would be reassuring to find that both methods give consistent results for a given observational sample.

6.3. Monte Carlo tests

To get a better sense of the reliability, strengths and uncertainties of the presented likelihood fitting method we used extensive Monte Carlo simulations of the $M_\bullet - M_\mathrm{Bulge}$ relation. The Monte Carlo samples were generated as outlined in section 5.3.1. We build samples with different AGN luminosity limits and different sample sizes. For each investigated luminosity limit and sample size, we generated 1000 Monte Carlo realisations. The $M_\bullet - M_\mathrm{Bulge}$ relation is assumed to be linear, with slope b and zero point a and log-normal intrinsic scatter with dispersion σ. Each realisation is fitted, first with a, b and σ as free parameters, and second with b fixed to the assumed input value from Häring & Rix (2004), $b = 1.12$.

In Fig. 6.1 we present results for the fit to the conditional probability $p(\mu \,|\, s, \lambda\,, z)$ for two inspected AGN luminosity limits and two different sample sizes. In the right panels we compare the histogram of fitted parameters from our corrected maximum likelihood fit (black solid histogram) with the results without correction for selection effects (green dashed histogram). The decrease of the bias in the fit parameters of the $M_\bullet - M_\mathrm{Bulge}$ relation is apparent, but this is accompanied by an increase in the dispersion of the distribution. In the left panels we show two representative results for the best fit to a particular Monte Carlo sample, a good case and a poor case, both for a fit with free and with fixed slope. We also indicate 1σ confidence regions, as computed from the ΔS likelihood distribution. We verified that these confidence regions provide a fair estimate of the uncertainty in the $M_\bullet - M_\mathrm{Bulge}$ relation.

In Fig. 6.2, we show the median and 68% confidence limits of the 1000 realisations over a larger range of AGN luminosity limits and sample sizes. In the top panels we left all three parameters (zero point a, slope b and intrinsic scatter σ)free, and determine them from the best fit. The results are always statistically fully consistent with the input value. For a large sample size and a low luminosity limit a and b are also unbiased in the median, while they are slightly biases for a small sample size and a very bright luminosity limit. The reason for this is that

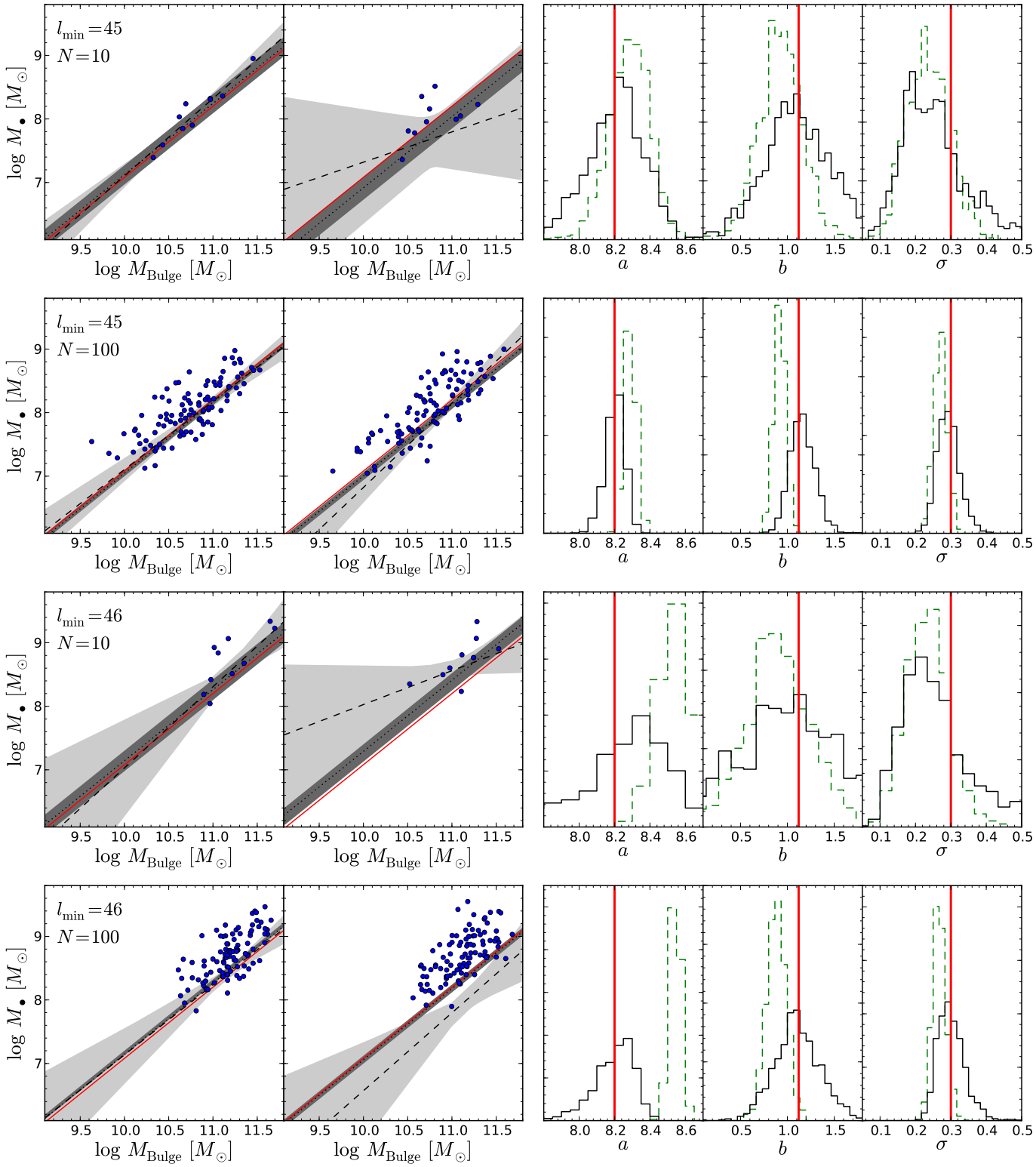

Fig. 6.1. Results of Monte Carlo tests on the fit to the conditional probability distribution of μ given s ($p(\mu\,|\,s,\lambda\,,z)$) for different applied AGN luminosity limits and sample sizes. These two values are always given in the upper left corner of the individual panels. The left subpanels show two examples from the Monte Carlo realisations, a good one and a poor one. The blue circles show the used sample, the red line is the input $M_\bullet - M_{\rm Bulge}$ relation. The black dashed line is the best fit relation when fitting for the zero point a, slope b and intrinsic scatter σ simultaneously, the light grey area is their corresponding 1σ confidence region. The black dotted line and the dark grey area give the best fit to the zero point, with slope and intrinsic scatter fixed, and their confidence region. The three right subpanels show the histograms for the best fit parameters a, b and σ for the full set of 1000 Monte Carlo realisations. The black histograms are for the fit, properly accounting for selection effects, while the green dashed histograms are for a fit, ignoring selection effects. The thick vertical red line indicates the input value. The input relation is better recovered when selection effects are taken into account, although with increased uncertainty.

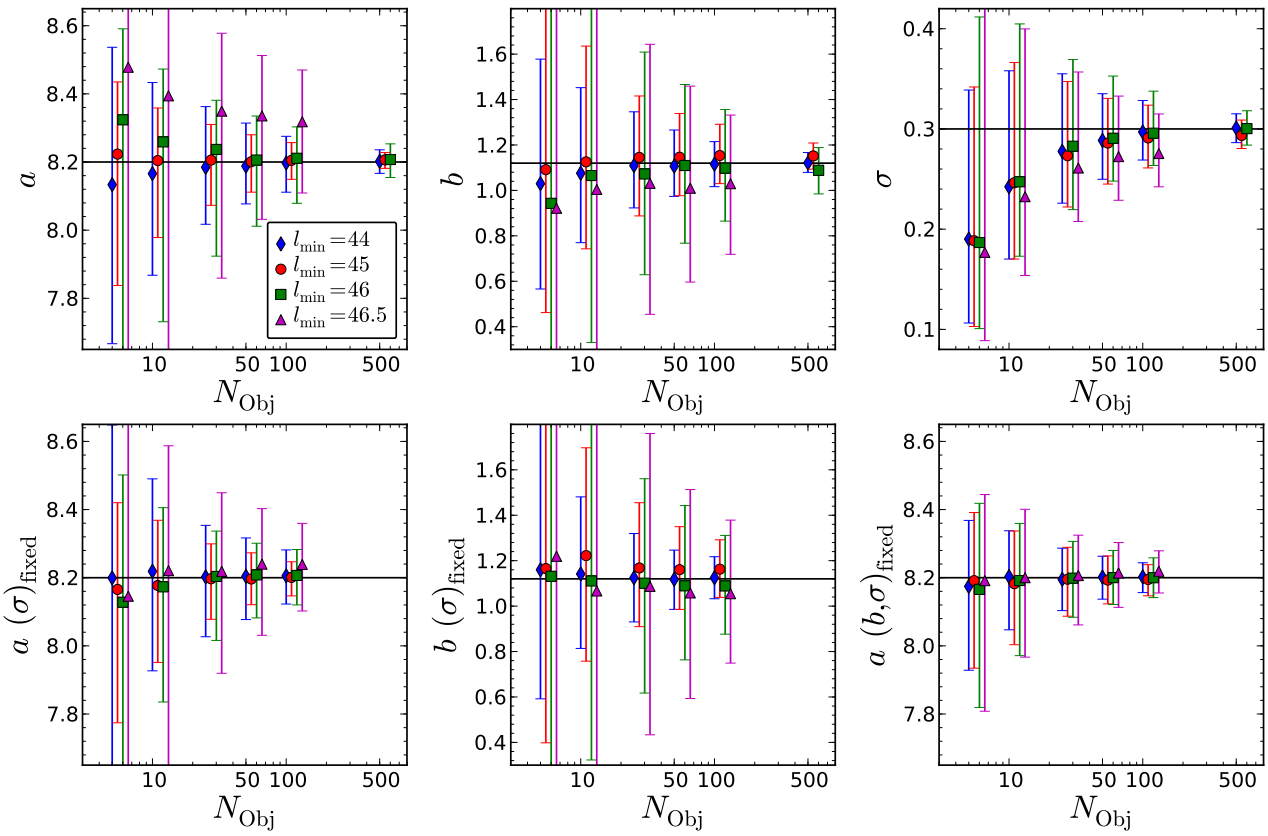

Fig. 6.2. Median results of Monte Carlo tests on the fit to the conditional probability distribution of μ given s ($p(\mu\,|\,s,\lambda\,,z)$) for different applied AGN luminosity limits and sample sizes. In the individual panels, we show the median and the 68% confidence interval of the zero point a, the slope b and the intrinsic scatter σ of the $M_\bullet - M_{\rm Bulge}$ relation for 1000 realisations. In the upper panels all are left free in the fit, while in the lower panels we first fix σ and then also b. We investigated a range of sample sizes ($N_{\rm Obj}$) and assumed AGN luminosity limits ($l_{\rm min}$), with x-positions slightly shifted for better visibility. The horizontal black line indicates the input value.

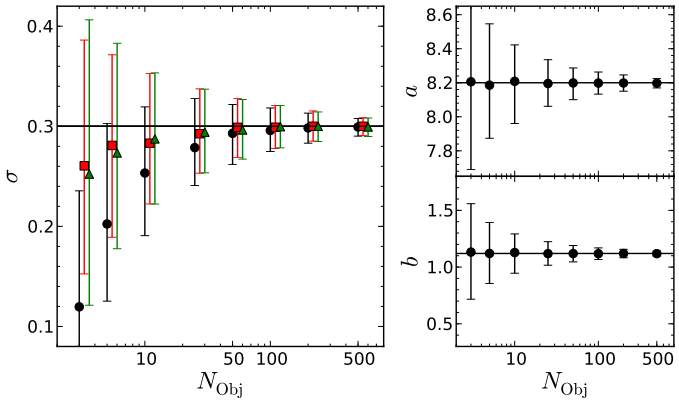

Fig. 6.3. Results for a fit to the intrinsic $M_\bullet - M_{\rm Bulge}$ relation (without selection effects). We show the median and the 68% confidence interval for the fit with a, b and σ as free parameters (black circles) and with a and b fixed (red squares). We recover a and b unbiased. The intrinsic scatter σ is systematically underestimated for a small sample size, because the fit determines the sample standard deviation (green squares) instead of the population standard deviation (black solid line).

we systematically underestimate σ for a small sample size. A smaller value of σ then demands a higher zero point to explain the high mass outliers detected for a bright luminosity limit (the low mass outliers are not detected). The reason for the underestimation of σ is that we are effectively determine the sample standard deviation ($\hat{s} = \sqrt{(n-1)^{-1}\sum_{i=1}^{n}(x_i - \bar{x})}$), which is known to be not an unbiased estimator for the standard deviation σ, but tends to be an underestimate of the true population standard deviation. In Fig. 6.3 we illustrate that this bias is already present in the maximum likelihood fit without the presence of selection effects, while the zero point and slope are unbiased. While the value of σ has no effect on a and b for the fit without selection effects, it is an important quantity for the selection effect correction, and therefore will bias the determination of a and b in our case if it is biased itself. This suggests fixing σ, as we did in the lower panels of Fig. 6.2. In this case a and b are recovered unbiased. Thus, we confirm that we can reconstruct the input $M_\bullet - M_{\rm Bulge}$ relation unbiased with our maximum likelihood fitting method on the conditional probability distribution $p(\mu\,|\,s,\lambda\,,z)$.

In Figures 6.4 and 6.5 we show similar results, but for the fit to the conditional probability $p(s\,|\,\mu)$. We also find that the intrinsic scatter is underestimated for a small sample size, as discussed above. The slope b seems to be systematically over-

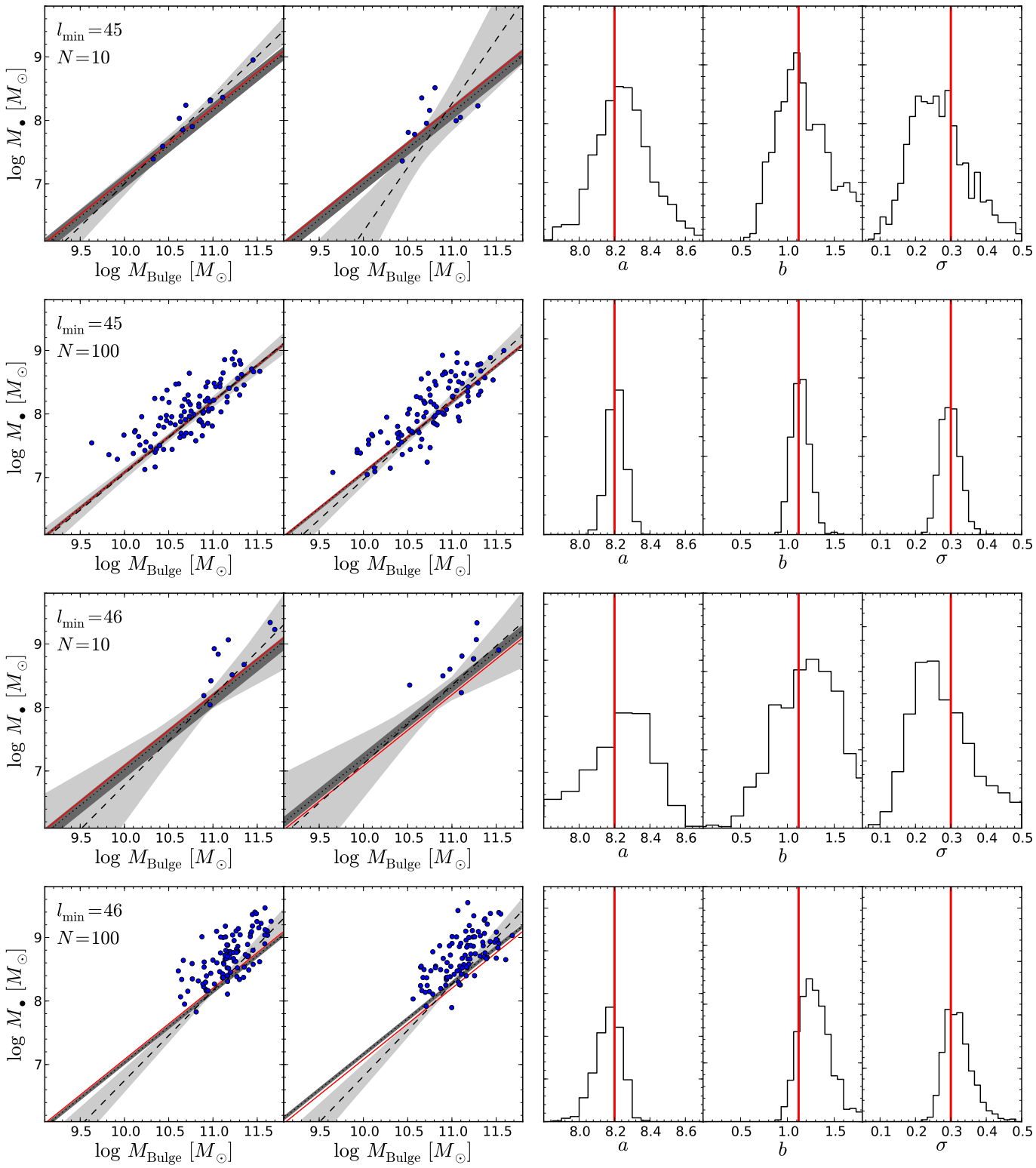

Fig. 6.4. Same as Fig. 6.1, but for the fit to the conditional probability distribution of s given μ ($p(s\,|\,\mu)$). In the left subpanels we show exactly the same examples as in Fig. 6.1 and their respective results for the fit to $p(s\,|\,\mu)$.

estimated for a small sample size and in particular for a bright luminosity limit. This may indicate a limitation of this fitting option for data that are sampled from the decreasing part of the spheroid mass function. There may be also an issue with the used Monte Carlo sample, as this was constructed over a predefined, fixed range in bulge mass. However, we find that the zero point a is well recovered in the median, in particular if the slope b and the intrinsic scatter σ are fixed.

As we are interested in the evolution of the $M_\bullet$ – $M_{\rm Bulge}$ relation with redshift, we can also fix the local relation and only fit for their redshift evolution, given a flux limited AGN sample in a specific redshift range. As an example,

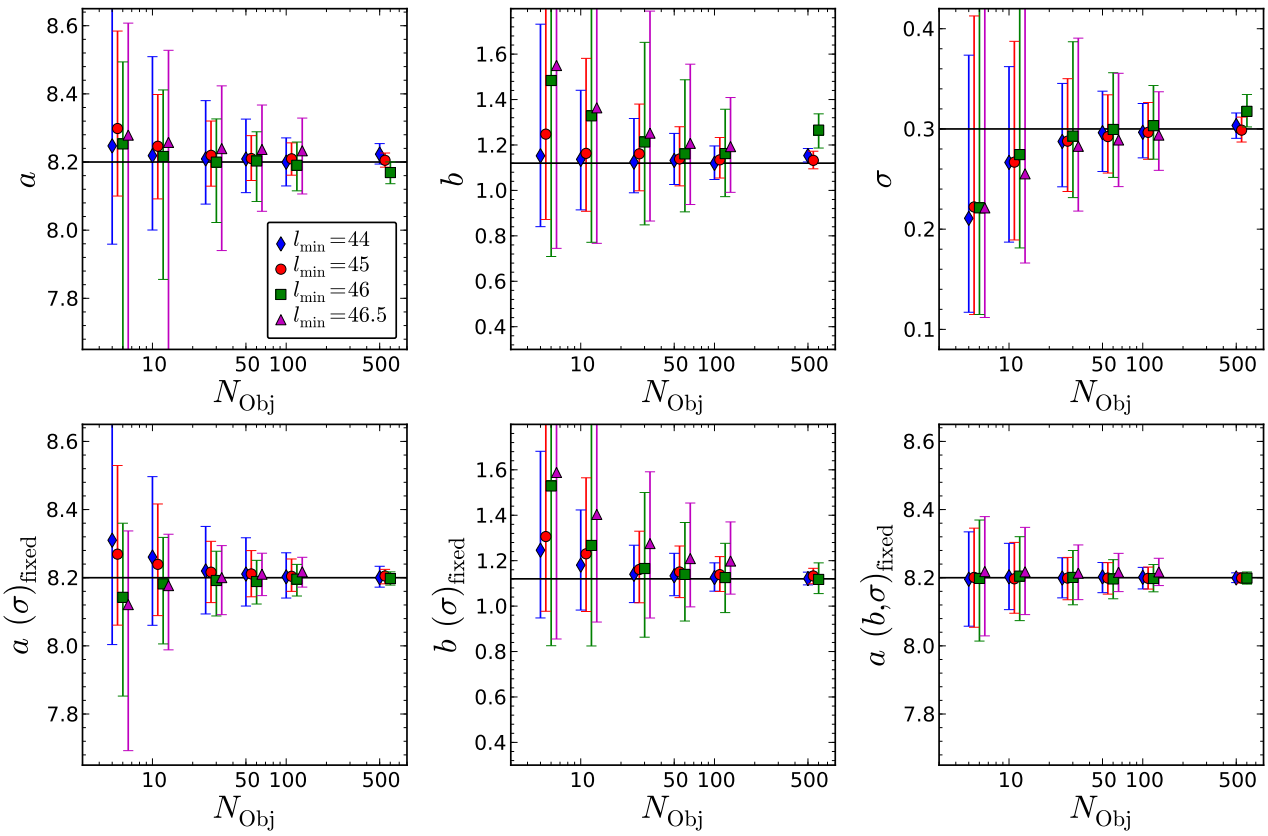

Fig. 6.5. Same as Fig. 6.2, but for the fits to the conditional probability distribution of s given μ, $p(s\,|\,\mu)$.

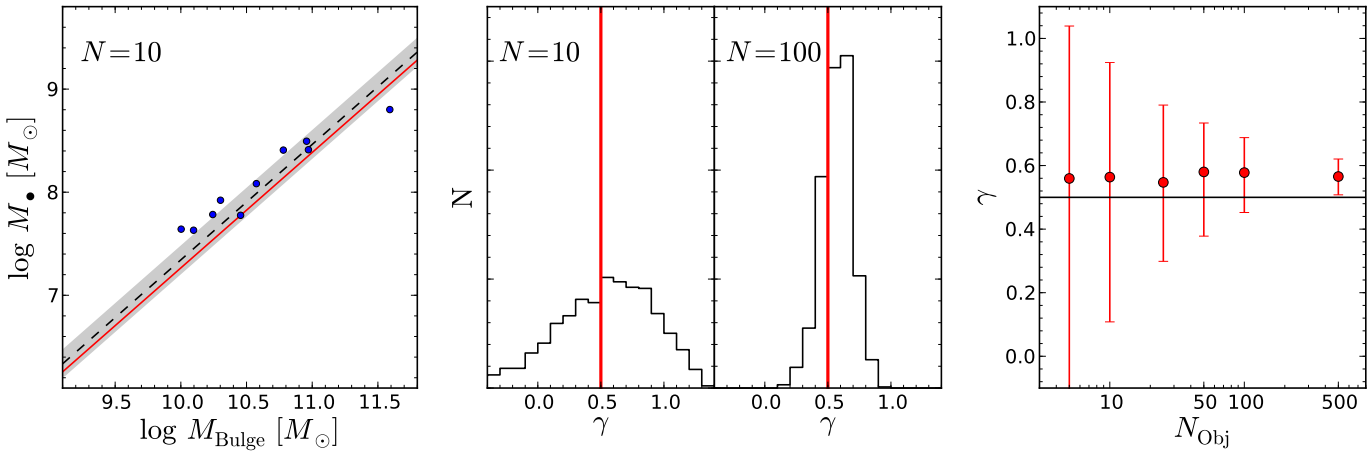

Fig. 6.6. Results of Monte Carlo test for a fit to redshift evolution in the $M_\bullet - M_{\rm Bulge}$ relation. A flux limited sample, with magnitude limit of 22 mag in the B band, in the redshift range $1 < z < 2$ and mild redshift evolution $\gamma = 0.5$ has been generated and fitted to the conditional probability $p(\mu\,|\,s, \log\lambda\,, z)$. We fixed the local relation and fitted for the evolution term γ. The left panel shows an example for a sample of 10 objects (blue circles). The red solid line gives the input relation at the mean redshift of the sample, the black dashed line shows the best fit relation at the same mean redshift and the grey area indicates the 1σ confidence region. The middle panels show the histogram of γ values for 1000 realisations, for sample sizes of 10 and 100 objects. The red vertical line gives the input value. The right panel shows the dependence of the median value and the 68% confidence interval on the sample size (red circles and error bars). The black line indicates the input value.

we generated a Monte Carlo sample with B band flux limit of 22 mag in the redshift range $1 < z < 2$, drawn from the local distribution functions (see section 5.3.1). We assumed a redshift evolution in the zero point $a(z) = a_0 + \gamma \log(1 + z)$ and chose a mild evolution case of $\gamma = 0.5$ for our example. We again chose different sample sizes and generated 1000 Monte Carlo realisations for each sample size. We fitted for γ, fixing the other parameters. The results are shown in Fig. 6.6 for the conditional probability $p(\mu\,|\,s, \lambda\,, z)$ and in Fig. 6.7 for the conditional probability $p(s\,|\,\mu, z)$. In both cases we recover the input evolution slope γ fairly well. However, we seem to slightly overestimate γ for the $p(\mu\,|\,s, \log\lambda\,, z)$ fit and underestimate it for the $p(s\,|\,\mu, z)$

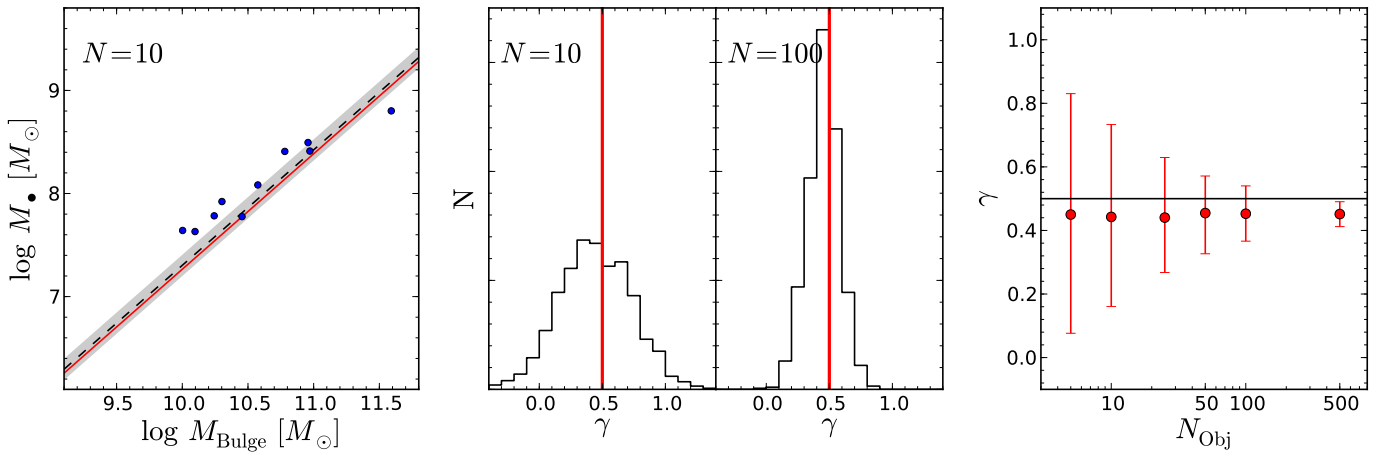

Fig. 6.7. Same as Fig. 6.6, but for the conditional probability distribution $p(s\,|\,\mu, z)$.

fit by ~ 0.05 dex, respectively. We have to admit that we do not fully understand the reason for this deviation yet. It may indicate a limitation in our method, in our implementation of it, or may indicate an issue with the Monte Carlo sample. Anyway, a further investigation of this issue is demanded. Nevertheless, this effect is much smaller than current other uncertainties, and our results are consistent with the input value with at least 1σ confidence. Given a large enough statistical sample, the null hypothesis of no evolution in the $M_\bullet - M_{\rm Bulge}$ relation can be excluded confidently. Even for a small sample, the no evolution case deviates from the best fit by more than 1σ.

Thus, we conclude that our fitting method is already a significant improvement over a direct assessment of the $M_\bullet - M_{\rm Bulge}$ relation in evolutionary studies, in principle able to recover an underlying evolutionary trend. However, an important issue that we have ignored so far is the influence of measurement uncertainties in the black hole mass and galaxy property on our method.

6.4. Measurement uncertainties

So far, we neglected measurement errors on μ and s. However, ignoring them in the fitting approach can lead to its own bias. Here, we discuss measurement uncertainties and their consequences separately for μ and for s. We first discuss the effect on the fit to the conditional probability $p(\mu\,|\,s, \lambda\,, z)$ and then briefly comment on the implications for the fit to $p(s\,|\,\mu, z)$.

If we have measurement uncertainties in μ, the main effect will be a smoothing of the probability distribution in the μ direction, without affecting the slope and normalisation of the recovered relation, as already discussed in section 5.3.2. Following this discussion we have to use $\Psi_{\rm o}(s, \mu_{\rm o})$, given by Equation (5.22), to compute the conditional probability for the maximum likelihood fit. The probability distribution is then given by

$$p(\mu_{\rm o}\,|\,s, \lambda\,, z) = \frac{\int \Psi_{\rm o}(s, \mu, \lambda\,, z)\, g(\mu_{\rm o}\,|\,\mu)\, {\rm d}\mu}{\int \Psi_{\rm o}(s, \mu, \lambda\,, z)\, g(\mu_{\rm o}\,|\,\mu)\, {\rm d}\mu{\rm d}\mu_{\rm o}} = \frac{\int \Omega\, p_{\rm ac}(\mu, z)\, g(\mu\,|\,s, z)\, g(\mu_{\rm o}\,|\,\mu)\, {\rm d}\mu}{\int \Omega\, p_{\rm ac}(\mu, z)\, g(\mu\,|\,s, z)\, {\rm d}\mu}\,, \tag{6.8}$$

with $g(\mu_{\rm o}\,|\,\mu)$ given by Equation (5.21). Thus, if we know the uncertainty in the black hole mass, usually the uncertainty in the virial method (e.g. Vestergaard & Peterson 2006), it is straightforward to incorporate it into the likelihood estimate.

Secondly, we discuss the effect of measurement uncertainties in the bulge property s. As discussed in section 5.3.3, contrary to the black hole mass, this uncertainty will change the slope of the respective $M_\bullet$–bulge relation. On the other hand, the normalisation is not affected. For the conditional probability follows

$$p(\mu\,|\,s_{\rm o}, \lambda\,, z) = \frac{\int \Psi_{\rm o}(s, \mu, \lambda\,, z)\, g(s_{\rm o}\,|\,s)\, ds}{\int \Psi_{\rm o}(s, \mu, \lambda\,, z)\, g(s_{\rm o}\,|\,s)\, ds{\rm d}\mu} = \frac{\int \Omega\, p_{\rm ac}(\mu, z)\, g(\mu\,|\,s, z)\, g(s_{\rm o}\,|\,s)\, \Phi_s(s)\, ds}{\int \Omega\, p_{\rm ac}(\mu, z)\, g(\mu\,|\,s, z)\, g(s_{\rm o}\,|\,s)\, \Phi_s(s)\, ds{\rm d}\mu}\,. \tag{6.9}$$

While at least the Eddington ratio distribution cancels, the galaxy distribution function remains in the conditional probability distribution in this case, complicating the situation. Thus, for an unbiased fit, we again have to know or assume the shape of the galaxy distribution function.

When there is measurement uncertainty in s and μ, the conditional probability is

$$p(\mu_{\rm o}\,|\,s_{\rm o}, \lambda\,, z) = \frac{\int \Omega\, p_{\rm ac}(\mu, z)\, g(\mu\,|\,s, z)\, \Phi_s(s)\, g(s_{\rm o}\,|\,s)\, g(\mu_{\rm o}\,|\,\mu)\, {\rm d}s{\rm d}\mu}{\int \Omega\, p_{\rm ac}(\mu, z)\, g(\mu\,|\,s, z)\, \Phi_s(s)\, g(s_{\rm o}\,|\,s)\, {\rm d}s{\rm d}\mu}\,. \tag{6.10}$$

For the fit to the conditional probability $p(s\,|\,\mu, z)$ the reverse is true. Measurement uncertainty in s only broadens the conditional probability and can be directly accounted for if the uncertainty is known,

$$p(s_{\rm o}\,|\,\mu, z) = \frac{\int \Psi_{\rm o}(s, \mu, \lambda\,, z)\, g(s_{\rm o}\,|\,s)\, {\rm d}s}{\int \Psi_{\rm o}(s, \mu, \lambda\,, z)\, g(s_{\rm o}\,|\,s)\, {\rm d}s{\rm d}s_{\rm o}} = \frac{\int g(\mu\,|\,s)\, \Phi_s(s)\, g(s_{\rm o}\,|\,s)\, {\rm d}s}{\int g(\mu\,|\,s)\, \Phi_s(s){\rm d}s}\,. \tag{6.11}$$

However, uncertainty in μ introduces a dependence on the AGN selection that is absent otherwise. The conditional probability

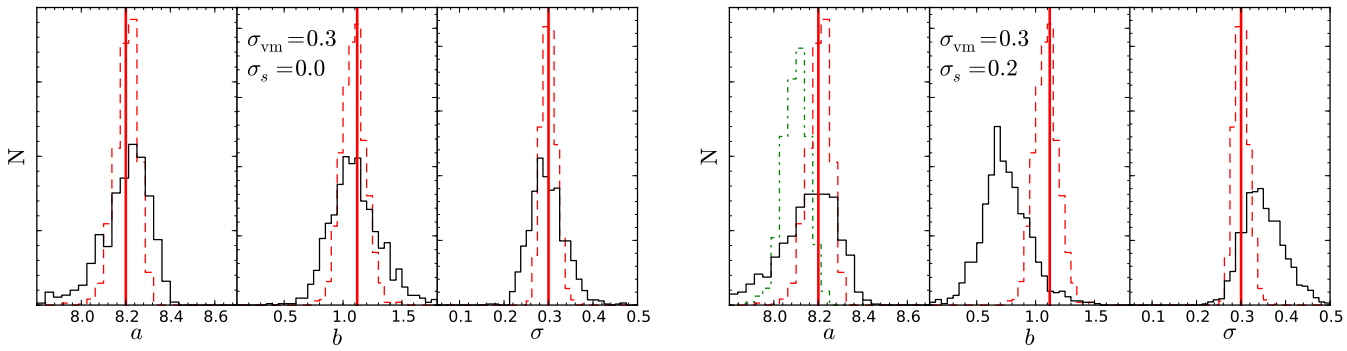

Fig. 6.8. Monte Carlo results for the fit to the conditional probability distribution $p(\mu \,|\, s, \log \lambda\,, z)$ with measurement uncertainties. We show the histograms of the best fit parameters for 1000 realisations of a sample of 500 objects with AGN luminosity limit $l_{\rm min} = 46$. The red dashed histograms are for realisations without measurement uncertainties, the solid black histograms are for realisations with measurement uncertainty, as indicated in the respective middle subpanel. In the fit, we only accounted for measurement uncertainty in μ, but not in s. In the right panel, the green dashed dotted histogram shows the distribution of a, with b and σ fixed to the input value.

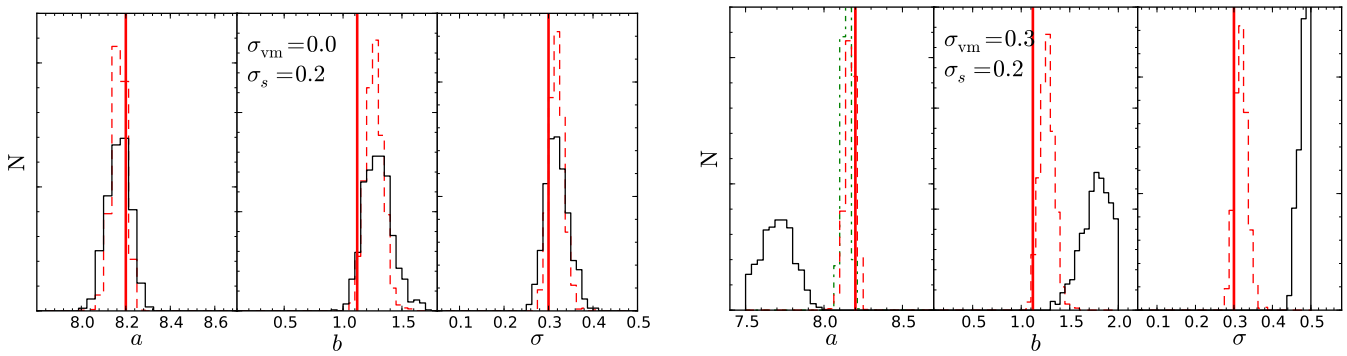

Fig. 6.9. Monte Carlo results for the fit to the conditional probability distribution $p(s \,|\, \mu, z)$ with measurement uncertainties. We show the histograms of the best fit parameters for 1000 realisations of a sample of 500 objects with AGN luminosity limit $l_{\rm min} = 46$. The red dashed histograms are for realisations without measurement uncertainties, the solid black histograms are for realisations with measurement uncertainty, as indicated in the respective middle subpanel. In the fit, we only accounted for measurement uncertainty in s, but not in μ. In the right panel, the green dashed dotted histogram shows the distribution of a, with b and σ fixed to the input value.

in this case becomes

$$p(s \,|\, \mu_{\rm o}, \lambda\,, z) = \frac{\int \Psi_{\rm o}(s, \mu, \lambda\,, z)\, g(\mu_{\rm o} \,|\, \mu)\, {\rm d}\mu}{\int \Psi_{\rm o}(s, \mu, \lambda\,, z)\, g(\mu_{\rm o} \,|\, \mu)\, {\rm d}s{\rm d}\mu} \qquad (6.12)$$

$$= \frac{\int \Omega\, p_{\rm ac}(\mu, z)\, g(\mu \,|\, s, z)\, g(\mu_{\rm o} \,|\, \mu)\, \Phi_s(s)\, {\rm d}\mu}{\int \Omega\, p_{\rm ac}(\mu, z)\, g(\mu \,|\, s, z)\, g(\mu_{\rm o} \,|\, \mu)\, \Phi_s(s)\, {\rm d}s{\rm d}\mu}\,.$$

Thus, a dependence on the active fraction and the selection function is introduced into the conditional probability through the measurement uncertainty in μ.

We also ran first Monte Carlo tests, incorporating measurement uncertainties. We show our results for an example of an AGN luminosity limit of $l_{\rm min} = 46$ and a sample size of 500 in Fig. 6.8 for the fit to $p(\mu \,|\, s, \lambda\,, z)$ and in Fig. 6.9 for the fit to $p(s \,|\, \mu, z)$. In the left panel of Fig. 6.8 we add a log-normal error of $\sigma_{\rm vm} = 0.3$ dex to the samples and fit them with the conditional probability distribution of Equation (6.9), thus accounting for this error. For comparison we also show the histogram of the results without measurement uncertainties as dashed red lines. The input relation is equally well recovered, only with increased dispersion. Next, we add an additional log-normal error of $\sigma_s = 0.2$ dex to the spheroid mass. The histograms in the right panel of Fig. 6.8 show the results using $p(\mu_{\rm o} \,|\, s, \lambda\,, z)$ from Equation (6.9), i.e accounting for $\sigma_{\rm vm}$, but ignoring the error in the spheroid mass. While the zero point is reasonably well recovered, the slope is underestimated, a result already expected from our discussion in section 5.3.3. However, we also fixed the slope b and intrinsic scatter σ and fitted only for the zero point. The result is given by the dashed dotted histogram. The input value is almost recovered, but slightly underestimated by ~ 0.1 dex. On the other hand, when we use the proper conditional probability for this case, given by Equation (6.10), and again have a as only free parameter, we properly recover the input value in the median.

Next, we investigated the fit to the conditional probability distribution $p(s \,|\, \mu, z)$. We first added a log-normal error of $\sigma_s = 0.2$ dex to the spheroid mass and fitted the samples with the conditional probability distribution of Equation (6.12), i.e accounting for σ_s. We show the results in the left panel of Fig. 6.9. The input value is also as well recovered as without measurement uncertainties, just with larger dispersion. Then we added an error of $\sigma_{\rm vm} = 0.3$ dex to the black hole mass and

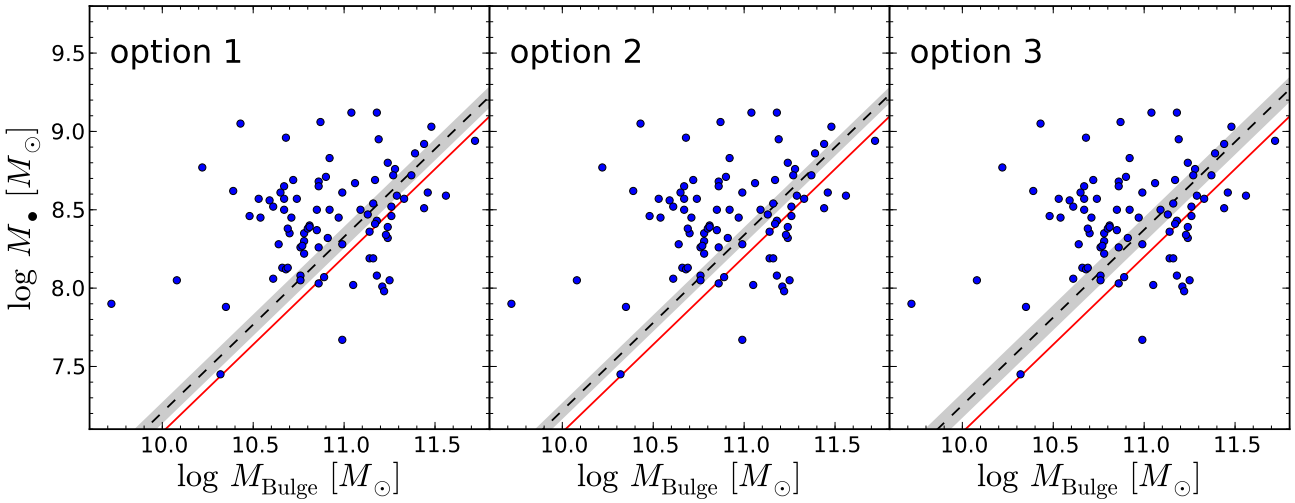

Fig. 6.10. Redshift evolution fit to the QSO sample from Merloni et al. (2010). We fitted their data (blue circles) to the conditional probability distributions $p(\mu_o \,|\, s, \lambda, z)$ (option 1; left panel), $p(s_o \,|\, \mu, z)$ (option 2; middle panel), and $p(\mu_o \,|\, s_o, \lambda, z)$ (option 3; right panel), determining the evolution term γ. The red solid line shows the local relation from Häring & Rix (2004), the black dashed line gives the best fit relation at the mean redshift of the sample. The grey area is the 1σ confidence region. A mild redshift evolution is implied

fitted the samples with the same conditional probability distribution, thus ignoring this error. The result is given in the right panel of Fig. 6.9. When all parameters are left free, the result is strongly biased. However, when the slope and the intrinsic scatter are fixed, the zero point is closely recovered, underestimated by only ~ 0.05 dex.

Thus, when we are interested in the redshift evolution in the $M_\bullet - M_{\rm Bulge}$ relation the most reliable approach is to fix the slope and the intrinsic scatter and only fit for the zero point a, which is expected to vary with redshift. This is particularly true if the dynamical range of the observations is small. In the spirit of presenting preliminary results, we suggest three possible options to fit the $M_\bullet - M_{\rm Bulge}$ relation under the presence of AGN selection effects and measurement uncertainties in both variables.

1. Fit the conditional probability $p(\mu_o \,|\, s, \lambda, z)$ given by Equation (6.9), i.e. accounting for the error in μ, but not in s.
2. Fit the conditional probability $p(s_o \,|\, \mu, z)$ given by Equation (6.12), i.e. accounting for the error in s, but not in μ.
3. Fit the conditional probability $p(\mu_o \,|\, s_o, \lambda, z)$ given by Equation (6.10), i.e. accounting for the error in μ and s.

The advantage of the first two options is that they individually require less assumptions on the underlying distribution functions and they are computationally less expensive. However, they only use a simplified estimate of the true conditional probability, and hence may be slightly biased. The third option is more precise, but requires more assumptions. In principle, we could also fit to $p(s_o \,|\, \mu_o, \lambda, z)$, accounting for the error in μ and s, but this estimate deviates from the third option only slightly, requiring the same information, so we neglect it. In the following, we will use all three options to derive constraints on observational studies on evolution in the $M_\bullet - M_{\rm Bulge}$ relation.

6.5. Application to observational studies

We further illustrate our fitting method to the $M_\bullet$–bulge relations and their evolution by applying it to a few observational studies. This requires assumptions on the mass dependence of the active fraction and on the galaxy distribution function. We assumed a constant active fraction. The mass dependence of the active fraction at high redshifts is not well known, but is probably flattening compared to $z = 0$ (Merloni & Heinz 2008; Shankar et al. 2009), thus a constant active fraction is a reasonable assumption. It also provides an upper limit to the evolution in the $M_\bullet - M_{\rm Bulge}$ relation, when we assume that the active fraction will not increase with mass in this redshift range. For the galaxy spheroid mass function we used our high redshift estimate, presented in section 5.4.2. To investigate the degree of evolution, we again assumed a redshift evolution in the zero point $a(z) = a_0 + \gamma \log(1+z)$, fixed the local relation to the values from Häring & Rix (2004) and fitted for the evolution term γ.

The first study we investigated is the QSO sample from Merloni et al. (2010), already discussed in section 5.5. We took their data, computed bolometric luminosities and Eddington ratios, and applied their $I_{\rm AB}$-band flux limit of 22.5. We fitted all three options for the conditional probability distributions to the data. The results are shown in Fig. 6.10. For the fit to the conditional probability $p(\mu_o \,|\, s, \lambda, z)$ we get $\gamma_{\mu,s} = 0.32 \pm 0.16$, for the fit to the conditional probability $p(s_o \,|\, \mu, z)$ we found $\gamma_{s,\mu} = 0.35 \pm 0.12$ and for the fit to $p(\mu_o \,|\, s_o, \lambda, z)$, fully incorporating measurement uncertainties, we obtain $\gamma_{\mu_o,s_o} = 0.43^{+0.18}_{-0.19}$. It is reassuring and encouraging that all estimates are fully consistent with each other. They all indicate mild evolution in the $M_\bullet - M_{\rm Bulge}$ relation. However, the null hypothesis of no evolution in the $M_\bullet - M_{\rm Bulge}$ relation lies formally within 2σ of our results, thus it is not rejected with statistical significance. Furthermore, note that our stated confidence region only accounts for the statistical uncertainty. We have fixed our assump-

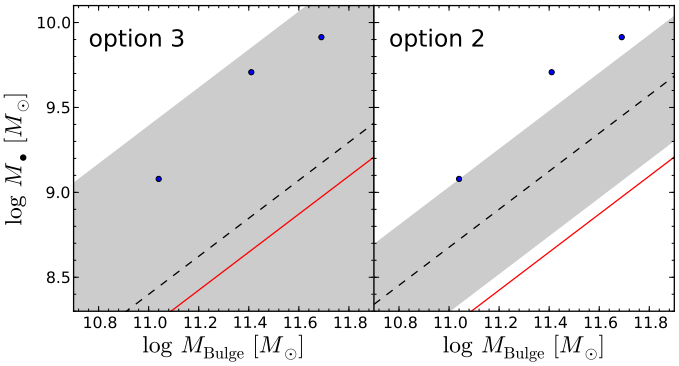

Fig. 6.11. Redshift evolution fit to the QSO sample from Schramm et al. (2008). We fitted their data (blue circles) to the conditional probability distributions $p(\mu_o \,|\, s_o, \lambda, z)$ (left panel) and $p(s_o \,|\, \mu, z)$ (right panel), determining the evolution term γ. The red solid line shows the local relation from Häring & Rix (2004), the black dashed line gives the best fit relation at the mean redshift of the sample. The grey area is the 1σ confidence region. As the sample is small, the uncertainty on the evolution is large.

tions on the underlying distribution functions and the uncertainty in $M_\bullet$ and M_*. Uncertainties in these assumptions further increase the errors on the best fit solution. Thus, our stated errors are probably too optimistic.

Alternatively, we can assume no evolution in the zero point a of the $M_\bullet - M_{\rm Bulge}$ relation, but instead in the intrinsic scatter. We parametrised this evolution as $\sigma(z) = \sigma_0 + \delta \log(1+z)$, assuming $\sigma_0 = 0.3$. We again fixed the local relation and fitted the conditional probability $p(s_o \,|\, \mu, z)$ to the data with δ as only free parameter. We obtained $\delta = 0.18^{+0.13}_{-0.12}$, corresponding to $\sigma(z = 1.5) = 0.37$. Thus, also a mild evolution in the intrinsic scatter provides an adequate fit to the data.

The sample by Merloni et al. (2010) is well suited for our study, as it provides a relative large sample which also covers the faint end of the AGN luminosity function. But, we also want to illustrate the constraints we can derive from this methods from a sample with small sample size, only covering bright QSOs. For this purpose, we used the sample from (Schramm et al. 2008), which we also already discussed in section 5.5. We adopt a B-band flux limit of 18 mag and again assume a constant active fraction and our estimate of the spheroid mass function. The results are shown in Fig. 6.11. For the fit to the conditional probability $p(\mu_o \,|\, s, \lambda, z)$ we get $\gamma_{\mu,s} = 0.93^{+1.16}_{-\infty}$, for the fit to the conditional probability $p(s_o \,|\, \mu, z)$ we derive $\gamma_{s,\mu} = 0.82^{+0.61}_{-0.69}$ and from $p(\mu_o \,|\, s_o, \lambda, z)$ we obtain $\gamma_{\mu_o,s_o} = 0.34^{+1.73}_{-\infty}$. All constraints are consistent with each other, but the uncertainties in the fits to $p(\mu_o \,|\, s, \lambda, z)$ and $p(\mu_o \,|\, s_o, \lambda, z)$ are substantial. These results are also consistent with the constraints we derived above from the Merloni et al. (2010) QSO sample. They also tentatively suggest at least a mild redshift evolution in the $M_\bullet - M_{\rm Bulge}$ relation. For an evolution in the intrinsic scatter we get $\delta = 0.17^{+1.37}_{-2.75}$, with large uncertainty.

6.6. Conclusions

We here presented a novel fitting method to the $M_\bullet$–bulge relations and their evolution. This is based on a maximum likelihood fit to two independent conditional probability distributions, the probability of finding a specific black hole mass μ for a given spheroid property s, $p(\mu \,|\, s)$, and the probability to find a specific galaxy property s given a black hole with mass μ, $p(s \,|\, \mu)$. As already discussed in Chapter 5, the former is affected by the AGN selection, while the latter is affected by the shape of the galaxy distribution function. If these effects are well understood and known, both can be used to determine the underlying intrinsic relation.

We presented the theoretical framework for this approach and verified its reliability by means of Monte Carlo simulations. We also took into account the effect of measurement uncertainties in μ and s. When measurement uncertainties in the variables μ and s have to be considered, the dependencies on the respective distribution functions and selection function for both conditional probability distributions become entangled and they all need to be taken into account for a proper determination of the intrinsic relation. We suggest three practical solutions to determine the intrinsic relation from observational data. In any case, the best fit is achieved by fixing the slope and intrinsic scatter and fit for the zero point as only free parameter.

We illustrated the ability of our method to constrain the evolution in the $M_\bullet - M_{\rm Bulge}$ relation by applying it to two observational studies, the zCOSMOS QSO sample from Merloni et al. (2010) and the small bright QSO sample from Schramm et al. (2008). Their data reveal evidence for mild redshift evolution, either in the zero point or in the intrinsic scatter of the $M_\bullet - M_{\rm Bulge}$ relation.

Our presented technique still needs further tests, but already shows promising prospects for a better understanding of the $M_\bullet - M_{\rm Bulge}$ relation and its evolution. Compared to our estimates in Chapter 5, this method allows a strict statistical statement on the evolution in the $M_\bullet$–bulge relations, including confidence intervals.

References

Gültekin, K., Richstone, D. O., Gebhardt, K., et al. 2009, ApJ, 698, 198
Häring, N. & Rix, H.-W. 2004, ApJ, 604, L89
Merloni, A., Bongiorno, A., Bolzonella, M., et al. 2010, ApJ, 708, 137
Merloni, A. & Heinz, S. 2008, MNRAS, 388, 1011
Schramm, M., Wisotzki, L., & Jahnke, K. 2008, A&A, 478, 311
Shankar, F., Bernardi, M., & Haiman, Z. 2009, ApJ, 694, 867
Vestergaard, M. & Peterson, B. M. 2006, ApJ, 641, 689

Chapter 7

Effect of a dark matter halo on the determination of black hole masses⋆

Andreas Schulze[1] and Karl Gebhardt[2]

[1] Leibniz-Institut für Astrophysik Potsdam (AIP), An der Sternwarte 16, 14482 Potsdam, Germany
[2] Department of Astronomy, The University of Texas at Austin, 1 University Station, C1400, Austin, TX 78712, USA

ABSTRACT

Stellar dynamical modeling is a powerful method to determine the mass of black holes in quiescent galaxies. However, in previous work the presence of a dark matter halo has been ignored in the modeling. Gebhardt & Thomas (2009) showed that accounting for a dark matter halo increased the black hole mass of the massive galaxy M87 by a factor of two. We used a sample of 12 galaxies to investigate the effect of accounting for a dark matter halo in the dynamical modeling in more detail, and also updated the masses using improved modeling. The sample of galaxies possesses *Hubble Space Telescope* and ground-based observations of stellar kinematics. Their black hole masses have been presented before, but without including a dark matter halo in the models. Without a dark halo, we find a mean increase in the estimated mass of 1.5 for the whole sample compared to previous results. We attribute this change to using a more complete orbit library. When we include a dark matter halo, along with the updated models, we find an additional increase in black hole mass by a factor of 1.2 in the mean, much less than for M87. We attribute the smaller discrepancy in black hole mass to using data that better resolve the black hole's sphere of influence. We redetermined the $M_\bullet - \sigma_*$ and $M_\bullet - L_V$ relationships using our updated black hole masses and found a slight increase in both normalization and intrinsic scatter.

7.1. Introduction

It is now well established that almost every massive galaxy harbors a supermassive black hole in its center. Furthermore, close relations between the mass of this supermassive black hole and the properties of the galaxy's spheroid component have been found, namely with the mass (Magorrian et al. 1998; Häring & Rix 2004), luminosity (Kormendy & Richstone 1995; Kormendy & Gebhardt 2001; Marconi & Hunt 2003; Gültekin et al. 2009b), and with the velocity dispersion (Gebhardt et al. 2000a; Ferrarese & Merritt 2000; Tremaine et al. 2002; Gültekin et al. 2009b). These relations imply a link between the growth of black holes and galaxy evolution, usually attributed to active galactic nucleus (AGN) feedback (e.g., Silk & Rees 1998; Di Matteo et al. 2005; Springel et al. 2005; Ciotti & Ostriker 2007), but at least to some degree they are a natural result within a merger-driven galaxy evolution framework (Peng 2007; Hirschmann et al. 2010; Jahnke & Maccio 2010). In general, the black hole-bulge relations and especially their evolution with cosmic time are able to provide deep insight into galaxy formation and black hole growth. Therefore, it is essential to properly establish the local relationships as precisely as possible.

The black hole-bulge relations are based on a sample of $\sim$ 50 quiescent black holes, whose masses have been determined based on maser emission (e.g., Greenhill et al. 2003; Herrnstein et al. 2005; Kuo et al. 2011), gas kinematics (e.g., Ferrarese et al. 1996; Marconi et al. 2001; Dalla Bontà et al. 2009), and stellar kinematics (e.g., van der Marel et al. 1998; Gebhardt et al. 2000b; Shapiro et al. 2006; Gebhardt et al. 2007; Gültekin et al. 2009a). In particular, stellar dynamical modeling using orbit superposition is a powerful method to estimate black hole masses in quiescent galaxies, also recovering the orbital structure within the galaxy. Usually, axisymmetry is assumed in these models. However, there are still uncertainties and possibly systematic biases within these methods. Uncertainties may arise from the deprojection of the observables onto three dimensions as the true inclination of the galaxy often is not well known, the presence of dust, some triaxiality that cannot be modeled properly with axisymmetric models (van den Bosch & de Zeeuw 2010), or the presence of an AGN at the center. So far, in most models the contribution of the galaxy's dark matter (DM) halo has been neglected. Gebhardt & Thomas (2009) recently showed that the black hole mass can be underestimated in this case. For the massive galaxy M87 they found an increase of more than a factor of two in the measured black hole mass, just by including a DM halo in the modeling. The reason is that without a DM halo the mass-to-light ratio is overestimated in order to account for the mass in the outer parts of the galaxy. Under the usually applied assumption of a constant mass-to-light ratio for the whole galaxy, this will propagate inward and lead to an underestimation of the black hole mass at the center due to overestimation of the stellar contribution.

A similar result has been obtained by McConnell et al. (2011). They measured the black hole mass in the brightest cluster galaxy NGC 6086. They report a factor of six difference between the black hole mass obtained from models without a DM halo and their most massive DM halo models. However,

⋆ This chapter is published in *Astrophysical Journal*, 2011, 729, 21.

the black hole's sphere of influence is barely resolved in their work.

Shen & Gebhardt (2010) found for NGC 4649, also a massive galaxy, no change in the black hole mass by including a DM halo. In this case the sphere of influence is well resolved by the data. A larger sample, especially spanning a larger range in mass, is clearly required.

Gebhardt et al. (2003) (hereafter G03) studied a sample of 12 galaxies with kinematics derived from *Hubble Space Telescope* (*HST*) and ground-based observations, using axisymmetric orbit superposition models. They do not include a DM halo in their modeling. Since then the orbit superposition code used by our group has been improved (Thomas et al. 2004, 2005; Siopis et al. 2009), by including a more complete orbit sampling.

The aim of this paper is to reanalyze the data set presented by G03, using the most up-to-date dynamical modeling code and investigating the effect of accounting for the dark matter contribution on the derived black hole masses. One of the galaxies in the G03 sample, NGC 4649, was recently analyzed by Shen & Gebhardt (2010), including a DM halo. We have reanalyzed this galaxy for consistency with the remaining sample, but find consistent results with this previous investigation.

7.2. Data

The data set used in this work is identical to those used in the work of G03. Thus, we will only give a brief summary and refer to G03 for more detail. The data consist of three sets of observations for each galaxy: imaging, *HST* stellar kinematics, and ground-based stellar kinematics.

High-resolution imaging is required to obtain the stellar surface brightness profile for each galaxy. This imaging has been obtained in the V band with the *HST* WFPC2 (Lauer et al. 2005), except for NGC 4697, which was observed with the *HST* WFPC1 (Lauer et al. 1995). Surface brightness profiles were measured from the pont-spread function deconvolved images and were augmented with ground-based imaging at the outer parts, not covered by *HST*. For the deprojection of the surface brightness profile to a luminosity density profile, we assume axisymmetry, an inclination angle of 90°, which we refer to as edge-on, and used the technique outlined in Gebhardt et al. (1996).

The *HST* observations and kinematics are presented by Pinkney et al. (2003) and G03. They consist of Space Telescope Imaging Spectrograph (STIS) long-slit spectra along the major axes, except for NGC 3377 and NGC 5845, which have Faint Object Spectrograph (FOS) aperture spectra. The spectra cover the Ca 2 triplet around 8500 Å. For the dynamical modeling, the line-of-sight velocity distributions (LOSVDs), extracted from the spectra, are used. The LOSVDs are given in a non-parametric form, binned into 15 equidistant bins, compared to 13 bins in G03.

The ground-based kinematics are presented by Pinkney et al. (2003) and G03 as well. They consist of long-slit spectra along several position angles, mainly obtained at the MDM observatory. They also cover the Ca 2 triplet, or alternatively the Mg*b* absorption at 5175 Å. The individual LOSVDs are binned into 15 points as well.

7.3. Dynamical Models

The dynamical modeling uses the orbit superposition method, first proposed by Schwarzschild (1979). This general method has been widely used by various groups (Rix et al. 1997; van der Marel et al. 1998; Cretton et al. 1999; Valluri et al. 2004). Our technique is described in detail in G03, Thomas et al. (2004, 2005) and Siopis et al. (2009). We will give a brief summary here and especially point out the differences compared to the work of G03. The basic approach consists of the following steps: (1) deprojection of the surface brightness profile to a three-dimensional luminosity distribution, (2) computation of the specified gravitational potential, (3) generation of a representative orbit library in this potential, (4) fitting the orbit library to the observed light distribution and kinematics, and (5) modifying the input potential to find the best match to the data, based on a χ^2 analysis.

As described in Section 7.2, we deproject the surface brightness profile following Gebhardt et al. (1996) and assume an edge-on configuration, as used by G03. The only exception is NCG 4473, where we assume an inclination of 72°, as has been done in G03. To determine the potential, we assume a constant mass-to-light ratio throughout the galaxy, a specific black hole mass and optionally also include a DM halo. The mass distribution is then given by

$$\rho(r,\theta) = M_\bullet \delta(r) + \Upsilon \nu(r,\theta) + \rho_{\rm DM}(r) \qquad (7.1)$$

where $M_\bullet$ is the black hole mass, Υ is the mass-to-light ratio, ν is the stellar luminosity distribution, and $\rho_{\rm DM}$ is the DM density profile. The potential $\Phi(r,\theta)$ is derived by integrating Poisson's equation.

In this potential, a representative orbit library is constructed that samples the phase space systematically. The generation of the orbit library is described in detail in Thomas et al. (2004) and Siopis et al. (2009). For the comparison with the data, we use a spatial grid of $N_r = 20$ radial bins and $N_\theta = 5$ angular bins and use $N_v = 15$ velocity bins for the LOSVD at each spatial gridpoint. The galaxy potential and the forces are evaluated on a grid with 16 times finer resolution. For our axisymmetric code, there are three integrals of motion that sample the phase space accordingly: the energy E, the angular momentum L_z, and a non-classical third integral I_3. The (E, L_z)-plane is sampled based on the spatial binning (Richstone & Tremaine 1988). We choose E and L_z such that the respective orbits have their pericenter and apocenter in every pair of the radial grid bins. The third integral I_3 is sampled as outlined by Thomas et al. (2004). First, orbits are dropped from the zero-velocity curve (defined by $E = L_z^2/(2r^2\cos^2\theta) + \Phi(r,\theta)$), as in G03. This is done by using the intersections of the angular rays of the spatial grid with the zero-velocity curve as starting points for the integration of the orbit's motion. However, this does not ensure a representative sampling of orbits. Such a sampling is indicated by a homogeneous coverage of the surface of section, i.e., the position of radii and radial velocities of orbits during their upward crossing of the equatorial plane. Therefore, additional orbits are launched

Table 7.1. Results for the Galaxy Sample

Galaxy	D (Mpc)	$M_{\bullet,\mathrm{G03}}$ ($M_\odot$)	M/L_{G03}	$M_{\bullet,\mathrm{noDM}}$ ($M_\odot$)	M/L_{noDM}	$M_{\bullet,\mathrm{DM}}$ ($M_\odot$)	M/L_{DM}	V_c (km s^{-1})	r_c (kpc)	R_{inf} ($''$)
(1)	(2)	(3)	(4)	(5)	(6)	(7)	(8)	(9)	(10)	(11)
NGC 821	25.5	$9.9 \pm 4.1 \times 10^7$	6.8	$1.1 \pm 0.4 \times 10^8$	7.7 ± 0.5	$1.8 \pm 0.8 \times 10^8$	6.2 ± 0.7	450	14.0	0.14
NGC 2778	24.2	$1.6 \pm 1.0 \times 10^7$	7.2	$1.4 \pm 1.1 \times 10^7$	11.9 ± 1.1	$1.5 \pm 1.5 \times 10^7$	11.8 ± 1.2	300	5.0	0.02
NGC 3377	11.7	$1.1 \pm 0.6 \times 10^8$	2.7	$1.6 \pm 1.0 \times 10^8$	2.6 ± 0.5	$1.9 \pm 1.0 \times 10^8$	2.3 ± 0.4	350	6.0	0.69
NGC 3384	11.7	$1.8 \pm 0.2 \times 10^7$	2.5	$8.0 \pm 4.2 \times 10^6$	2.4 ± 0.1	$1.1 \pm 0.5 \times 10^7$	2.2 ± 0.1	400	8.0	0.04
NGC 3608	23.0	$1.9 \pm 0.9 \times 10^8$	3.7	$4.6 \pm 0.9 \times 10^8$	3.5 ± 0.3	$4.7 \pm 1.0 \times 10^8$	3.3 ± 0.3	400	10.0	0.55
NGC 4291	25.0	$3.2 \pm 1.6 \times 10^8$	6.0	$9.7 \pm 2.0 \times 10^8$	6.0 ± 0.5	$9.2 \pm 2.9 \times 10^8$	6.0 ± 0.8	400	8.5	0.56
NGC 4473	17.0	$1.3 \pm 0.7 \times 10^8$	5.1	$5.9 \pm 5.0 \times 10^7$	7.4 ± 0.2	$1.0 \pm 0.5 \times 10^8$	6.8 ± 0.3	400	10.0	0.15
NGC 4564	17.0	$6.9 \pm 0.7 \times 10^7$	1.6	$9.8 \pm 2.3 \times 10^7$	1.6 ± 0.1	$9.4 \pm 2.6 \times 10^7$	1.5 ± 0.1	350	7.0	0.19
NGC 4649	16.5	$2.1 \pm 0.6 \times 10^9$	8.8	$3.9 \pm 1.0 \times 10^9$	8.6 ± 0.6	$4.2 \pm 1.0 \times 10^9$	8.0 ± 0.7	500	20.0	1.51
NGC 4697	12.4	$2.0 \pm 0.2 \times 10^8$	4.2	$2.2 \pm 0.3 \times 10^8$	4.5 ± 0.3	$2.0 \pm 0.5 \times 10^8$	4.3 ± 0.3	450	12.0	0.45
NGC 5845	28.7	$2.9 \pm 1.1 \times 10^8$	4.5	$4.5 \pm 1.2 \times 10^8$	5.4 ± 0.2	$5.4 \pm 1.7 \times 10^8$	5.1 ± 0.2	300	5.0	0.30
NGC 7457	14.0	$4.1 \pm 1.4 \times 10^6$	2.8	$7.4 \pm 4.2 \times 10^6$	2.7 ± 0.5	$1.0 \pm 0.6 \times 10^7$	2.6 ± 0.5	300	5.0	0.14

Notes. Column 1: name. Column 2: distance. Columns 3-4: black hole mass and mass-to-light ratio from study of Gebhardt et al. (2003). Columns 5-6: black hole mass and mass-to-light ratio using updated code but without including a DM halo in the dynamical modeling. Columns 7-8: black hole mass and mass-to-light ratio when a DM halo is included. Column 9-10: parameters of the circular velocity and the core radius for the logarithmic DM density profile used. Column 11: radius of the black hole's sphere of influence, based on the black hole mass including the contribution of DM.

to give such a homogeneous coverage. This method provides a complete sampling of the surface of section for given E and L_z and thus a proper coverage of phase space. We typically have 13,000−16,000 orbits in our library. The allocation of the individual orbits to the spatial grid points is based on the time they spend there.

Given this orbit library, the orbit weights are chosen by matching the orbit superposition to the observed light distribution and the LOSVDs of the galaxy on the spatial grid. To fit the orbit library to the data, we use the maximum entropy technique of Richstone & Tremaine (1988). This method maximizes the function

$$\hat{S} = S - \alpha\chi^2 \,, \tag{7.2}$$

where χ^2 is the sum of the squared residuals over all spatial and velocity bins, e.g.,

$$\chi^2 = \sum_{k=1}^{N_d} \frac{(l_{\mathrm{mod},k} - l_{\mathrm{dat},k})^2}{\sigma_k^2} \,, \tag{7.3}$$

where l_k is the light in the kth bin, with the bins composed of the spatial position on the sky and the line-of-sight velocity, thus the bin in the LOSVD, at that position. Hence, k is varying from 1 to $N_d = N_r N_\theta N_v$. While $l_{\mathrm{dat},k}$ refers to the measured light at that position, $l_{\mathrm{mod},k}$ is given by the weighted sum of the contribution of all orbits to the kth bin.

S is the Boltzmann entropy

$$S = \sum_{i=1}^{N_{\mathrm{orb}}} w_i \log\left(\frac{w_i}{V_i}\right) \,, \tag{7.4}$$

where w_i is the weight of the individual orbit and V_i is the phase space volume of this orbit, i.e., the volume of the region in phase space that is represented by this orbit i, given by

$$V = \Delta E \Delta L_z \int T(r, v_r) \mathrm{d}r \mathrm{d}v_r \,, \tag{7.5}$$

where $T(r, v_r)$ is the time between two successive crossings of the equatorial plane and ΔE and ΔL_z are the ranges in energies and angular momenta of the respective orbits (Binney et al. 1985; Thomas et al. 2004).

The parameter α in Equation (7.2) controls the relative weight of entropy and χ^2 for the maximization. We start with a small α, being dominated by the entropy maximization in the fit, and then iteratively increase it until there is no longer an improvement in the χ^2.

This procedure provides a value for the χ^2 for one combination of $M_\bullet$, Υ and DM halo. The best fit is found by the global minimum of χ^2 for the variation of these parameters. For the estimation of the parameter uncertainties we adopt the usual $\Delta\chi^2 = 1$ criterion (Press et al. 1992) to obtain the 68% confidence intervals for one degree of freedom, thus when marginalizing over the other free parameters.

7.4. Results

7.4.1. Models without a DM halo

We first ran a set of models without including the contribution of a DM halo; thus, we set $\rho_{\mathrm{DM}} = 0$ in Equation (7.1). This assumption is consistent with most previous studies on black hole masses using dynamical models as well as with G03. As we are using the same data asthose of G03, the main difference is the improved modeling code. Thus, we would expect to recover similar black hole masses as in G03. We also use slightly different distances to the galaxies, as given by Gültekin et al. (2009b).

For each galaxy we ran models on a fine grid in $M_\bullet$ and mass-to-light ratio (M/L). Each model gives a best-fitting orbit superposition, and thus orbital structure for the galaxy, with a corresponding value of χ^2. The best fit $M_\bullet$ and M/L are determined by the global minimum of the χ^2 distribution.

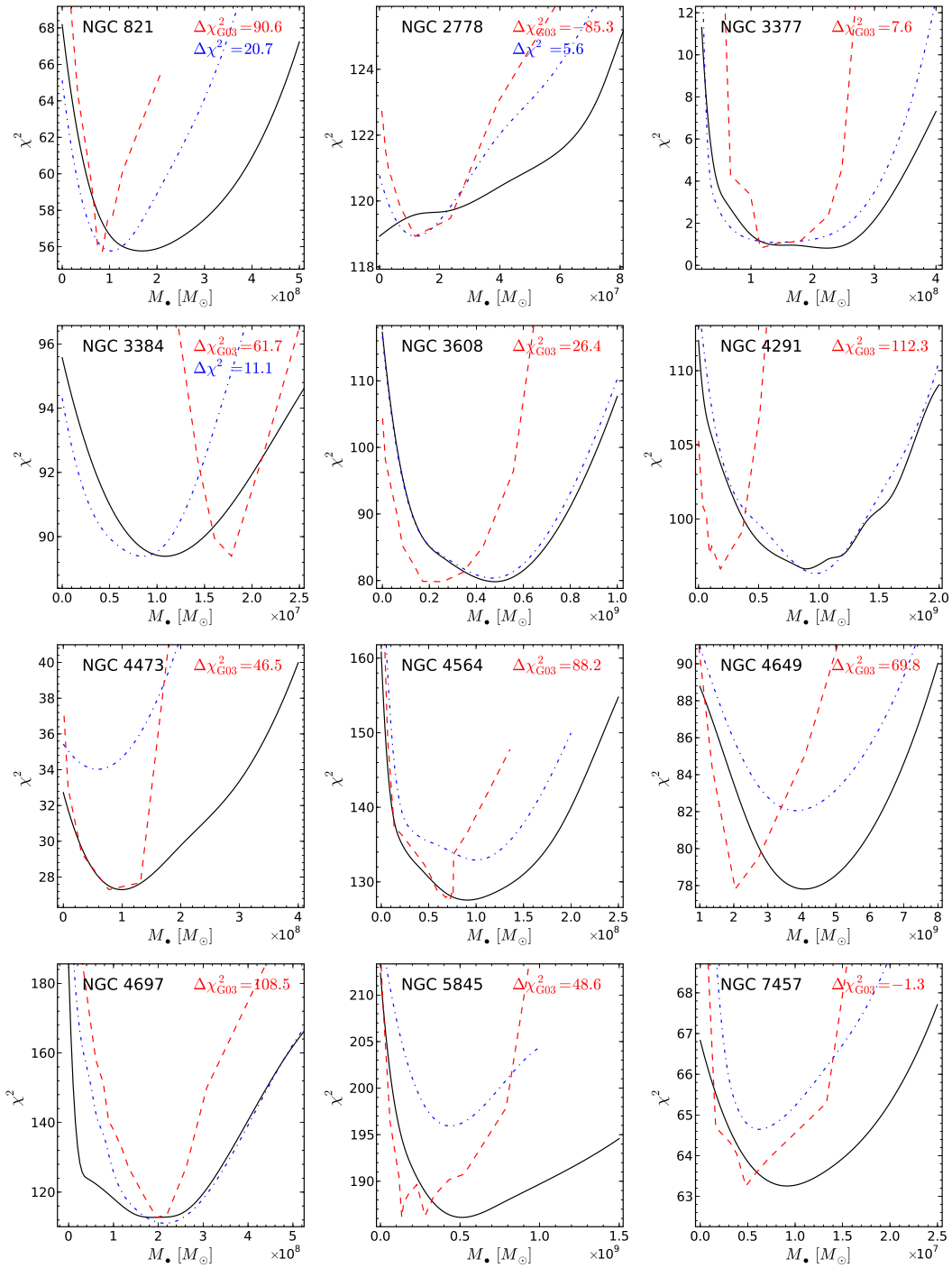

Fig. 7.1. Comparison of the χ^2 distributions as a function of $M_\bullet$ (marginalized over M/L). The black solid line shows the models including a DM halo. Their χ^2 values always show the actual modeling result. The χ^2 distribution for the models without a DM halo is shown as the blue dashed-dotted line. The zero point has been shifted for NGC 2778 and NGC 3384 by an offset given in the figure as $\Delta\chi^2$ (in blue). The χ^2 distribution of G03 is shown as the red dashed line, offset by the value given as $\Delta\chi^2_{\rm G03}$ (in red). The distributions have been scaled in $M_\bullet$, to account for the difference in the assumed distance.

The χ^2 distribution as a function of $M_\bullet$ (marginalized over M/L) is shown as the blue line in Figure 7.1. We determined our stated best fit $M_\bullet$ and M/L from their marginalized χ^2 distributions, using the mid-point of the $\Delta\chi^2 = 1$ interval, which corresponds to a 1σ uncertainty. The results are presented in Table 7.1.

7.4.2. Models with a DM halo

It has been shown that dynamical models are clearly able to detect and constrain the presence of a DM halo, if the data range sufficiently far in radius (Rix et al. 1997; Kronawitter et al. 2000; Thomas et al. 2007; Weijmans et al. 2009; Forestell & Gebhardt 2010). Due to the faintness of the stellar component

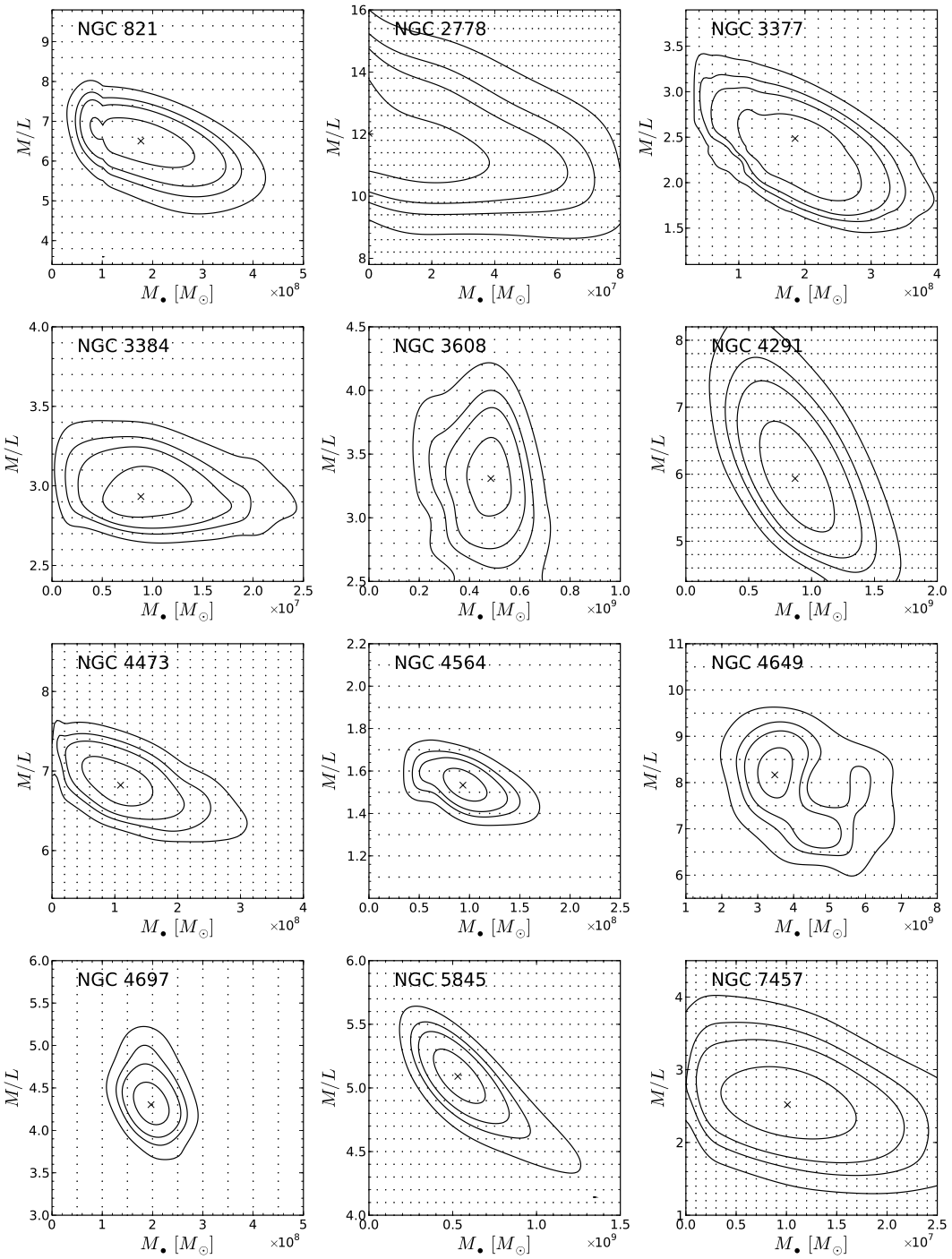

Fig. 7.2. Two-dimensional contour plot of χ^2 as a function of $M_\bullet$ and M/L for each galaxy. Here the models with a DM halo included are shown. The contour lines show $\Delta\chi^2$ values of 1.0, 2.71, 4.0, and 6.63 (corresponding to 68%, 90%, 95%, and 99% confidence for one degree of freedom). The points indicate the individual models we ran. The contours are derived from a smoothing spline to these models. The cross represents the best fit.

at large radii, other kinematic tracers such as globular clusters (Zepf et al. 2000; Pierce et al. 2006; Bridges et al. 2006) or planetary nebulae (Méndez et al. 2001; Romanowsky et al. 2003; Coccato et al. 2009) have to be used. Furthermore, if dynamical coverage of both the central and the outer regions of the galaxy is present, it is possible to constrain $M_\bullet$, M/L, and the dark halo parameters by dynamical modeling (Gebhardt & Thomas 2009; Shen & Gebhardt 2010).

Two common parameterizations for the DM halo are a Navarro-Frenk-White (NFW) profile (Navarro et al. 1996) and a DM distribution based on a cored logarithmic potential (Binney & Tremaine 1987; Thomas et al. 2005). For a sample of 17 early-type galaxies, Thomas et al. (2007) found both profiles

to give consistent results, with tentative evidence to favor a logarithmic dark halo. Gebhardt & Thomas (2009) confirmed this result for M87, and McConnell et al. (2011) found consistent results for $M_\bullet$ using either a logarithmic dark halo or an NFW profile. In the following, we will use a DM halo with a cored logarithmic potential, whose density profile is given by

$$\rho_{\rm DM}(r) = \frac{V_c^2}{4\pi G}\frac{3r_c^2 + r^2}{(r_c^2 + r^2)^2}\,, \tag{7.6}$$

where V_c is the asymptotically constant circular velocity and r_c is the core radius, within which the DM density is approximately constant.

Our data in general do not constrain the DM profile, as we are lacking kinematic information at large radii. While for a few galaxies in our sample, large radii kinematic information for the stars, globular clusters or planetary nebulae exist in the literature, we do not include them in this analysis. In this work, we are not aiming at constraining the DM halo itself, but we are mainly interested in the effect of including such a halo for the recovered black hole mass. We leave a more detailed investigation of the combined DM halo and black hole properties for these individual galaxies to future work. This also allows a better direct comparison to the work of G03 and the models without a DM halo, presented in the previous section.

Therefore, we assume a fixed DM halo, with fixed parameters V_c and r_c. These are taken from the scaling relations presented by Thomas et al. (2009), based on the galaxy luminosity:

$$\log r_c = 1.54 + 0.63(\log(L_B/L_\odot) - 11) \tag{7.7}$$

$$\log V_c = 2.78 + 0.21(\log(L_B/L_\odot) - 11)\,, \tag{7.8}$$

and given in Table 7.1. These scaling relations have been established based on a sample of 12 early-type galaxies in the Coma cluster with old stellar populations. While our sample does not have to follow these scaling relationships exactly, they at least provide well motivated parameters for the DM halo. Younger early-type galaxies and disk galaxies have been found to have on average a less massive halo, thus our approach tends to maximize the DM contribution. We investigate the effect of changing the assumed DM halo on the central black hole mass further below.

Thus, for each galaxy, we ran a grid of models for varying $M_\bullet$ and M/L with fixed DM halo. We show the two-dimensional distribution of χ^2 as a function of $M_\bullet$ and M/L in Figure 7.2. The contours are based on the χ^2 values of the underlying grid points, applying a two-dimensional smoothing spline (Dierckx 1993). The marginalized χ^2 distribution as a function of $M_\bullet$ is shown as the black line in Figure 7.1. We again determined the best-fit values for $M_\bullet$ and M/L from the marginalized distribution and have given them in Table 7.1.

7.5. Comparison of black hole masses

7.5.1. Comparison with Gebhardt et al. (2003)

As we are using the same data as those in G03, the only difference between the work presented in Section 7.4.1 and in G03 is the improved modeling code. Thus, we would expect to recover the same black hole masses as in G03.

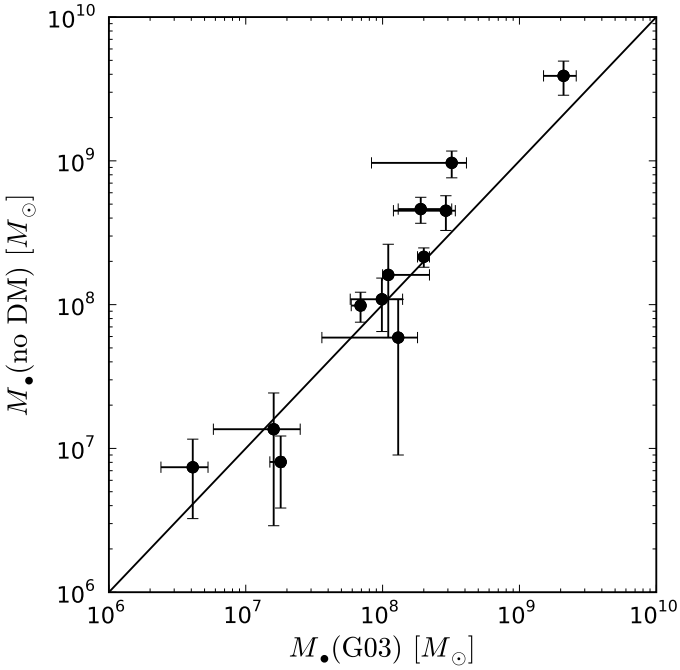

Fig. 7.3. Black hole masses given by Gebhardt et al. (2003) vs. the black hole masses determined in this work (without a dark halo). The solid line shows a one-to-one correspondence.

For a comparison with G03, their masses are first increased by a factor of 1.09, due to a unit conversion error (Siopis et al. 2009), and then are rescaled, according to the difference in the adopted distance, assuming $M_\bullet \propto d$. These masses are listed in Gültekin et al. (2009b), apart from NGC 821. This galaxy has an erroneous black hole mass in G03, corrected in Richstone et al. (2004). After accounting for the factor of 1.09 and the distance difference, the black hole mass for NGC 821 is $M_\bullet = 9.9 \times 10^7\,M_\odot$.

In Figure 7.3 we compare the black hole masses, determined without including a DM halo, with the black hole masses given in G03. In Figure 7.4 we show as blue squares the ratio between both mass determinations as a function of the G03 mass. The marginalized χ^2 distributions for the individual objects are shown in Figure 7.1, as blue dashed-dotted lines for the current work masses and as red dashed lines for the G03 distributions. Note that the G03 distributions are offset in χ^2, such that the minimum corresponds to the minimum of the χ^2 distribution including a dark halo, shown in black. The reason for the offset in χ^2 is mainly due to the larger number of orbits used in the current modeling, compared to G03.

For three objects (NGC 821, NGC 2778, and NGC 4697) the difference in $M_\bullet$ is less than 20 %, thus consistent with our previous work. The internal structures of the dynamical models (as discussed below) are similar for these three galaxies in the old and new models, which explains the reason for lack of change. The small difference is probably due to the presence of numerical noise in the models. This noise is mainly caused by the use of a finite number of individual orbits instead of a smooth orbit

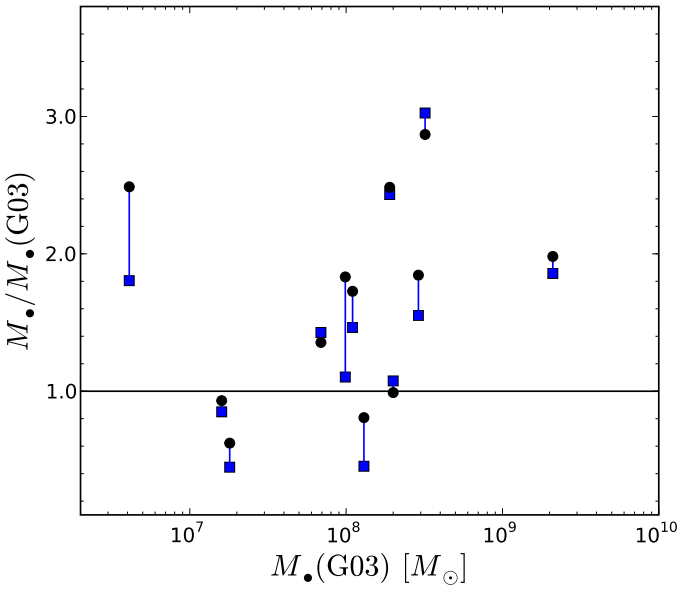

Fig. 7.4. Ratio between the $M_\bullet$ determined in this work and the $M_\bullet$ given in Gebhardt et al. (2003), as a function of the G03 $M_\bullet$. The blue squares are for the models without a dark halo, while the black circles correspond to the result, when a dark halo is included in the models. The solid line is a one-to-one correspondence to the G03 values.

distribution function. The comparison of the χ^2 distribution for the three objects shows that they are basically consistent, while the distribution may widen, possibly due to a more complete orbit library. Also, for NGC 3377 and NGC 4564 ,the difference in $M_\bullet$ is within the stated uncertainties.

However, for the rest of the objects the new $M_\bullet$ is significantly offset from the previous estimate, not simply explained by numerical noise. For two objects, NGC 3384 and NGC 4473, $M_\bullet$ decreases; for the rest there is an increase in $M_\bullet$, by up to a factor of three. The mean increase for this sample is a factor of 1.46 with the standard deviation of 0.73. This result is in line with the findings of Shen & Gebhardt (2010), who found an increase in the mass by a factor of two for NGC 4649. This object is included in Figures 7.3 and 7.4 as the highest mass point. Shen & Gebhardt (2010) attribute the mass difference to the better orbit sampling in the new models. In particular, they argue that the old orbit sampling lacks high energy, nearly circular orbits, which lead to an underestimate of $M_\bullet$. NGC 4649 is a core galaxy, and it is important to note that all galaxies with an increase in mass by more than a factor of two are core galaxies as well. This seems to indicate that the previous orbit sampling was not able to properly model core galaxies.

To investigate this issue further for our whole sample, we inspect the internal orbit structure, looking for any clear difference between the models. To do so, we examine the shape of the velocity dispersion tensor, represented by the ratio of radial to tangential dispersion σ_r/σ_t. The tangential dispersion includes contributions from random as well as from ordered motion; thus, it is given by $\sigma_t^2 = \sigma_\theta^2 + \sigma_\phi^2 + V_\phi^2$. In Figure 7.5, we compare the internal dispersion ratio σ_r/σ_t for the best-fit models presented here, with and without a DM halo (as blue solid and black dashed dotted lines, respectively), with the ratio for the models in G03, shown as red dashed lines. We also indicate the black hole sphere of influence $R_{\rm inf} = GM_\bullet\sigma^{-2}$, assuming the new $M_\bullet$ (without DM halo). The galaxies with consistent black hole masses, such as NGC 3377 and NGC 4697, also exhibit consistent internal structure. On the other hand, the galaxies with the largest mass increase, especially the core galaxies such as NGC 4291 and NGC 3608 show a clear difference in the internal structure. First, there is a strong radial bias at large radii for these galaxies, especially compared to the previous dispersion ratio. However, this radial bias is mainly outside the range for which kinematic data are available and is therefore driven by the maximization of the entropy. We do not expect these orbits to have an influence on the black hole mass determination. Second, there is a stronger tangential bias inside the black hole sphere of influence. In particular, the previous models exhibit a radial bias within $R_{\rm inf}$ for the largest outliers. G03 only sampled the zero-velocity curve, instead of the whole phase space, and due to the coarse sampling of drop points they missed the orbits near the pole that are nearly circular. This sampling then causes a radial orbital bias. This radial bias is removed in the models presented here, using a better orbit sampling. An increase in tangential orbits will reduce the projected line-of-sight velocity dispersion and therefore a more massive black hole is required to match the observed velocity dispersion profile. On the other hand, NGC 4473 which shows a decrease in the determined black hole mass, exhibits a stronger radial bias in the new modeling compared to G03. This radial bias is probably caused by the presence of a nuclear disk in this galaxy.

Thus, we find that the main reason for the change in black hole mass is the different orbit sampling used, as already found by Shen & Gebhardt (2010) for NGC 4649. We now cover the phase space more completely and therefore also include orbits missed by the previous sampling. This issue is of special importance for core galaxies, as they often show a significant tangential orbital bias in their center, i.e., they usually have the largest σ_t (G03).

To illustrate this point, we computed the difference of the dispersion ratio between G03 and this new model in a shell inside the black hole sphere of influence:

$$\Delta R_\sigma = \int_{r_{\rm min}}^{r_{\rm max}} \left[(\sigma_r/\sigma_t)_{\rm G03} - (\sigma_r/\sigma_t)\right] {\rm d}r \,, \qquad (7.9)$$

with $r_{\rm min} = 0.1R_{\rm inf}$ and $r_{\rm max} = R_{\rm inf}$. This quantity is just a simple and quick way of quantifying the change in the orbital structure and is just meant to highlight the relation between the change in orbital structure and the change in black hole mass. In Figure 7.6 we plot it against the ratio of the black hole masses $M_\bullet/M_{\bullet,{\rm G03}}$. There is a clear correlation between the quantities, confirming our previous argument. We have also tested the effect of decreasing the number of orbits in the modeling, but saw no clear influence on the best-fit black hole mass. Thus we confirm our previous results in finding that the recovered black hole mass is not affected by the number of orbits (Gebhardt 2004; Richstone et al. 2004; Shen & Gebhardt 2010).

This investigation emphasizes the need for a complete orbital sampling of phase space for dynamical modeling of galaxies, especially of core galaxies.

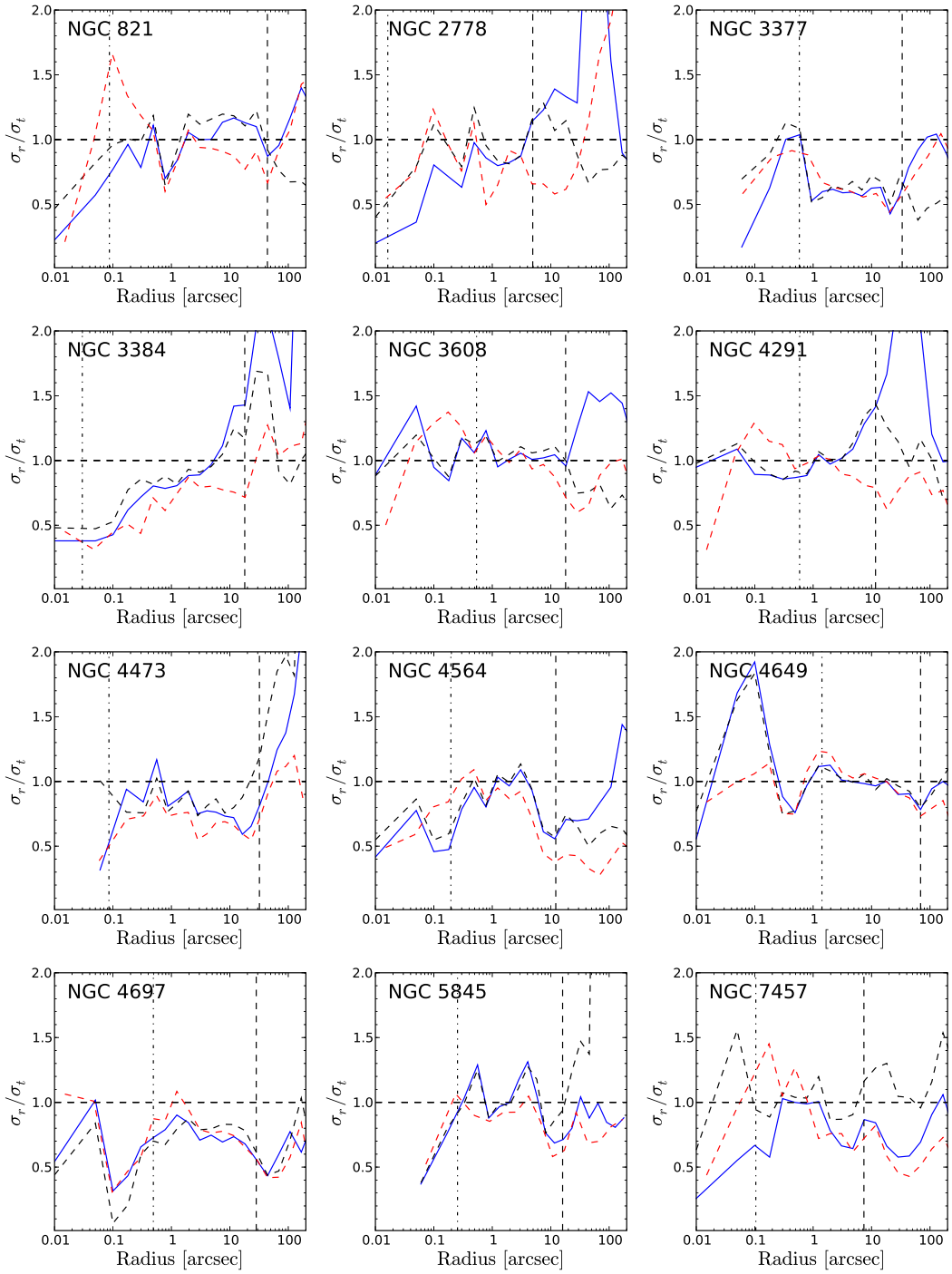

Fig. 7.5. Ratio of the internal velocity dispersions as a function of radius for the best model of each galaxy. Shown is the ratio σ_r/σ_t along the major axis. The result with a DM halo, without a DM halo, and the result of Gebhardt et al. (2003) (without a dark halo) are shown as the black dashed, blue solid and red dashed lines, respectively. The horizontal dashed line corresponds to a non-rotating isotropic model. The vertical dashed-dotted line indicates the black hole's sphere of influence, assuming the black hole mass, determined without including a DM halo. The vertical dashed lines show the radial extent of the ground-based data.

7.5.2. Effect of a dark matter halo on the determined black hole mass

The main motivation of this paper is to investigate the effect of the inclusion of a DM halo in the dynamical modeling on the determined black hole mass. In Figure 7.7 we show the difference in black hole mass between the models with and without the inclusion of a DM halo as a function of the resolution of the black hole sphere of influence divided by the spatial resolution of the kinematic observation ($R_{\rm inf}/d_{\rm res}$). For the computation of $R_{\rm inf}$ we used the black hole mass including a DM halo (given in Table 7.1). The spatial resolution is given by the seeing and the

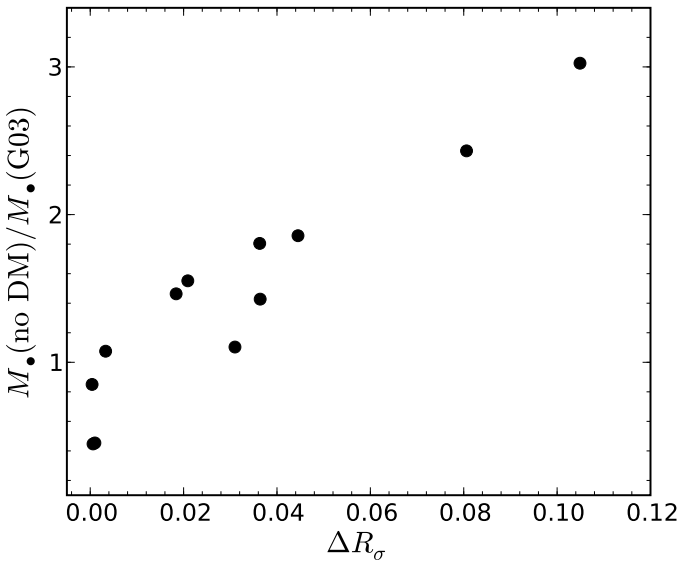

Fig. 7.6. Ratio between the $M_\bullet$ determined in this work and the $M_\bullet$ given in Gebhardt et al. (2003), as a function of the excess in radial motion in the internal structure of the models of Gebhardt et al. (2003), as defined by Equation (7.9). A correlation between both quantities is apparent.

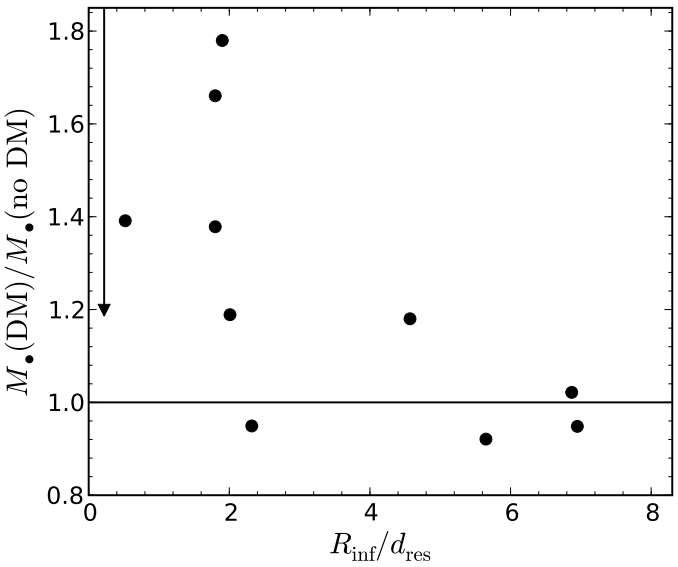

Fig. 7.7. Ratio between the $M_\bullet$ without accounting for the DM halo and the $M_\bullet$ including a DM halo in the model, as a function of the ratio of black hole sphere of influence over the spatial resolution. The arrow indicates the upper limit for the mass of NGC 2778 when DM is included. The solid line shows a one-to-one correspondence between both masses.

aperture of the *HST* kinematic observations; thus, $d_{\mathrm{res}} = 0.08$ for the STIS data and $d_{\mathrm{res}} = 0.15$ for the FOS data.

As expected, there is a general trend of an increase in $M_\bullet$ when a DM halo is included. For five objects, we find almost no change in $M_\bullet$, while for one object – NGC 2778 – the significance of the black hole detection even vanishes, with the minimum χ^2 for no black hole. The other six galaxies show an increase in the measured $M_\bullet$ between 20% and 80% when a DM halo is included. The most extreme case is NGC 4473 probably due to the presence of a nuclear disk, with an increase of a factor of 1.8 when a DM halo is included. For the whole sample we find a mean increase of a factor of 1.22 with standard variation of 0.27. This increase is much less than the factor of more than two found for M87. In contrast to M87, our data set contains no stellar kinematic information at large radii but includes *HST* data at small radii. Thus, we are better able to probe the region affected by the presence of the black hole at the center.

In Figure 7.7, there appears to be a trend of a larger bias for objects where R_{inf} is less well resolved, as would be expected. However, due to the black hole mass uncertainties there is no statistically significant relation. The most massive galaxy in our sample, NGC 4649, is not shown in the figure, as it would appear at $R_{\mathrm{inf}}/d_{\mathrm{res}} \approx 20$ with no significant change in black hole mass. M87 would lie at $R_{\mathrm{inf}}/d_{\mathrm{res}} \approx 1.5$ and $M_{\bullet,\mathrm{DM}}/M_{\bullet,\mathrm{no\,DM}} \approx 2.8$. In contrast to M87, the galaxies in our sample with a less well resolved sphere of influence exhibiting a smaller change in the determined $M_\bullet$ are less massive and probably reside in less massive DM halos. This indicates that especially for massive galaxies properly resolving R_{inf} is important to determine $M_\bullet$ under the consideration of DM.

In Figure 7.1, the marginalized χ^2 distributions for the individual objects with (solid black line) and without (dotted dashed blue line) a DM halo are shown. For the five objects with almost no change in $M_\bullet$ (NGC 3377, NGC 3608, NGC 4291, NGC 4649, and NGC 4697), there is also no change in the χ^2 (apart from NGC 4649). For the other galaxies, including a reasonable DM halo improves the fit in terms of χ^2. The most convincing cases are NGC 821 and NGC 3384, where the model without a DM halo is excluded at more than 3σ significance. Thus, while we are not able to constrain the shape of the DM halo, at least for some galaxies the presence of such a halo is supported. In total, for six galaxies (NGC 821, NGC 2778, NGC 3384, NGC 4473, NGC 4564, and NGC 5845), the model without a DM halo is excluded with at least 2σ significance.

The mean increase of the black hole mass goes along with a decrease of the mass-to-light ratio, as expected. This indicates the degeneracy present between the stellar mass-to-light ratio and the DM contribution in dynamical models. For the whole sample we find a decrease in M/L of 6% with a scatter of 5%.

Even if our choice of DM halo is well motivated by the scaling relations of Thomas et al. (2009), it is basically an ad hoc assumption we had to make as we do not have the data to robustly constrain the DM halo profile. To at least test the effect of changing the assumed DM halo on the black hole mass, we ran a set of models, changing V_c in the logarithmic DM potential. We restrict ourselves to changing only this one parameter, as we want to avoid sampling the whole four-dimensional parameter space. It has also been found that V_c and r_c are degenerate, especially if the large radii coverage is poor (Shen & Gebhardt 2010; Forestell 2009). For each galaxy, we assume a twice as massive DM halo and a DM halo about half as massive, as well as some additional values. The results are shown in Figure 7.8. We confirm the basic trends of an improved χ^2 for a reasonable massive halo and an increase in $M_\bullet$ for a more massive halo. The range of given $M_\bullet$ approximately covers the range consistent with the

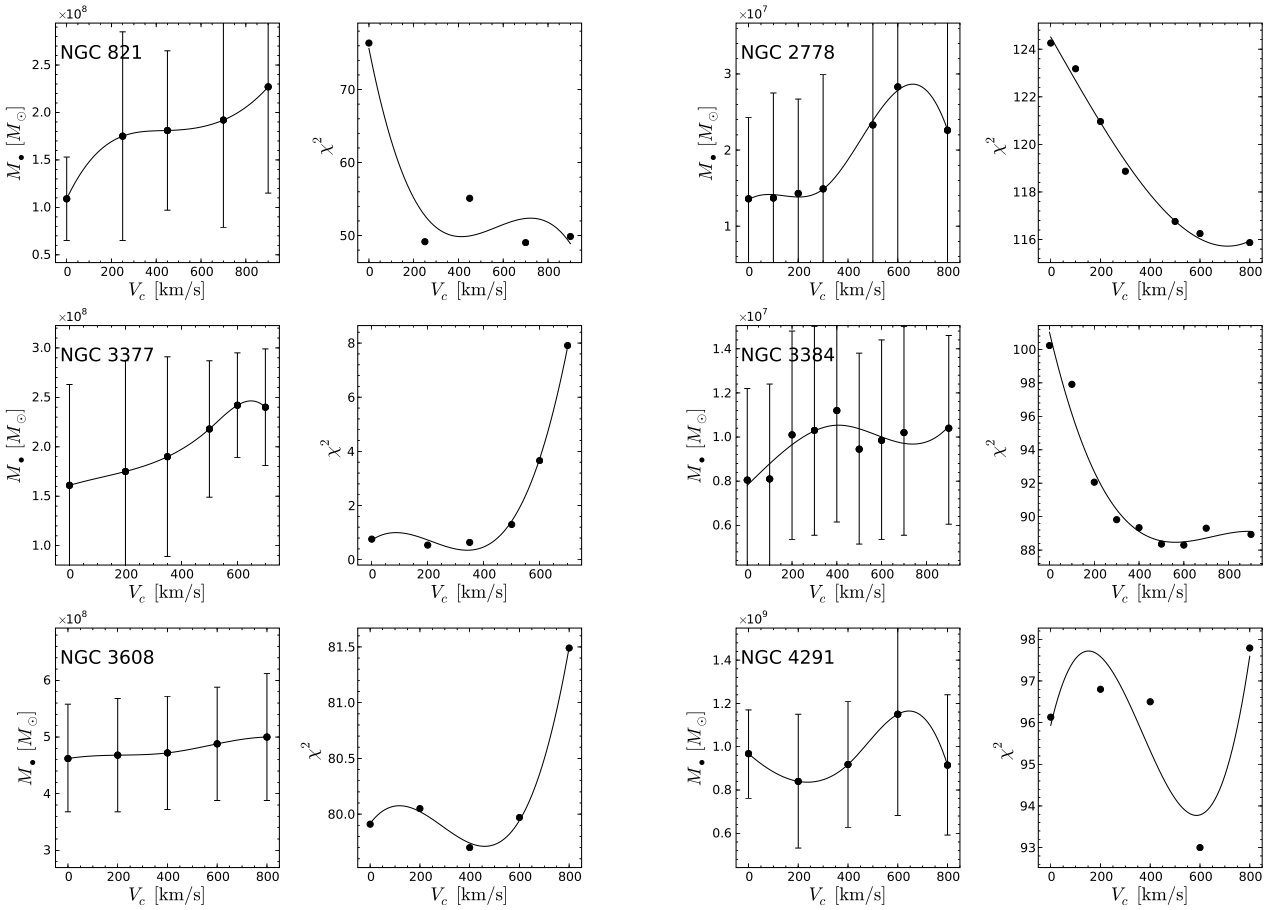

Fig. 7.8. Variation of the black hole mass and the minimal χ^2 as a function of the assumed DM halo for each galaxy. In the left columns of the subpanels the change in $M_\bullet$ for various values of $V_{\rm DM}$ is shown. The error bars correspond to 1σ (i.e., $\Delta\chi^2 = 1$). In the right columns the corresponding value of χ^2 is shown. A spline interpolation is shown as the solid line.

current data, as long as the DM halo is not constrained for these galaxies.

7.5.3. Notes on individual galaxies

In the following, we provide more detailed information on the black holes for some individual galaxies.

NGC 821. There are two recent studies on the DM halo of this galaxy, providing large radii data. Weijmans et al. (2009) used SAURON data to measure LOSVDs out to $\sim$ 4 effective radii. Their assumed DM halo gives $M_{\rm DM} = 9 \times 10^9\,M_\odot$ within the effective radius (assuming $R_e = 5.1$ kpc), using an NFW profile. Forestell & Gebhardt (2010) used long-slit data from the Hobby-Eberly Telescope to measure the LOSVD out to $\sim 2R_e$. Assuming their power law fit to the DM halo, we find $M_{\rm DM} = 8 \times 10^9\,M_\times$ within R_e. Our assumed DM halo is more than twice as massive. Thus, $M_\bullet$ for the true DM halo should be contained within the range spanned by our no DM and DM solution. Including these large radii data into the dynamical models is beyond the scope of this paper. The nuclear supermassive black hole in NGC 821 has been detected as a weak X-ray source, implying a very weak level of activity ($L_{\rm X}/L_{\rm Edd} \sim 10^{-8}$; Pellegrini et al. 2007). There is also evidence for the presence of a jet (Fabbiano et al. 2004; Pellegrini et al. 2007).

NGC 2778. This galaxy already had the least confident black hole detection in G03. Assuming the value for $M_\bullet$ of our no DM halo model, we do not resolve the black hole's sphere of influence ($R_{\rm inf}/d_{\rm res} = 0.2$). Including a DM halo in the model improves the fit significantly, but the significance of the black hole detection disappears. However, the previous $M_\bullet$ estimate is still fully consistent with the 1σ upper limit of $M_{\bullet,{\rm up}} = 2.99{\times}10^7\,M_\odot$ that we derive for NGC 2778 under the presence of a DM halo. This behavior might indicate the need to properly resolve $R_{\rm inf}$ when a DM halo is included to properly determine $M_\bullet$.

NGC 3377. The black hole mass for this galaxy increased by $\sim$ 70%, compared to G03, mainly caused by the stronger widening of the confidence contours at the high-mass end than at the low-mass end. The previous value is still fully consistent within 1σ. Copin et al. (2004) reported a black hole mass of $M_\bullet = 8.3 \times 10^7\,M_\odot$ (for our assumed distance) based on IFU observations with SAURON and OASIS, also still consistent with our results within 1σ. The first detection of a black hole in NGC 3377 has been reported by Kormendy et al. (1998), based on ground-based observations. Using an isotropic model, they found $M_\bullet = 2.1 \times 10^8\,M_\odot$ and $M/L_V = 2.0$ (for our assumed distance), in good agreement with our results. NGC 3377 is a rapid rotator and close to isotropy, justifying the isotropic assumption for this galaxy. NGC 3377 exhibits a nuclear X-ray source, showing a jet like feature (Soria et al. 2006).

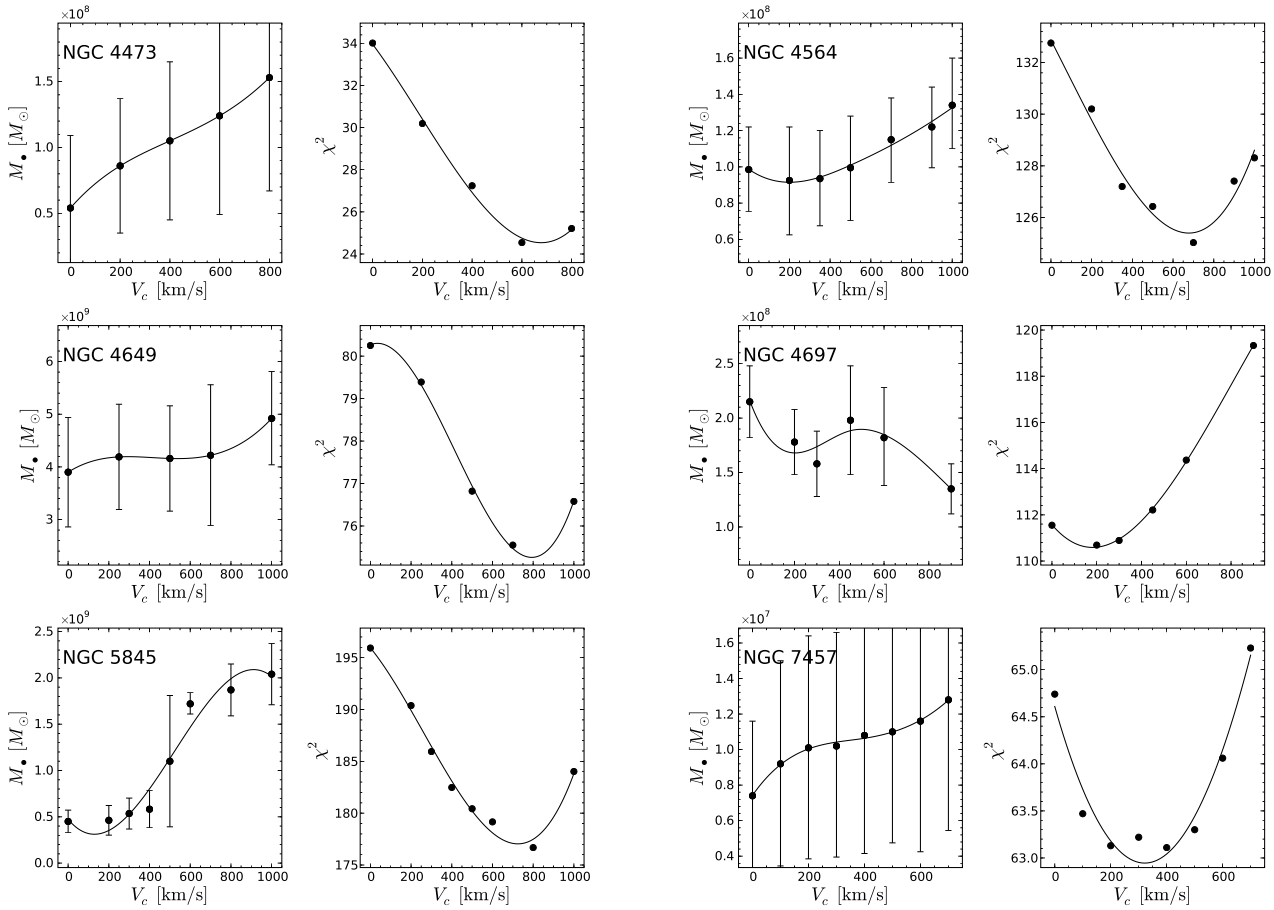

Fig. 7.9. Same as Figure 7.8 for the second half of the galaxy sample.

NGC 3384. Besides NGC 2778, this is the only other galaxy for which the sphere of influence is not resolved. While for NGC 2778 the new code does not lead to a change of the χ^2 distribution, for NGC 3384 $M_\bullet$ decreases. This might indicate a larger uncertainty in the determination of $M_\bullet$ using different modeling codes when $R_{\rm inf}$ is not resolved. NGC 3384 is the galaxy with the strongest constraints on the presence of a DM halo. For this galaxy, we ran a grid of models changing r_c as well as V_c, but we found no change in χ^2 for different values of r_c. However, we are able to set a lower limit on V_c with $V_c >\sim 350$ km s^{-1} at 1σ confidence. The no DM halo model is excluded at more than 3σ confidence (see Figure 7.8).

NGC 4473. NGC 4473 shows evidence for a central stellar disk both in the imaging and the kinematics, as discussed by G03. We followed G03 and include a central exponential disk and also assumed a galaxy inclination of 71°, as found for the disk component. Thus this galaxy is the only case in our sample not modeled with an edge-on inclination. The presence of the disk has a distinct influence on the measured black hole mass causing a relatively large difference between the models with and without a DM halo.

NGC 4564. This galaxy is known to have a nuclear X-ray source (Soria et al. 2006), indicating the presence of an extremely sub-Eddington accreting AGN.

NGC 4649. This object has recently been studied by Shen & Gebhardt (2010) including a DM halo in the models. In addition to the stellar kinematics used in this work, they included globular cluster velocities from Hwang et al. (2008). Thus, our results are not directly comparable. They report values of $M_\bullet = (4.5 \pm 1.0) \times 10^9$ when including a DM halo in the models and $M_\bullet = (4.3 \pm 0.7) \times 10^9$ without a DM halo. Our results for $M_\bullet$ are consistent with their work.

NGC 4697. The black hole mass for this galaxy is basically unchanged using the modified code and including a DM halo. This result is consistent with Forestell (2009). She used the same data and model code as we did, but augmented by kinematics of planetary nebulae at large radii (Méndez et al. 2001, 2008, 2009), constraining $M_\bullet$ and the DM halo at the same time. Her best-fit model has $M_\bullet = 2.1 \times 10^8\ M_\odot$, $M/L = 4.35$, $V_c = 388$ km s^{-1}, and $r_c = 9$ kpc, assuming a logarithmic halo. We find identical values for $M_\bullet$ and M/L, using slightly different DM halo parameters. NGC 4697 has a nuclear point source detected in X-rays (Soria et al. 2006), showing that its black hole is active at a low rate.

NGC 5845. While there is a moderate increase in $M_\bullet$ when a DM halo is included in the model, the χ^2 distribution flattens at the high-mass end, due to an increased degeneracy between $M_\bullet$ and M/L. Increasing the mass of the DM halo strongly enhances this degeneracy, leading to an almost unconstrained $M_\bullet$ over a wide mass range, until for $V_c \approx 600$ km s^{-1} the minimum switches to $M_\bullet \approx 1.7 \times 10^9\ M_\odot$, still with strong degeneracy between $M_\bullet$ and M/L. Kinematic data at large radii, to better constrain the DM halo and M/L would be desirable for this galaxy. The model without a DM halo is excluded with more than 3σ

significance for NGC 5845. There is a nuclear X-ray source here as well (Soria et al. 2006). There is evidence for obscuration of the black hole by a dusty disk, with the X-ray emission originating from scattering of the AGN continuum emission on the surrounding plasma.

7.6. The black hole-bulge relations

As our sample constitutes a significant fraction of the galaxy sample for which dynamical black hole masses are available, it is worth looking at the effect of these new black hole mass measurements on the black hole-spheroid relations, namely the $M_\bullet - \sigma_*$ and $M_\bullet - L_V$ relationships. We used the sample of Gültekin et al. (2009b) as the reference sample, containing 49 $M_\bullet$ measurements and 18 upper limits, including our 12 objects.

For the fitting, we used a generalized maximum likelihood method as described by Gültekin et al. (2009b, ; see also Woo et al. (2010)). We minimize the likelihood function $S = -2 \ln \mathcal{L}$, with $\mathcal{L} = \prod_i l_i(\mu_i, s_i)$ being the product of the likelihoods for the individual measurements of black hole mass $\mu = \log M_\bullet$ and bulge property $s = \log \sigma_*$ or $s = \log L_V$. The likelihood for measuring the mass μ_i and bulge property s_i for given true mass μ and true bulge property s is:

$$l_i(\mu_i, s_i) = \int Q_\mu(\mu_i \mid \mu) Q_s(s_i \mid s) P(\mu \mid s) \, \mathrm{d}\mu \, \mathrm{d}s \, . \qquad (7.10)$$

We assume Q_μ, Q_s and P to have a log-normal form, with σ_{Q_μ} and σ_{Q_s} corresponding to the measurement uncertainty in the black hole mass and bulge property, and $\sigma_P = \epsilon_0$ is the intrinsic scatter in the black hole mass-bulge property relation. Upper limits are incorporated in the fit, following Gültekin et al. (2009b). Thus, we minimize

$$S = \sum_{i=1}^{N} \left[\frac{(\mu_i - \alpha - \beta s_i)^2}{\epsilon_{\mathrm{tot},i}^2} + 2 \ln \epsilon_{\mathrm{tot},i} \right] + 2 \sum_{j=1}^{M} \ln l_{\mathrm{ul},j} \, , \qquad (7.11)$$

with α and β being the normalization and the slope of the black hole-bulge relations, $\epsilon_{\mathrm{tot},i}^2 = \sigma_{Q_\mu,i}^2 + \sigma_{Q_s,i}^2 + \epsilon_0^2$, N is the number of black hole measurements, M is the number of upper limits, and $l_{\mathrm{ul},j}$ is the likelihood of the upper limit as in Gültekin et al. (2009b).

We first fit the $M_\bullet - \sigma_*$ and $M_\bullet - L_V$ relationships using the sample of Gültekin et al. (2009b), finding identical results. We then updated their black hole masses with our new values for the 12 objects in our sample. We find

$$\log(M_\bullet/M_\odot) = (8.18 \pm 0.06) + (4.32 \pm 0.31) \log(\sigma_*/200\,\mathrm{km\,s^{-1}}) \qquad (7.12)$$

with intrinsic scatter $\epsilon_0 = 0.44 \pm 0.06$ and

$$\log(M_\bullet/M_\odot) = (9.01 \pm 0.10) + (1.06 \pm 0.15) \log(L_V/10^{11}\, L_{\odot,V}) \qquad (7.13)$$

with intrinsic scatter $\epsilon_0 = 0.41 \pm 0.04$. They are shown in Figure 7.10.

Note that both relations are not based on exactly the same samples. As in Gültekin et al. (2009b), for the determination of the $M_\bullet - L_V$ relationship we restricted the sample to elliptical and S0 galaxies with reliable bulge−disk decomposition. When using the same restricted subsample for the $M_\bullet - \sigma_*$ relationship, we find a shallower slope ($\beta = 3.80 \pm 0.33$) and a reduced intrinsic scatter ($\epsilon_0 = 0.34 \pm 0.05$), lower than for the $M_\bullet - L_V$ relationship for the same sample. Restricting the sample in this manner is supported by observations that suggest that spiral galaxies do not follow the $M_\bullet - \sigma_*$ relation of ellipticals (Greene et al. 2010).

We also used a generalized least squares method to incorporate measurement uncertainties in both variables and intrinsic scatter as described in Tremaine et al. (2002), omitting the upper limits, which yields consistent results. Compared to Gültekin et al. (2009b), we find only a slight change for the best-fit. While the slope of the relation is consistent, the normalization increased slightly as well as the intrinsic scatter in both relations. We also fitted the sample of Gültekin et al. (2009b) with our updated black hole masses, without accounting for a DM halo. Most of the change in the $M_\bullet - \sigma_*$ and $M_\bullet - L_V$ relationships is caused by the improved masses. The effect of the inclusion of a DM halo on these relationships is marginal.

However, this is not a full correction of the black hole-bulge relationships for the effect of a DM halo on the black hole masses, as it is restricted to our sample of 12 galaxies. The rest of the galaxies with stellar dynamical black hole mass measurements potentially suffer from the same systematic bias. Ideally, a correction would consist of a re-modeling of these galaxies including a DM halo, as performed in this work for the sample of G03. However, we can use Figure 7.7 as a guideline for an average correction. Figure 7.7 indicates that the correction factor depends on the resolution of the sphere of influence. For $R_{\mathrm{inf}}/d_{\mathrm{res}} \gtrsim 3$ including or ignoring a DM halo in the modeling gives consistent results, while for lower values there is on average a systematic bias with a mean $\langle M_{\bullet,\mathrm{DM}}/M_{\bullet,\mathrm{no\,DM}} \rangle = 1.5$ for our sample.

To estimate the effect on the black hole-bulge relations, we increased all stellar dynamical black hole mass measurements in the sample of Gültekin et al. (2009b) with $R_{\mathrm{inf}}/d_{\mathrm{res}} < 3$ by this average factor and re-fitted the relations. To investigate the pure change due to the DM halo, we also fitted the black hole-bulge relations to the sample of Gültekin et al. (2009b), but with $M_\bullet$ of the 12 galaxies of our work replaced by our results without a DM halo. Compared to the best-fit to this sample, we found a slightly increased slope, a consistent intrinsic scatter, and an increase in normalization by 0.04 dex. We found a normalization, slope, and intrinsic scatter of (8.21,4.38,0.42) for the $M_\bullet - \sigma_*$ and (9.05,1.07,0.41) for the $M_\bullet - L_V$ relationship.

Additionally, we fitted only our sample with the values for $M_\bullet$ with and without including a DM halo in the models. We recovered an increase in the normalization of ~ 0.07 dex, corresponding to the mean increase in $M_\bullet$ in the sample, while the slope is consistent and the intrinsic scatter decreases.

7.7. Conclusions

We investigate the influence of accounting for the presence of a DM halo in the stellar dynamical modeling of galaxies on the measured black hole masses. We use a sample of 12 galaxies, already analyzed by Gebhardt et al. (2003), which have ground

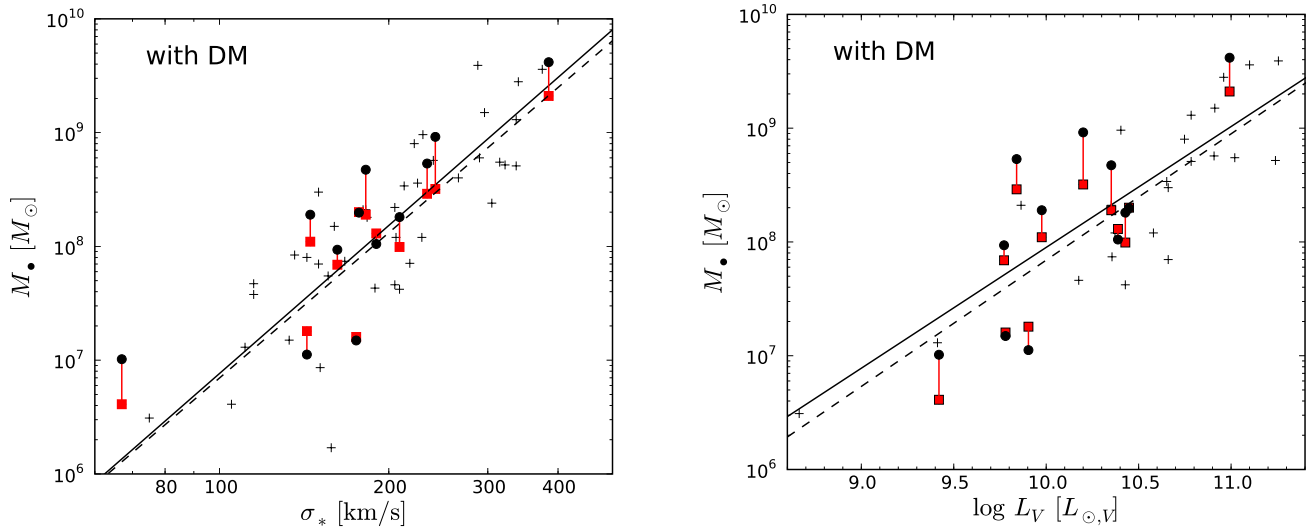

Fig. 7.10. Left panel: $M_\bullet - \sigma_*$ relationship. The red squares show our sample with the $M_\bullet$ values given by Gebhardt et al. (2003), the black circles give the $M_\bullet$ determined in this work with the inclusion of a DM halo. The black solid line shows our updated result for the $M_\bullet - \sigma_*$ relation, while the dashed line shows the relation by Gültekin et al. (2009b). The crosses show the rest of their sample. Right panel: $M_\bullet - L_V$ relationship. The symbols are the same as in the left panel. The solid line is our best-fit when including a DM halo for our 12 galaxies. The dashed line and crosses are again from Gültekin et al. (2009b).

based as well as high-resolution *HST* observations of the stellar kinematics to address this issue.

We model these galaxies without and with the presence of a DM halo. In the first case we found a significant difference of the measured black hole masses between our previous results for a large fraction of the sample. For most of the objects the mass increased compared to the values given by Gebhardt et al. (2003). We ascribe this difference to the improved code, exhibiting a better coverage of the phase space for the generated orbit library. This shows the importance of a dense coverage of phase space in the dynamical models.

Second, we include a reasonable DM halo into the models, using a scaling relationship based on the galaxy luminosity (Thomas et al. 2009). We find an increase of the measured black hole mass, but much less than what has been found for M87 and NGC 6086. For these two galaxies, kinematic information is available only at large radii, whereas for our sample we have high-resolution data covering the central parts of the galaxies. Thus, the black hole mass is better constrained by central kinematic observations and less affected by the presence of a DM halo in the models.

Using different massive DM halos for the same galaxy, we confirm the trend of an increase of the recovered black hole mass for a more massive halo as well as a decrease of the mass-to-light ratio. Based on a χ^2 analysis, the presence of a DM halo is implied for five of the 12 galaxies with at least 2σ significance, although we are not able to constrain the shape of the DM halo.

We study the consequence of our new black hole mass measurements on the $M_\bullet - \sigma_*$ and $M_\bullet - L_V$ relationships, updating the sample of Gültekin et al. (2009b) with our results. We found only a mild change in the best-fit values, still consistent with the previous estimate, with a slight increase in the normalization and the intrinsic scatter. We estimated the total effect of a black hole mass increase for galaxies studied by stellar dynamics by accounting for a DM halo which will lead to an increase in the normalization by $\sim 0.04 - 0.07$ dex.

Even if our sample shows only a mild influence of the DM halo on the black hole mass, a DM halo is clearly present. Thus it is necessary to take it into account in the modeling of the galaxy to avoid a systematic bias.

References

Binney, J., Gerhard, O. E., & Hut, P. 1985, MNRAS, 215, 59
Binney, J. & Tremaine, S. 1987, Galactic dynamics, ed. Binney, J. & Tremaine, S.
Bridges, T., Gebhardt, K., Sharples, R., et al. 2006, MNRAS, 373, 157
Ciotti, L. & Ostriker, J. P. 2007, ApJ, 665, 1038
Coccato, L., Gerhard, O., Arnaboldi, M., et al. 2009, MNRAS, 394, 1249
Copin, Y., Cretton, N., & Emsellem, E. 2004, A&A, 415, 889
Cretton, N., de Zeeuw, P. T., van der Marel, R. P., & Rix, H. 1999, ApJS, 124, 383
Dalla Bontà, E., Ferrarese, L., Corsini, E. M., et al. 2009, ApJ, 690, 537
Di Matteo, T., Springel, V., & Hernquist, L. 2005, Nature, 433, 604
Dierckx, P. 1993, Curve and surface fitting with splines, ed. Dierckx, P.
Fabbiano, G., Baldi, A., Pellegrini, S., et al. 2004, ApJ, 616, 730
Ferrarese, L., Ford, H. C., & Jaffe, W. 1996, ApJ, 470, 444
Ferrarese, L. & Merritt, D. 2000, ApJ, 539, L9
Forestell, A. D. 2009, PhD thesis, The University of Texas at Austin
Forestell, A. D. & Gebhardt, K. 2010, ApJ, 716, 370
Gebhardt, K. 2004, in Coevolution of Black Holes and Galaxies, ed. L. C. Ho, 248–+
Gebhardt, K., Bender, R., Bower, G., et al. 2000a, ApJ, 539, L13
Gebhardt, K., Lauer, T. R., Pinkney, J., et al. 2007, ApJ, 671, 1321
Gebhardt, K., Richstone, D., Ajhar, E. A., et al. 1996, AJ, 112, 105
Gebhardt, K., Richstone, D., Kormendy, J., et al. 2000b, AJ, 119, 1157
Gebhardt, K., Richstone, D., Tremaine, S., et al. 2003, ApJ, 583, 92
Gebhardt, K. & Thomas, J. 2009, ApJ, 700, 1690
Greene, J. E., Peng, C. Y., Kim, M., et al. 2010, ApJ, 721, 26
Greenhill, L. J., Booth, R. S., Ellingsen, S. P., et al. 2003, ApJ, 590, 162
Gültekin, K., Richstone, D. O., Gebhardt, K., et al. 2009a, ApJ, 695, 1577
Gültekin, K., Richstone, D. O., Gebhardt, K., et al. 2009b, ApJ, 698, 198
Häring, N. & Rix, H.-W. 2004, ApJ, 604, L89
Herrnstein, J. R., Moran, J. M., Greenhill, L. J., & Trotter, A. S. 2005, ApJ, 629, 719

Hirschmann, M., Khochfar, S., Burkert, A., et al. 2010, MNRAS, 407, 1016
Hwang, H. S., Lee, M. G., Park, H. S., et al. 2008, ApJ, 674, 869
Jahnke, K. & Maccio, A. 2010, arXiv:1006.0482
Kormendy, J., Bender, R., Evans, A. S., & Richstone, D. 1998, AJ, 115, 1823
Kormendy, J. & Gebhardt, K. 2001, in American Institute of Physics Conference Series, Vol. 586, 20th Texas Symposium on relativistic astrophysics, ed. J. C. Wheeler & H. Martel, 363–381
Kormendy, J. & Richstone, D. 1995, ARA&A, 33, 581
Kronawitter, A., Saglia, R. P., Gerhard, O., & Bender, R. 2000, A&AS, 144, 53
Kuo, C. Y., Braatz, J. A., Condon, J. J., et al. 2011, ApJ, 727, 20
Lauer, T. R., Ajhar, E. A., Byun, Y., et al. 1995, AJ, 110, 2622
Lauer, T. R., Faber, S. M., Gebhardt, K., et al. 2005, AJ, 129, 2138
Magorrian, J., Tremaine, S., Richstone, D., et al. 1998, AJ, 115, 2285
Marconi, A., Capetti, A., Axon, D. J., et al. 2001, ApJ, 549, 915
Marconi, A. & Hunt, L. K. 2003, ApJ, 589, L21
McConnell, N. J., Ma, C., Graham, J. R., et al. 2011, ApJ, 728, 100
Méndez, R. H., Riffeser, A., Kudritzki, R., et al. 2001, ApJ, 563, 135
Méndez, R. H., Teodorescu, A. M., & Kudritzki, R. 2008, ApJS, 175, 522
Méndez, R. H., Teodorescu, A. M., Kudritzki, R., & Burkert, A. 2009, ApJ, 691, 228
Navarro, J. F., Frenk, C. S., & White, S. D. M. 1996, ApJ, 462, 563
Pellegrini, S., Baldi, A., Kim, D. W., et al. 2007, ApJ, 667, 731
Peng, C. Y. 2007, ApJ, 671, 1098
Pierce, M., Beasley, M. A., Forbes, D. A., et al. 2006, MNRAS, 366, 1253
Pinkney, J., Gebhardt, K., Bender, R., et al. 2003, ApJ, 596, 903
Press, W. H., Teukolsky, S. A., Vetterling, W. T., & Flannery, B. P. 1992, Numerical recipes in C. The art of scientific computing, ed. Press, W. H., Teukolsky, S. A., Vetterling, W. T., & Flannery, B. P.
Richstone, D., Gebhardt, K., Aller, M., et al. 2004, arXiv:0403257
Richstone, D. O. & Tremaine, S. 1988, ApJ, 327, 82
Rix, H., de Zeeuw, P. T., Cretton, N., van der Marel, R. P., & Carollo, C. M. 1997, ApJ, 488, 702
Romanowsky, A. J., Douglas, N. G., Arnaboldi, M., et al. 2003, Science, 301, 1696
Schwarzschild, M. 1979, ApJ, 232, 236
Shapiro, K. L., Cappellari, M., de Zeeuw, T., et al. 2006, MNRAS, 370, 559
Shen, J. & Gebhardt, K. 2010, ApJ, 711, 484
Silk, J. & Rees, M. J. 1998, A&A, 331, L1
Siopis, C., Gebhardt, K., Lauer, T. R., et al. 2009, ApJ, 693, 946
Soria, R., Fabbiano, G., Graham, A. W., et al. 2006, ApJ, 640, 126
Springel, V., Di Matteo, T., & Hernquist, L. 2005, ApJ, 620, L79
Thomas, J., Saglia, R. P., Bender, R., et al. 2005, MNRAS, 360, 1355
Thomas, J., Saglia, R. P., Bender, R., et al. 2007, MNRAS, 382, 657
Thomas, J., Saglia, R. P., Bender, R., et al. 2009, ApJ, 691, 770
Thomas, J., Saglia, R. P., Bender, R., et al. 2004, MNRAS, 353, 391
Tremaine, S., Gebhardt, K., Bender, R., et al. 2002, ApJ, 574, 740
Valluri, M., Merritt, D., & Emsellem, E. 2004, ApJ, 602, 66
van den Bosch, R. C. E. & de Zeeuw, P. T. 2010, MNRAS, 401, 1770
van der Marel, R. P., Cretton, N., de Zeeuw, P. T., & Rix, H. 1998, ApJ, 493, 613
Weijmans, A., Cappellari, M., Bacon, R., et al. 2009, MNRAS, 398, 561
Woo, J., Treu, T., Barth, A. J., et al. 2010, ApJ, 716, 269
Zepf, S. E., Beasley, M. A., Bridges, T. J., et al. 2000, AJ, 120, 2928

Chapter 8

Conclusions & Outlook

8.1. Summary

In this thesis I studied various topics in the general framework of supermassive black holes, their properties and demographics. These range from detailed dynamical studies of local quiescent galaxies and their central black holes, over a statistical study of the $z < 0.3$ optical type 1 AGN population, to an investigation on black hole - galaxy coevolution, affecting both, quiescent and active black holes. My results can be summarised as follows:

8.1.1. Local AGN distribution functions

I utilised the well defined optically selected type 1 AGN sample of the Hamburg/ESO survey for an investigation of the local ($z \approx 0$) AGN and active SMBH demography. The sample contains 329 quasars and Seyfert 1 galaxies with $z < 0.3$, selected from an effective area of almost 7000 deg^2. An important statistical quantity are the distribution functions of the AGN properties. These properties are first of all the AGN luminosity, but also the direct physical quantities, black hole mass and accretion rate.

In Chapter 2 I determined the local AGN luminosity function (LF), using common methods. I used broad band B_J magnitudes and AGN broad Hα emission line luminosities, giving consistent results. I combined my results with the low-luminosity AGN luminosity function from the SDSS by Hao et al. (2005a) and constructed a single $z = 0$ AGN LF spanning more than 4 orders of magnitude. My work provides a well-determined local optical AGNLF and thereby resolves a long-standing problem of AGN demographics. The shape of the local AGNLF shows only mild curvature, distinct from the LF at higher redshift. This is strong evidence for luminosity-dependent evolution and therefore for "AGN cosmic downsizing".

However, the knowledge of the AGNLF alone is not sufficient for a full understanding of black hole demographics and black hole growth. In the LF, black hole mass and black hole accretion rate are degenerate, and a separate assessment of their distribution functions is required. In Chapter 3 I tackled this issue for the same low-redshift type 1 AGN sample of the Hamburg/ESO survey. Firstly, I estimated black hole masses and Eddington ratios for the same low redshift AGN sample, employing the "virial method" on the broad Hβ line. Secondly, it is important to clearly define what we mean by an *active* black hole. Detailed studies of apparently normal galaxies often reveal AGN at low levels (e.g. Ho et al. 1997; Soria et al. 2006; Gallo et al. 2010). I chose to define nuclear activity by the Eddington ratio and employ a lower Eddington ratio cut of 0.01 as a practical definition of an *active* black hole. With this definition, flux-limited AGN samples are systematically devoid of active black holes with low mass and low Eddington ratio, as they are selected on AGN luminosity and not on mass. I developed a maximum likelihood fitting method to estimate the *intrinsic* active black hole mass function (BHMF) and the Eddington ratio distribution function (ERDF) simultaneously. This approach takes the sample selection function fully into account and thus avoids a selection bias. I applied this method to the low-redshift HES AGN sample.

The *intrinsic* ERDF is well-characterised by a Schechter function with a low-λ slope of $\alpha_\lambda \approx -1.9$, thus with a wide distribution of Eddington ratios. I compared my results for the local active BHMF with the local total BHMF and found a decreasing active fraction with increasing black hole mass. This shows that presently the most massive black holes are less active, while low mass black holes exhibit a high degree of activity, supporting the current picture of anti-hierarchical growth of black holes. Further support for this picture comes from a comparison of our local active BHMF with the active BHMF at higher redshift from Vestergaard et al. (2008) and Vestergaard & Osmer (2009).

I confirmed the results from the maximum likelihood fits by performing extensive Monte Carlo simulations, comparing the predicted observable distributions with the observations.

In Chapter 4 I extended the maximum likelihood fitting method to incorporate measurement uncertainties, in particular the intrinsic scatter in the virial method. I found tentative evidence for a small intrinsic scatter in the virial method, $\sigma_{\rm VM} < 0.21$ at 1σ confidence. This is consistent with an independent direct estimate of $\sigma_{\rm VM}$. However, as this is a preliminary result, I have to verify or refute it in the future.

8.1.2. Selection effects in the black hole - bulge relations

The observed black hole - bulge relations and especially their redshift evolution put essential constraints on theoretical models of coeval growth of black holes and galaxies and on galaxy evolution models in general. Determining these relations observationally out to high redshift requires a proper handle on the underlying systematics and selection effects. In Chapter 5 I in-

vestigated the issue of selection effects in more detail, starting from the bivariate distribution function of black hole mass and spheroid property and applying a survey selection function to this distribution function. I identified several sources of potential bias.

- Only a fraction of all black holes are in an active stage at a particular point in time, and this fraction may depend on the mass of the black hole. In this case, there will be a bias on the AGN sample, depending on the mass dependence of the active fraction.
- AGN samples are selected based on their AGN luminosity, which is correlated with the black hole mass. This selection also modifies the bivariate distribution function and may bias the analysis. This bias is most severe for a bright AGN luminosity limit of the respective sample. Modelling this bias requires knowledge on the underlying distribution functions. These are reasonably well known at low redshift but only poorly known at high redshift.
- The cosmic evolution of the underlying distribution functions introduces an additional uncertainty, as the predicted sample bias changes with redshift. Without proper knowledge of the underlying distribution functions evolution in the black hole bulge relations and in the AGN population itself can be degenerate.

The deeper cause for all these sources of bias is the intrinsic scatter in the black hole-bulge relations. The size of the intrinsic scatter critically regulates the magnitude of the bias.

The mean offset from the local relation as well as the mean relation for the black hole mass at a given galaxy property are affected by these selection effects. On the other hand, the mean galaxy property at a given black hole mass is unaffected, offering an opportunity to circumvent AGN selection effects if the bivariate distribution is known.

I illustrated my approach to tackle the black hole - bulge relations by comparing particular model predictions with observational studies. A very strong positive evolution is implausible, whereas a range from mild evolution to no evolution at all is consistent with current observations. This work demonstrates the importance and complexity of sample selection effects on the study of the black hole bulge relations at high redshift. It should make a contribution to a better understanding of the high redshift black hole - bulge relations and the conclusions that can be drawn from its observation.

In Chapter 6 I used the framework presented before to develop a maximum likelihood fitting approach that can recover the intrinsic black hole-bulge relation from an observational sample that is affected by sample selection effects. I took care to include the effect of measurement uncertainties on the apparent black hole-bulge relation. I tested this method on Monte Carlo samples, thereby verifying its reliability, and presented a first application to observational studies. This method supplies an avenue for a strict statistical investigation of observational samples, rigorously accounting for the inherent selection effects.

8.1.3. Black hole masses from dynamical modelling with dark matter

While our knowledge of the black hole - bulge relations at high redshift is very limited and affected by systematics and selection effects, even the local relations are still not free of possible systematic effects. One such systematic effect on the determination of the black hole mass is the inclusion or exclusion of a dark matter halo in stellar dynamical modelling. This issue has been raised by Gebhardt & Thomas (2009) for the massive galaxy M87. I investigated the influence of accounting for a dark matter halo on stellar dynamical black hole masses in more detail. For this purpose I carefully modelled a sample of 12 galaxies, already previously analysed by Gebhardt et al. (2003), including and excluding a dark matter halo in the model. For the latter case I found a significant difference in the black hole mass for a large fraction of the objects, compared with the previous analysis. This difference is induced by the improved dynamical modelling code used, compared to previous work that apparently suffered from an incomplete orbit library. This emphasises the importance of a dense coverage of the phase space of the orbits, i.e. a complete orbit library.

When a dark matter halo is included into the modelling the determined black hole mass increases, but less than for M87. I found evidence that the systematic bias can be significant when the black hole's sphere of influence is only poorly resolved by the observations, whereas almost no bias in induced when the sphere of influence is well resolved. This result is further supported by the recent work of Gebhardt et al. (2011) on M87, using higher spatial resolution observations for the central region of the galaxy. With these improved data the dynamical black hole mass determination is not affected by the treatment of the dark matter halo, as it was the case before in the study by Gebhardt & Thomas (2009).

I also inspected the ramifications of the updated black hole masses for the black hole - bulge relations. While the pure inclusion of the updated masses only causes a mild change, accounting for a dark matter halo for the full stellar dynamical black hole mass sample may lead to an increase in the normalisation in the $M_\bullet - \sigma_*$ relation by $\sim 0.04 - 0.07$ dex.

8.2. Future perspectives

8.2.1. Systematics in the quiescent black hole - bulge relations

Before we can draw firm conclusions on the redshift evolution in the black hole - bulge relations, we have to ensure that the local relations itself are properly well known and are not affected by systematics and selection effects. I demonstrated that stellar dynamical black hole masses can be erroneous when an incomplete orbit library is used for the dynamical modelling and/or when the presence of a dark matter halo is neglected in the modelling. I present updated black hole masses for a sample of 12 galaxies, but there are more galaxies that may be affected by these systematics. A useful service would be to re-model more galaxies that are suspected to be affected by these effects consistently with an up-to-date dynamical modelling code, including a dark matter halo.

A potentially even more severe effect can be caused by selection effects on the local quiescent black hole sample. I briefly discussed the influence of a black hole's sphere of influence restriction on the inferred relations. A more detailed investigation of this issue will be valuable. In particular it should be studied whether the observed tight log-linear relation could be an artifact of the sample selection process and there may be a much wider intrinsic relation, as suggested by Batcheldor (2010). It is an interesting question if this potential intrinsic relation can be inferred from current observations when the selection function is properly taken into account. Furthermore, the results from AGN samples have to be considered as well, as these are unaffected by this kind of selection effect.

8.2.2. Constrain the growth of black holes through the cosmic ages

In this thesis, I developed a simple maximum likelihood method to determine the active BHMF and the ERDF jointly, and applied it to the local type 1 AGN sample from the Hamburg/ESO survey. However, the approach itself is very general and can easily be applied to other samples to determine the two distribution functions. Of special interest is the redshift evolution of the two functions, i.e. their determination from the local volume up to high redshift. This will break the degeneracy between black hole mass and accretion rate in the luminosity function and therefore can directly reveal the mass evolution and an AGN downsizing behaviour in black hole mass. Furthermore, the evolution of the ERDF may contain information about the physical mechanism of the accretion process in AGN and their redshift evolution.

A comprehensive study requires the coverage of a wide redshift range and in particular also a wide luminosity range, including the faint end of the luminosity function (LF). Otherwise, only the high mass, high Eddington ratio regime can be accessed. This is not achievable within a single survey, but demands the usage of multiple surveys. These surveys should ideally already provide a well-defined sample for which the AGNLF is already determined and the existence of spectral measurements for the black hole mass estimation. There are a number of surveys that are perfectly suited for such a global investigation of black hole growth through the cosmic ages.

The Hamburg/ESO survey (Wisotzki et al. 2000) provides especially the low redshift zero point for the study, established in this thesis, but also covers the bright end of the LF for $z \lesssim 3$. The LF for a subsample was presented in Wisotzki (2000) and in this thesis, black hole masses for $z < 0.3$ are presented in this thesis, the rest still has to be determined. The SDSS AGN luminosity function (Richards et al. 2006) covers in particular the bright end of the LF over a wide redshift range $0.3 < z < 5$. Black hole masses have been estimated for the SDSS QSOs (Vestergaard et al. 2008; Shen et al. 2008; Rafiee & Hall 2011). Kelly et al. (2010) already determined the BHMF and ERDF from this sample, using a different approach to ours. However, these surveys are not deep enough to cover the faint end of the LF at high redshift. Therefore they need to be augmented by deep surveys. This is in particular the VVDS AGN sample (Gavignaud et al. 2006). The LF was determined by Bongiorno et al. (2007), black hole mass estimates are given in Gavignaud et al. (2008). Also the COSMOS survey provides a faint AGN sample (Trump et al. 2009a; Merloni et al. 2010). The LF is not yet determined, but black hole masses have been estimated (Trump et al. 2009b; Merloni et al. 2010). Finally, also the 2SLAQ AGN sample (Croom et al. 2009a) can be added. The LF is presented in Croom et al. (2009b), the black hole masses in Fine et al. (2008, 2010). In general, also other samples could be included, as long as they constitute a well-defined sample and posses spectral measurements to estimate black hole masses and Eddington ratios. In the future, the HETDEX survey will make an important contribution to the faint end of the LF, and thus to the coverage of intermediate to low black hole masses and Eddington ratios. The AGN LF can be included as an additional observational constraint in redshift and luminosity ranges that are otherwise less well covered. Of course, special care has to be taken when combining different samples with different selection functions. Also, it needs to be ensured that the black hole mass estimates are as consistent as possible to avoid systematic effects and artifacts.

In the end, the combination of these samples will allow an unprecedented determination of the two underlying physical distribution functions of the AGN population and will bring our currently poor knowledge of the BHMF and ERDF to a similar level as that of the optical AGNLF.

8.2.3. Black hole growth in low luminosity AGN

The local BHMF and ERDF presented in this thesis are well established at high and intermediate masses and Eddington ratios, but suffer from low number statistics in the low mass / low Eddington ratio regime. This is caused by the lower luminosity limit of the Hamburg/ESO survey sample. Probing fainter luminosities would resolve this issue. A better coverage of the low mass, low Eddington ratio regime will also allow to probe for a mass dependence in the ERDF or an Eddington ratio dependence in the BHMF. Such a faint type 1 AGN sample can be extracted from the SDSS galaxy catalogue (Hao et al. 2005b; Greene & Ho 2007), which will directly continue the AGN luminosity coverage to low levels. This will improve the determination of the local BHMF and ERDF, especially at the low mass, low Eddington ratio end.

8.2.4. Black hole growth in obscured and unobscured AGN

Broad line AGN samples do not provide a complete census of growing black holes, as obscured (type 2) AGN are missing from these samples. This AGN class can be selected from galaxy samples using emission-line diagnostic diagrams. The local active BHMF and also the ERDF of type 2 AGN have already been studied before (Heckman et al. 2004; Yu et al. 2005; Kauffmann & Heckman 2009), but not jointly, but rather by employing a simple binning approach. An interesting prospect is to use either their data or an updated type 2 AGN sample, based on the SDSS DR7, to determine the active BHMF and ERDF of type 2 AGN jointly by my maximum likelihood approach, thus consistent with the type 1 AGN sample. In particular, this can be combined with my results on the type 1 AGN sample to derive at

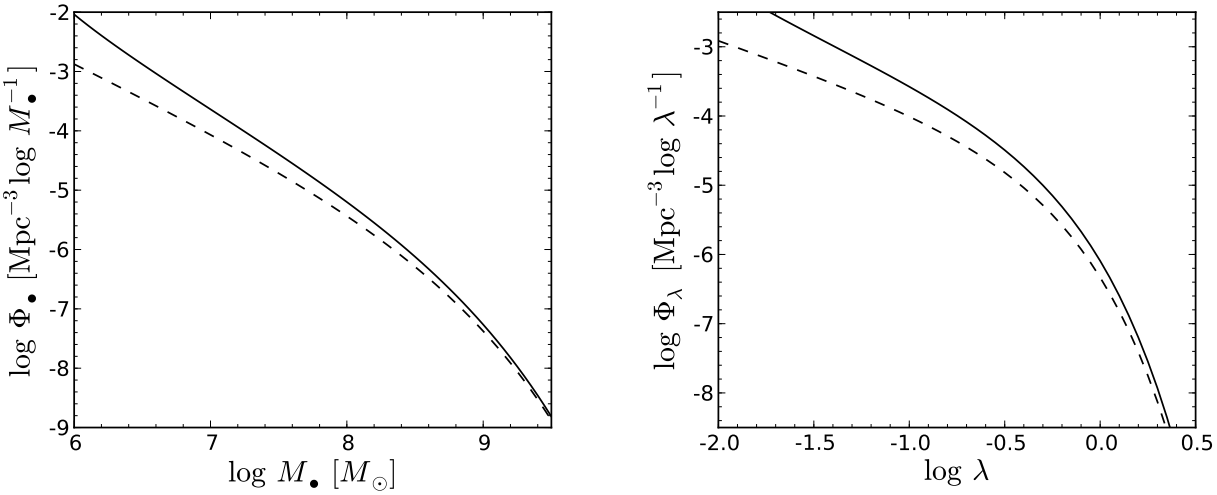

Fig. 8.1. Illustrative prediction of the type 1 + type 2 AGN active BHMF (left panel) and ERDF (right panel), derived from our type 1 AGN distribution functions and applying the luminosity dependent obscuration correction from Hasinger (2008). The solid line shows the type 1 + type 2 AGN distribution functions and the dashed line gives the type 1 AGN only distribution functions.

a full census of all local active black holes, directly comparable to theoretical model predictions. Also differences in the black hole properties of type 1 and type 2 AGN can be investigated. Furthermore, the type 2 fraction is known to be luminosity dependent, decreasing with increasing luminosity (e.g. Simpson 2005; Hasinger 2008). This study would be able to distinguish between a true luminosity dependence, a black hole mass dependence or an Eddington ratio dependence of the type 2 fraction. This should improve our picture of AGN unification and their physical drivers.

As an illustration, Fig. 8.1 shows a prediction for the total (type 1 and type 2) BHMF and ERDF, applying the luminosity dependent type 2 fraction from Hasinger (2008) to the type 1 BHMF and ERDF determined in this thesis. Note that the X-ray type 2 fraction may miss a population of optically identified obscured AGN (e.g. Reyes et al. 2008) and thus Fig. 8.1 should only be taken as illustrative outlook on the result of such an analysis. For a true luminosity dependence both, BHMF and ERDF for the total population, should be steeper at the low mass / low Eddington ratio end, compared with the type 1 AGN distribution functions.

References

Batcheldor, D. 2010, ApJ, 711, L108
Bongiorno, A., Zamorani, G., Gavignaud, I., et al. 2007, A&A, 472, 443
Croom, S. M., Richards, G. T., Shanks, T., et al. 2009a, MNRAS, 392, 19
Croom, S. M., Richards, G. T., Shanks, T., et al. 2009b, MNRAS, 399, 1755
Fine, S., Croom, S. M., Bland-Hawthorn, J., et al. 2010, MNRAS, 409, 591
Fine, S., Croom, S. M., Hopkins, P. F., et al. 2008, MNRAS, 390, 1413
Gallo, E., Treu, T., Marshall, P. J., et al. 2010, ApJ, 714, 25
Gavignaud, I., Bongiorno, A., Paltani, S., et al. 2006, A&A, 457, 79
Gavignaud, I., Wisotzki, L., Bongiorno, A., et al. 2008, A&A, 492, 637
Gebhardt, K., Adams, J., Richstone, D., et al. 2011, ApJ, 729, 119
Gebhardt, K., Richstone, D., Tremaine, S., et al. 2003, ApJ, 583, 92
Gebhardt, K. & Thomas, J. 2009, ApJ, 700, 1690
Greene, J. E. & Ho, L. C. 2007, ApJ, 667, 131
Hao, L., Strauss, M. A., Fan, X., et al. 2005a, AJ, 129, 1795
Hao, L., Strauss, M. A., Tremonti, C. A., et al. 2005b, AJ, 129, 1783
Hasinger, G. 2008, A&A, 490, 905
Heckman, T. M., Kauffmann, G., Brinchmann, J., et al. 2004, ApJ, 613, 109
Ho, L. C., Filippenko, A. V., & Sargent, W. L. W. 1997, ApJ, 487, 568
Kauffmann, G. & Heckman, T. M. 2009, MNRAS, 397, 135
Kelly, B. C., Vestergaard, M., Fan, X., et al. 2010, ApJ, 719, 1315
Merloni, A., Bongiorno, A., Bolzonella, M., et al. 2010, ApJ, 708, 137
Rafiee, A. & Hall, P. B. 2011, arXiv:1104.1828
Reyes, R., Zakamska, N. L., Strauss, M. A., et al. 2008, AJ, 136, 2373
Richards, G. T., Strauss, M. A., Fan, X., et al. 2006, AJ, 131, 2766
Shen, Y., Greene, J. E., Strauss, M. A., Richards, G. T., & Schneider, D. P. 2008, ApJ, 680, 169
Simpson, C. 2005, MNRAS, 360, 565
Soria, R., Fabbiano, G., Graham, A. W., et al. 2006, ApJ, 640, 126
Trump, J. R., Impey, C. D., Elvis, M., et al. 2009a, ApJ, 696, 1195
Trump, J. R., Impey, C. D., Kelly, B. C., et al. 2009b, ApJ, 700, 49
Vestergaard, M., Fan, X., Tremonti, C. A., Osmer, P. S., & Richards, G. T. 2008, ApJ, 674, L1
Vestergaard, M. & Osmer, P. S. 2009, ApJ, 699, 800
Wisotzki, L. 2000, A&A, 353, 853
Wisotzki, L., Christlieb, N., Bade, N., et al. 2000, A&A, 358, 77
Yu, Q., Lu, Y., & Kauffmann, G. 2005, ApJ, 634, 901

Acknowledgements

First and foremost I want to thank my supervisor Lutz Wisotzki for all the support, good advice, encouragement, criticism and fruitful discussions throughout my time at the AIP. His knowledge, experience and comments were always essential input and stimulation for my work.
I want to thank the Deutsche Forschungsgemeinschaft (DFG) under its priority programme SPP1177 and the Deutscher Akademischer Austauschdienst (DAAD) for their financial support. I am grateful to the DAAD for funding my research stay at the University of Texas at Austin and to Lutz Wisotzki and Karl Gebhardt who made this stay possible for me. This has been a wonderful experience I do not want to miss. I also want to thank Karl for the support and encouragement he gave my during my time in Austin and beyond. I am thankful to the University of Texas at Austin for hosting me and to their staff, scientists and students for their support and the warm welcome they gave to me. I also want to express my gratitude to all the great people I met in Austin that made my stay there so pleasant, in particular to Petra Nesensohn and Mari Garaas Løchen.
I am deeply grateful to my current and former colleagues at the AIP, especially to Isabelle Gavignaud, Natasha Maddox, Bernd Husemann, Sebastian Kamann, Aldo Dall'Aglio, Dasha Dubinovska, Gabor Worseck, Malte Schramm and Jakob Walcher for their advice, discussions or simply friendship they shared with me. It was a pleasure and honour to work with all of you. Special thanks goes to Natasha Maddox for sharing her language skills with me that improved the clarity of my papers. Much thanks goes to my friends and former fellow students at Potsdam University, Matthias Müller, Marcel Kappel, Marc Herzog, David Haack, Kay Bergemann and Falk Dambowski for their support and their contribution to the great time I had in Potsdam. I am indebted to my family, in particular to my parents and my brother for their steady support, encouragement and love. Thank you.

List of publications

Refereed Publications

- Schulze A. & Gebhardt K.: “Effect of a dark matter halo on the determination of black hole masses”, 2011, ApJ, 729, 21

- Schulze A. & Wisotzki L.: “Low redshift AGN in the Hamburg/ESO Survey: II. The active black hole mass function and the distribution function of Eddington ratios”, 2010, A&A 516, 87

- Schulze A., Wisotzki L. & Husemann B.: “Low redshift AGN in the Hamburg/ESO Survey: I. The local AGN luminosity function”, 2009, A&A 507, 781

Non-refereed Publications

- Schulze, A., & Wisotzki, L.: “An Estimate of the Local Active Black Hole Mass Function and the Distribution Function of Eddington Ratios”, 2010, IAU Symposium, 267, 266

- Schulze A. & Wisotzki L.: “The mass function of local active black holes”, 2008, Memorie della Societa Astronomica Italiana, 79, 1318